

# **Dynamics of Stratifying Foam Films**

BY

YIRAN ZHANG

B. Eng., Southeast University, 2010

M.S., New Jersey Institute of Technology, 2012

THESIS

Submitted as a partial fulfillment of the requirements  
for the degree of Doctor of Philosophy of Chemical Engineering  
in the Graduate College of the  
University of Illinois at Chicago, 2016

Chicago, Illinois

Defense Committee:

Vivek Sharma, Chair and Advisor  
Belinda S. Akpa  
Ying Liu  
Ludwig C. Nitsche  
Lewis E. Wedgewood  
Mark Schlossman, Physics

To my beloved parents

张钢平 and 陆敏,

and wife

冯莹.

Thank you for all the love and support.

## ACKNOWLEDGEMENTS

It is a great pleasure express my deep sense of gratitude to my thesis advisor Dr. Vivek Sharma, for his continuous support of my PhD study and research. His passion, patience and immense knowledge inspired me to learn and explore a wide range of research topics. Under his guidance, I transformed from a student to a real scientific researcher. I was privileged to have him not only as my academic advisor, but also as a mentor for life.

I would also like to thank the rest of my thesis committee: Dr. Belinda S. Akpa, Dr. Ying Liu, Dr. Ludwig C. Nitsche, Dr. Lewis E. Wedgewood, and Dr. Mark Schlossman, for their encouragement, insightful comments, and stimulating questions.

My sincere thanks to every member of the ODES Soft Matter research group. I am grateful to Subinuer Yilixiati for her insights on thin film thermodynamics, and for performing many experiments on stratification with me. I thank Collin Pearsall, Adam Lewis and Rabees Rafiq for helping with the foam film experiments. I also thank Jelena, Nallely, Prerana, Tiep, Mohammed, Prasanth, Norman, Billy, Luna, Camila, Nikhila, Akshaya, and many more graduate and undergraduate students, for broadening my knowledge with interesting discussions on a variety of research topics, for their tremendous help inside and outside the laboratory, and for keeping me company and keeping this four-year journey fun.

I thank the staff members of the Department of Chemical Engineering for their constant support in administration, laboratory and IT. My special thanks to Will Abbott-Klostermann for the help in building in-house instruments, and for all the informative discussions on mechanical and electrical work.

My greatest gratitude is to my parents, Min Lu and Gangping Zhang, and my wife Ying Feng, for their unconditional love and encouragement. My parents worked hard throughout their lives to make my life comfortable and worthwhile. I learned from my mother to stay patient and to pay attention to details, and from my father to stay optimistic and curious. I dedicate this thesis and all my accomplishment to them. Marrying to my wife was the absolute highlight of my four years in graduate school. Although we were temporarily separated by the ocean, our hearts are always together. Her faith in me is what kept me confident, and her love is what kept me motivated. I could not imagine finishing this thesis research without her spiritual support.



# LIST OF CONTENTS

<u>CHAPTER</u>	<u>PAGE</u>
CHAPTER 1. INTRODUCTION AND LITERATURE REVIEW .....	1
1.1 Background .....	1
1.2 Stratification of thin liquid films .....	5
1.2.1 Early studies on thin films and discovery of stratification phenomenon .....	5
1.2.2 Modern view on thin film stratification .....	8
1.2.3 Models for dynamics of stratifying films .....	10
1.3 Experimental methods for foam films .....	15
1.3.1 Thin film apparatus .....	16
1.3.2 Thickness characterization of foam films .....	20
1.4 Disjoining pressure in foam films .....	22
1.4.1 DLVO and steric forces .....	24
1.4.2 Supramolecular structural oscillatory disjoining pressure .....	27
1.5 Thin film hydrodynamics .....	30
1.5.1 Thin film hydrodynamic equation .....	33
1.5.2 Boundary conditions at gas-liquid or solid-liquid interfaces .....	36
1.5.3 Structures and patterns formed during dewetting of supported thin films .....	45
1.6 Objectives of this study .....	48
CHAPTER 2. CHARACTERIZATION OF STRATIFYING FOAM FILMS USING INTERFEROMETRY DIGITAL IMAGING OPTICAL MICROSCOPY (IDIOM) .....	52
2.1 Introduction .....	52
2.2 Experimental method .....	53
2.2.1 Materials .....	53
2.2.2 Experimental setup .....	54
2.2.3 Interferometry digital imaging optical microscopy (IDIOM) .....	58
2.3 Results .....	61
2.3.1 Observation of stratification in foam films .....	61
2.3.2 Thickness measurement .....	63
2.3.3 Rich dynamics of stratifying films revealed by IDIOM .....	66

## LIST OF CONTENTS (Continued)

<u>CHAPTER</u>	<u>PAGE</u>
2.4 Discussion.....	70
2.4.1 Applicability of IDIOM .....	70
2.4.2 Error estimation .....	73
2.4.3 Nanoscopic structures resolved by IDIOM.....	76
2.5 Conclusions.....	78
CHAPTER 3. DOMAIN EXPANSION DYNAMICS IN STRATIFYING FOAM FILMS .....	80
3.1 Introduction.....	80
3.2 Methods .....	81
3.2.1 Experimental setup.....	81
3.2.2 Domain tracking.....	82
3.3 Results.....	84
3.3.1 Stratification observed with customer-grade camera.....	84
3.3.2 Domain expansion kinetics: influence of the Plateau border.....	85
3.3.3 Domain expansion kinetics: white spot formation.....	89
3.3.4 Similarities between two kinetic transition.....	92
3.3.5 Concentration dependence .....	94
3.4 Discussion.....	96
3.5 Conclusions.....	101
CHAPTER 4. FORMATION AND EVOLUTION OF A RIDGE DURING DOMAIN GROWTH IN STRATIFYING FOAM FILMS .....	103
4.1 Introduction.....	103
4.2 Methods .....	105
4.3 Axisymmetric ridge shape and its evolution.....	107
4.3.1 Equilibrium disjoining pressure measurement.....	107
4.3.2 Ridge shape and evolution .....	108
4.3.3 Thin film equation and scaling analysis of the ridge formation .....	114
4.3.4 Asymptotic solutions of the ridge .....	117
4.3.5 Discussion .....	125

## LIST OF CONTENTS (Continued)

<u>CHAPTER</u>	<u>PAGE</u>
4.4 The ridge after topological instability.....	130
4.4.1 Formation of white spots within the ridge .....	130
4.4.2 Evolution of the remaining ridge after instability .....	134
4.5 Conclusions.....	138
 CHAPTER 5. MODELING OF THE RIDGE FORMATION AND GROWTH DURING DOMAIN GROWTH IN STRATIFYING FOAM FILMS .....	 140
5.1 Introduction.....	140
5.2 Model and numerical methods.....	142
5.2.1 Thin film equation.....	142
5.2.2 Disjoining pressure isotherm .....	145
5.2.3 Model setup for domain growth dynamics .....	150
5.2.4 Numerical solving scheme .....	153
5.3 Results and discussion .....	155
5.3.1 Ridge shape and evolution compared with experimental results.....	155
5.3.2 Discussion on boundary conditions .....	158
5.3.3 Force contributions and validation of asymptotic solutions .....	162
5.3.4 Thickness and concentration dependence of the ridge shape .....	169
5.3.5 Ridge shape at later time.....	174
5.3.6 Limitations of 1D thin film model .....	178
5.4 Conclusions.....	181
 CHAPTER 6. CONCLUSIONS .....	 184
 REFERENCES .....	 188
 APPENDIX.....	 202
 VITA .....	 215

## LIST OF TABLES

<u>TABLE</u>	<u>PAGE</u>
Table I Advantages and disadvantages of each thin film apparatus .....	19
Table II Summary of mobility factor calculated for drainage of thin film containing soluble surfactant.....	44
Table III List of cameras tested with IDIOM protocol and their specification .....	70
Table IV Ideal minimum measurable thickness and average intrinsic error in IDIOM method ..	74
Table V Comparison of contact line velocity with white spots and with contact to the Plateau border. ....	94
Table VI Parameters used in the hydrodynamic equation and disjoining pressure estimation ..	153

## LIST OF FIGURES

<u>FIGURE</u>	<u>PAGE</u>
Figure 1.1 Structure of foams on different length scales. ....	2
Figure 1.2 Surfactant used in this study. ....	4
Figure 1.3 Early photographs of stratification in foam films. ....	7
Figure 1.4 Illustration of spherical micelles form layered structure in a stratifying foam film. ....	9
Figure 1.5 Illustration of the diffusive osmotic mechanism of domain formation and growth. ...	11
Figure 1.6 Time evolution of the radial thickness profile during domain nucleation and growth. .....	13
Figure 1.7 Different types of thin film apparatus. ....	16
Figure 1.8 Illustration of the interference between the light reflected from two gas-liquid interfaces. .....	21
Figure 1.9 Schematic illustration of a typical disjoining pressure isotherm. ....	26
Figure 1.10 Disjoining pressure isotherm in foam film made with 100 mM SDS. ....	27
Figure 1.11 Different geometries in thin film drainage. ....	31
Figure 1.12 The free-standing thin film geometry used for deriving the thin film equation. ....	33
Figure 1.13 The geometry of thin film supported on a solid substrate. ....	35
Figure 1.14 Navier slippage model. ....	39
Figure 1.15 Formation, shape and instability of the ridge formed during thin film dewetting. ...	47
Figure 2.1 Schematic of the experimental setup consisting thin film holding cell, reflected light microscope, and high resolution digital imaging. ....	54
Figure 2.2 Schematic of Scheludko-type cell for forming a single thin film and controlling its drainage. ....	55
Figure 2.3 Porous plate film holding cell. ....	57
Figure 2.4 Comparison between (a) conventional interferometry methods and (b) IDIOM. ....	60

## LIST OF FIGURES (Continued)

<u>FIGURE</u>	<u>PAGE</u>
Figure 2.5 Montage of foam film stratification in SDS 50mM solution. ....	62
Figure 2.6 Thickness evolution in the stratifying foam film. ....	64
Figure 2.7 The step sizes obtained by IDIOM compared with conventional interferometry results. .....	65
Figure 2.8 Illustration of the balance between applied capillary pressure and disjoining pressure at discrete film thicknesses. ....	66
Figure 2.9 Micrographs showing the stratification of a thin film made from SDS 50 mM solution, and the associating 3D thickness maps for the entire film area. ....	67
Figure 2.10 Comparison between thickness profile measured by conventional interferometry methods and IDIOM. ....	69
Figure 2.11 Calibration for camera output RGB values. ....	72
Figure 2.12 The intrinsic error in thickness measurement. ....	74
Figure 2.13 Histogram of background intensity recorded in individual pixels of the 12-bit high speed camera. ....	75
Figure 2.14 Shape of nanoscopic structures formed during domain growth. ....	77
Figure 3.1 Domain tracking scheme to separate regions of domain, film and Plateau borders....	82
Figure 3.2 Stratification of thin film with 100 mM SDS solution, captured with the Nikon D5200 camera. ....	84
Figure 3.3 Domain expansion kinetics in a 100 mM SDS foam film. ....	86
Figure 3.4 The time evolution of domain boundary in the two distinct regimes. ....	88
Figure 3.5 Domain expansion kinetics in a 25 mM SDS foam film. ....	89
Figure 3.6 Different types of white spot formation. ....	90
Figure 3.7 Similarities between domain growth with white-spots formed and in contact with the Plateau border. ....	92

## LIST OF FIGURES (Continued)

<u>FIGURE</u>	<u>PAGE</u>
Figure 3.8 Domain growth dynamics when both topological instability and contacting the Plateau border occur successively. ....	94
Figure 3.9 Concentration dependence of (a) apparent diffusivity $D$ in Regime A and (b) apparent contact line velocity in Regime B. ....	95
Figure 4.1 Equilibrium disjoining pressure measurement in stratifying foam film. ....	107
Figure 4.2 Domain growth and ridge formation during stratification. ....	109
Figure 4.3 Time evolution of the axisymmetric ridge thickness profile. ....	110
Figure 4.4 The shape and its evolution of the ridge formed around a growing domain. ....	111
Figure 4.5 Volume conservation during domain expansion. ....	114
Figure 4.6 The build-up part of the ridge profiles plotted as $h - h_{\infty}$ vs. $r - R$ . ....	119
Figure 4.7 Rescaled ridge thickness profiles plotted as $h - h_{\infty}$ vs. $r / (Dt)^{1/2}$ . ....	124
Figure 4.8 Formation of white spots. ....	130
Figure 4.9 Time and spatial evolution of maximum thickness $h_{\max}$ within the ridge region. ....	132
Figure 4.10 Time dependence of maximum thickness in two white spots, $h_{\max}$ . ....	134
Figure 4.11 Distribution of change in liquid volume in different part of the domain growth geometry. ....	135
Figure 4.12 Evolution of the remaining ridge after topological instability. ....	137
Figure 5.1 Comparison between IDIOM measured $\Delta h$ and $h_0$ with predictions from Equation (5.11) and Equation (5.16), as a function of surfactant concentration. ....	149
Figure 5.2 Illustration of the starting film thickness for domain growth study. ....	151
Figure 5.3 Comparison between experimental and numerical ridge profiles and evolution. ....	155

## LIST OF FIGURES (Continued)

<u>FIGURE</u>	<u>PAGE</u>
Figure 5.4 Comparison of ridge shape (at $\bar{R} = 20$ ) obtained from experiment and numerical solution.....	157
Figure 5.5 Comparison of ridge shapes solved from different models for boundary condition on gas-liquid interfaces. ....	162
Figure 5.6 Comparison of the magnitude of three terms in Equation (5.6). ....	164
Figure 5.7 Asymptotic solution of the shape of the build-up part of the ridge. ....	165
Figure 5.8 Numerical resolved ridge thickness profiles plotted as $\bar{h}$ vs. $\bar{r}/(\bar{D}t)^{1/2}$ . ....	169
Figure 5.9 Effect of the number of micelle layer contained in the thin film, $n$ , on the ridge shape. ....	170
Figure 5.10 Effect of surfactant concentration on the ridge shape. ....	171
Figure 5.11 Dimensionless decay length, $\bar{\lambda}$ , obtained through numerically fitting. ....	172
Figure 5.12 The diffusive growth rate of domain expansion, $D = dR^2/dt$ , versus surfactant concentration, $c_s$ , from both experimental and numerical measurements. ....	174
Figure 5.13 Numerical ridge shape and evolution with $c_s = 70$ mM, $n = 2$ . ....	175
Figure 5.14 Time dependence of maximum thickness $\bar{h}_{\max}$ .....	176
Figure 5.15 Time dependence of thinner domain radius. ....	177
Figure 5.16 Example of axisymmetric ridge shape captured by 2D thin film model.....	179



## LIST OF ABBREVIATIONS

AFM	Atomic Force Microscopy
CBF	Common Black Film
CMC	Critical Micelle Concentration
CP-AFM	Colloidal-Particle Atomic Force Microscopy
DO	Diffusive Osmosis
ED	Thin Film Model by Erneux and Davis
IDIOM	Interferometry Digital Imaging Optical Microscopy
LUT	Look-up Table
NBF	Newton Black Film
PDE	Partial Differential Equation
RDI	Thin Film Model by Radoëv, Dimitrov and Ivanov
TEM	Transmission Electron Microscopy
TFB	Thin Film Balance
SDS	Sodium Dodecyl Sulfate
SFA	Surface Force Apparatus

## SUMMARY

Liquid foams are nearly indispensable in daily lives, in nature, as well as in numerous industrial processes. The stability and lifetime of foams is closely correlated with the drainage and stability of thin liquid films between adjacent gas bubbles. Free-standing thin liquid films (foam films) containing micelles, nanoparticles, polyelectrolyte-surfactant complexes or smectic liquid crystals undergo drainage in a discontinuous, step-wise fashion termed stratification. The oscillatory disjoining pressure, which originates from the layering of the aforementioned supramolecular structures under the thin film confinement, stabilizes the foam film at discrete thicknesses while destabilized it at thickness in between.

The stratification via layer-by-layer removal of the supramolecular structures displays rich patterns and dynamics, involving the coexistence and evolution of domains and nanostructures of discretely different thickness. We developed novel Interferometry Digital Imaging Optical Microscopy (IDIOM) protocols by combining the principle of interferometry, optical microscopy, and digital image analysis techniques. IDIOM is used to characterized the topography of stratifying free-standing foam films made from sodium dodecyl sulfate (SDS) micellar solutions with high spatial (1 nm in thickness and 0.5  $\mu\text{m}$  laterally) and temporal resolution (1 ms) for the first time. We constructed exquisite thickness maps of the film, recognized and followed the emergence and growth of nanoscopic ridges, mesas and craters during foam film stratification. In particular, the formation and evolution of craters (thinner domains) and ridges are analyzed.

## SUMMARY (Continued)

We find two distinct regimes in the expansion dynamics of a single thinner domain. Initially, the domain radius increases as  $R \propto t^{1/2}$ , with a constant apparent diffusivity (Regime A), after the domain comes in contact with the Plateau border surrounding the foam film, the boundary between the thinner domain and the rest of the film expands linearly over time, *i.e.*  $R \propto t$ , with a constant apparent contact line velocity (Regime B). For isolated domain, a similar transition could occur when a topological instability sets in at the domain boundary, which also leads to formation of white spots around the growing domain. The change in dynamics observed after domains contact with the Plateau border is reported and analyzed for the first time, and the similarities between two regime transitions, brought out by domain coalescence with the Plateau border and topological instability around isolated domain, are recognized and discussed.

Though the domain expansion dynamics and the scaling transitions are proposed theoretically to be linked to the existence of a ridge formed around the growing domain, experimental evidence of ridge formation is lacking in the literature. By utilizing IDIOM protocol, we visualize and characterize the nanoscale ridge formation and growth for the first time. The axisymmetric ridge formed has a highly asymmetric cross-sectional profile, with a sharp build-up from the thinner domain, and a slow decay from the ridge peak to the outside unperturbed film. The total width of the ridge exhibits the same time dependence as the domain radius evolution, *i.e.*  $R, W \propto t^{0.5}$ , while the maximum thickness of the ridge grows logarithmically, *i.e.*  $h_{\max} - h_{\infty} \propto \log t$ . Using lubrication-based thin film hydrodynamic equation and scaling analysis, two types of asymptotic behavior are recognized for different parts of the ridge profile. The ridge shape in the build-up part is time independent, with nearly constant apparent contact angle ( $\sim 0.2^\circ$ ), while the

## SUMMARY (Continued)

leeward part of the ridge shows a self-similar profile, and can be fitted by an approximated analytical asymptotic solution. A topological instability within the ridge can set in and lead to formation and growth of white spots (much thicker circular regions). The formation of white spots is found unlikely to be through Rayleigh-type instability of the ridge, but rather driven by the supramolecular structural disjoining pressure. The oscillatory nature of the disjoining pressure leads to rapid thickness jump during white spot growth, the range of which correspond to the unstable region of the disjoining pressure isotherm. On the other hand, the regions of the ridge unperturbed by white spot formation cease to grow in width and thickness after instability.

To gain more insight in the dynamics of foam film stratification, and to better understand the contribution of supramolecular structural disjoining pressure, we model the formation and evolution of ridges during domain growth with the thin film hydrodynamics equation. Using a semi-empirical estimation of the supramolecular structural oscillatory disjoining pressure, and no-slip boundary condition for the film interfaces, the thin film equation is solved numerically. The numerical results of ridge evolution, its concentration and thickness dependence, and instability at later stage, are all in quantitative agreement with experimental observations. Conversely, part of the experimentally resolved ridge shape can be fitted to the numerical thickness profiles to obtain values of decay length in the oscillatory disjoining pressure isotherm, which provides a valuable measure of the strength and range of the structural disjoining pressure, and cannot be determined accurately through direct equilibrium measurement.

# CHAPTER 1.

## INTRODUCTION AND LITERATURE REVIEW

### 1.1 Background

Liquid foams are nearly indispensable in daily lives, in nature, as well as in numerous industrial processes. Foams with varied stability are desirable for different applications: slow draining, more stable foams are desired in firefighting [1], mining industry [2], certain foods and beverages (*e.g.* beers) [3] and cosmetics [4,5], while rapid draining, less stable foams are preferred in champagnes [6] and for undesirable foams created by pollution in water bodies [7,8]. Understanding, and therefore controlling the stability and lifetime of foams, is a longstanding challenge, and one of the underlying motivations for this study.

Foams are colloidal dispersions of gas bubbles in a continuous liquid phase, where gas bubbles are separated by liquid thin films (foam films). In an absolute sense, all foams (as well as other colloidal dispersions like emulsions and colloidal sols) are thermodynamically unstable and will eventually phase separate [9]. The foams break down via three main processes: coalescence of gas bubbles resulting from the thinning and eventual rupture of foam films, drainage of bulk liquid through the foam structure, and disproportionation of bubbles due to gas diffusion between neighboring bubbles [10]. Practically however, these destabilization mechanisms can be significantly delayed to make foams relatively long-lived (timescale of minutes to hours to years), both by thermodynamic means (*e.g.* addition of surface active agent) and by hydrodynamic means (*e.g.* increasing liquid viscosity or modifying interfacial rheology).

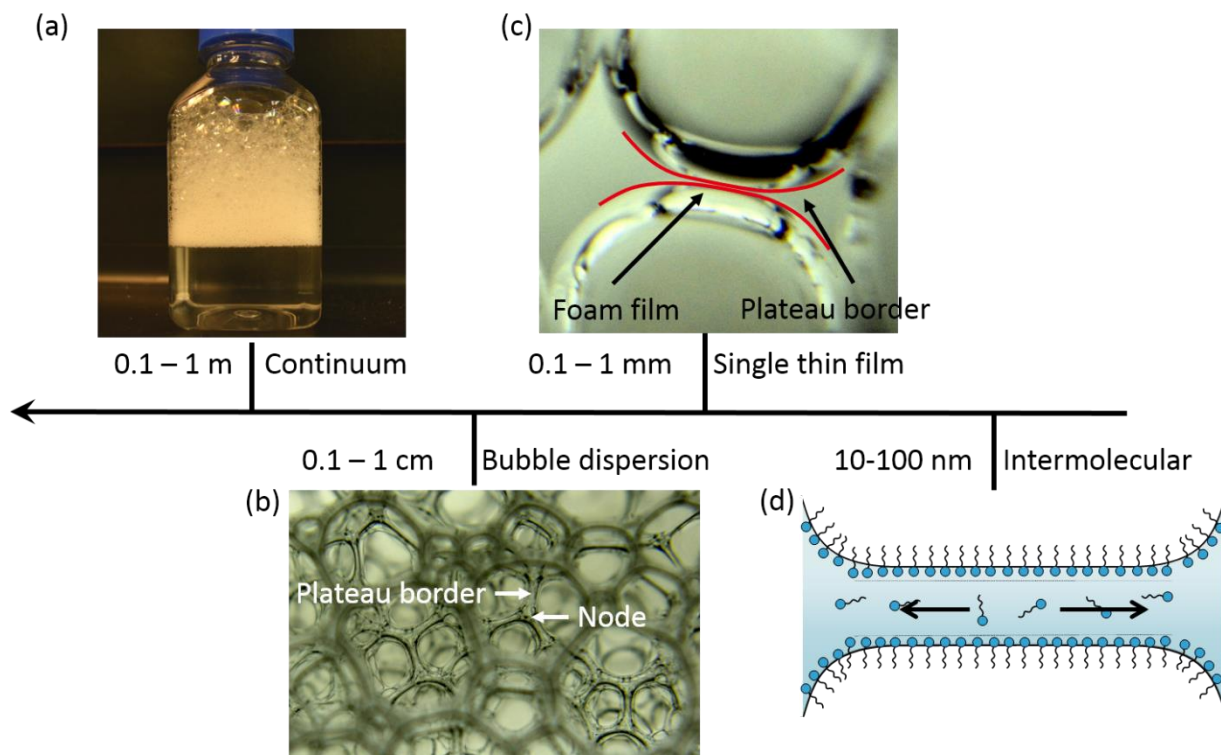


**Figure 1.1** Structure of foams on different length scales. (a) Foams can be treated as continuum fluid or porous media in the macroscopic level. (b) Local foam structure consists of gas bubbles separated by thin liquid films, and a network of Plateau borders and nodes. (c) Single foam film keeping two gas bubbles from coalescing, the film is connect to the thicker Plateau border around it. (d) The drainage and stability of a foam film can be modified by the addition of surfactants.

The thermodynamic and hydrodynamic properties of foams, and their evolution over time can be studied on multiple length scales (Figure 1.1). Macroscopically, at a length scale much larger than the bubble size (Figure 1.1a), foams appear homogenous and can be modeled as a flowing continuum with complex rheological properties, including viscoelasticity, yielding/jamming and thixotropy [11–13]. Conversely, the foams can be modeled as porous media to study the macroscopic flows through it [13,14]. On the length scale of a few bubble diameter (Figure 1.1b), foam structure comprises of an assembly of gas bubbles. The gas pockets are separated by thin liquid films, Plateau borders where three films meet, and vortices or nodes where four borders

meet. These structures undergo deformations and topological rearrangements in response to an applied outside stresses, in order to minimize the free energy of the system. The collective motion of these structures is related to the macroscopic rheological properties [15]. At the length scale of single bubble (Figure 1.1c), the basic building block of foam structure is two gas bubbles separated by a single liquid thin film in between. The thinning and stability of this foam film controls the rate of bubble coalescence, therefore is greatly correlated with the lifetime and stability of the macroscopic foam [16]. Capillary pressure originates from the two curved gas-liquid interfaces of the foam film. The gradient of the pressure drives liquid to drain from the foam film to the adjacent Plateau borders, and the film thins and eventually ruptures. Rheological properties of the thin liquid film (both interfacial and bulk rheology) affects drainage kinetics, and the lifetime of the foam [16,17]. When the thickness of the film approaches molecular length scales (typically  $< 100$  nm), film drainage can be further enhanced or suppressed by contributions from surface forces (see Section 1.4 for a review). Fundamental understanding of the nature of these surface forces and their manifestation in drainage dynamics of single foam film, is crucial to further our understanding of their effects on the stability of the macroscopic foams, as well as all the other colloidal systems [18]. It is one of the main objectives of this study to gain insights of the surface forces in foam films, through both experimental characterizations and theoretical modelling of the film drainage process.

Apart from the significant role played in foam, emulsion and other colloidal systems, the stability and dynamics of liquid thin films are also widely studied in many other contexts. The flow and dynamics of either free-standing films (*e.g.* foam film) or supported films (*e.g.* film on a solid substrate) are encountered in phenomena like liquid wetting/dewetting [19], film rupture [20]

and tears of wine [21], and are found in industrial applications like coating [22], printing [23] and nano-device fabrication, as well as in biological systems like lungs [24] and tear films [25–27].

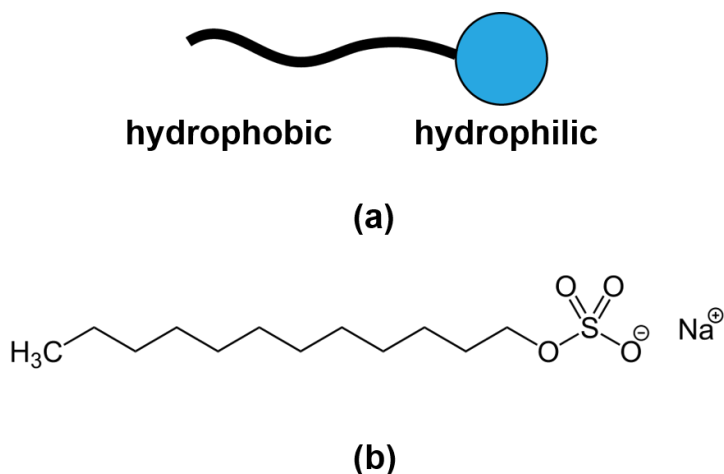


**Figure 1.2** Surfactant used in this study. (a) A schematic representation of surfactant molecule. The “head” is hydrophilic group while the “tail” is hydrophobic. (b) Molecular formula of ionic surfactant sodium dodecyl sulfate (SDS).

Foams are often formed with solutions containing amphiphilic surface-active agents, or surfactants (Figure 1.2). At the molecular level (Figure 1.1d), the surfactants adsorb to the gas-liquid interfaces, and reduce the surface tension [28]. During thinning of the foam film, the presence of surfactants affects both the capillary pressure and surface forces, and could also alter the rheological response of the interfaces as well as the bulk fluid [14,29,30].

Above a threshold value of surfactant concentration, known as critical micelle concentration (CMC), surfactant monomers in the bulk solution self-assemble into supramolecular structures (micelles) [9]. The micelle assembly gives rise to extra supramolecular structural



contribution to the surface forces in stabilizing the foam films. The manifestation of such structural forces in foam film drainage is a non-monotonic, step-wise thinning (called stratification), instead of a monotonic thickness observed in surfactant solution below CMC. The same stratification phenomenon also occurs in thin films (both foam and emulsion films) with nanoparticles, polyelectrolyte-surfactant mixtures, smectic liquid crystals, etc. (see the following sections for a detailed review). During the stratification process, rich and complex dynamics, including formation and evolution of various transient nanoscopic structures, can be observed [31]. Although the phenomenon of stratification has been reported for over a century and significant progress made in understanding its origin [32], the dynamics involved in the process are not yet fully explored and have many unresolved questions (outlined in Section 1.6). This thesis study attempts to further our knowledge of the hydrodynamics and thermodynamics involved in stratifying foam films, and address some of the unresolved problems in stratification dynamics.

## **1.2 Stratification of thin liquid films**

### **1.2.1 Early studies on thin films and discovery of stratification phenomenon**

The study of thin liquid films, their shapes, colors, as well as their dynamics and stability, have fascinated generations of scientists. Hooke [33] and Newton [34], in their pioneering work on optics and mechanics, discussed colors and patterns observed in soap films. In the *Opticks* [34], Newton related the color reflected from the thin film to its thickness and the refractive index of the medium, which is the underlying principle of modern day interferometry techniques for film thickness determination. He noted that the thinnest film appears “very black”, since it’s so thin

that all visible light interferes destructively. Today the thinnest (typically less than 7 nm), steric stabilized foam films are therefore named after him as Newton black film (NBF).

After one and a half century, Plateau [35] examined the thinning dynamics of soap bubbles and the formation of the black films on the top of the bubble. He estimated the thickness of the black films to be less than 100 nm. Suggesting the formation and stabilization of the black films is a result of molecular interactions between the two interfaces, he quoted half of the thickness as “the upper limit of the radius of significant activity of the molecular attraction.” Reinold and Rucker [36,37] later improved Plateau’s estimation with both optical and electric resistance measurements. They found the thickness to be  $< 20$  nm, and concluded that the black film is spatially uniform, with a sharp thickness transition and a distinct boundary to the rest thicker region of the film. Moreover, they reported the observation that “two different shades of black are ... frequently seen in a film” [37]. These findings led them to suggest the possibilities for molecular interactions to stabilize multiple film thicknesses while destabilizing films with thickness in between.

Johannott [38,39], at the turn of the 20th century, used the interferometer developed by A. A. Michelson, and quantified the thickness of “first” and “second” black film to be about 12 nm and 6 nm, respectively. In modern terms, the two films are likely to correspond to the electrostatically stabilized common black film (CBF) and the sterically stabilized Newton black film (NBF). Johannott observed a total of five different shades of black film beyond these two thickness layers, and therefore speculated that molecular forces alternate between attraction and repulsion as the thickness pass through different layers of black films. This forms the first report of foam film stratification.

The formation and coexistence of multiple black films was first documented as photographs by Stansfield [40] in a vertical, rectangular soap film in 1906, and later by Lawrence [41] in a horizontal circular film (Figure 1.3). These photographs clearly shows different shades of black or grey film, with distinct, mostly circular boundaries. The layers with different film thicknesses form complex mosaic patterns during the thinning process. Figure 1.3a captured the stratification taking place, with a circular, thinner (darker) domain growing on a thicker film. Around the darker domain, multiple white circular spots formed adjacent to the domain boundary. In this study, we found that these white spots are nanoscopic mesas. The formation of these white spots and their effects on dynamics of stratifying foam films are studied in detail, both experimentally and theoretically

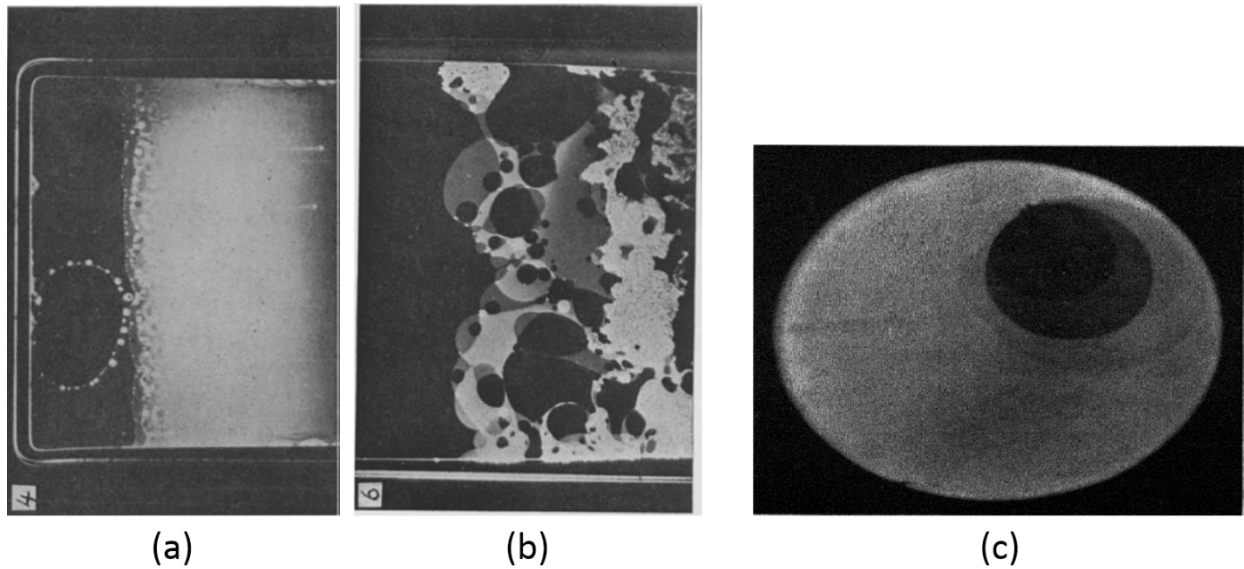


**Figure 1.3** Early photographs of stratification in foam films. (a) and (b) are reprinted from ref [40] (public domain), (c) is reprinted from ref [41] (public domain).

The next major contributions to the study of the stratification phenomena in soap films were made by Perrin [42], among others [43–45]. The thickness difference between layers was found to be a multiple of the same elementary thickness. Their studies suggested that stratification is a result of layer-by-layer removal of the lamella phase formed by surfactants. In his 1926 Nobel Prize lecture, Perrin included stratification as an evidence for molecular reality, and discontinuous and periodic structure of matter [46]. Numerous studies, *e.g.* ref [47–49], continued to investigate the stratification of thin films formed with smectic liquid crystals. Recent advances in this topic summarized in an extensive review by Oswald and Pieranski [50]. In this study we focus on stratifying foam film with isotropic systems containing supramolecular structures (*e.g.* micelles).

### **1.2.2 Modern view on thin film stratification**

The studies on surfactant concentration dependence of stratification phenomena, both in foam films [51,52] and emulsion films [53], showed the step-wise thinning phenomenon at surfactant concentrations below the concentration at which liquid crystalline phase forms in the bulk solution. Lyklema and Bruil [51] hypothesized that the confined environment imposed by the film surfaces promoted the lamella structure to form in thin films. However, the experimental [54,55] and theoretical work [56] done by Wasan, Nikolov and coworkers in the late 1980s demonstrated the stratification phenomenon in foam films made with particle suspensions, and revealed the fundamental role of laying of self-assembled supramolecular structures (*e.g.* micelles in surfactant solutions). They argued that the spherical micelles or nanoparticles form ordered structures under confinement, and give rise to the non-DLVO oscillatory structural disjoining pressure [56]. The pressure is an oscillatory function of film thickness, and stabilizes the foam film at discrete thicknesses while intermediate thicknesses are unstable, as shown schematically in

Figure 1.4. The layer-by-layer removal of these supramolecular structures results in the macroscopic step-wise thinning of the film.

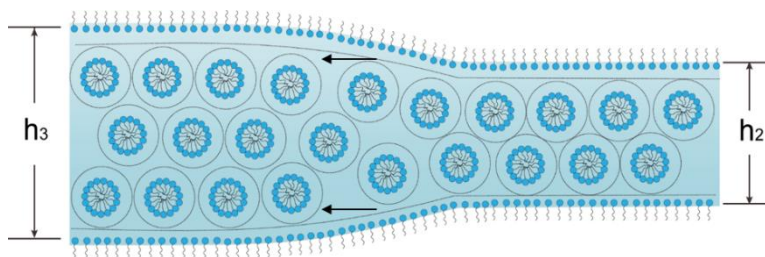


**Figure 1.4** Illustration of spherical micelles form layered structure in a stratifying foam film.

This explanation is supported by various experimental and theoretical evidences. In non-ionic systems, the thickness change of each step in stratification was found to correspond to the diameter of the micelle or colloidal particle [54]. The ordering of micelles or particles during stratification is also probed through scattering methods [57,58] and direct transmission electron microscopy (TEM) imaging of vitrified foam films [59]. The vitrified film made with micellar solutions showed “no bilayer (lamella structure) are present in the neighborhood of the film surface in the (tested) concentration range” [59]. This observation suggested the stratification is indeed due to the layered ordering of spherical micelles instead of surfactant bilayers.

In addition to the observations of ordering of micelle or colloidal particle, the oscillatory structural disjoining pressure resulted from the supramolecular ordering were also directly detected and measured. A brief review of the experimental and theoretical studies of this non-DLVO, structural disjoining pressure is provided in Section 1.4.2.

The stratification phenomena is universal in thin liquid films containing supramolecular structures [32]. It is observed not only in horizontal films (for most studies cited above), but also vertical film where the driving force of the film drainage is gravity [60]. Besides foam films, stratification is also reported in emulsion films [53,61], asymmetrical films (film with one gas-water interface and one water-oil interface) [62] and films supported by solid substrate [63]. In addition to surfactant micelles (both ionic and non-ionic) and colloidal particles, stratification also occurs in foam films made with protein aggregates [64], amphiphilic diblock copolymers [65], worm-like micelles [66], and polyelectrolyte-surfactant mixtures [67–70]. While certain proteins and copolymers form self-assembled near-spherical structures which can play a similar role as micelles formed with ionic surfactant, transient network structures formed in solutions of worm-like micelles and polyelectrolyte can also lead to film stratification [67,71]. The thickness steps in such systems match the correlation length found in neutron scattering of the bulk solution [72]. The extensive research on polyelectrolyte stabilized foam films is summarized in review by Kristen and von Klitzing [71].

### 1.2.3 Models for dynamics of stratifying films

While many studies have focused on the equilibrium thickness steps and the corresponding equilibrium disjoining pressure isotherm in stratifying foam films, the dynamics of stratification is not fully characterized and understood. During foam film stratification, the thickness transition proceeds through nucleation and expansion of single or multiple thinner, circular domains within the thicker film (*cf.* Figure 2.5). The growth dynamics of a single isolated domain is first characterized by Kralchevsky et al. [73] for micellar solution, they reported that the area the domain increases linearly over time,  $A \propto t$  (*i.e.* radius is proportional to square root of time,

$R \propto t^{1/2}$  ). Similar diffusive-like scaling is later reported for colloidal particle suspensions [74,75] and polyelectrolyte-surfactant mixtures [69,76,77]. Sonin and Langevin [78] first reported that an alternative linear scaling,  $R \propto t$ , is observed in some films, after the growing domain reaches a certain “critical size” and one or multiple white circular spots appear around the domain. The white spots have been termed lenses, pancakes, droplets and globules in the literature [10,75,76,78,79], and they appear white and brighter due to their much larger thicknesses compared to the rest of the film.

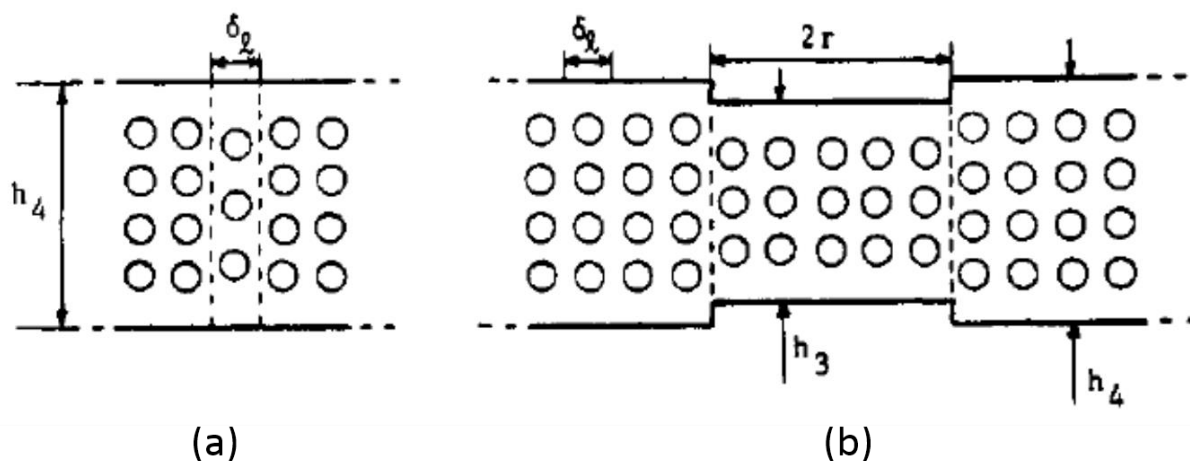


**Figure 1.5** Illustration of the diffusive osmotic mechanism of domain formation and growth. (a) A three-layered vacancy site is formed after one micelle has left the four-layered thin film. (b) The vacancies aggregate to form a thinner domain containing three layers of micelles. Reprinted with permission from ref [73]. Copyright © 1990 American Chemical Society.

There are two models describing the domain growth dynamics. Kralchevsky et al. [73] first proposed that the formation and growth of the thinner domain occurs through a “diffusive osmotic (DO) mechanism”. They argued that the micelles inside the thin film keep diffusing out to the

surrounding meniscus (Plateau border), due to a gradient of chemical potential (osmotic pressure). “Vacancies” are then formed in place of the micelles which have left the film, as shown schematically in Figure 1.5a. The vacancies are free to move within the film through self-diffusion of the micelles. After reaching a critical concentration, the vacancies start to aggregate to minimize the free energy of the film, and therefore nucleating a thinner domain (Figure 1.5b). The further growth of the domain is driven by the constant influx of vacancies created by micelles diffusing out of the thin film region:

$$\frac{d(\pi R^2)}{dt} = \delta_l^2 J \quad (1.1)$$

where  $\delta_l^2$  is the area of one vacancy (shown in Figure 1.5a) and  $J$  is the constant total flux of vacancies (number of vacancies per time). Equation (1.1) can be easily integrated to recover the diffusive growth scaling of  $R \propto t^{1/2}$ .

After white spots appear and the scaling transition occurs, additional term is needed to account for the vacancy flux generated by white spots formation [78]. However the origin of these fluxes and the transition from diffusive to linear scaling cannot be understood using the DO mechanism. Moreover, Heinig et al. [77] demonstrated experimentally that growth rates of multiple domains growing on the same film are the same and unaffected by each other. In contrast, Equation (1.1) predicts a decrease in growth rate when additional domains form, since the total vacancy flux is shared by multiple domains. More recently, Lee et al. [80] built upon this mechanism and suggested a model in which the local vacancy concentration gradient across the domain boundary is responsible for the diffusive-like growth dynamics. However, this model does not explain some of our experimental observations presented in this study, including growth



dynamics of domain in contact with the Plateau border (Chapter 3, ref [81]), ridge formation (Chapter 4 and 5), and dynamics of topological instability and white spots formation (Chapter 4).

Bergeron et al. [79] proposed a “hole sheeting” model for the formation and growth of thinner domain in stratifying films. In this lubrication based thin film hydrodynamic model, a governing equation of thickness evolution was derived. The formation and expansion of the thinner domain is driven by the gradient of disjoining pressure and dissipated by viscous forces. Their numerical calculation of thickness evolution is shown in Figure 1.6. As the flat thinner domain is established, a “rim” or “ridge” with larger thickness is formed in front of the thinner domain, resulted from the accumulation of liquid drained from the expanding domain.

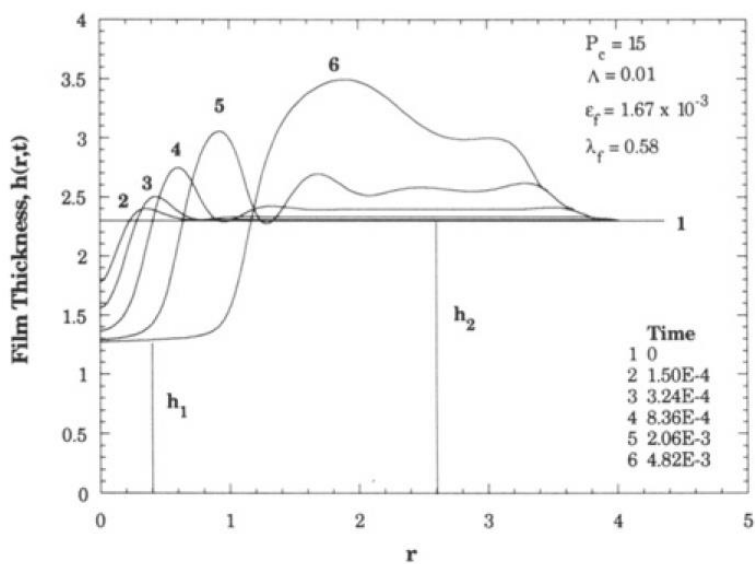


**Figure 1.6** Time evolution of the radial thickness profile,  $h$  vs.  $r$ , during domain nucleation and growth. A thicker ridge is formed between the thinner domain and outside film. Reprinted with permission from ref [79]. Copyright © 1992 American Chemical Society.

de Gennes [82] first theoretically described the formation and growth of similar ridges during growth of dry spots in thin films supported by solid substrate. Beltrán and Langevin [76], and Heinig et al. [77] subsequently proposed a similar model for the ridge formed in free-standing stratifying foam films. Their model showed the thickness evolution within the ridge is diffusive-like, which results in the diffusive scaling of domain growth.

Although lubrication-based thin film models have been widely used in various thin film hydrodynamic problems [83,84], especially in understanding the dynamics of spreading/dewetting of supported films (a comprehensive review is provided in Section 1.5), there are only countable few papers applied of such model to the stratifying foam films [76,77,79,85]. The experimental detection and characterization of the shape and shape evolution of the ridge and white spots during domain growth is completely absent in the literature. The difficulty lies in the lack of reliable experimental method to spatially resolve the ridge, which we show later is only a few nanometers higher than the outside film. When the experimental measured growth rates of domain are compared with the predictions from the hydrodynamic model, quantitative discrepancies are significant. In polyelectrolyte-surfactant systems, Langevin and co-workers [76,77,85,86] found that the thin film viscosity value needed to be substantially different from the bulk fluid viscosity, in order to match the model predicted domain growth rate with experimental measurements. The needed viscosity values varied from 60 times larger than the bulk viscosity to 10 times smaller, depending on the polyelectrolyte-surfactant mixture.

At the later stage of domain growth, white spot formation has been attributed to instabilities and breakup of the ridge. This process is thought [76,79] to be akin to Rayleigh-like instability, which describes the breakup of liquid jets into individual droplets [87]. However, the recent studies [88,89] on Rayleigh breakup of a toroidal shaped liquid drop showed little resemblance to the

white spot formation observed in our experiments (*cf.* Figure 3.6). More detailed experimental characterizations of the topological instability and the dynamics of white spot formation are needed to fully understand this process. Our investigations on shapes and thickness evolution of the white spots, their spatial distribution and their effects on domain growth dynamics, are presented in Chapter 4.

### 1.3 Experimental methods for foam films

The stability and drainage of a single foam film are studied in two typical cases: (i) small film formed horizontally, where the driving force of film drainage is capillary pressure originated from surface curvature, and (ii) large film formed vertically, where drainage is mainly gravitational. In this study, we focus on the former case with horizontal foam film smaller than capillary length ( $\lambda_c = \sqrt{\sigma/\rho g}$ , around 2 mm for water), so that gravity effect is negligible. For the latter case, an extensive review of the fundamentals is provided by Mysels [90].

The experimental setup to investigate drainage and stability of horizontal foam film is typically comprised of two main parts: the thin film apparatus that creates and holds the foam film in place, and the characterization system that records film evolution (most importantly thickness evolution) as the film drainage takes place.

### 1.3.1 Thin film apparatus

Many different apparatuses for forming and controlling foam films have been developed in the literature. Based on the way the thin film is held in place, we can categorize the apparatuses into two types: bubble holder (Figure 1.7a&b) and film holder (Figure 1.7c-e).

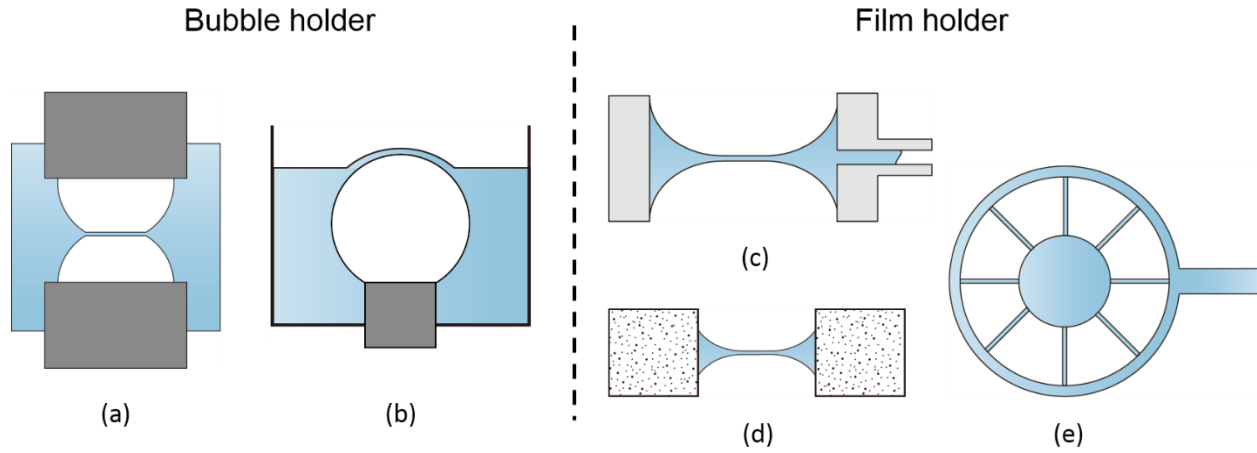


**Figure 1.7** Different types of thin film apparatus. (a) Thin film between two bubbles, (b) curved film between bubble and liquid surface, (c) Scheludko cell, (d) porous plate cell, (e) Bike-wheel cell.

In the typical bubble holding apparatus (Figure 1.7a), the foam film is formed by pushing two gas bubbles against each other, while the bubbles are held on two nozzles or plates. The force exerted on the bubbles can be measured very precisely, by attaching the one of the bubbles to an atomic force microscopy (AFM) cantilever [91]. However, the direct visualization of the film is obstructed by the nozzle/plate, so direct film thickness measurement is not available. In the AFM setup, the thickness can only be inferred from models accounting for the distance of the two nozzles or plates, size of the bubbles, and their deformation [92]. An alternative setup is introduced

by Derjaguin and Titijevskaya [93], which uses all glass plates to allow direct film visualization and interferometry thickness measurement (reviewed in Section 1.3.2). However, such glass apparatus is difficult to miniaturize to obtain small ( $\sim 1$  mm) bubbles ideal to form thin film with size comparable to that in a real foam.

Nikolov and Wasan [94] developed a different bubble holding thin film apparatus, where the foam film is formed between one gas bubble and the plane liquid surface (Figure 1.7b). This setup allows easy film visualization and interferometry thickness measurement from the top, while partially retains the control over driving force for film drainage, by monitoring the size of the bubble and its deformation [94], or by monitoring the pressure in the bubble with a pressure transducer [74,75]. However, gravitational drainage and curvature dependent disjoining pressure are likely introduced due to the fact that the film is curved. Indeed Nikolov and Wasan [94] found experimentally that the curved stratifying micellar foam films thins faster than the plane-parallel film with the same composition.

The other type of thin film apparatuses is designed to hold the foam film in place and manipulate its size and the pressure applied to it. Figure 1.7c shows one of the simplest version of the film holder. The foam film is formed in a small (several millimeters in diameter) cylindrical glass cell, and the film size is controlled by changing the fluid volume in the cylinder through a side arm. This design is often referred to as Scheludko cell [95] or Scheludko-Exerowa cell [96]. It allows good control over the formation and size of the foam film (emulsion or supported film alike), and easy thickness measurement using interferometry methods. Due to its simplicity and versatility, many researchers adopted this type of film holder to investigate various thin film systems [54,97–100].

In the Scheludko cell setup, the capillary pressure applied on the plane-parallel film can be varied by changing the film size. However, for typical millimeter size Scheludko cell, the pressure accessible is low and the range is limited (about 10-100 Pa). Velez et al. [101] fabricated a miniaturized cell, which was able to access capillary pressure up to nearly 1000 Pa. However, the design was not widely adopted, due to difficulties in the micromachinery fabrication of the cell, and in the visualization and thickness characterization of the miniaturized foam film.

Another widely used film holder is the porous plate holder (Figure 1.7d), which uses porous glass cylinder instead of solid glass used in Scheludko cell. It is first developed by Mysels and Jones [102], and later refined by Exerowa and Scheludko [103], Bergeron and Radke [104], and Dimitrova et al. [105]. The porous plate is soaked with the test solution, and the foam film is formed and controlled either by controlling the surrounding air pressure [102–104], or by controlling the volume of fluid in the plate [105]. Given its large accessible capillary pressure range (depending on porosity of the plate and detailed geometry of the holder, typically  $10^2$  -  $10^4$  Pa), the film holder is often connected to a pressure transducer or barometer to measure the pressure difference across film interfaces. Together with interferometry thickness measurement, the setup is often referred to as the thin film balance (TFB) [66,97,104,105], as it enables the measurement of disjoining pressure isotherm of the film.

The foam film disjoining pressure, as well as many other film interfacial properties, are sensitive to contaminants in the solution. The reusability of the porous plate film holder suffers from the difficulty in thoroughly cleaning the plate with typically  $< 100\ \mu\text{m}$  porosity. To overcome the disadvantages of both Scheludko and porous plate setup, Cascao Pereira et al [106] developed the bike-wheel cell setup shown in top view in Figure 1.7e. The foam film is formed at the center hole and the fluid flows through the multiple small channels ( $\sim 20\ \mu\text{m}$ ). The small dimension of

the channels ensure high maximum pressure, and the range of accessible pressure is about  $10 - 10^4$  Pa, comparable to that of the porous plate setup. The bike wheel cell was used in disjoining pressure measurements in foam film made with surface-active protein [107], and recently, in study of millimeter sized lipid bilayer film [108].

The advantages and disadvantages of each thin film apparatus are summarized in Table I. In this study, we use two film holding cell for the experiments with stratifying foam films, one Scheludko-type cell and one porous plate cell. The two setups complement each other and allow us to fully explore the dynamics of foam film stratification.

**Table I** Advantages and disadvantages of thin film apparatuses

Setup	Advantage	Disadvantage
<b>Two bubbles</b>	Build-in force measurement (AFM)	Thickness measurement Requires AFM or glass fabrication
<b>Bubble-surface</b>	Thickness measurement Control of film pressure	Curved film
<b>Scheludko</b>	Simple fabrication Thickness measurement Easy control of film size/pressure	Low accessible pressure Significant evaporation
<b>Porous plate</b>	Same as Scheludko cell + Large range of accessible pressure	Cleaning Possible pore blockage
<b>Bike wheel</b>	Thickness and pressure measurement Large range of accessible pressure	Requires photolithography fabrication Possible channel blockage

### 1.3.2 Thickness characterization of foam films

In order to study the drainage dynamics, stability and particularly stratification dynamics of foam films, the film thickness needs to be characterized and followed over time. The ideal thickness measurement method for studying stratifying foam films should have the following features: (i) non-intrusive, (ii) nanometer level accuracy, and (iii) high spatial and temporal resolution. Due to the lack of solid substrate in free standing foam films, many widely-used thickness characterization methods for supported films, including surface force apparatus (SFA), fluorescence imaging, atomic force microscopy (AFM), total internal reflection microscopy, ellipsometry, and electron microscopy, are not suitable for free-standing films. The suitable techniques for foam films are optical methods (interferometry and spectroscopy) and electrical methods (resistance/conductance measurement). While the electrical resistance/conductance measurement has been deployed in some foam film studies [38,109], it only measures average thickness over the entire film, and it is more appropriate for large films, where the Plateau border region is relatively small. UV-vis spectroscopy is used to measure foam film in a handful of papers [110,111], however it is also more suitable for larger films, its time resolution is limited by the spectral scanning time, and the film dynamics are not visualized. Interferometry is the most used method in the literature for foam film thickness measurement, owing to its high accuracy (sub-nanometer), non-intrusiveness, and instant measurement time. The interferometry can also be easily accompanied by direct visualization of the foam film, in order to investigate pattern formation and evolution during film drainage or stratification.

Interferometry utilizes the interference between two light rays reflected from the two gas-liquid interfaces (or liquid-liquid interfaces for emulsion films) to obtain film thickness (see Figure 1.8). The intensity or color of the interfered light is used to back calculate the interference path



length, therefore the thickness of the film [95]. This principle and its application to film thickness measurement dates back to Newton [34], who described the colors of thin films under natural light and recorded the corresponding thickness. For thick foam films (thickness 0.1 to 1  $\mu\text{m}$ ), the thickness can be measured by matching the color reflected under white light illumination to the standard interference color chart [112]. For thinner films ( $< 100\text{ nm}$ ), the light in the entire visible wavelength range is interfered destructively, therefore the film seem colorless (gray or black) even under white light illumination. Nevertheless, the light intensity is still modulated by thin film interference, and it can still be used to provide a measure of film thickness, even for black films that are only a few molecular-layers thick.

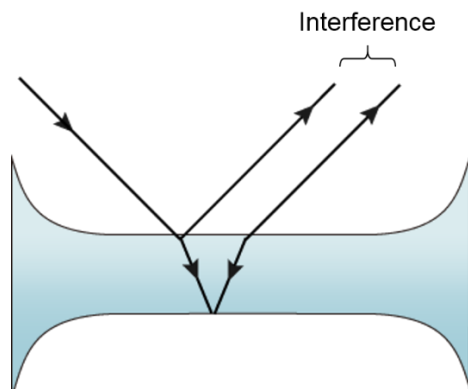


**Figure 1.8** Illustration of the interference between the light reflected from two gas-liquid interfaces. The thickness of the film determines the phase difference between the interfering light.

In most interferometry measurement (*e.g.* ref [55,95,96,104]), the film is illuminated with a monochromatic light source such as laser or filtered light. The light intensity reflected from a spot size of 1-100  $\mu\text{m}$  are tracked over time using a photodetector, in order to compute the film

thickness. This method allows non-intrusive, nanometer accuracy thickness measurement, but it lacks the spatial resolution of the thickness measured, which is particularly crucial for study of dynamics and pattern formation in foam films. Manev et al. [113] used rapid scan over the film area to obtain spatial distribution of film thickness, however the temporal resolution was compromised as each scan took seconds to complete. More recent advancement in digital imaging technology saw the use of digital camera to substitute for the photodetector [114–118]. The images taken were then processed to determine the thickness of the film with spatial resolution. So far the digital image analysis method has not reached nanometer resolution for thickness measurement, and it was therefore mostly applied to thicker films [114,116–118]. In this study, we introduce the interferometry digital imaging optical microscopy (IDIOM) protocol, which combines the conventional interferometry principle with digital filtration and image analysis, to obtain nanometer accuracy for thickness determination, while having high spatial and temporal resolution. This method is ideal for the study of dynamics of stratifying foam films.

## 1.4 Disjoining pressure in foam films

A foam film consists of two interfaces between the gas and liquid phase. The interfacial regions are thin transition regions with their thermodynamic properties deviating from those of the two bulk phases [119]. When the thickness of the foam film becomes comparable to the thickness of interfacial regions, the properties of the entire film are no longer the same as the bulk properties. The deviations give rise to thickness-dependent Gibbs free energy of the foam film,  $G^f(h)$ . At constant temperature  $T$ , pressure  $P$ , film area  $A$  and mole numbers of each component  $N_i$ , the

derivative of  $G^f(h)$  with respect to the film thickness  $h$ , gives the thermodynamic definition of disjoining pressure [18,120,121]:

$$\Pi(h) = - \left( \frac{1}{A} \frac{dG^f}{dh} \right)_{T,P,A,N_i} \quad (1.2)$$

Disjoining pressure is a measure of the repulsive (positive  $\Pi$ ) or attractive (negative  $\Pi$ ) macroscopic surface forces generated by the overlapped the two interfacial regions. Mechanically, the disjoining pressure is defined by Derjaguin and Churaev [122] as the difference at equilibrium between the normal pressure at the interface and the bulk pressure. During foam film drainage, the thickness-dependent disjoining pressure contributes to the driving force of the drainage flow. For plane-parallel foam films, when the disjoining pressure satisfies the criteria  $\Pi(h) = P_c$  and  $d\Pi/dh < 0$ , the further drainage is completely stopped and the foam film becomes stable [123,124]. The drainage dynamics and stability of thin foam films are greatly influenced by the disjoining pressure, including its magnitude and thickness dependence.

The disjoining pressure isotherm of a thin foam film,  $\Pi(h)$ , is given by the sum of the contributions from Multiple intermolecular and surface forces [18]:

$$\Pi = \Pi_{vdw} + \Pi_{el} + \Pi_{steric} + \Pi_{os} + \dots \quad (1.3)$$

Here the subscripts represent different contributions including van der Waals attraction (vdw), electrostatic double-layer repulsion (el), steric repulsion (steric) and specifically for stratifying foam films, supramolecular structural oscillatory forces (os). We now briefly review the disjoining pressure contributions listed in Equation (1.3) individually, with an emphasis on the

supramolecular structural forces, since it is specific to stratifying foam films. More comprehensive and exhaustive reviews are available in the literature [18,125].

#### 1.4.1 DLVO and steric forces

The combination of van der Waal and electrostatic contributions constitutes the classical DLVO theory [126,127]. It has been applied to many colloid systems to understand the interactions and stability [9]. The DLVO forces combined with short-ranged steric forces describe the stability of thin foam film in absence of supramolecular structures like micelles.

The van der Waals dispersion forces (also referred to as London–van der Waals forces) originate from the interactions between instantaneously induced dipoles. The van der Waals contribution to the disjoining pressure isotherm can be calculated by

$$\Pi_{vdw}(h) = -\frac{A_H}{6\pi h^3} \quad (1.4)$$

where  $A_H$  is the Hamaker constant. At large film thickness, the electromagnetic retardation effect (delayed response of the induced dipoles) can become important. This effect can be taken into account by letting the Hamaker constant depend on film thickness, *i.e.*  $A_H = A_H(h)$  [128]. Nevertheless Equation (1.4), as well as the scaling of  $\Pi_{vdw} \propto -1/h^3$  have been widely adopted in studies of hydrodynamics of thin film involving van der Waals forces [79,129–132].

When a foam film contains ionic surfactant, the electrostatic disjoining pressure arises from the overlapping of the electric double layers developed at the two charged gas-liquid interfaces. This repulsive interaction is screened by a diffuse electric double layer of counter-ions due to

neutralization of charged surface. The characteristic length of the diffuse layer is given by the Debye length,  $\kappa^{-1}$ , where  $\kappa^2 = 8\pi L_B c_e$ . Here  $L_B$  is the Bjerrum length, and it equals to 0.72 nm for water at the room temperature of 298 K.  $c_e$  is the total charge concentration in molar units.

The electrostatic double layer forces can be computed by solving the Poisson–Boltzmann equation. The precise expression for the repulsion force depends upon the assumptions about the distribution of counter-ions, and about the electrical boundary conditions of the interfaces. Under the assumptions of constant surface potential, large separation between interfaces, and small surface charge and potential, the electrostatic double layer disjoining pressure is given by:

$$\Pi_{el} = 64k_B T n^0 \tanh^2 \left( \frac{2e\psi_0}{4k_B T} \right) \exp(-\kappa h) \quad (1.5)$$

Where  $k_B$  is the Boltzmann constant,  $n^0$  is total number density of ions,  $e$  is elementary charge, and  $\psi_0$  is constant surface potential. Equation (1.5) shows the electrostatic disjoining pressure decays exponentially with increasing film thickness  $h$ , and the decay length is given by Debye length  $\kappa^{-1}$ .

At very small film thickness ( $h < 10$  nm), the strong steric repulsion forces arises as the surfactant molecules adsorbed at the interfaces ultimately approach each other. This type of forces has very short, molecular length scale range, and very sharp increase in strength as the electron clouds of molecules in the two interfaces starts overlapping. The detailed, quantitative nature of the forces is still an active area of research [125], nevertheless the steric disjoining pressure is known to be responsible for the stability the ultrathin Newton black film.

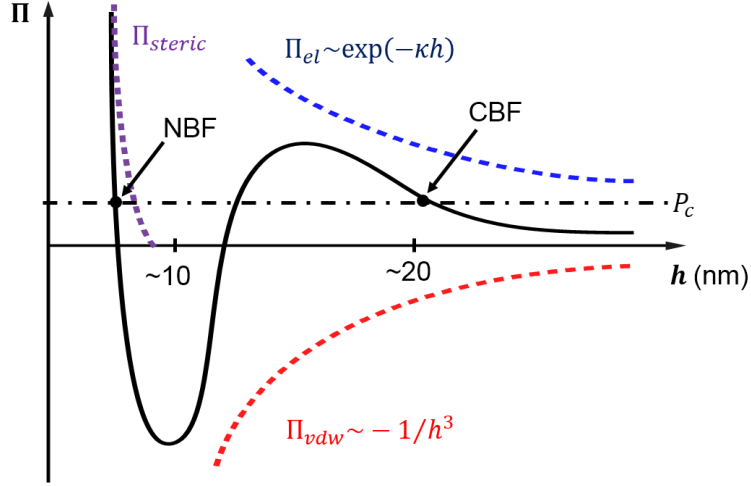


**Figure 1.9** Schematic illustration of a typical disjoining pressure isotherm  $\Pi$  vs.  $h$  (shown in black solid line). It includes contributions from van der Waals (red), electrostatic (blue) and steric (purple) forces. The disjoining pressure can balance the applied pressure  $P_c$  (black dash dot line) at two thicknesses corresponding to the common black film (CBF) thickness and the Newton black film (NBF) thickness.

In fact, the combination of DLVO and steric forces is sufficient to explain the two stable thicknesses often observed in foam films containing ionic surfactant (without micelles). As illustrated in Figure 1.9, the DLVO forces form the first local maxima in disjoining pressure isotherm, at around  $h = 15$  nm, while the steric forces arise at  $h < 10$  nm to form a large barrier. The foam film with capillary pressure of  $P_c$  therefore meets the stability criteria ( $\Pi(h) > P_c$  and  $d\Pi/dh < 0$ ) at two different thicknesses. The DLVO stabilized thicker film is referred to common black film (CBF), while the steric stabilized one is Newton black film (NBF) [18]. When the foam film contains supramolecular structures like micelles, additional disjoining pressure contribution is needed to account for the multiple stable thicknesses observed during stratification.

### 1.4.2 Supramolecular structural oscillatory disjoining pressure

In stratifying foam films containing supramolecular structures like micelles or colloidal particles, the ordering of these structures under thickness confinement gives rise to additional non-DLVO contribution to the disjoining pressure. The structural disjoining pressure isotherm is oscillatory in nature, corresponding to the layered ordering of the structures.

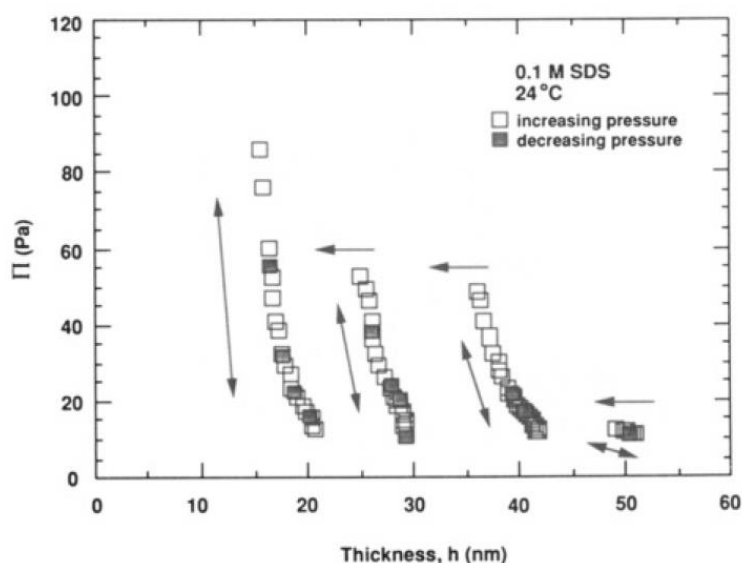


**Figure 1.10** Disjoining pressure isotherm in foam film made with 100 mM SDS. Only the region  $\Pi(h) = P_c$  and  $d\Pi/dh < 0$  is accessed. Arrows indication the direction of pressure scans. Reprinted with permission from ref [104]. Copyright © 1992 American Chemical Society.

Richetti and Kekicheff [133] first measured the oscillatory forces between two mica surfaces submerged in ionic surfactant micellar solutions, using the surface force apparatus (SFA) [134]. They found the supramolecular structural forces to resemble the oscillatory solvation forces manifested in pure solvent under molecular length scale confinement [125]. In free-standing

stratifying foam films, Bergeron and Radke [104] first quantified the structural oscillatory disjoining pressure directly, with the porous plate thin film balance (TFB) (see Section 1.3.1). Since the TFB can only measure the film disjoining pressure at equilibrium, only stable parts of the disjoining pressure isotherm are experimentally accessible. Nevertheless, the multiple discrete stable branches and the thickness jumps between them clearly indicated the layer-by-layer supramolecular structural contribution to the disjoining pressure (Figure 1.10).

Theoretically, the structural disjoining pressure in non-ionic surfactant micellar solution or uncharged particle suspension was modeled as hard sphere suspension. The disjoining pressure isotherm was quantified by both statistical mechanics calculations [135,136] and Monte Carlo simulations [137,138]. The simulation showed that the hard spheres display oscillatory density distribution under the confinement of two surfaces, and it gives rise to the structural oscillatory disjoining pressure. The period of the oscillation corresponds to the sphere diameter. Kralchevsky and Denkov [135] proposed a semi-empirical explicit expression of the disjoining pressure in hard sphere suspension, which takes the form of a damped oscillation function. This estimation of disjoining pressure showed good agreement with the experimental measurements in non-ionic micellar systems, carried out with both TFB [97] or colloid-probe atomic force microscopy (CP-AFM) [139].

For charged systems (*e.g.* ionic surfactant micelles, charged particles or polyelectrolyte), the electrostatic interactions and counter-ions distributions were included in density function theory calculations (DFT) [140] and numerical simulations [141] to model the oscillatory disjoining pressure. The period of oscillation was found to decrease with increasing supramolecular structure concentration, which agrees with experimental observation [99,128] that stratification step thickness decreases with increase in concentration of ionic surfactant. However,



Pollard and Radke [140] found quantitative discrepancies between DFT calculation and the TFB measurements of disjoining pressure in stratifying foam films. They noted that in the DFT calculation the two film surfaces were modelled by two charged, rigid wall, while the real gas-liquid interfaces in foam films are deformable in response to stresses. Local thickness variations results in nucleation and growth of thinner domains, and therefore the foam film is destabilized at a lower pressure than model prediction with two rigid walls. We posit that study of the dynamics of free-surface flows in the stratifying foam film is needed for better understanding of the effects of free surfaces to the stability of the film.

Unlike the uncharged systems, a reliable theoretical expression of the oscillatory disjoining pressure is not yet available [142] for charged systems. Nikolov and Wasan [55] first proposed to treat charge micelles as hard spheres with effective micelle radius being the micelle radius plus Debye length. Analogous to the uncharged systems, the period of the oscillatory disjoining pressure was then related to the effective micelle diameter. However, recent measurement [128] of the step thicknesses in stratification showed that the oscillation period is more closely correlated to the mean distance between micelles in the solution, which is larger than the effective micelle size. In this study, we modify the semi-empirical disjoining pressure expression for uncharged systems proposed by Kralchevsky and Denkov [135], and account for the correlation between oscillation period and mean micelle distance, in order to explicitly estimate the oscillatory structural disjoining pressure in ionic surfactant micelle solution.

## 1.5 Thin film hydrodynamics

The hydrodynamics of thin liquid films are of importance in understanding the dynamics of stratification, as well as various other phenomena include film rupture, drop spreading and dewetting. Thin liquid films, both supported and free-standing ones, often display rich and complex hydrodynamic pattern formations and instabilities. In thin films that contain one or two free gas-liquid interfaces, the flows within the films are coupled with flows and deformations of the interface(s), and the dynamics are greatly affected by the interfacial properties as well as bulk rheology. The hydrodynamics can be further coupled with mass and/or heat transfer, since possible concentration gradient of surfactant or temperature gradient can induce Marangoni flows on the interfaces. In addition, the dynamics are often modified by various thickness-dependent surface forces, especially when considering thin films with nanoscale thicknesses,

One effective approach to reveal the physics underneath the aforementioned complexity is to apply lubrication approximation to the basic governing hydrodynamic equations, since the lateral size of the thin film ( $R > 100 \mu\text{m}$ ) is usually much larger compare to the thickness of it ( $h < 1 \mu\text{m}$ ). Furthermore the thickness variations along the film are very gradual ( $dh/dx \ll 1$ ). This approach simplifies the system of coupled partial differential equations (PDEs) to a single nonlinear PDE describing the thickness of the film as a function of space and time ( $h = h(x, t)$  in the case of one spatial dimension as discussed therein). Lubrication based thin film models had been developed for different geometry, boundary conditions, surface forces and/or other coupling effects. An extensive review on the development and manifestations of these models is provided by Oron et al. [84]. Reviews or books on more specific topics are also available: on wetting and spreading dynamics of supported films by de Gennes [143] and Bonn et al. [144], on dewetting of

soft matter supported films by Kalliadasis and Thiele [145] and Mukherjee and Sharma [146], and on free-standing foam film drainage by Ivanov [16] and Karakashev and Manev [147].

In the context of the drainage of foam films (free-standing films), two main scenarios are investigated extensively [148]: (i) two deformable drops approaching each other to form relatively small (radius  $\sim 10 \mu\text{m}$ ), thick (thickness  $> 1 \mu\text{m}$ ) film with non-uniform thickness in between (Figure 1.11a), and (ii) at later stage of drainage, a larger (radius  $> 100 \mu\text{m}$ ) and thinner (thickness  $< 100 \text{ nm}$ ) plane-parallel film is formed (Figure 1.11b).

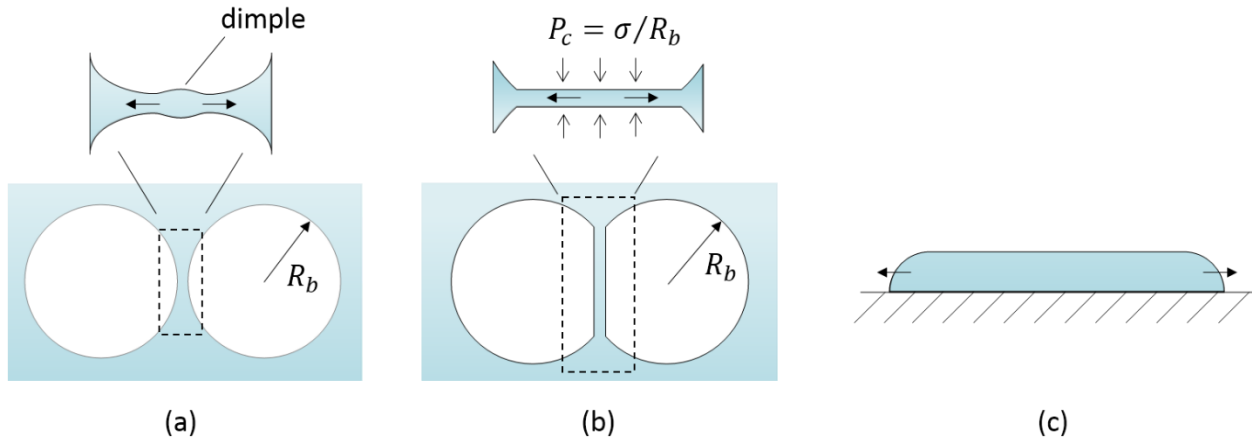


**Figure 1.11** Different geometries in thin film drainage. (a) Relatively thick film formed between two slightly deformed gas bubbles. The film can be curved to form dimples. (b) Thinner film formed between largely deformed bubbles. The film is almost plane- parallel mainly due to the effect of disjoining pressure. (c) Flat film on a solid substrate, which has a similar geometry as the free-standing one in (b).

The first scenario corresponds to films in a wet foam (water volume fraction  $\sim 20\%-35\%$  [149]), where the gas bubbles are mostly spherical and the thicknesses of the films are large. Approaching bubbles can deform slightly under the influence of hydrodynamic and intermolecular

interactions. Various curved shapes that can appear in the film region are categorized as “dimple”, “pimple”, or “wimple”. The drainage of the thin film is affected by the formation and shape of these structure [150], theoretical and experimental progresses were summarized in an extensive review by Chan et al. [151]. In foam films containing surfactants, the aforementioned shapes are quickly driven out of the film through hydrodynamic instability due to Marangoni effects [152]. After the thicker dimple drains out, the foam film left is near plane-parallel with thickness around 100 nm and much thicker meniscus region surrounding it. For films containing the supramolecular structures, the oscillatory structural disjoining pressure then becomes significant and the stratification phenomenon is observed. The present study will focus on the dynamics of such thin films.

The plane-parallel films connected with the Plateau border is more similar to the actual thin films in a dry foam (water volume fraction  $<5\%$  [149]), where the gas bubbles are polygonal. The large lateral size ( $\sim 300\ \mu\text{m}$  in this study) of the film indicates that the dissipation and flows in the surrounding meniscus region are mostly insignificant compare to those within the film region. The meniscus also has much larger volume than the film, therefore can be considered to remain unchanged during film drainage. The film drainage is driven by the capillary pressure difference the flat film and the curved meniscus. At small film thickness, this capillary pressure difference can be balanced by the thickness-dependent disjoining pressure in the film thus the drainage is impeded.

As illustrated by Figure 1.11b&c, the geometry of the nearly plane-parallel foam film appears similar to the geometry of thin films supported by solid substrate. In the following sections, we will present the derivation of lubrication based thin film model that describes the hydrodynamics of both free-standing and supported films, and thereafter discuss the possible

boundary conditions, and showcase the effects of surface forces on pattern formation and instabilities in thin films.

### 1.5.1 Thin film hydrodynamic equation

The foundations of the lubrication theory were laid by Reynolds [153]. In his pioneering work, he applied the Navier–Stokes equations to describe the slow, viscous dominated flow of liquid squeezed out of a small gap between two solid surfaces, where the gap size is much smaller than the lateral size of the solid surfaces. Due to the success of this method in many fluid dynamics problems, derivation and analysis is presented in many text books [83,154]. Here we show the application of lubrication theory to thin film drainage by considering the geometry shown in Figure 1.12.

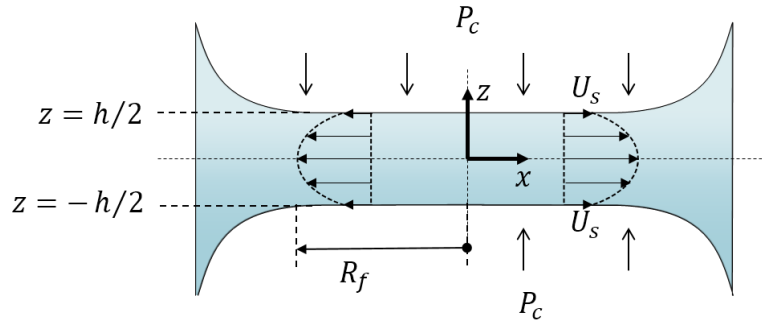


**Figure 1.12** The free-standing thin film geometry used for deriving the thin film equation.

The plane-parallel thin film is symmetrical about the  $x$ -axis, with  $z = 0$  corresponds to the middle plane of the thin film, and  $z = \pm h/2$  being the two gas-liquid interfaces. The assumptions used for using lubrication approximation includes: (1) inertia and body forces (*e.g.* gravity) are

negligible in comparison with the viscous forces; (2) the bulk fluid is Newtonian and incompressible; (3) the interfaces are nearly parallel and the film thickness is much smaller than the lateral extent of the film, *i.e.*  $\varepsilon \sim \frac{h}{R_f} \ll 1$ ; (4) the velocity in  $z$ -direction,  $u_z$ , is much smaller than that in  $x$ -direction,  $u_x$ , *i.e.*  $\frac{u_z}{u_x} \sim O(\varepsilon) \ll 1$ ; (5) variation of  $u_x$  with  $x$  is much smaller than that with  $z$ , *i.e.*  $\frac{\partial u_x}{\partial x} \sim \varepsilon \frac{\partial u_x}{\partial z}$ .

The Navier – Stokes and continuity equations simplify to the following:

$$\frac{\partial P}{\partial x} = \eta \frac{\partial^2 u_x}{\partial z^2} \quad (1.6)$$

$$\frac{\partial P}{\partial z} = 0 \quad (1.7)$$

$$\frac{\partial u_x}{\partial x} + \frac{\partial u_z}{\partial z} = 0 \quad (1.8)$$

Where  $P$  is the pressure and  $\eta$  is the bulk viscosity. The boundary conditions include: symmetry at film mid-plane  $z = 0$

$$\frac{\partial u_x}{\partial z} = u_z = 0 \quad (1.9)$$

And velocities at the film interfaces  $z = \pm h/2$  satisfies:

$$u_x = U_s(x, t) \quad (1.10)$$

$$u_z = \pm \frac{1}{2} \left( \frac{\partial h}{\partial t} + U_s \frac{\partial h}{\partial x} \right) \quad (1.11)$$

In order to keep the derivation more general,  $u_x$  at the interfaces is left to be  $U_s$ , where  $U_s = U_s(x, t)$  is determined by the specific surface conditions discussed in the following section.

Integrating Equation (1.6) with boundary condition Equation (1.9) and (1.10) leads to:

$$u_x = \frac{1}{2\eta} \left( \frac{\partial P}{\partial x} \right) \left( z^2 - h^2/4 \right) + U_s \quad (1.12)$$

Substitution Equation (1.12) into continuity Equation (1.8) and then integration with Equation (1.11) leads to:

$$\frac{\partial h}{\partial t} = \frac{1}{12\eta} \frac{\partial}{\partial x} \left( h^3 \frac{\partial P}{\partial x} \right) - \frac{\partial}{\partial x} (hU_s) \quad (1.13)$$

which is the governing evolution equation of the thickness of the thin film  $h(x, t)$ .

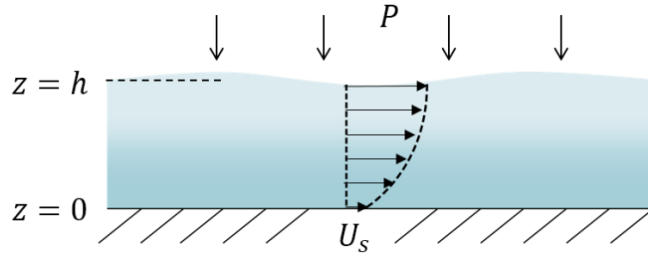


**Figure 1.13** The geometry of thin film supported on a solid substrate.

Analogous result to Equation (1.13) can be derived for thin film supported by a planar solid substrate (Figure 1.13). Assuming no tangential stress on the gas-liquid interface ( $\partial u_x / \partial z = 0$  at  $z = h$ ) and a general “slip velocity” on the solid-liquid interface ( $u_x = U_s$  at  $z = 0$ ), the evolution of film thickness is given by:

$$\frac{\partial h}{\partial t} = \frac{1}{3\eta} \frac{\partial}{\partial x} \left( h^3 \frac{\partial P}{\partial x} \right) - \frac{\partial}{\partial x} (hU_s) \quad (1.14)$$

Which only differs from Equation (1.13) by a pre-factor. Noted that here the surface velocity  $U_s$  is defined at the solid-liquid interface ( $z = 0$ ), while in free-standing film it's defined at the two gas-liquid interfaces ( $z = \pm h/2$ ).

### 1.5.2 Boundary conditions at gas-liquid or solid-liquid interfaces

The boundary conditions at the gas-liquid or solid-liquid interfaces are affected by many factors including fluid slippage on solid substrate for supported films, adsorption/mass transfer dynamics for surfactant-laden films, Marangoni effects, interfacial rheology, etc. The different mobility of the interface is reflected in the thin film equations mainly by having different forms of surface velocity  $U_s$ .

**Case (i) immobile surface.** The no-slip boundary condition is applied to the thin film equations, when the gas-liquid interfaces of free-standing foam films are immobile and able to withstand the surface shear stresses generated by the drainage flow. The resulting thickness evolution equation is obtained by setting  $U_s = 0$  in Equation (1.13) to give:

$$\frac{\partial h}{\partial t} = \frac{1}{12\eta} \frac{\partial}{\partial x} \left( h^3 \frac{\partial P}{\partial x} \right) \quad (1.15)$$

For a draining plane-parallel thin film with thickness  $h = h(t)$  and radius  $R_f$ , the drainage velocity can be obtained by integrating Equation (1.15) twice (in cylindrical coordinates for circular films). The results are referred to as Reynolds equation/velocity:

$$V_{\text{Re}} = -\frac{dh}{dx} = \frac{2h^3 \Delta P}{3\eta R_f^2} \quad (1.16)$$



where  $\Delta P = P(0) - P(R_f)$  is the pressure drop from the film to the adjacent Plateau border.

In his seminal paper on foam films, Sheludko [95] recognized that surfactant (both small and large molecule surfactants) adsorption can immobilize the gas-liquid interfaces of free-standing films. Flow on the surfactant-laden interfaces induces concentration gradient of the surfactant, which results in concentration driven Marangoni effect that act against the surface flow. Moreover, surfactant adsorption can also increase interfacial shear viscosity or yield stress of the gas-liquid interfaces, especially with large molecule surfactants. Both the Marangoni and rheological effects can contribute to the immobilization of the interfaces.

In the case of stratifying foam films containing surfactant micelles, the surfactant concentration is well above critical micelle concentration. The high surface concentration of surfactant might lead to higher surface viscosity (*i.e.* less surface mobility) [155]. Experimental measurements of surface shear viscosity of SDS have shown vast disagreement among the literature, with results range from  $10^{-3}$  to  $10^2$   $\mu\text{N}\cdot\text{s}/\text{m}$  [156]. And the most recent work by Zell et al. [157] put the value on the lowest end, suggesting the interface is effectively inviscid.

The adsorption of surfactant promotes concentration driven Marangoni effect. Scheludko [95] estimated the surface tension gradient needed to withstand the surface shear stress during drainage is  $d\sigma \sim h dP$ , which can be satisfied with high surface concentration of surfactant, small film thickness and relatively low driving pressure. These criteria are usually met when studying stratification in micellar foam films, therefore the simple no-slip condition is often assumed in hydrodynamic studies of stratifying films [76,77,79,104]. This assumption is examined in detail later in Section 5.3.2.

The drainage of thin film containing surface active protein [107,158], high molecular weight polymeric surfactant [159], or polyelectrolyte-surfactant mixture [85], also agree reasonably well with Equation (1.15), mainly due to their large surface viscoelasticity immobilizes the adsorbed gas-liquid interface. However, more complex rheology of these interfaces, often due to significant surface aggregation and gelation [160,161], may lead to very solid-like and heterogeneous surfaces, drastically alter the dynamics of the drainage [67,107,162].

**Case (ii) completely mobile surface.** As the opposite of the completely immobile surface in case (i), here the condition assumes that the gas-liquid interface can withstand no shear stress. This is usually the case for gas-liquid interface without any surface active species. The flow in the drainage of thin films therefore becomes plug-like:

$$u_x = U_s(x, t) \quad (1.17)$$

Equation (1.13) then becomes:

$$\frac{\partial h}{\partial t} = -\frac{\partial}{\partial x}(hU_s) \quad (1.18)$$

which does not provide the tangential velocity  $U_s(x, t)$ . The lack of closure of this equation is resolved by retaining the higher order terms in lubrication approximation [130]. The resulting set of governing equations comprises of Equation (1.18) and:

$$\rho \frac{\partial U_s}{\partial t} + \rho U_s \frac{\partial U_s}{\partial x} = \frac{4\eta}{h} \frac{\partial}{\partial x} \left( h \frac{\partial U_s}{\partial x} \right) - \frac{\partial P}{\partial x} \quad (1.19)$$

where  $\rho$  is the liquid density.

This model was mainly applied to study the dynamics of surfactant-free foam films, specifically the film rupture driven by van der Waals forces [130,132]. The model was also extended to study rupture of thin films of non-Newtonian power law fluids [163]. Recently, a model similar to Equation (1.18) and (1.19) was also derived to study capillarity-driven levelling of step thickness in free-standing polymeric films [164]. In our study, we contrast the results from this model with those from the immobile surface model and from surfactant-laden model (discussed later), in order to showcase the effects of surface mobility on the stratification dynamics.

**Case (iii) partially mobile surface: surface slippage.** Between the aforementioned limiting cases of completely immobile (no-slip) and the completely mobile (no-stress) surface, partial mobility of the gas-liquid or solid-liquid interface can be introduced, either by phenomenological slippage models (often used in wetting/dewetting of supported films), or by relating the mobility with heat/mass transfer (in problems involving Marangoni effect). We here review the results from both approach.

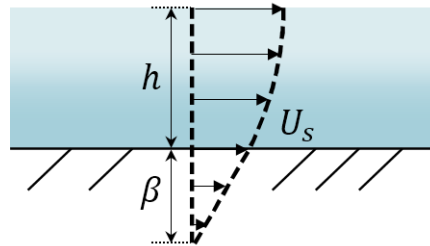


**Figure 1.14** Navier slippage model. The extrapolation to zero velocity defines the slip length  $\beta$ , and surface velocity is given by Equation (1.20).

In modelling spreading, wetting, or dewetting dynamics of thin films supported by solid substrate, the classical no-slip boundary condition for the solid-liquid interface appears to fail at the three-phase contact line [165,166], leading to a stress singularity at the contact line. The singularity can be relieved by allowing some form of slippage (surface mobility) in the proximity of the contact line. The Navier slippage model (illustrated in Figure 1.14) assumes the extent of slip velocity  $U_s$  is proportional to the wall shear stress at the solid-liquid interface:

$$U_s = \beta \frac{\partial u_x}{\partial z} \quad (1.20)$$

Where  $\beta$  is the slip length, which is a phenomenological parameter characterizing the extent of slippage. Combined with Equation(1.12) and Equation (1.14), the resulting film thickness equation reads:

$$\frac{\partial h}{\partial t} = \frac{\partial}{\partial x} \left[ \frac{1}{\eta} \left( \frac{h^3}{3} + \beta h^2 \right) \frac{\partial P}{\partial x} \right] \quad (1.21)$$

Which includes the slippage term  $\beta h^2$ . The whole pre-factor,  $M(h) = \frac{1}{\eta} \left( \frac{1}{3} h^3 + \beta h^2 \right)$ , is often referred to as the mobility function [145,167].

The significant role of slippage played in the dewetting dynamics of supported films, especially polymeric thin films, has been studied experimentally and theoretically extensively [168]. The magnitude of slippage, characterized by the slip length  $\beta$ , is related to the magnitude of viscous dissipation during dewetting [169,170]. The dynamics of growth of circular dry patch [171,172], formation and shape of ridge formed at the dewetting front [173–175], and ridge instabilities are all affected by the slippage [176–178].

For free-standing foam films containing surfactants (*e.g.* stratifying foam film), the surface mobility is a result of surface adsorption of surfactants. Models coupling surfactant mass transfer and thin film hydrodynamics are developed (discussed in Case (iv)), nevertheless the Navier slip model (Equation (1.21)) can serve as the useful starting point, emulating the studies of supported films regarding growth dynamics, pattern formation and instabilities.

**Case (iv) partially mobile surface: surfactant-laden.** The effect of surfactant adsorption on the mobility of gas-liquid interfaces of the draining free-standing films is multi-fold. First, the convection on the gas-liquid interface generates surface concentration gradient of surfactant, inducing Marangoni effect which reduces the mobility of the surface. Second, surfactant adsorption modifies interfacial rheology of the gas-liquid interface, increases surface viscosity/elasticity and hence reduces the mobility of the surface. Lastly, for ionic surfactants (*e.g.* SDS), charge transport on the surface during drainage also affects the mobility.

One general approach to study the surfactant effect is to solve the system of thin film equation (Equation (1.13)), coupled with the mass balance of the surfactant, and stress balance on the interfaces [16]. Under the assumption of uniform film thickness, the resulting drainage velocity,  $V = -dh/dt$ , is compared with the Reynolds' velocity given by Equation (1.16) to obtain a mobility factor,  $f = V/V_{\text{Re}}$ . Since Reynolds' velocity is obtained with a completely immobile surface, the mobility factor is usually larger than unity.

Equation (1.13) is re-written for cylindrical coordinates to obtain:

$$\frac{\partial h}{\partial t} = \frac{1}{12\eta} \frac{1}{r} \frac{\partial}{\partial r} \left( rh^3 \frac{\partial P}{\partial r} \right) - \frac{1}{r} \frac{\partial}{\partial r} (rhU_s) \quad (1.22)$$

The surfactant mass balance in the bulk solution is given by:

$$\frac{1}{r} \frac{\partial}{\partial r} \left( r \frac{\partial c}{\partial r} \right) + \frac{\partial^2 c}{\partial z^2} = 0 \quad (1.23)$$

where  $c$  is the bulk concentration of the surfactant. The convective and time dependent terms are neglected due to small Péclet number in the slow flowing thin film system. Mass balance is also applied to the surfactant at the gas-liquid interfaces to obtain:

$$\frac{1}{r} \frac{\partial}{\partial r} (r U_s \Gamma) = D_s \frac{1}{r} \frac{\partial}{\partial r} \left( r \frac{\partial \Gamma}{\partial r} \right) \pm D \left( \frac{\partial c}{\partial z} \right)_{z=\pm h/2} \quad (1.24)$$

where  $\Gamma$  is the surface excess of adsorbed surfactant at the interfaces,  $D$  and  $D_s$  are the bulk and surface diffusivity of the surfactant, respectively. Again, the convective and time dependent terms are neglected. The shear stress on the interface due to surface flow is balanced by Marangoni stress and surface viscous stress:

$$\frac{d\sigma}{dr} + \eta_s \frac{\partial}{\partial r} \left( \frac{1}{r} \frac{\partial r U_s}{\partial r} \right) = \pm \eta \left( \frac{\partial u_r}{\partial z} \right)_{z=\pm h/2} = \frac{h}{2} \frac{\partial P}{\partial r} \quad (1.25)$$

The second equality is from Equation (1.12). The relations between  $c$ ,  $\Gamma$  and  $\sigma$  are assumed to be linear, as their deviations are small from the equilibrium values:

$$\frac{\partial \Gamma}{\partial r} \approx \alpha_0 \frac{\partial c}{\partial r} \quad (1.26)$$

$$\frac{\partial \sigma}{\partial r} \approx \frac{\partial \sigma}{\partial \Gamma} \frac{\partial \Gamma}{\partial c} \frac{\partial c}{\partial r} = -E_0 \Gamma_0 \alpha_0 \frac{\partial c}{\partial r} \quad (1.27)$$

where  $\alpha_0 = (\partial\Gamma/\partial c)_0$  is the adsorption length,  $E_0 = -(\partial\sigma/\partial\ln\Gamma)_0$  is a measure of surface elasticity (often referred to as the Gibbs elasticity).

The set of Equation (1.22) to (1.27) has been solved analytically with various approximations and additional assumptions by several authors [148,179–183]. A brief summary of the resulting formulas for the mobility factor  $f = V/V_{\text{Re}}$  is provided in Table II. All formulas are rewritten using consistent notations and dimensionless groups for better comparison.  $f$  becomes progressively complicated as more realistic assumptions are used. In zeroth order approximation,  $f$  is related to the mobility function in thin film equations (see Equation (1.21)) by  $M(h) = fh^3/12\eta$ . Interestingly, the model by Radoëv Dimitrov and Ivanov [179] has very similar mobility function form to the Navier slippage model for supported film: both follow the  $Ah^3 + Bh^2$  format, with the former reads  $M(h) = (1/12\eta + D/4E_0\alpha_0)h^3 + (D_s/2E_0)h^2$ , while the latter is  $M(h) = (1/12\eta)h^3 + (\beta/4\eta)h^2$ .

**Table II** Summary of mobility factor calculated for drainage of thin film containing soluble surfactant

Reference	Assumptions	Mobility factor, $f = V/V_{\text{Re}}$
[179]	Zero surface viscosity	$1 + N_D + N_{Ds}$
[180]	Maximum surface velocity ( <i>i.e.</i> $\partial U_s / \partial r = 0$ at $r = R_f$ )	$\frac{1}{16} \left[ \sum_{k=1}^{\infty} \frac{2}{\lambda_k^4} \frac{1 + \lambda_k^2 N_{\eta} (N_D + N_{Ds})}{1 + (N_D + N_{Ds})(1 + \lambda_k^2 N_{\eta})} \right]^{-1}$
[181]	Zero shear stress at $r \geq R_f$ Surface viscosity only	$\frac{1}{8} \frac{N_{\eta}^{-3/2} I_0(N_{\eta}^{-1/2})}{2I_1(N_{\eta}^{-1/2}) - N_{\eta}^{-1/2} I_0(N_{\eta}^{-1/2})}$
[182]	Maximum surface velocity ( <i>i.e.</i> $\partial U_s / \partial r = 0$ at $r = R_f$ ) Included radial mass convection	$\left[ \frac{1}{1 + N_D + N_{Ds}} (1 - N_c) + 4N_{\eta} \left( \frac{N_D + N_{Ds}}{1 + N_D + N_{Ds}} \right)^2 \left( \frac{2I_1(\xi) - \xi I_0(\xi)}{I_1(\xi) - \xi I_0(\xi)} \right) \right]^{-1}$
[148]	Considered flow in the surrounding meniscus Zero surface viscosity	$\left\{ \frac{1}{1 + N_D + N_{Ds}} + \frac{2}{N_{Ds} N_{Rb}^2} \left[ \left( \frac{1}{N_{Ds}} (1 + b)(1 - N_{Rb}) + 1 \right) \ln \left( 1 + \frac{N_{Ds}}{1 + N_D} \right) + N_{Rb} - 1 \right] \right\}^{-1}$
[183]	Included surface velocity gradient in calculation driving force	$\left\{ 1 - 32 \sum_{k=1}^{\infty} \frac{1/\lambda_k^4 - (\varepsilon/\lambda_k)^2/6}{1 + N_{\eta} \lambda_k^2 + 1/\left[ N_{Ds} + (N_D/\varepsilon \lambda_k) \tanh(\varepsilon \lambda_k/2) \right]} \right\}^{-1}$

Dimensionless numbers:  $N_D = \frac{3\eta D}{E_0 \alpha_0}$ ,  $N_{Ds} = \frac{6\eta D_s}{h E_0}$ ,  $N_{\eta} = \frac{\eta_s h}{6\eta R_f^2}$ ,  $N_c = \frac{c_0 h}{4\Gamma_0}$ ,  $N_{Rb} = \frac{R^2}{R_b h}$ ,  $\xi = \left[ \frac{1 + N_D + N_{Ds}}{N_{\eta} (N_D + N_{Ds})} \right]^{1/2}$ ,  $\varepsilon = \frac{h}{R_f}$

$\lambda_k$  is the  $k$ th root of the zero order Bessel function of first kind, *i.e.*  $J_0(\lambda_k) = 0$ .  $I_0$  and  $I_1$  are the modified Bessel function of the first kind.



Karakashev and coworkers [98,183,184] surveyed the experimental thin film drainage results with a few surfactant solutions (both ionic and non-ionic) and compared with a series of theoretical models. They found that the most of the models are in reasonable agreement with experiment results of non-ionic surfactant, while ionic surfactant film drain significantly slower than predicted [184]. Subsequently, models are developed to account for charge transport effect in drainage of thin film containing ionic surfactant [185–187].

For stratifying micellar foam films, the conventional wisdom has been to apply no-slip boundary condition on the gas-liquid interfaces, arguing that high surface concentration of surfactant immobilizes the interfaces [79,95,104]. In this study, we examine the proper boundary condition for modeling stratifying foam films in detail, by contrasting experimental results with model calculations with three boundary condition: immobile, mobile and surfactant-laden (specifically the model by Radoëv et al. [179]).

### **1.5.3 Structures and patterns formed during dewetting of supported thin films**

The dynamics of dewetting of supported thin film have been studied extensively [145,146]. During the dewetting process of the thin film with uniform thickness initially, microscopic or nanoscopic structures and patterns with varying thickness form and evolve, under the influences of capillarity, surface forces, fluid rheology, etc [146]. Reviewing the understanding of dewetting dynamics is beneficial to studying dynamics of free-standing stratifying foam films, due to the similarities of the film geometry and the underlying hydrodynamics.

The rupture of a flat homogenous thin film and development of the dry patches can take place either through nucleation and growth of holes in the film, or through spinodal dewetting

[188,189]. The morphology is dependent on the functional shape and magnitude of the surface interaction (or interfacial potential, disjoining pressure) [190–192]. Many different combinations of stabilizing or destabilizing functions of thickness are used to quantify the disjoining pressure isotherm. One commonly used interfacial potential function (sometime referred to as Sharma potential [193,194]) comprises of the power law ( $\propto h^{-3}$ ) function accounting for the van der Waals interaction and an exponential function ( $\propto \exp(-h)$ ) for the electrostatic interaction. The structural oscillatory disjoining pressure is not discussed in the context of stability and rupture of supported thin films.

After the thin film ruptures and dry spots are developed, the dry circular holes grow over time. Redon et al. [171] showed that the hole radius grow linearly over time, *i.e.*  $R \propto t$ , when viscous dissipation at the solid-liquid contact line is the dominating dissipation mechanism, and the thin film slippage on the substrate is negligible ( $\beta \ll h$ ). When the surface slippage becomes non-negligible ( $\beta \sim h$ ), as for many polymeric films on passive, smooth substrate [169], the time dependence of hole radius changes to  $R \propto t^{2/3}$  [170–172,175]. Exponential hole radius scaling,  $R \propto e^t$ , was also reported [195–197], but only in highly viscoelastic polymer films and at the early stage of hole growth, where the rheological properties of the film play a significant role. The similarities between the growth of dry holes during dewetting and the growth of thinner domains in stratifying foam films was first suggested by de Gennes [82], and later used by Langevin and co-workers [76,77,85] to model stratification of foam films with polyelectrolyte-surfactant mixture. However, despite the similarity in the geometry, growth kinetics of the dry holes and thinner domains are not identical. In stratifying foam films the thinner circular domain grow as  $R \propto t^{1/2}$  without topological instability around the contact line [73,76–78]..

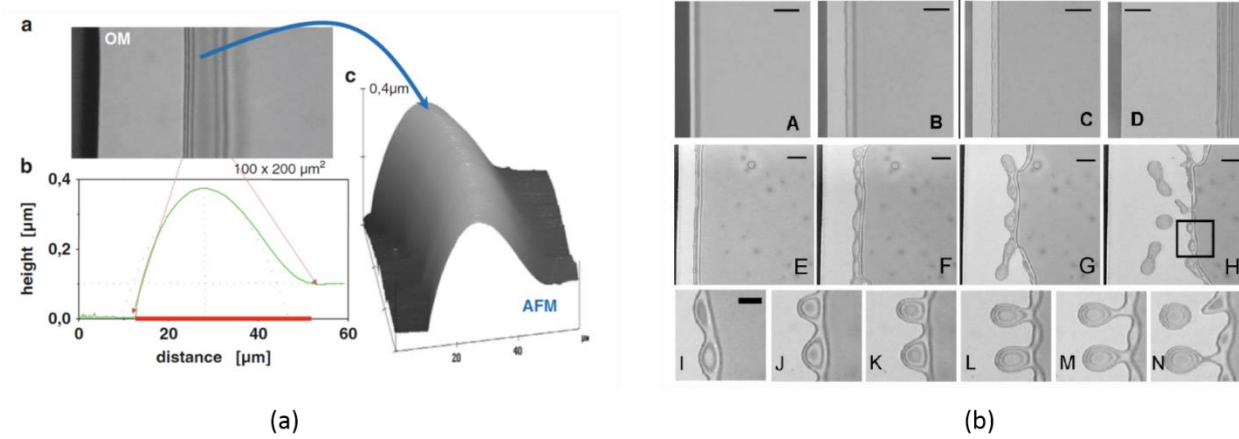


**Figure 1.15** Formation, shape and instability of the ridge formed during thin film dewetting. (a) The experimental characterization of the ridge, using optical microscopy and atomic force microscopy. Reprinted from ref [198] with permission. (b) Ridge instability (A-H) and the detailed droplet formation (I-N). Scale bars: 10  $\mu\text{m}$  in A, B, I-N and 25  $\mu\text{m}$  in C-H. Reprinted from ref [176] with permission.

For dewetting films, the growth of the dry hole is accompanied by a ridge (or rim) formed at the liquid front, due to the accumulation of the fluid removed from the dry hole. The cross-section of the ridge typically has a symmetrical, circular profile [178,199], similar to shown in Figure 1.15a. The shape of the ridge is circular, with the height of the ridge comparable to its width, so that near uniform Laplace pressure is maintain within the ridge. At the region where the region merges into the flat unperturbed thin film, Seemann et al. [200] found that the ridge thickness can drop below the unperturbed film thickness, resulting in a trough and a damping oscillation shaped ridge. The growth of the trough can eventually lead to nucleation of satellite holes around the primary hole [189]. The shape of the ridge becomes asymmetrical when significant surface slippage is present [174]. In fact, the shape and evolution of the ridge characterized experimentally can be utilized to determine the slippage length [173]. The shape of the ridge is also sensitive to

many other film properties, including surface forces (disjoining pressure isotherm) [190], viscoelasticity and residual stresses in glass transition [198,201].

At dewetting continues and ridge size increases, small thickness fluctuations on the ridge can amplify and eventually leads to a Rayleigh-type instability and ridge breakup [176–178]. Figure 1.15b shows a montage of ridge instability. The retreating contact line undulates in snapshot D and E, then the cylindrical ridge breaks up to form periodically distributed droplets (snapshot F), which are left behind the retreating contact line in the dry region (snapshot I-N).

For stratifying foam films, the ridge formed during thinner domain growth has only been proposed theoretically (see Figure 1.6) [77,79]. So far no experimental detection and characterization of the ridge shape and its evolution is available. The formation of white spots at later stage of domain growth was thought to be akin to the Rayleigh-type instability of the ridge in dewetting film [79], however detailed, experimental analysis on the evolution and morphology of the white spots is still lacking.

## **1.6 Objectives of this study**

The stability and lifetime of foams depends on the hydrodynamics and thermodynamics of the thin liquid films separating the gas bubbles. Ultrathin foam films (usually <100 nm) containing micelles, nanoparticles, polyelectrolytes-surfactant complex, and smectic liquid crystals exhibit film stratification as the aforementioned supramolecular structures is drained out from the film in layer-by-layer fashion. The oscillatory surface forces originated from these structures contribute to the stability of the foam film and often prolong its lifetime. Upon reviewing the literature,

several unanswered questions are recognized in the current understanding of the dynamics and stability of the stratifying foam films:

- i) Is it possible to develop an experimental technique to characterize the thickness evolution, complex pattern formations and instabilities in stratifying foam films, with the required high spatial and temporal resolutions to help in better analysis and deeper understanding of the stratification process of free-standing ultrathin ( $< 100$  nm) foam films?
- ii) What is the mechanism underlying the formation and growth of thinner circular domains within the thicker film during stratification? The two proposed theories in the literature (i.e. diffusive osmosis mechanism [73] and “hole sheeting” [79]) are incompatible with each other, and do not capture all the experimental observations.
- iii) What is the effect of the Plateau border on the dynamics of domain growth? Only growth of single, isolated domain has been investigated in the literature.
- iv) Does a nanoscopic ridge form around the growing thinner domain during stratification? Such structure has only been theorized before [77,79] without experimental detection and characterization.
- v) If the ridge is formed, how is its shape and evolution involved in the dynamics of thinner domain expansion and the stability/instability of the ridge?
- vi) Can a comprehensive thin film hydrodynamic model be developed, which is consistent with all the experimental observations of domain expansion, ridge formation and instabilities during stratification? The model needs to consider the free surface flows, the surface curvature driven flows, the effects of the supramolecular structural oscillatory disjoining pressure, among other things.

This study is aimed to answer all these questions, with the chapters organized as follows:

Chapter 2 introduces the experimental technique of Interferometry Digital Imaging Optical Microscopy (IDIOM) [31]. This technique combines interferometry principles with digital imaging and image analysis to characterize the thickness profile and variations in stratifying foam films. Unlike conventional interferometry methods, IDIOM retains the thickness information of the entire film area with high spatial and temporal resolution, therefore allows detections and detailed analysis on the nanoscopic structures formed during film stratification, including ridges, mesas, craters and terraces.

Chapter 3 discusses the dynamics of thinner, circular domains growing within thicker film during film stratification [81]. An image object tracking scheme is used to discern two distinct regimes of the time dependences of domain radii. While an isolated domain grows with its radii proportional to square root time initially, after a section of the expanding domain coalesces with the Plateau border, the radii increase linearly with time. A similar scaling transition also takes place when topological instability sets in at the contact line between the expanding domain and the rest of the film, and leads to formation of mesa-like white spots. A comprehensive theoretical framework is proposed to explain these observations self-consistently.

Chapter 4 reports the first experimental detection and characterization of a ridge formed around the growing domain during stratification, using the protocol of IDIOM. The shape and evolution of the ridge, both before and after the white spot forming topological instability, are examined and compared with a newly developed thin film hydrodynamic model. Asymptotic solutions to the ridge are recognized with scaling analysis. The underlying mechanisms of the topological instability and the subsequent white spots growth are discussed.

Chapter 5 presents results of numerical solution to the thin film hydrodynamics model for domain growth and ridge formation, and compares them with the experimental characterizations. In order to quantify the contribution of structural oscillatory disjoining pressure, an explicit semi-empirical formula is outlined to estimate the disjoining pressure isotherm for ionic micellar solutions. The model predictions are mostly in quantitative agreement with the experimental observations.

Chapter 6 concludes the fundamental insights gained through the experimental and theoretical explorations of the dynamics of stratifying foam films, and provides perspective for future studies.

# **CHAPTER 2.**

## **CHARACTERIZATION OF STRATIFYING FOAM FILMS USING INTERFEROMETRY DIGITAL IMAGING OPTICAL MICROSCOPY (IDIOM)**

### **2.1 Introduction**

Experimental visualization and characterization of the thickness evolution in free-standing thin liquid films is crucial to understand their stability, drainage dynamics and pattern formation. During stratification of foam films, the film thickness and its spatial and temporal evolution embeds rich information about the underlying hydrodynamics and intermolecular interactions (surface forces or disjoining pressures). Significant progress in understanding of the structure and stability of supported thin films (with at least one solid/liquid interface) has occurred through the emergence and advances in several microscopy and force-based experimental techniques, including surface force apparatus (SFA), fluorescence imaging, atomic force microscopy (AFM), total internal reflection microscopy, ellipsometry, and electron microscopy. However, most of the aforementioned techniques are inapplicable to free-standing films, due to the lack of the supporting substrate and often fast dynamics (in the order of seconds). It has been a long-standing challenge to develop experimental characterization techniques suitable for free-standing foam films, with high spatial (thickness  $< 10$  nm, lateral  $\sim 1$   $\mu\text{m}$ ) and temporal resolution ( $< 1$  ms).

Interferometry techniques utilize the interference between reflected light from the two gas-liquid interfaces of the free-standing film to obtain film thickness. The conventional interferometry method uses monochromatic light source and photodiode for light intensity measurement. This setup is only capable of measuring average thickness within one sample spot of size 1-100  $\mu\text{m}$ , it



lacks the spatial resolution needed to gain more insight to the dynamics and pattern formation in stratifying foam films. In this chapter, we introduce the novel technique of Interferometry Digital Imaging Optical Microscopy (IDIOM), which achieves the desired high spatial and temporal resolution for visualizing and characterizing the evolution of stratifying films. The IDIOM protocol combines the interferometry principles with digital image filtration and analysis. This protocol in this chapter to reveal the complex dynamics and nanoscopic structure formation during the stratification of micellar foam films.

## **2.2 Experimental method**

### **2.2.1 Materials**

The stratifying foam films studied are made with solutions of sodium dodecyl sulfate (SDS). The SDS (anionic surfactant, molecular weight 288.4 g/mol, Sigma-Aldrich Co., L6026, >99.0%) is used as received, without further purification. The surface tension of SDS solutions are measured using both maximum bubble pressure tensiometry and pendant drop tensiometry. The critical micelle concentration (CMC) is measured to be 8 mM, within the reported range of 7 mM-10 mM at 25 °C. The surface tensions of SDS solutions above CMC remain almost constant at 35 mN/m. All solutions are prepared with deionized water with resistivity of 18.2M $\Omega$ .

Impurities in the SDS solutions, in particular small amount of 1-dodecanol resulted from SDS hydrolysis, can affect the SDS micellization, surface adsorption and interfacial rheology of the solution, and therefore alters the drainage dynamics of the foam films. The concentration-dependent surface tension of aqueous SDS solutions shows a smooth transition near the CMC of 8 mM, indicating that the as-made solutions are relatively free of impurities [183]. In order to

minimize the effect of hydrolysis of SDS, all the solutions are used in thin film experiments within 2-3 days after they are made. No electrolytes are added to the solutions in the present study, as high ionic strength of the solution is reported to suppress the film stratification [55,104].

### 2.2.2 Experimental setup

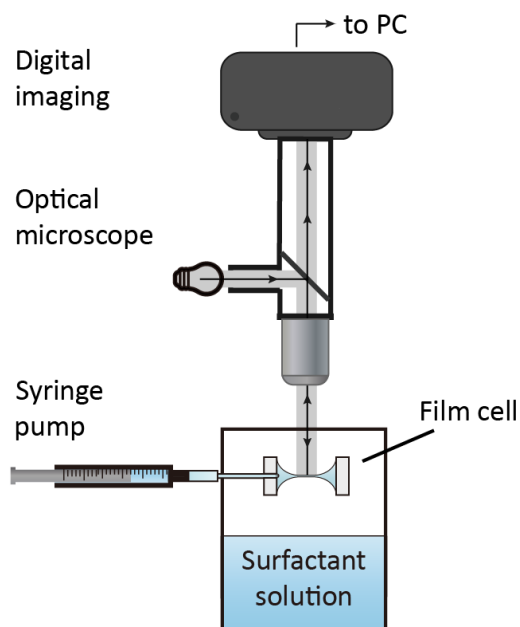


**Figure 2.1** Schematic of the experimental setup consisting thin film holding cell, reflected light microscope, and high resolution digital imaging.

Drainage and stratification of a single horizontal foam film is visualized and characterized with the thin film apparatus and imaging system shown schematically in Figure 2.1. The foam film is formed and controlled in a film cell. Two types of film cell geometries are used throughout this study: (i) a Scheludko-type cell (Figure 2.2) and (ii) a porous plate cell (Figure 2.3). In both cases,

a circular thin film with nearly plane-parallel gas-liquid interfaces is formed at the center of the cell, and a syringe pump is used to control the fluid volume contained in the cell. The film is surrounded by a thicker meniscus, which is analogous to the Plateau border in real foams (*cf.* Figure 1.1c). The cell is placed within a closed chamber, containing the same surfactant solution as used in experiments, in order to minimize the effect of evaporation.

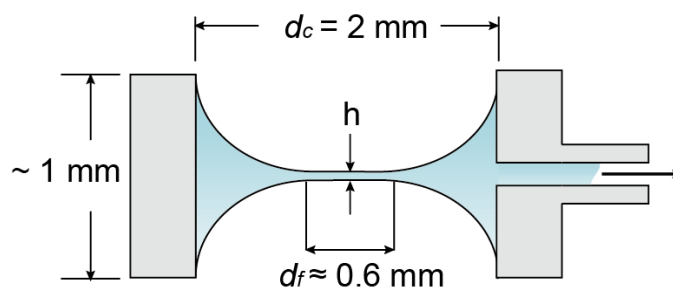


**Figure 2.2** Schematic of Scheludko-type cell for forming a single thin film and controlling its drainage. Adapted from ref [81] with permission of The Royal Society of Chemistry.

The first cell geometry is shown schematically in Figure 2.2. It is similar to the Scheludko cell [95] introduced in Section 1.3.1. The cell consists a miniature glass cylinder (inside diameter  $d_c \approx 2$  mm) with a small orifice ( $< 0.1$  mm) drilled on the side wall, and a stainless steel needle fixed in the orifice to connect liquid in the cell to a syringe pump (New Era NE-1000). The test solution is loaded into the cell to form a biconcave drop. A circular thin film is then formed by slowly withdrawing liquid from the drop using the syringe pump. Once the desired film diameter,  $d_f$ , is reached, the withdrawal is stopped to maintain a constant fluid volume throughout the film drainage process. The drainage is driven by capillary pressure difference between the plane-

parallel thin film and the curved Plateau border. This capillary pressure difference,  $P_c$ , can be estimated with the assumption that the surfactant solution completely wets the glass cell wall, and the contact angle between the thin film and the Plateau border is small.  $P_c$  is then given by: [55]

$$P_c \approx \frac{4\sigma d_c}{d_c^2 - d_f^2} \quad (2.1)$$

where  $\sigma$  is the surface tension of the test solution. It has been suggested that the kinetics of stratification is influenced by the size of the film [74,75,80]. As a result, we maintain the initial size of the film ( $d_f \approx 0.6$  mm) across experiments with different surfactant concentrations, in order to make meaningful comparisons. The initial capillary pressure in the experiments is  $P_c \approx 50$  Pa. At later stage of the film drainage, the film reaches small thicknesses, and the micellar structural disjoining pressure becomes large enough to completely balance the driving capillary pressure and bring the drainage to a halt. Further stepwise thinning is then induced by withdrawing more liquid and increasing  $d_f$ . In an alternative protocol [97,99] emulated for comparison, the cell container is opened briefly to allow evaporation, which results in an increase in the capillary pressure and consequently in a step transition.

A porous plate cell is the second cell used in this study (Figure 2.3). The porous plate thin film balance is first developed by Mysels and Jones [102], and later refined by several researchers [103–105] (see Section 1.3.1). The design used in this study is close to that developed by Dimitrova et al. [105]. The cell is made with fritted glass disk (Wilma-LabGlass) with porosity of 10-15  $\mu$ m. The cell geometry is shown in Figure 2.3a. The film holding hole is drilled at the center of the disk with 1 mm diamond-coated drill bit, and tapered with spherical grinding head. The disk thickness

around the hole is reduced to  $\sim 0.1$  mm. This geometry permits formation of foam film with low applied capillary pressure ( $P_c \sim 35$  Pa), which is beneficial for probing meta-stability at higher film thicknesses when the disjoining pressure is small. On the other hand, the small porosity of the fritted disk permits a maximum attainable capillary pressure of  $\sim 4000$  Pa, much larger than that in the Scheludko-type cell. In addition, the porous plate cell is connected via Teflon tubing (Cole-Parmer) to a pressure transducer (Omega, PX409-001G5V) and the syringe pump (New Era NE-1000). This configuration is often referred to as the thin film balance (TFB) setup [104], which allows direct measurement of the pressure difference across the thin film interfaces, therefore the equilibrium disjoining pressure.

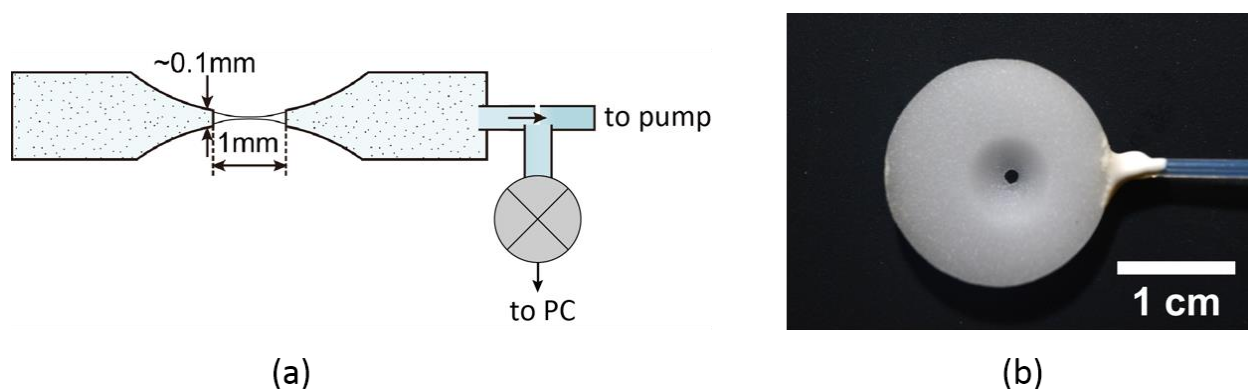


**Figure 2.3** Porous plate film holding cell. (a) The schematic showing the side view and its connection to a syringe pump and a pressure transducer. (b) The top view photo of the porous plate. Adapted from ref [31] with permission. Copyright © 2016 American Chemical Society.

Compare to the Scheludko-type cell, porous plate setup is advantageous in its wider range of accessible pressure, and better control and measure of the pressure applied. However, the porous

plate cell suffers from difficulties in cleaning, due to its small porous structure. The porous plate used in this study are thoroughly rinsed with large amount (liters) of DI water, and then soaked in the surfactant solution with same concentration as the test solution overnight, before loading in fresh test solution for experiments. In order to prevent contaminations, each cell is only used for single type of surfactant, only varying solution concentration.

### **2.2.3 Interferometry digital imaging optical microscopy (IDIOM)**

The drainage process of the single horizontal foam films formed in the thin film apparatus is captured by a reflected light microscope imaging system, consist of precision microscope lens system (Navitar Zoom 6000 with 10x microscope objective), and a high resolution high speed color camera (FASTCAM Mini UX100). The illumination is provided by a white LED light source (Fiilex P360EX) with adjustable color temperature (set to 5100K for most experiments). The protocol of IDIOM as described below is also tested with various other cameras and illumination light sources, which is discussed in Section 2.4.1.

The RAW format images/videos, recorded from the reflected light microscope and high speed color camera assembly, is analyzed in MATLAB R2014a (or R2015a) with specially developed codes. Every color image is loaded as a three-dimensional matrix in which each image pixel contains three values associated with the light intensities of red (wavelength  $\lambda \approx 650$  nm), green ( $\lambda \approx 546$  nm) and blue ( $\lambda \approx 470$  nm) light. The light intensity recorded in each color channel is represented as a value in the range of 0-4095 (12 bit depth for the specific camera used). Following Scheludko [95], a relatively accurate measure of thickness,  $h$  can be obtained by using the following equation based on a normalized measure of intensity,  $\Delta = (I - I_{\min}) / (I_{\max} - I_{\min})$ ,

that minimizes the influence of source intensity and background/detector errors. The thickness equation reads:

$$h = \left( \frac{\lambda}{2n\pi} \right) \arcsin \left( \sqrt{\frac{\Delta}{1 + 4R(1 - \Delta)/(1 - R)^2}} \right) \quad (2.2)$$

where  $h$  is the film thickness,  $I_{\max}$  and  $I_{\min}$  are maxima and minima intensities of the last order of interference, and  $R = (n - 1)^2 / (n + 1)^2$  is the Fresnel coefficient of the air-liquid interface. Here  $n$  is the refractive index of the bulk solution. For the dilute surfactant solutions used in this study, water refractive index is used,  $n = 1.33$ .

The value of  $I_{\max}$  is determined by tracking the intensity over time and finding its last maxima, which corresponds to a bright white color in the images and a film thickness of 80 to 100 nm. This procedure is typically repeated several times at different region within the thin film area, in order to ensure the value obtained is not affected by film thickness (hence light intensity) inhomogeneity. The minimum intensity in zeroth order interference,  $I_{\min}$ , is reached at zero film thickness. After each experiment, the thin film apparatus is removed from the field of view and the background intensity is recorded as  $I_{\min}$ . Care is taken to avoid stray reflections from the apparatus and the container. The gas-liquid interface of the surfactant solution in the closed container is kept out of focus at all time to avoid reflection (distance from the thin film >10 cm, 10 times focal length).

The thickness determined from Equation (2.2) is a measure of “equivalent film thickness”, assuming the bulk solvent refractive index for the entire thin film, even though the two interfaces are surfactant enriched. Three-layer model is available which uses different refractive indices for the adsorbed surfactant layers and the aqueous solution in between [202]. However if appropriate

values for thickness and refractive index of the adsorbed layer are obtained, the correction introduced by the model turns out to be negligible for SDS films [95,203,204]. Equation (2.2) also neglects visible light absorption, includes multiple reflections within the film, assumes a near normal incidence and considers only zeroth order of interference, which are valid assumptions for films with thickness  $h < \lambda/2n\pi$  ( $h < 85$  nm for the shortest blue wavelength).

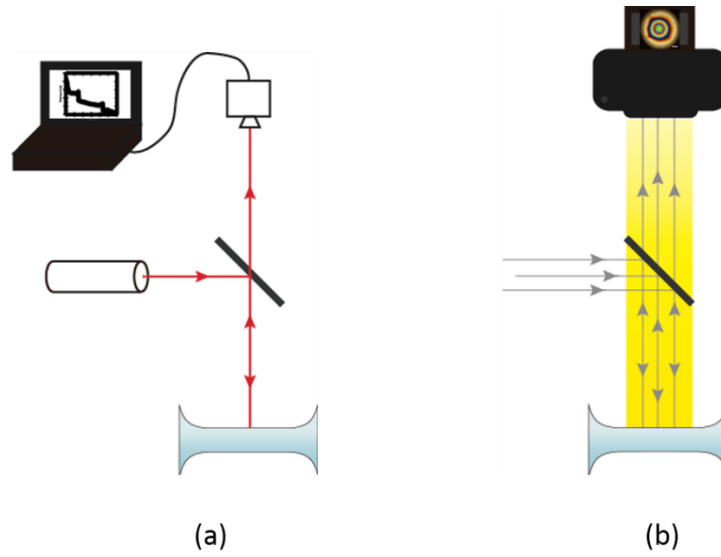


**Figure 2.4** Comparison between (a) conventional interferometry methods and (b) IDIOM.

In the conventional interferometry methods (schematic shown in Figure 2.4a), the film thickness is typically computed using a photodetector and a monochromatic light source [95,104,205]. The light intensity reflected from a spot size of 1-100  $\mu\text{m}$  are tracked over time to obtain  $I(t)$ , and it is converted into the evolution of the average thickness within the sampling spot. In contrast, the IDIOM protocols (shown in Figure 2.4b) use a white (with multiple



wavelengths) light source and rely on the high quality CMOS or CCD sensors of digital cameras for capturing a pixel-wise, spatially-resolved map of reflected light intensity, for three wavelengths and at each instant,  $I(x, y, t, \lambda)$ . The technique therefore allows mapping the thickness of the entire film area, instead of only averaged thickness from conventional interferometry. With the aforementioned microscope assembly, the thickness measurement reaches spatial resolution of 0.5  $\mu\text{m}/\text{pixel}$ , and millisecond temporal resolution. Thicknesses are measured simultaneously and separately from three color channels, instead of single wavelength measurement in conventional setup, and they can then be averaged to further reduce inaccuracy.

## 2.3 Results

### 2.3.1 Observation of stratification in foam films

Stratification in a foam film made from 50 mM SDS solution ( $c/\text{CMC} \approx 6$ ) is visualized with the thin film apparatus. Snapshots during the film thinning process from the reflected light microscope is shown in Figure 2.5. Immediately after the film is formed, the interference between light reflected from the two air-liquid interfaces of the film creates colorful rings, indicating a dimple with thicker center and thinner periphery forms. The dimple quickly exits from the film through asymmetrical drainage, and the vibrant interference colors disappear as the film thickness reaches below  $h \approx 100$  nm. Various shades of gray then appear within the film, and layers with progressively darker shades form and grow in expense of the lighter shaded layers, until the thinnest black film forms. The common black film ( $h \approx 20$  nm) formed after multiple thinning events can be stable for hours without rupturing, when evaporation and outside disruption are minimized.

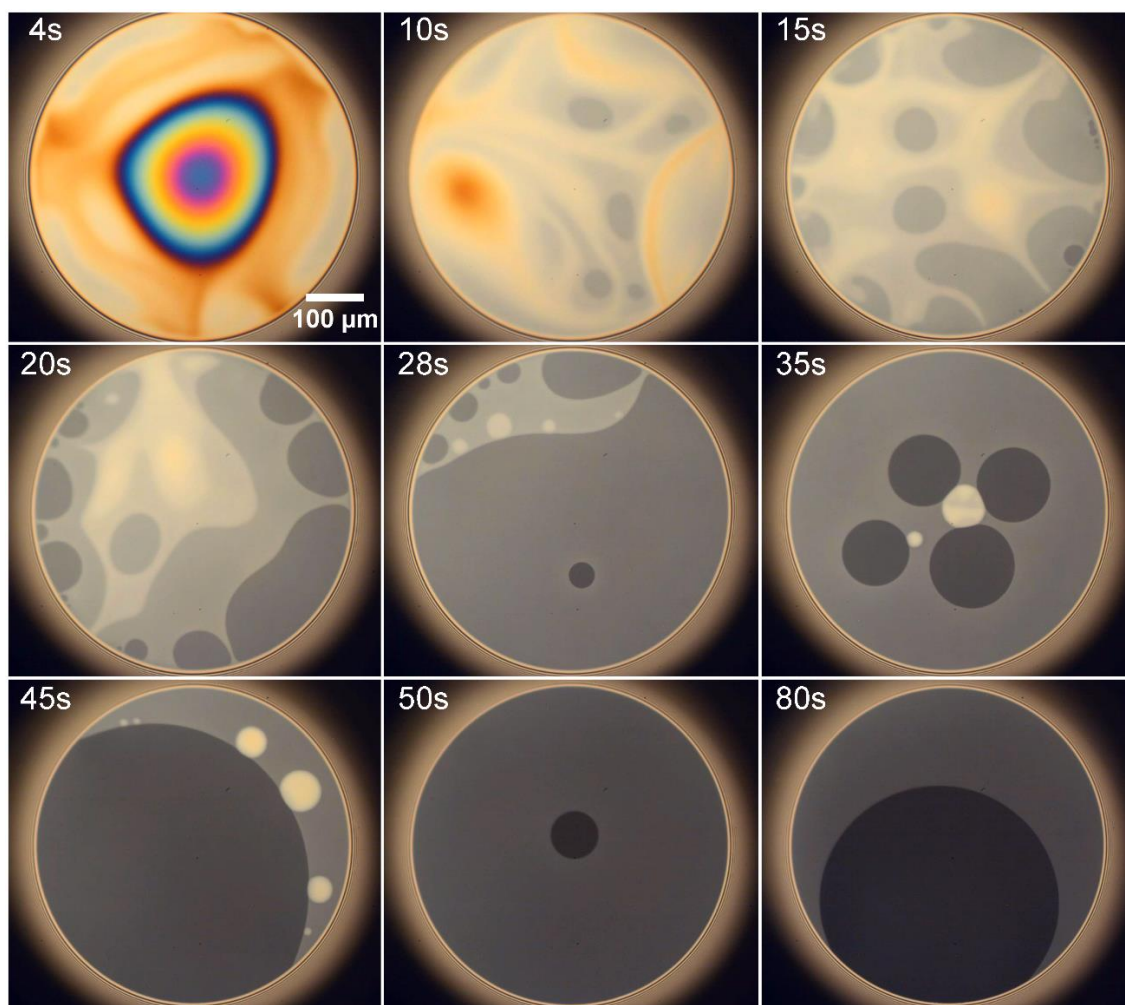


**Figure 2.5** Montage of foam film stratification in SDS 50mM solution.

During the thinning process, distinct regions with different film thicknesses (therefore different brightness) co-exist in the film. The film thickness decreases via spontaneous formation and growth of one or more thinner (appearing darker), circular domains. The domain boundaries are sharp, and expansion of the domain continues as the domains coalesce with each other or with the film periphery (the Plateau border), until the thickness of entire film is reduced to the next

thickness. This transition takes place multiple times, sometimes simultaneously, until a stable film thickness is reached.

### 2.3.2 Thickness measurement

The IDIOM protocol is used to measure the thickness of the thinning film in the porous plate cell setup with  $P_c \approx 130$  Pa . In Figure 2.6a, the time dependence of film thickness is presented by taking average of the thickness in a 40-pixel size square ( $\sim 20$   $\mu\text{m}$ ) sampling region at the center of the film (square region marked in Figure 2.6b). The time  $t = 0$  is define as the instant when zeroth order interference is reached for the shortest wavelength (blue light), i.e. when thickness measurement following Equation (2.2) becomes valid. The thicknesses measured from three color channels (plotted in their respective colors) are almost identical after  $t = 0$  . The differences between them are typically  $< 1$  nm. Figure 2.6a shows that the film thins in a step-wise fashion, with multiple thickness setups, corresponding to different shades of gray observed in the micrographs. Figure 2.6b shows one micrograph at  $t = 10$  s, where the three different shades co-exist and correspond to three of thickness steps. The transition from thicker to thinner step in the  $h$  vs.  $t$  plot (Figure 2.6a) takes place when the thinner part of the film grows into and occupies the sampling region. The step heights between thickness transitions,  $\Delta h = h_n - h_{n-1}$ , remain almost constant throughout the stratification.

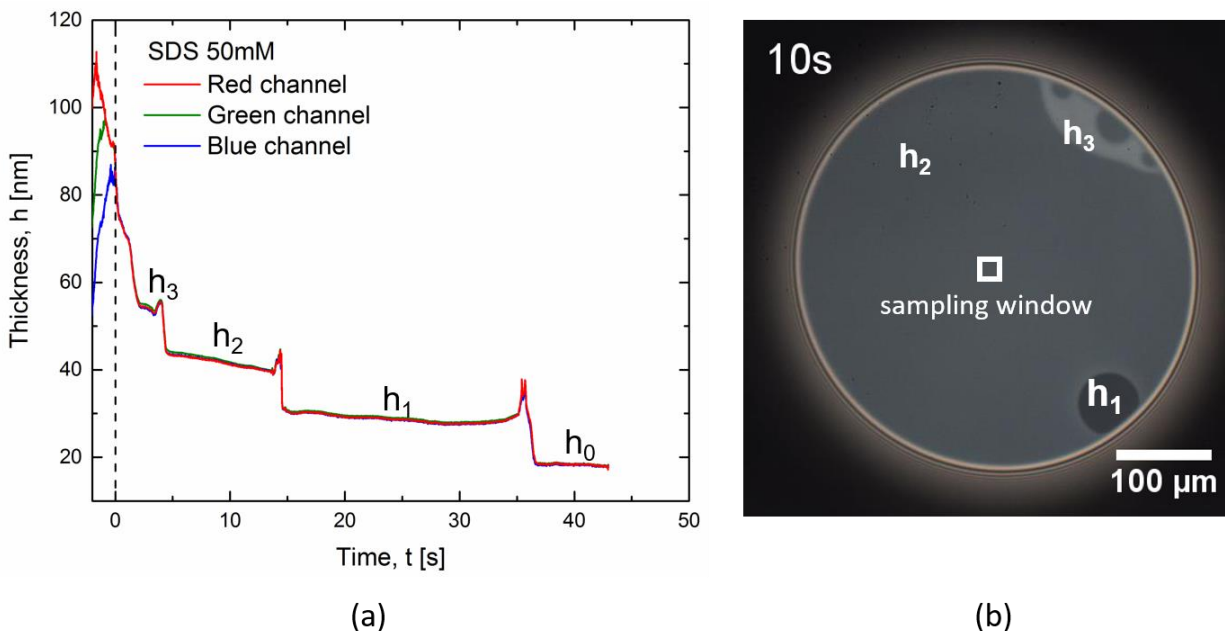


**Figure 2.6** Thickness evolution in the stratifying foam film. (a) Thickness vs. time plot obtained by tracking the average thickness within a 40-pixel sampling window. (b) The micrograph showing three different shades of grey corresponding to three thickness steps. Adapted from ref [31] with permission. Copyright © 2016 American Chemical Society.

The concentration dependence of thickness step height,  $\Delta h$ , for SDS solutions is plotted in Figure 2.7. In general,  $\Delta h$  decreases with increasing surfactant concentration,  $c$ . This is attributed to the increase in electrostatic screening effect as the concentration of charged macromolecules (micelles) is increased. The values of step size obtained from IDIOM are consistent with those reported in the literature [55,99,128,206,207].

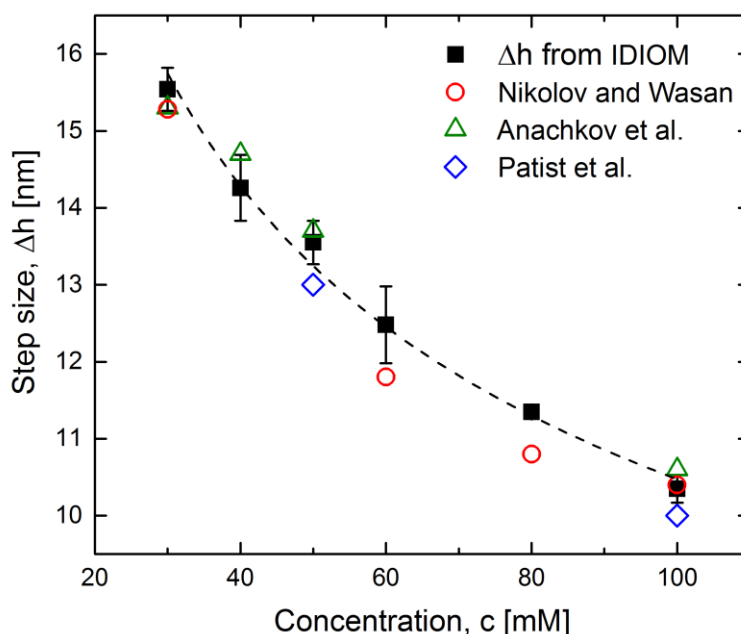


**Figure 2.7** The step sizes obtained by IDIOM compared with conventional interferometry results by Nikolov and Wasan [55], and Anachkov et al. [99], as well as theoretical estimates by Patist et al. [207]. The dash line shows  $\Delta h \propto c^{-1/3}$  scaling, expected for spherical micellar systems. Adapted from ref [31] with permission. Copyright © 2016 American Chemical Society.

The step size shows an inverse-cubic-root scaling,  $\Delta h \propto c^{-1/3}$ . This scaling for the period of oscillatory structural forces is found in many spherical colloidal systems [208], including stratifying micellar films [99,128]. It is correlated to the mean distance between the supramolecular structures in solution. As illustrated in Figure 2.8, the step size of stratification corresponds to the difference between thicknesses at which the applied capillary pressure is balanced by the disjoining pressure. As the long range disjoining pressure is dominated by supramolecular structural contributions, the step size effectively provides a measure of the period of the supramolecular oscillatory disjoining pressure. Anachkov et al. [99] posited that the concentration dependence of stratification step size can be further analyzed to determine micelle size, aggregation number. The

results show that IDIOM protocol provides measurements comparable to those obtained in spectroscopic and scattering studies [55,99,207].

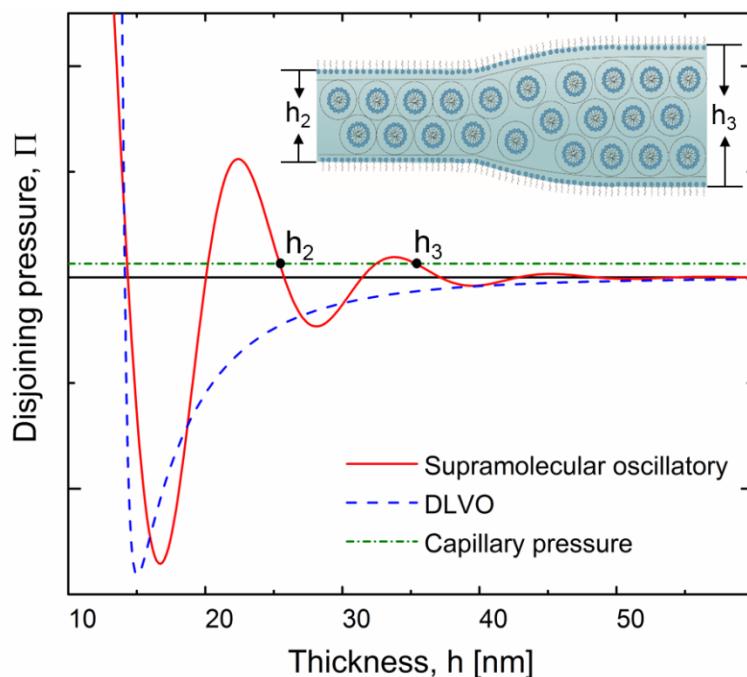


**Figure 2.8** Illustration of the balance between applied capillary pressure and disjoining pressure at discrete film thicknesses. The disjoining pressure is dominated by supramolecular contribution except in short range ( $h \sim 15$  nm). Adapted from ref [31] with permission. Copyright © 2016 American Chemical Society.

### 2.3.3 Rich dynamics of stratifying films revealed by IDIOM

The plot of thickness versus time shown in Figure 2.6a emulates conventional interferometry, for the thickness is computed using the averaged light intensity over a single sampling region. Similar datasets have been used for evaluating stabilities of different thickness layers [55], calculating effective viscosities in the film [209], and measuring disjoining pressure isotherm [16,104]. However, as illustrated in Figure 2.5, the stratification process involves much

richer and more complex dynamics, than that captured by the thickness sampled at individual regions. For example, the growth of a thinner domain is often associated with formation of white spots around the domain (e.g.  $t = 35$  s, 45 s in Figure 2.5). These spots are much larger in thickness, hence appears white in the micrograph. The detailed shapes and growths of these spots are unavailable with the conventional interferometry methods. The only evidence of white spot formation in Figure 2.6a is the small thickness spikes at the transition of thickness steps, which are indications of thicker spots sweeping through the sampling region.

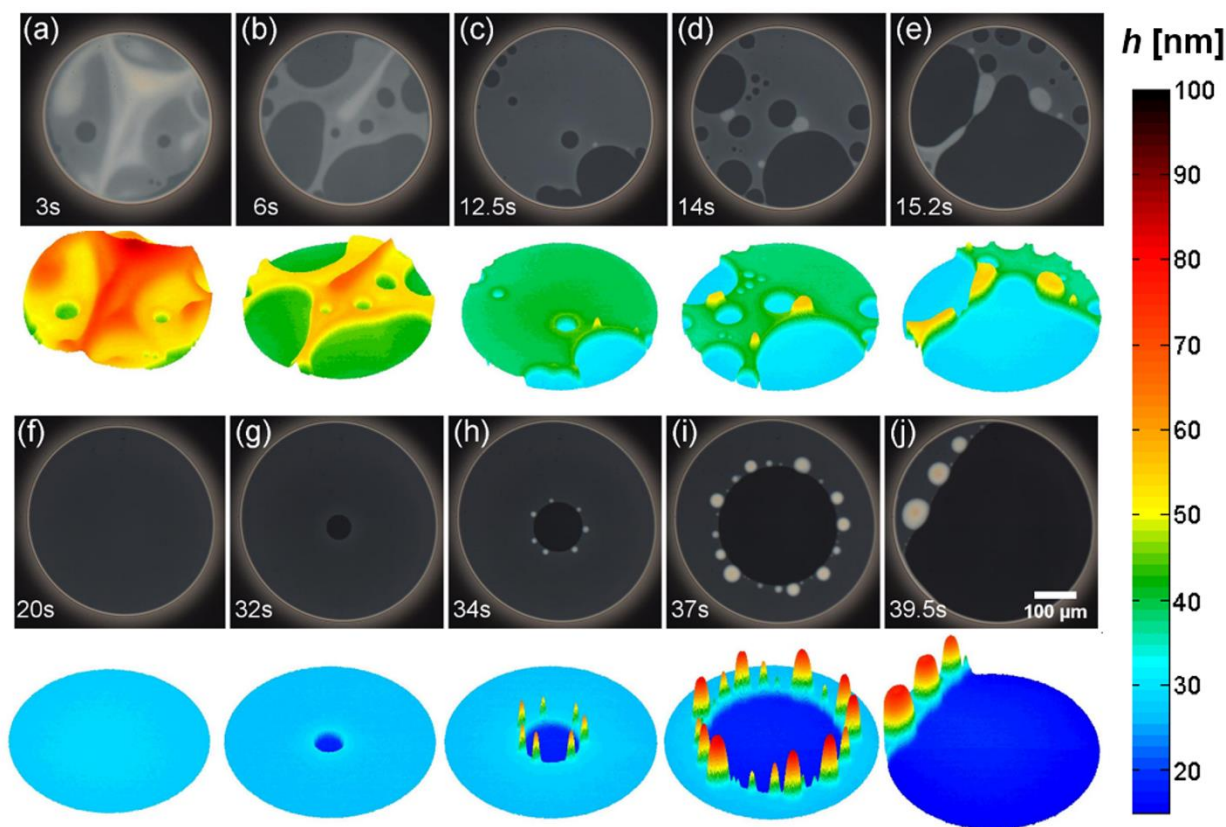


**Figure 2.9** Micrographs showing the stratification of a thin film made from SDS 50 mM solution, and the associating 3D thickness maps for the entire film area constructed by IDIOM. Reprinted from ref [31] with permission. Copyright © 2016 American Chemical Society.

In contrast, IDIOM protocols provide the high spatiotemporal resolution required for visualizing and characterizing the complex topography of stratifying films. Figure 2.9 shows the 3D thickness maps for the entire film area throughout the stratification process, constructed by IDIOM protocols. Coexistence of domains of multiple thicknesses, and complex transition dynamics from thicker to thinner layers are clearly visualized. The landscape contains nanoscopic shape that resembles mesas, ridges, terraces, and craters. The formation, growth, interaction and coalescence of multiple thinner domains can be followed (Figure 2.9b-c), and detailed dynamics of domain expansion and instabilities leading to white spot formation are also captured (Figure 2.9g-j).

The advantages of IDIOM in analyzing stratification dynamics are showcased in Figure 2.10, by comparing IDIOM measurement with the conventional interferometry measurement from two different sampling regions. As shown in Figure 2.10a&b, the thickness measured only from small sampling windows can be misleading, due to the complex dynamics and spatial heterogeneity. Significant differences are found between curves obtained from the two sampling regions of the same stratifying film. The thickness variations, onset of stepping, and the duration of each step, are all far from consistent. For example, at  $t = 36$  s, a white spot formed around the growing domain happens to enter sampling region 2, thus produce a big spike in the thickness plot (Figure 2.10a). The white spot formation is completely missed in measurement from sampling region 1, where the same thickness stepping appears featureless.



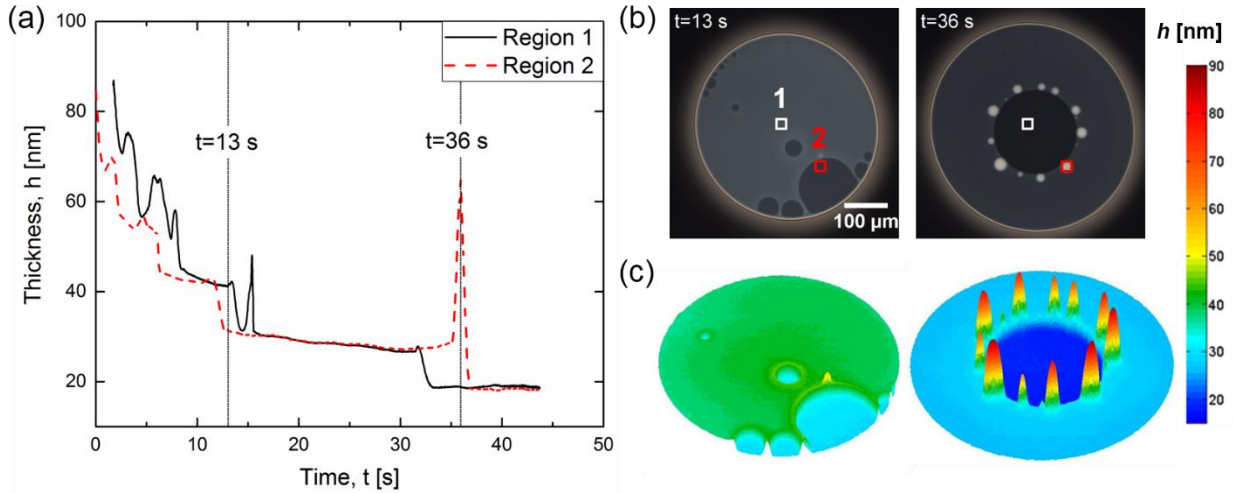


**Figure 2.10** Comparison between thickness profile measured by conventional interferometry methods and IDIOM. (a) Average thickness vs. time of the stratifying thin film of 50 mM SDS, by following the thickness variation in two different sampling regions. (b) Two micrographs taken during stratification showing the coexistence of different thickness domains and patterns. The two square marks show the sampling region measured in (a). (c) IDIOM thickness maps corresponding to the micrographs in (b).

These shortcomings of conventional interferometry may lead to potential inaccuracies when the hydrodynamics and stability of the stratifying films are discussed. For example, Bergeron and Radke [104] presented a “dynamic method” for measuring the disjoining pressure isotherm of the stratifying film solely from the interferometry results. The variations of the thickness over time, including the stepping and plateauing, are fitted to the thin film hydrodynamic model to obtain the magnitude of the pressure. This method could be problematic, since the same stratification process could generate different thickness vs. time curves (as the ones in Figure 2.10a), which then result in completely different disjoining pressure isotherms.

On the other hand, construction of thickness maps with the IDIOM method retains the complete thickness information (Figure 2.10c). With the capability of resolving detailed morphological features and their evolution during stratification, several unanswered questions can

be probed and addressed, regarding the hydrodynamics of thin freely standing films and the influence of intermolecular and surface forces.

## 2.4 Discussion

### 2.4.1 Applicability of IDIOM

IDIOM shows universality across multiple imaging systems, as the principles underlying IDIOM protocol are not specific to the imaging system used. The thickness measurement can be easily realized with a variety of cameras and light sources. To illustrate this, we carried out the thickness measurement of stratifying foam films with three different cameras, including a commercial, consumer-grade digital camera. The specifications of the cameras are listed in Table III. Two light sources are also used: a Fiilex P360EX LED light and a Schott ACE 1 halogen light.

**Table III** List of cameras tested with IDIOM protocol and their specification

Camera name	Record format	Bit depth	Pixel resolution	Frame rate (fps)
<b>Photron FASTCAM Mini UX100</b>	High speed movie (.mraw)	12	1280*1024	Up to 4000 (full frame)
<b>Tucsen ISH1000 CCD</b>	movie (.avi)	8	3664*2748	~3(full frame)
<b>Nikon D5200 DSLR</b>	RAW image (.nef)	14	6000*4000	~1
	Movie (.mov)	8	1920*1080	30

Variants of the image analysis routine are developed in MATLAB, in order to accommodate the different image/video file formats used in different cameras. In particular, the RAW images from Nikon camera cannot be read directly into MATLAB software, instead they are first converted to .tiff format with no data compression, using the open source program DCRaw. The resulting .tiff images are then analyzed with specially written MATLAB routine.

In general, the thicknesses of stratification layers are accurately measured using all the cameras and light sources. One complication is found when using the movie files taken with the customer-grade Nikon DSLR camera. A lossy compression is applied to the movie (.mov) file upon recording, resulting in a non-linear relation between output RGB values and the real light intensity received by the CMOS sensor. This non-linear compression is taken into account through careful intensity vs. RGB output calibration. Figure 2.11a shows the experimental setup for such calibration: a photodiode (Hinds Instruments DET-90) is used to measure the absolute light intensity (in terms of output voltage) and compare with RGB value recorded by the camera. By varying the intensity of the light source, a look-up table (LUT) is produced, relating the RGB output to the real light intensity. As shown in Figure 2.11(b), the movie recorded by Nikon camera indeed loses the linearity, while the uncompressed RAW format preserves it. In the thickness measurement protocol, the LUT can then be used to convert RGB information into absolute intensity, before normalizing it for further analysis. In addition, the movie RGB values are found to remain approximately linear in the low intensity range, so the non-linear conversion procedure is not necessary if the maximum recorded intensity is less than  $\sim 150$ .

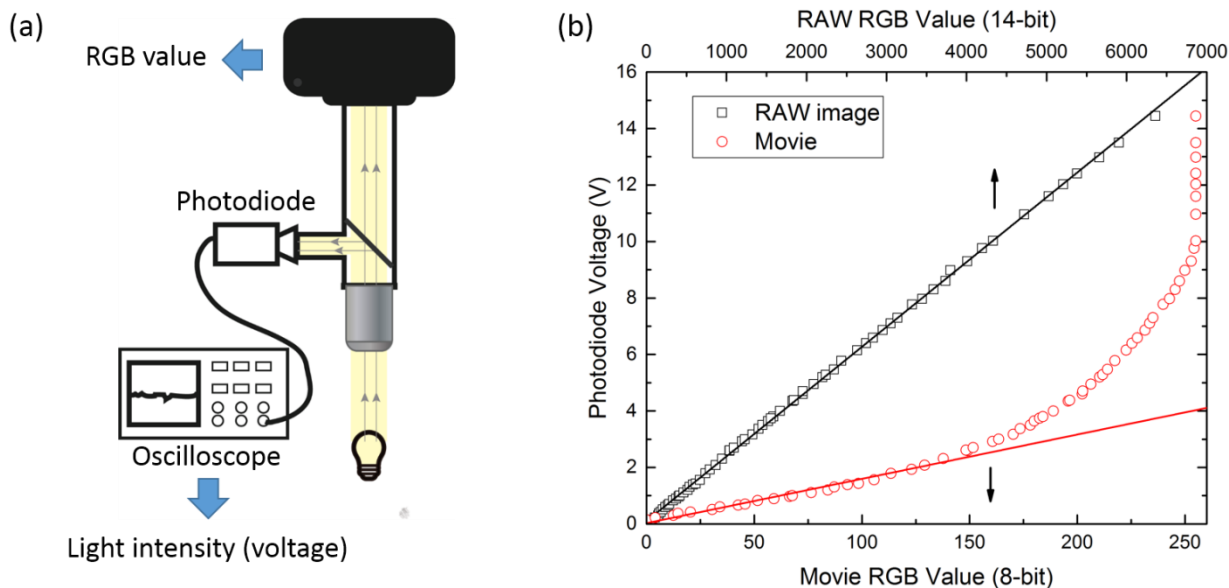


**Figure 2.11** Calibration for camera output RGB values. (a) Schematic of calibration setup. (b) Voltage output from the photodiode vs. RGB output from the Nikon D5200 DSLR camera.

Through an extensive literature survey, we were able to find several examples of the use of consumer-grade, off-the-shelf DSLR cameras as photometers, spectrophotometers, colorimeters and photodiodes in star gazing and astronomy [210–212], contrasting color of polymer nanocomposites made with gold nanoparticles dispersed in a polymer matrix [213], detection of fluorophores in so-called photoscopy applications [214], forensic investigations [215], and for investigation of colors in biology [216–219]. In the present study, we are able to quantitatively analyze the nanoscopic topographic structures in freely-standing foam films with a variety of cameras.

### 2.4.2 Error estimation

In this section, we discuss the resolution limits of the IDIOM protocol and the sources of error in thickness measurements. In an ideal case, the camera converts light intensity with no signal noise, and utilizes its entire dynamic range, *i.e.*,  $I_{\max} = 2^{\text{BitDepth}} - 1$ ,  $I_{\min} = 0$  in calculating  $\Delta$  in Equation (2.2). The intrinsic minimum measurable thickness and measurement error are then results of the quantization of light intensity to integer values as RGB output. With different camera bit depth, the available number of integers varies as  $2^{\text{BitDepth}}$ . Therefore the theoretical thickness resolution and lower limit of the measurement vary. The intrinsic error  $\varepsilon$  associated with rounding up the light intensity to integer RGB values can be estimated by

$$\varepsilon(I) = \frac{h(I+0.5) - h(I-0.5)}{2} \quad (2.3)$$

where  $h(I \pm 0.5)$  is computed by using Equation (2.2). Due to the non-linear relation between light intensity and film thickness (see Equation (2.2)), the magnitude of  $\varepsilon$  is different at different thickness, as shown in Figure 2.12 for the 12-bit camera. It approaches maximum when the light intensity is close to the interference extrema. For each color channel, the minimum measurable thickness is reached when the light intensity is enough to be distinguished from the background, *i.e.*  $I - I_{\min} = 1$ . The minimum measurable thickness (reached in blue channel) and the averaged intrinsic error (reached in red channel) are listed in Table IV, for several bit depths for typical cameras bit depths. Even with a low camera bit depth (8-bit), IDIOM method could in principle measure thicknesses well below 10 nm with good accuracy.

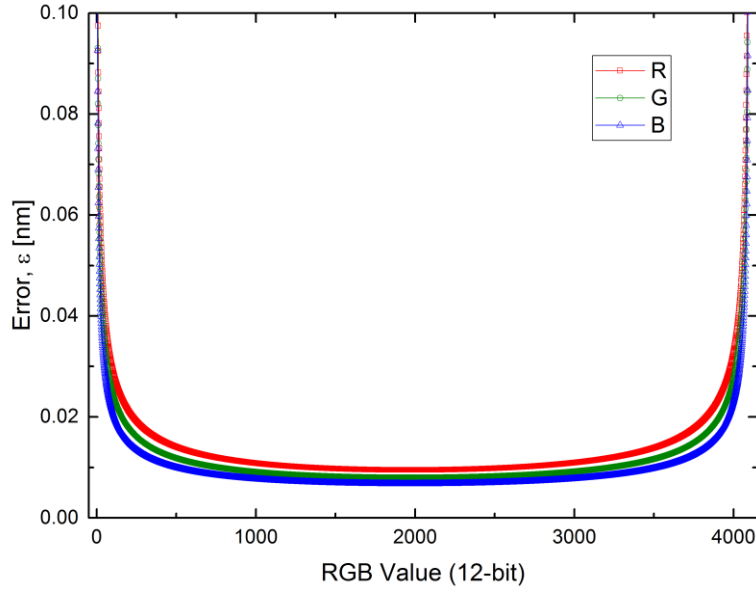


**Figure 2.12** The intrinsic error in thickness measurement,  $\varepsilon$  vs. RGB intensity for the high speed camera Photron FASTCAM Mini UX100 (12-bit). This error is associated with rounding up light intensity to integer values as RGB output.

**Table IV** Ideal minimum measurable thickness and average intrinsic error in IDIOM method

Bit depth	Intensity levels	Minimum measurable thickness [nm]	Average intrinsic error [nm]
8	0 - 255	3.39	0.192
12	0 - 4095	0.84	0.0125
14	0 - 16383	0.42	0.0031
16	0 - 65535	0.21	0.0008

However, the discussion so far is aimed to find the theoretical limits of the IDIOM method in ideal scenario. In the real experiments, outside stray light, imperfect lenses and the noises inherent to the CCD or CMOS camera sensors can all contribute to errors in determining intensity  $I$ . In the case of the high speed camera, fluctuations in the recorded RGB intensity are noticeable, due to the high sensitive level of the CMOS sensor (ISO is fixed at 5,000). In Figure 2.13, a histogram is constructed from a recording of the dark field background. Individual pixel intensities in the green channel are counted in a  $40 \times 40$  sampling region for 50 frames (1 second). A clear Gaussian distribution around the mean is obtained with a standard deviation of 26.5. This translates to an average error of  $\pm 0.3$  nm in thickness measurement, which is introduced by camera sensor noise.

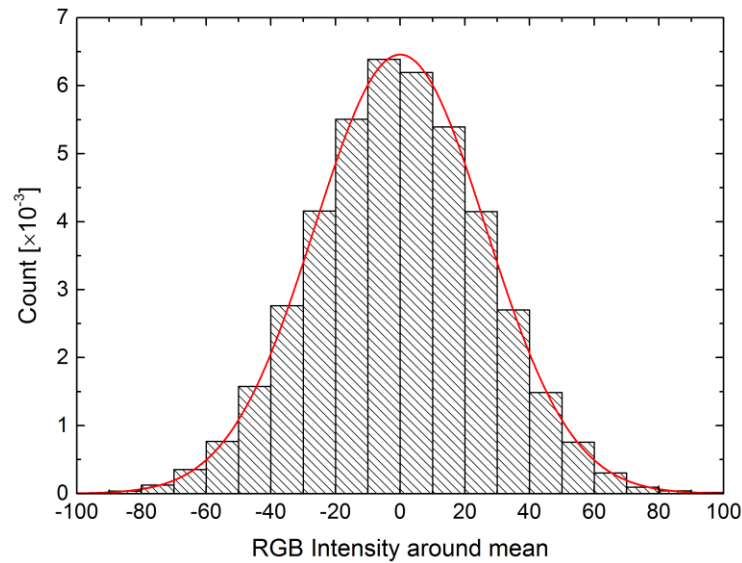


**Figure 2.13** Histogram of background intensity recorded in individual pixels of the 12-bit high speed camera. Intensity values are sampled from only the green channel, in a  $40 \times 40$  sampling region at the center of the images, and for 50 consecutive frames (1 second).

Other possible error could originate from the digital filtration, since one single averaged wavelength value is used for each color channel, while the actual filtered light has a spectrum of wavelengths around the averaged value. However, the thickness is linearly proportional to the wavelength ( $h \propto \lambda$ , see Equation (2.2)), so an uncertainty in wavelength of  $\pm 10$  nm would only result in a  $\sim 2\%$  relative uncertainty (for  $\lambda = 500$  nm) in thickness. Errors can also be introduced when determining the interference extrema  $I_{\max}$  and  $I_{\min}$ . They are therefore measured with care, and multiple measurements are taken to obtain the average values.

On the other hand, light intensity acquired in individual pixels can be averaged both spatially and temporally to reduce the noise. Overall, nanometer thickness resolution is readily achieved by the IDIOM protocols. Together with  $\sim 0.5$   $\mu\text{m}/\text{pixel}$  in-plane spatial and millisecond time resolution, it makes IDIOM the ideal method to study dynamics and pattern formation in freely standing thin films.

### **2.4.3 Nanoscopic structures resolved by IDIOM**

The capabilities of IDIOM in resolving detailed dynamics in stratifying foam film is demonstrated by characterizing the shapes of two nanoscopic structures formed during growth of the thinner domain. In Figure 2.14a, a ridge (or rim) formed at the periphery of a growing domain in stratifying foam films is detected. The thickness of the ridge, shown in the cross-section profile, is only  $\sim 5$  nm larger than the outside film thickness. Such small difference makes the ridge indistinguishable in the micrograph image, and its detection absent in the literature so far. The detailed shape, thickness profile and evolution of the ridge are characterized experimentally for the first time.



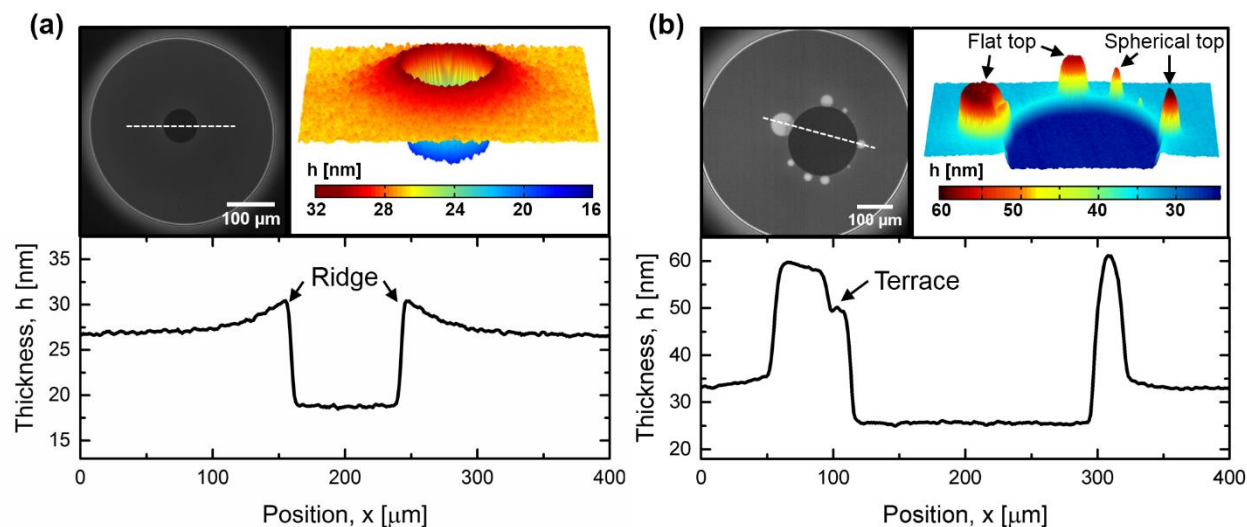


**Figure 2.14** Shape of nanoscopic structures formed during domain growth. (a) Thicker ridge around the growing domain, forming a crater-like shape. (b) Shapes of white spots. They are possible to have both flat and spherical top, and even have layered terraces within. Reprinted from ref [31] with permission. Copyright © 2016 American Chemical Society.

The shapes of white spots formed during domain growth are illustrated in Figure 2.14b. The particular image is taken from stratification in film made from 80 mM SDS, and shows the diversity of white spots, in size, thickness, and shape. Two distinct shapes are easily recognized: one with flat top, resembles the shape a mesa, and the other with a spherical top, resembles the shape of a lens or drop. Moreover, terraced nanostructures are observed with thickness stratification within individual mesas, often as results of coalescence of two spots, or the expansion of the adjacent thinner domain. All these structures are relatively low aspect ratio (thickness in nm, radius in microns), and their shape and shape evolution can be better comprehended by understanding the underlying interplay of contributions from oscillatory thickness-dependent disjoining pressure and curvature-dependent Laplace pressure. We gain much more insights in the

dynamics and lifetime of stratifying foam films, by utilizing the IDIOM protocols to characterize the formation of these nanoscopic structures and patterns. These progresses are mainly presented in the following chapters.

## 2.5 Conclusions

In this chapter, the foam film thickness measurement protocol combining interferometry, digital imaging and optical microscopy (IDIOM) is introduced. It offers visualization and characterization of nanoscopic thickness variation and topological transitions in freely standing thin films, with unprecedented spatial and temporal (1 ms) resolution. We utilize this novel method to shed new light on the drainage and stratification dynamics in micellar foam films made from aqueous SDS solutions. Several characteristic features of stratification are analyzed, including discrete changes in thickness, coexistence of regions with different nanoscopic thickness, growth of thinner (darker) domains, and topological transitions that create nonflat structures like ridges and mesas. The noninvasive imaging and characterization of ridges, mesas, and terraces in freely standing thin films will revolutionize the study of nanoscale rheology and of surface and intermolecular forces, especially the understanding of non-DLVO, supramolecular oscillatory surface forces that underlie stratification. Several new insights gained via IDIOM are the focus of the following chapters.

Owing to its simplicity and wide applicability, the IDIOM protocols can be easily extended for many other systems. Efforts in applying IDIOM to smectic liquid crystalline, polyelectrolyte, and lipid bilayer systems are currently underway. We hope that the widespread use of IDIOM

protocols will lead to a better understanding of interactions, flows, and self-assembly in biology, in chemical physics, and in foams and other colloidal systems.

## CHAPTER 3.

### DOMAIN EXPANSION DYNAMICS IN STRATIFYING FOAM FILMS

#### 3.1 Introduction

The dynamics of foam film stratification are rich and complex. The step-wise thinning of foam films containing SDS micelles involves spontaneous creation and evolution of nanoscopic structures like craters, ridges, mesas, and terraces, as observed by the IDIOM protocols presented in the previous chapter [31]. The dynamics of growth, instability, and coalescence of these structures are influenced by a variety of factors, including surface forces (supramolecular structural in origin), surface curvature (both local of the nanoscopic structures and the curvature of the Plateau border surrounding the foam film), bulk and interfacial rheology and surfactant adsorption and micellization.

In order to decipher the complex stratification dynamics, we first focus on a simpler case of nucleation and growth of thinner domain, which spontaneously form and expand at the expense of the surrounding thicker film. The thickness of the entire film is reduced to the next metastable thickness in this fashion. To the best of our knowledge, the published studies [73,74,77,79,80] have focused exclusively on the expansion of an isolated domain, where the outside thicker film is assumed infinite in size (see Section 1.2 for a comprehensive review). However, during any domain growth process, the domain eventually comes into contact with the surrounding Plateau border, and there is a sheer lack of discussion on the effect of Plateau border on the domain expansion dynamics. The present study aims to fill this gap of experimental understanding, and develop self-consistent theoretical framework to describe the growth dynamics for both isolated domain and domain in contact with Plateau border.

## 3.2 Methods

### 3.2.1 Experimental setup

The materials and methods used in this study are mainly presented in Section 2.2. The foam film are formed with SDS solution with concentrations above CMC (8-10 mM), and without any additional electrolyte.

Unless otherwise specified, the results in this chapter are obtained in the Schedluko-type cell thin film apparatus (see Figure 2.2). Since the kinetics of stratification is suggested to be influenced by the size of the film [74,75,80], the film formation is controlled to maintain similar initial film size ( $d_f \approx 0.6$  mm) in all experiments. For small film thicknesses, where capillary pressure applied (calculated by Equation (2.1)) is not sufficient to drive further thinning, the cell container is opened briefly to allow evaporation, which results in an increase in the capillary pressure and consequently induces a thickness step transition [97,99]. The cell is quickly closed once the thinner domain is formed.

IDIOM protocol is used for visualizing the domain growth process, and characterizing the film thicknesses. In particular, the image system used in this chapter consists of the Nikon D5200 DSLR, and the light source of Schott ACE 1 halogen light. As discussed in Section 2.4.1, the movie recorded from this consumer-grade camera can be used for thickness measurement after careful calibration. The maximum intensity recorded is kept low so that the RGB values lies in the linear regime in Figure 2.11, therefore avoiding further numerical non-linear conversion. Due to the low color temperature ( $\sim 3200$ K, appears yellow) of the halogen light source used, the incident light intensity in the blue spectrum is relatively low. This leads to much lower light intensity recorded in the camera blue channel than the red and green channel, rendering the thickness

measurement in the blue channel unreliable. We therefore only report thickness measured in red and green channels, or the mean value between the two.

### 3.2.2 Domain tracking

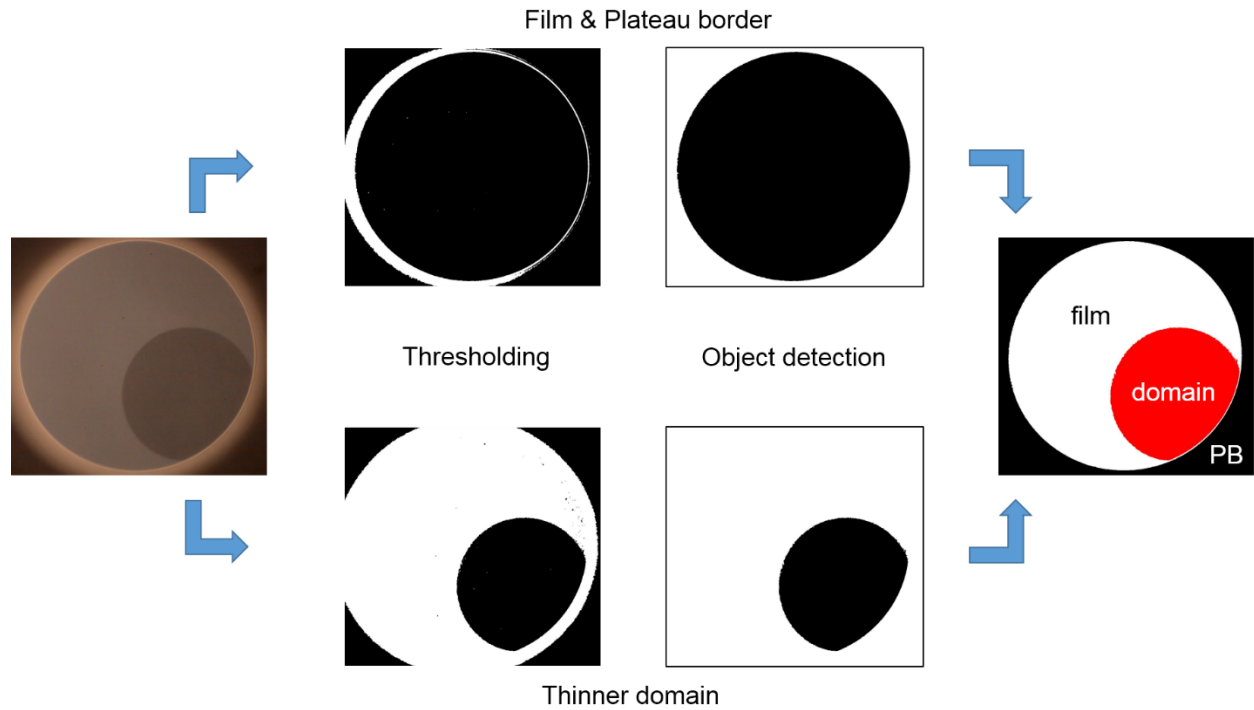


**Figure 3.1** Domain tracking scheme to separate regions of domain, film and Plateau borders.

The growth of a thinner domain is followed through a specially written object tracking routine in MATLAB R2014a. Due to the interest in studying the dynamics after the domain has come in contact with the Plateau border, we implement a double thresholding scheme to detect both the Plateau border and the thinner domain. This procedure is illustrated in Figure 3.1. Global

intensity thresholding is used for distinguishing different regions, instead of a local gradient-based edge detection method, because within each region the brightness is relatively consistent, and the boundaries in between are sharp and clear. During the growth of a thinner domain, ridges and mesas with larger thickness are likely formed around the domain. A local edge detection method would suffer from these nanoscopic structure interfering with the local intensity at the domain-film boundary.

The image analysis procedure starts by isolating the brighter “halo” around the whole thin film region (from reflection of the Plateau border), with a higher intensity threshold. The region inside the bright loop is then selected manually as the region of the thin film. This region is defined in a single movie frame, and assumed to remain unchanged throughout the domain growth process. A lower intensity threshold is then applied to distinguish between darker domain and brighter outside film. The thinner domain region is again selected manually for one movie frame, but then automatically tracked for all other frames. Since the domain center does not move fast, the tracking is easily achieved by selecting the region whose center is the closest to the center position in the preceding frame. The final result of this routine is the distinction of domain, film and Plateau border region, for every frame recorded in the movie.

When the domain is in contact with the Plateau border, it become non-circular in shape, and its boundary is comprised of a film/domain contact line and part of the film boundary to the Plateau border. Using the two-step procedure, the two parts of the domain boundary are separately detected and tracked. Since the Plateau border does not change over the period of domain growth, it is beneficial to isolate the film/domain contact line part and track its evolution.

### 3.3 Results

#### 3.3.1 Stratification observed with customer-grade camera

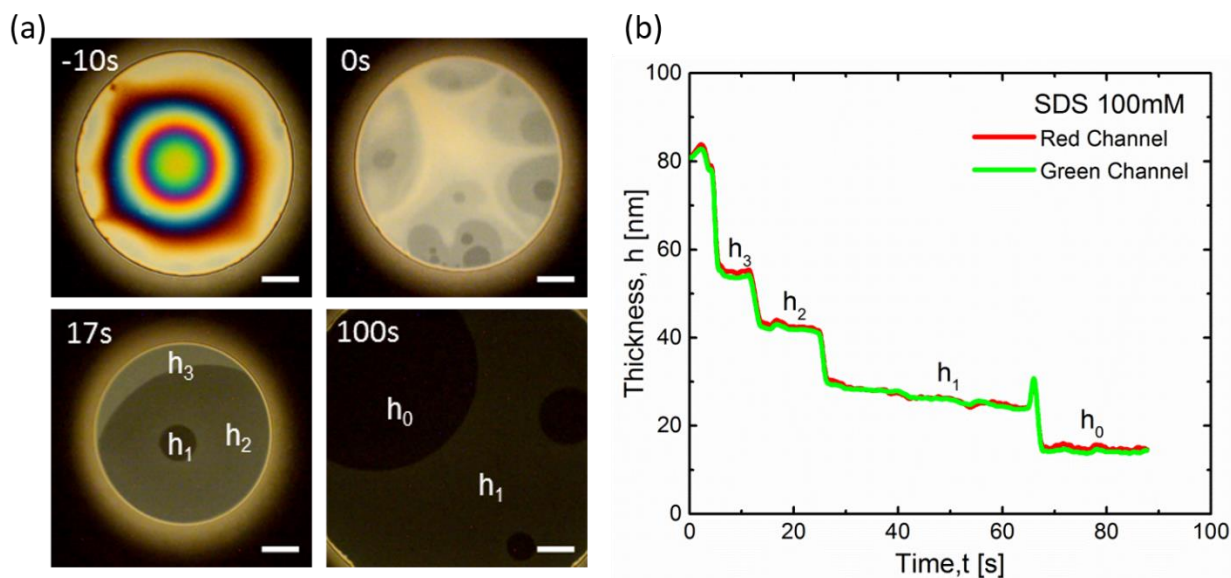


**Figure 3.2** Stratification of thin film with 100 mM SDS solution, captured with the Nikon D5200 camera. (a) Micrographs during the step wise thinning. The scale bars in the snapshots correspond to 100  $\mu\text{m}$ . (b) Thickness measurement at the center of the film. Adapted from ref [81] with permission of The Royal Society of Chemistry.

Stratification in a foam film made from 100 mM SDS solution ( $c/\text{CMC} \approx 12$ ) is formed in the Schedluko-type film cell, and visualized and characterized using the IDIOM protocols. As shown in Figure 3.2a, the features of the step wise thinning are similar to those shown in Figure 2.5 and Figure 2.9, despite the different thin film apparatus and image system used. The colorful ring interference patterns form initially, but quickly drain out of the film as the thickness reaches below  $\sim 100$  nm. Distinct regions with different shade of grey then appear and co-exist in the film. Thinner, darker, circular domains form and grow, until a meta-stable film thickness is reached (as



illustrated in Figure 2.8). The applied pressure is then raised by either increasing the film size (according to Equation (2.1), and shown in the snapshot at  $t = 100$  s), or by opening the thin film apparatus to allow evaporation.

The evolution of film thickness is determined using movies recorded with the consumer-grade camera. The separate measurements in the red and green channel shows good agreement in Figure 3.2b. The thickness steps corresponding to different shades in the micrograph are marked accordingly, with subscription number indicating the number of micelle layers contained in a given step. The step size is found to be nearly constant with  $\Delta h = 10.5 \pm 0.5$  nm, and the final black film thickness of  $h_0 = 14.6 \pm 0.6$  nm. Both of the values are comparable to those obtained using other cameras listed in Table III, as well as the literature values obtained by conventional interferometry [55,99].

### 3.3.2 Domain expansion kinetics: influence of the Plateau border

The step-thinning of the film proceeds as thinner, darker domains form and expand in expense of the thicker film. In some instances, a single domain emerges and grows, free from the influence of other domains, until it coalesces with the Plateau border and occupies the whole plane parallel film. We specifically select such single domain growth events from our stratification experiments, and a representative example is shown in Figure 3.3, for a thickness jump from  $h_2 = 40.3$  nm to  $h_1 = 26.2$  nm in a foam film made of 100 mM SDS solution.

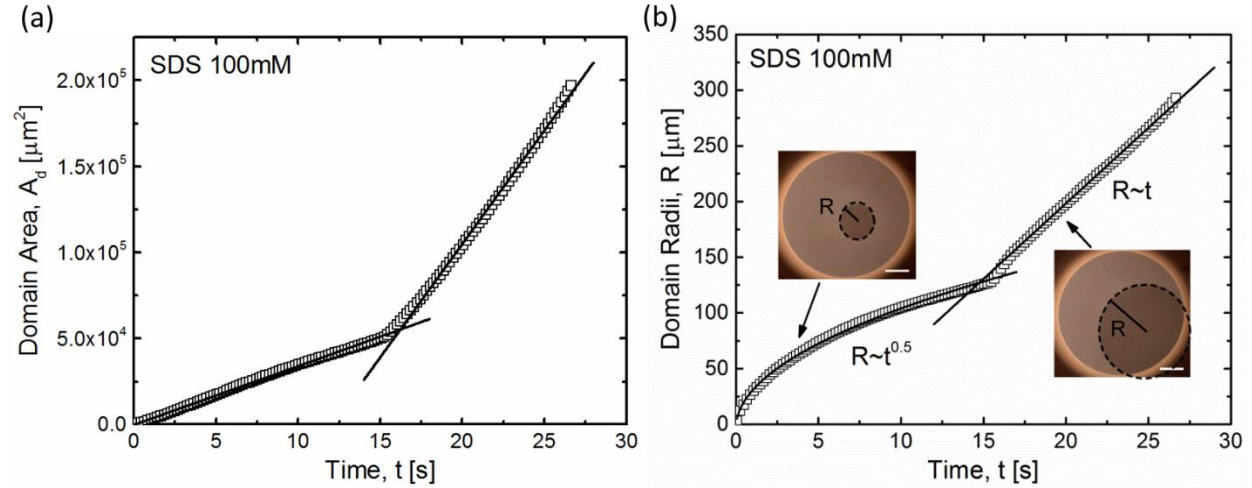


**Figure 3.3** Domain expansion kinetics in a 100 mM SDS foam film. (a) Domain area vs. time, an apparent growth rate increase takes place when domain comes in contact with the Plateau border. (b) Domain radii vs. time, the contact with the Plateau border changes the scaling from  $R \propto t^{0.5}$  to  $R \propto t$ . The scale bars in the snapshots correspond to 100  $\mu\text{m}$ . Reprinted from ref [81] with permission of The Royal Society of Chemistry.

We find that the domain expansion involves at least two distinct regimes: initially the domain expands in isolation (Regime A); then it comes in contact with the Plateau border around the film periphery, and expands with part of the domain deformed by the Plateau border (Regime B). It is found that the area of the growing domain,  $A_d$ , increases linearly with time in Regime A. This scaling ( $A_d \propto t$ ) has been reported and analyzed preciously in the literature, for stratification in various systems including micelles [73,78], colloidal particles [75] and polyelectrolytes [76]. However, after the Plateau border is involved, the areal growth rate of the domain (slope in Figure 3.3a) appears to increase. The apparent linear dependence of  $A_d \propto t$  remains unchanged, though the areal growth rate changes. However, as Regime B is reported here for the first time, none of the existing theoretical frameworks explicitly account for such a sharp growth rate increase in domain expansion [73,77,79,80]. Since the linear dependence,  $A_d \propto t$ , has been thought to be akin

to a diffusion-like process [73,77], the acceleration in Regime B, with no change in the scaling law, would suggest a faster diffusion with little change in the governing dynamics. The mechanism to allow such transition is not at all obvious. The experimental observation, and the advanced theoretical framework to explain the kinetics, require further scrutiny.

Driven to investigate the apparent acceleration of domain expansion rate upon domain contact with the Plateau border, we recognized that in Regime B, the domain is no longer circular but rather deformed by the Plateau border. As a result, the domain expansion only takes place at the contact line between the thinner domain and the thicker surrounding film. Instead of area, we plot the radii of the domain vs. time, and a clear scaling transition from  $R \propto t^{0.5}$  to  $R \propto t$  is observed (Figure 3.3b). Here the domain radii in Regime B is determined only by the portion of the domain boundary that are in contact with the thicker film (as illustrated in the snapshots in Figure 3.3b). The distinction in kinetic scaling laws between the two regimes suggests difference in underlying dynamics, and can be distinguished by two appropriate growth rates: an apparent constant diffusivity  $D = dR^2/dt = \frac{dA_d}{\pi dt}$  for Regime A, and an apparent constant contact line expansion velocity  $V = dR/dt$  for Regime B.

The difference in domain expansion dynamics is highlighted by the comparison of the domain/film contact line shift over time. In Figure 3.4, the line traces obtained by the domain tracking scheme show the position of the contact line over time. The time intervals between neighboring traces are kept constant, with red arrows indicating the contact line velocity at each time points. It is clear that in Regime A the contact line displacement becomes shorter in each successive time interval, and the expansion velocity decreases as the domain grows in size. In contrast, in Regime B the contact line moves the same amount within each time interval, resulting

in a linear growth in domain radii. It is worth noting that we choose to follow the change in radii of the domain/film contact line, as a measure of the average expansion rate. Alternatively, the growth in Regime B can also be characterized by following the movement of an individual point (e.g. the center point) in the contact line, which shows similar linear dependence on time.

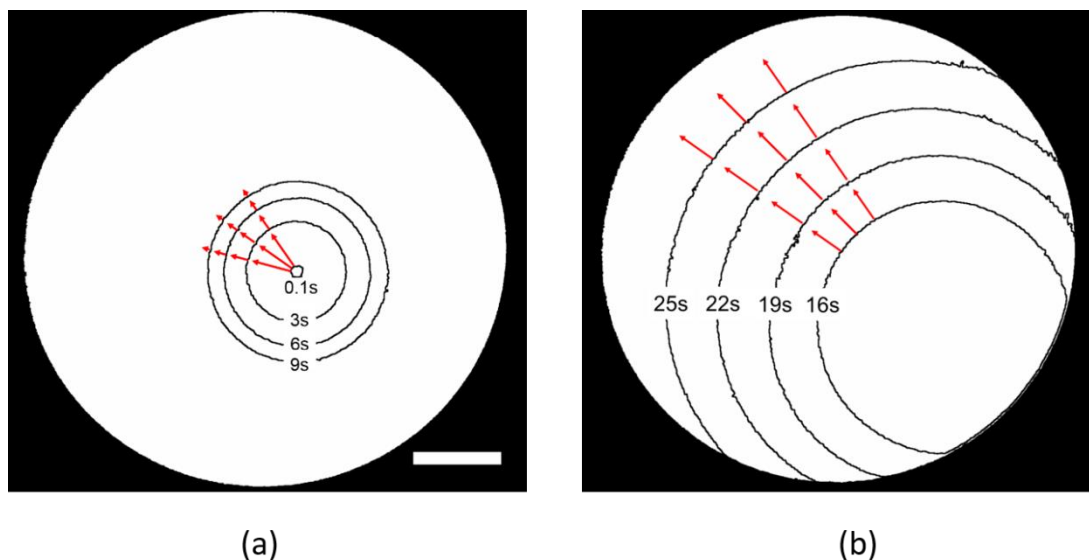


**Figure 3.4** The time evolution of domain boundary in the two distinct regimes. The time interval between neighboring line traces is constant  $\Delta t = 3$  s. (a) Regime A shows the expansion slows down over time and (b) Regime B shows constant expansion velocity. Adapted from ref [81] with permission of The Royal Society of Chemistry.

### 3.3.3 Domain expansion kinetics: white spot formation

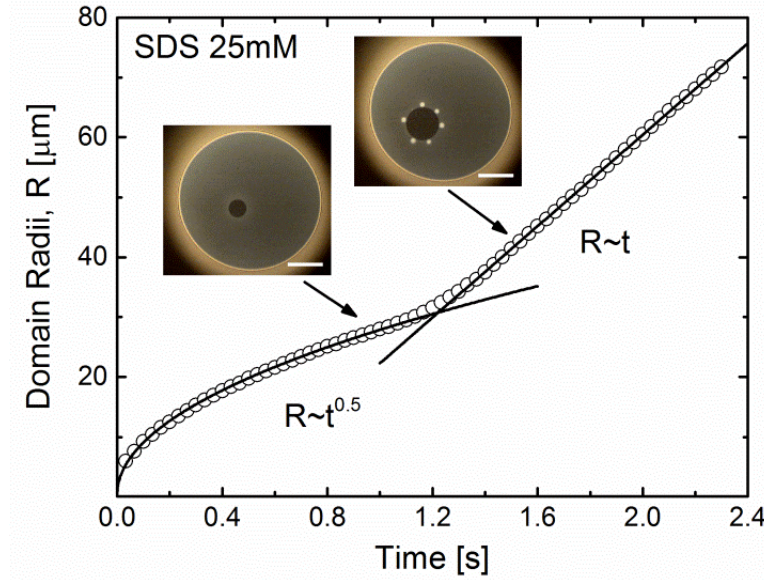


**Figure 3.5** Domain expansion kinetics in a 25 mM SDS foam film. The radius vs. time shows a scaling transition when white spots appear around the growing domain. The scale bars in the snapshots correspond to 100 μm. Adapted from ref [81] with permission of The Royal Society of Chemistry.

In Figure 3.5, the domain radius is followed over time in foam films made with 25 mM SDS solution, as the thickness steps from  $h_1 = 43.5$  nm to  $h_0 = 25.8$  nm. The scaling transition from  $R \propto t^{0.5}$  to  $R \propto t$  observed here is markedly similar to the time dependent domain growth observed in 100 mM solution. Interestingly, the scaling transition in this case occurs even though we are tracking growth of an isolated domain itself. Here the transition is triggered by an instability developed around the domain/film contact line, which leads to formation of white spots around it. These white spots are nanoscopic mesas or lenses that are thicker regions than the rest of the film (as shown in Figure 2.14b). The appearance of white spots coincides with the change in the domain

growth scaling, indicating that the topological instability that leads to the formation of white spots also triggers the change in domain growth dynamics.

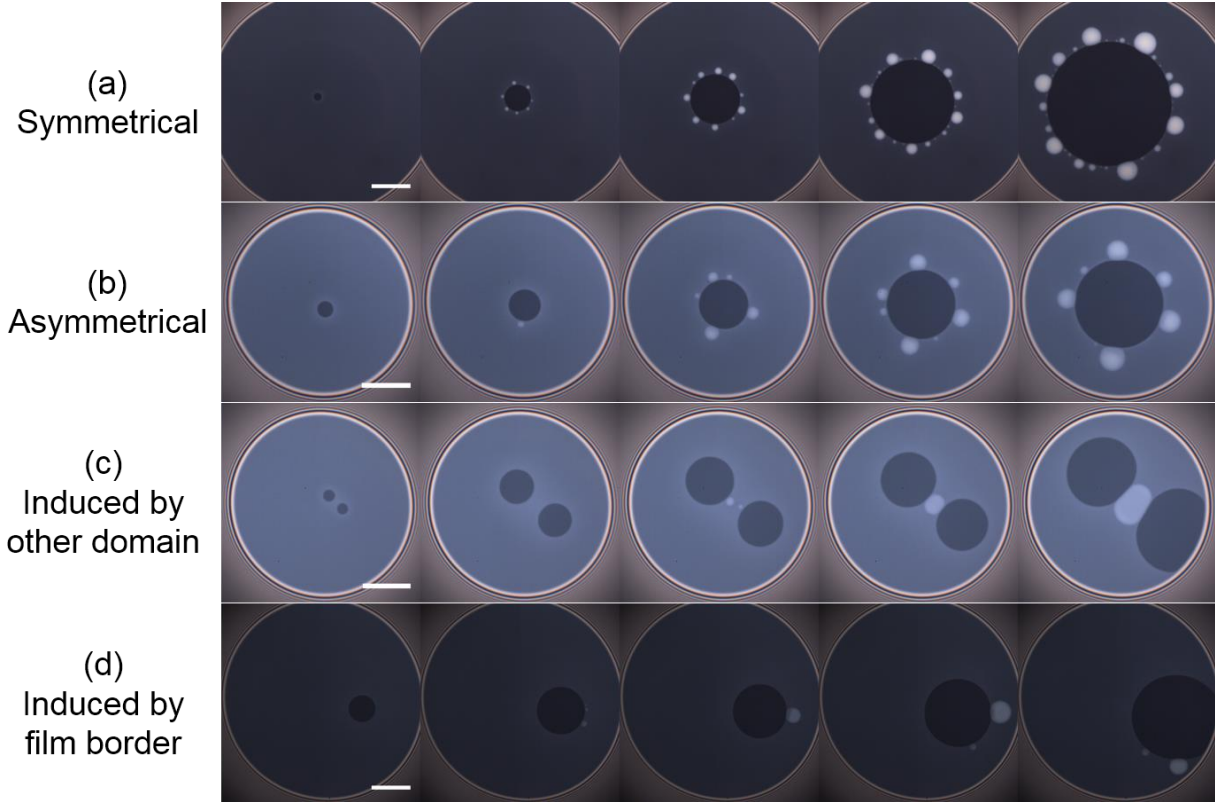


**Figure 3.6** Different types of white spot formation. (a) Symmetrical spots with almost periodic spot size, montage from  $h_1$  to  $h_0$  transition in 50 mM SDS. (b) Asymmetrical spots with aperiodic spot size, from  $h_2$  to  $h_1$  transition in 60 mM SDS. (c) Induced by presence of other domains, from  $h_3$  to  $h_2$  transition in 100 mM SDS. (c) Induced by proximity to the Plateau border, from  $h_2$  to  $h_1$  transition in 100 mM SDS. Scale bars correspond to 100  $\mu\text{m}$ .

The domain growth snapshot included in Figure 3.5 shows nearly uniformly sized white spots almost periodically distributed around the domain boundary. It is worth noting that this symmetrical arrangement of white spots is not universal. An extended range of experiments, with different film thickness and surfactant concentration, shows that the white spots formation and

growth can be asymmetrical, and the size of such spots can vary considerably, as shown in Figure 3.6. In some instances, the white spots form only when the growing domain comes in proximity to another domains or the Plateau border.

Bergeron et al. [79] and Beltrán and Langevin [76] proposed that the formation of white spots is due to a topological instability within a ridge, which was postulated to form around the growing thinner domain. The ridge formation and instability has not been characterized experimentally (we use IDIOM protocol to characterize it for the first time, see Chapter 4), nevertheless the instability is thought to be akin to Rayleigh instability of a liquid column, which breaks into the spots (drops). However, the periodicity and symmetry of spots predicted by Rayleigh-like instability is inconsistent with the formation of white spots shown in Figure 3.6. Moreover, recent studies on Rayleigh-type breakup of static toroidal rings into drops show very different evolutions and morphologies [88,89]. Arguably the differences arise as the formation of white spots in stratifying foam films involves the structural disjoining pressure, which is absent in the micron to millimeter sized toroidal rings. In addition, the topological instability and white spots formation occurs near an expanding contact line, instead of a static one in toroidal drops. The ridge itself also does not share the same circular cross-section as a toroid (*cf.* Figure 2.14a). More experimental and theoretical efforts are required to fully understand the topological instability in the nanoscopic ridge, and the formation of white spot thereafter.

### 3.3.4 Similarities between two kinetic transition

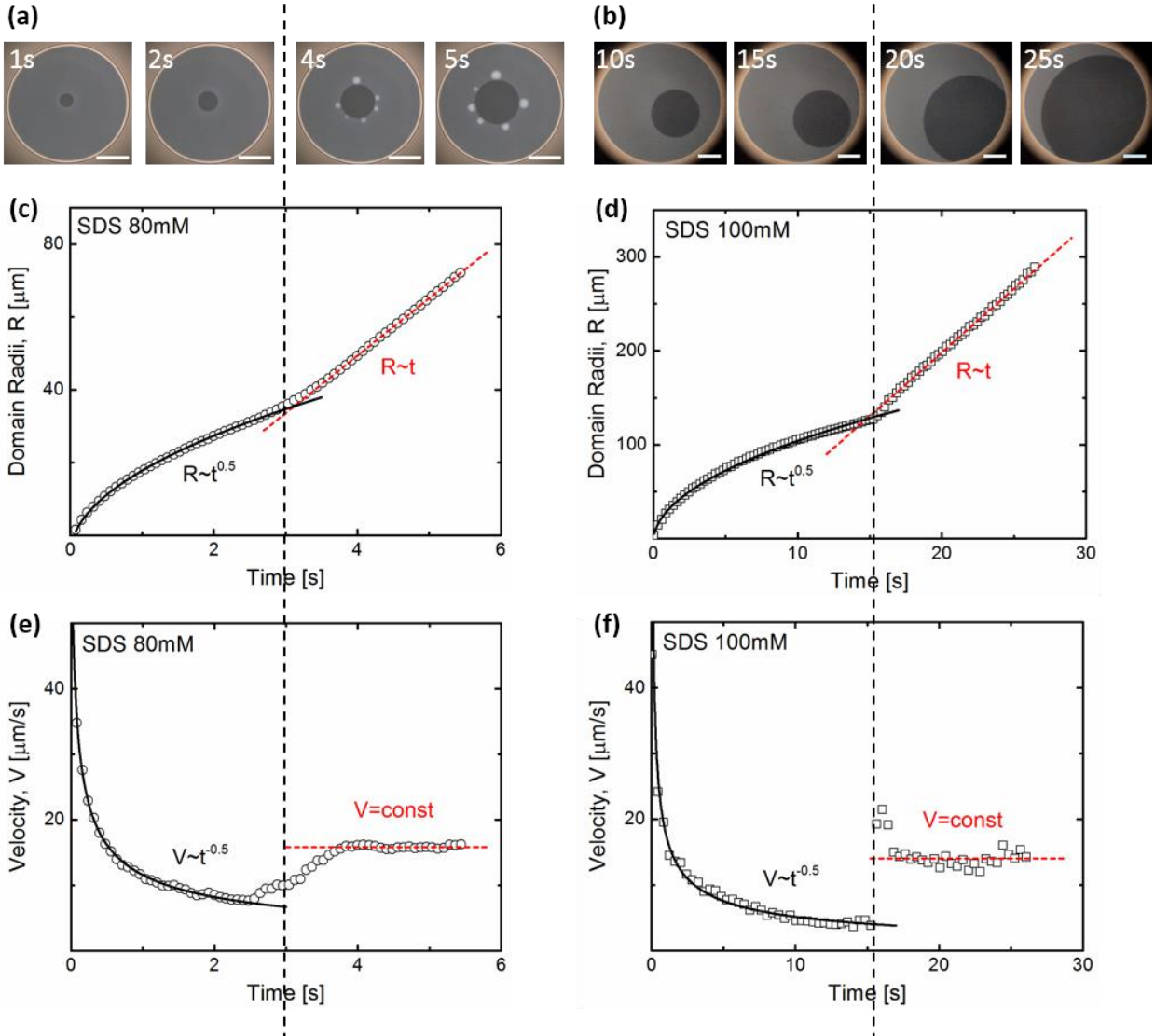


**Figure 3.7** Similarities between domain growth with white-spots formed and in contact with the Plateau border. Snapshots of domain expansion are captured for (a) with white spots formation, from  $h_2$  to  $h_1$  transition in 80 mM SDS solution, and (b) with domain in contact with the Plateau border, from  $h_2$  to  $h_1$  transition in 100 mM SDS solution. Scales bars correspond to  $100\mu\text{m}$ . (c) and (d) are plots of domain radii vs. time. (e) and (f) are plots of contact line velocity vs. time.

Comparing the domain growth kinetics shown in Figure 3.3 and Figure 3.5, it is clear that despite of the different geometric constraints, the film Plateau border and the white spots display



similar effects on the dynamics of domain growth. The similarities between the two kinetics transitions are summarized in Figure 3.7. In both cases, the domains initially grow with a constant diffusivity (Regime A), this results in domain radii scaling with time as  $R \propto t^{0.5}$ , and a contact line expansion velocity that decreases over time as  $V = dR/dt \propto t^{-0.5}$ . After the topological instability that leads to the white spot formation, or after domain contact with the Plateau border, the domain growth transitions to a constant velocity mode (Regime B), where the radii increases linearly with time,  $R \propto t$ , and the expansion velocity rapidly increases to a higher, constant value. The scaling change induced by topological instability has been only reported once in the literature for polymer-free micellar solutions [78], while the similar scaling change induced by coalescence of domain with the Plateau border is being reported here for the first time. While the topological instability is suppressed when the film is with higher concentration or more layers of micelle (higher thickness), the existence of the surrounding Plateau border is inevitable in foam films.

The similar effects of topological instability and the contact with the Plateau border are further demonstrated, by analyzing the expansion dynamics when both phenomena are involved sequentially. In Figure 3.8a, the growing domain goes through topological instability leading to the formation white spots, before the domain comes in contact with the Plateau border. On the other hand, Figure 3.8b shows the case when the white spot is formed after the domain is deformed by the Plateau border. In both cases, domain radii keeps growing linearly with time after the second event occurs, and the slopes, *i.e.* expansion velocity, remain unchanged. Furthermore, the domain expansion velocities are found to be similar, both after white spots formation after contact to the Plateau border (Table V), implying that similar physics underlies the change of domain expansion kinetics in the two cases.

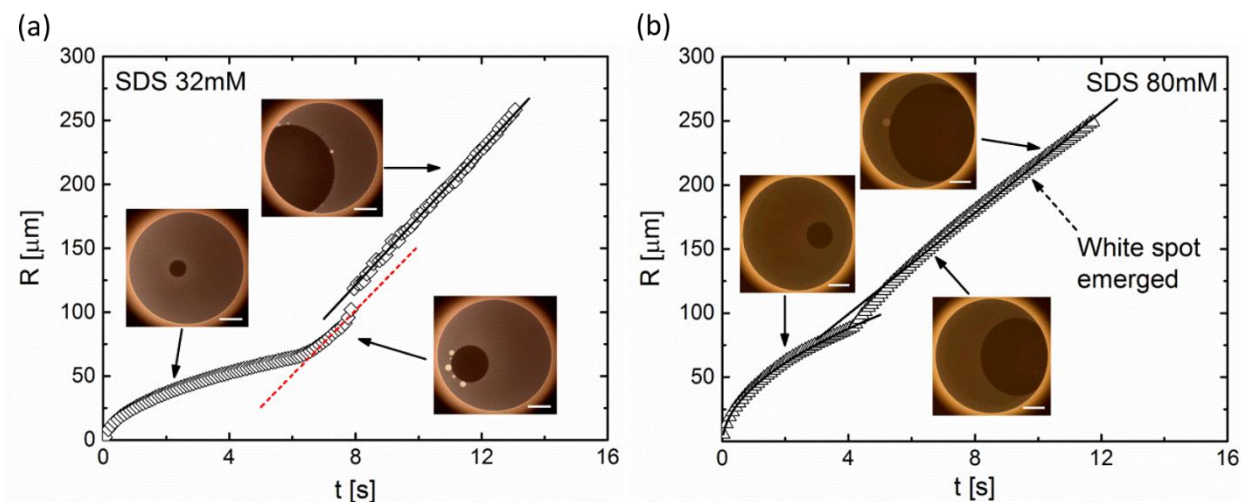


**Figure 3.8** Domain growth dynamics when both topological instability and contacting the Plateau border occur successively. The plots show domain radii vs. time for (a) 32mM SDS,  $h_1$  to  $h_0$ , and (b) 80mM SDS,  $h_1$  to  $h_0$ . The scale bars in snapshots correspond to 100  $\mu\text{m}$ . Adapted from ref [81] with permission of The Royal Society of Chemistry.

**Table V** Comparison of contact line velocity with white spots and with contact to the Plateau border. Adapted from ref [81] with permission of The Royal Society of Chemistry.

Concentration (mM)	$h_1$ (nm)	$h_0$ (nm)	$V_{w/spots}$ ( $\mu\text{m/s}$ )	$V_{periphery}$ ( $\mu\text{m/s}$ )
25	$41.3 \pm 1.3$	$25.2 \pm 0.4$	$31.6 \pm 1.2$	$31.7 \pm 3.2$
32	$36.5 \pm 2.1$	$21.9 \pm 1.4$	$25.2 \pm 3.0$	$28.3 \pm 0.9$

### 3.3.5 Concentration dependence

The constant diffusivities,  $D$ , in Regime A, and the constant velocity,  $V$ , in Regime B are determined from domain expansion kinetics data for a range of surfactant concentrations and three

different thickness steps. The results summarized in Figure 3.9 are all measured with stratification experiments conducted in the porous plate cell (see Figure 2.3) to ensure good control over film formation with a large range of the applied capillary pressure, since pressure variation may affect the obtained growth rates. It is found that both  $D$  and  $V$  measured in the Schedluko-type cell setup are not very consistent, especially when evaporation is introduced to induce the thickness transition. Evaporation can potentially result in an inconsistency in applied pressure and alteration of the solution concentration. The domain growth rates ( $D$  and  $V$ ) are reported in six surfactant concentrations, for the last three thickness steps, as long as the film is stable enough to permit well-controlled single domain growth.

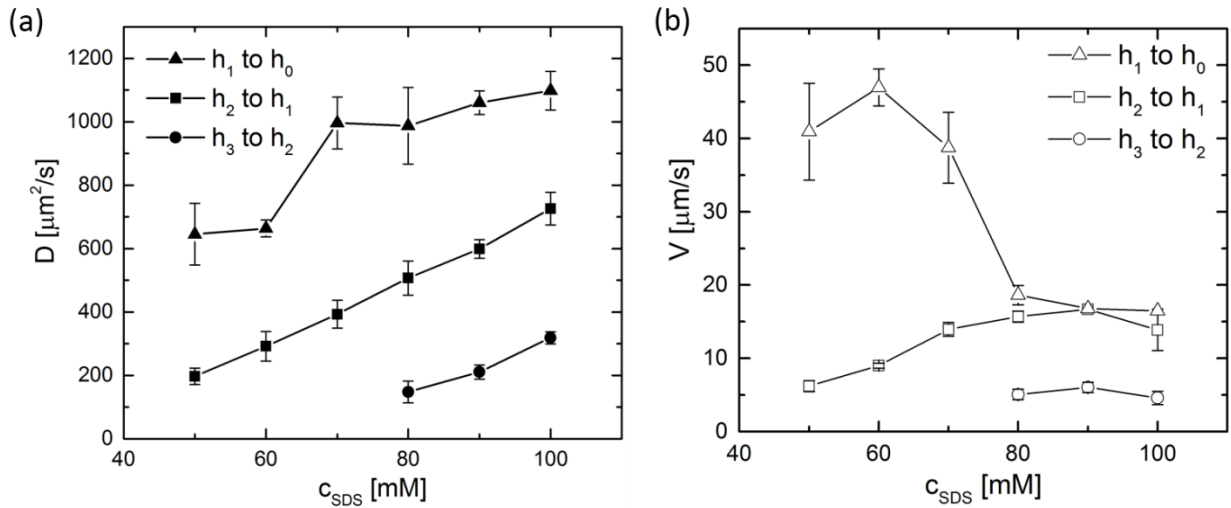


**Figure 3.9** Concentration dependence of (a) apparent diffusivity  $D$  in Regime A and (b) apparent contact line velocity in Regime B. The results are collected for last three thickness steps (if available) in six surfactant concentrations.

Overall, the concentration dependences is very different between Regime A and B. In Regime A, a monotonic increase in diffusivity is observed as surfactant concentration increases. Comparing data from the same concentration, a monotonic increase in diffusivity can also be found as film thickness (or number of micelle layers contained) decreases. On the other hand, in Regime B the concentration dependence of expansion velocity is not monotonic. In general it shows an increase in velocity at lower concentrations, reaches a peak (50 mM for  $h_1$  to  $h_0$ , 90 mM for other two thicker steps), and then starts decreasing. Through experimental observation, the decrease in expansion velocity at higher surfactant concentrations is likely to be associated with the suppression of topological instabilities, which becomes more pronounced as concentration increases.

The two regimes of domain expansion are different in both kinetic scaling and concentration dependence of growth rates. The overall time one thickness transition takes is therefore not trivial to predict. Detailed knowledge on the thermodynamics and hydrodynamics of stratifying foam films is needed to better understand the stability and drainage dynamics of the film.

### **3.4 Discussion**

We showed three distinct experimental observations on the dynamics of domain expansion, and a self-consistent theoretical framework capable of describing all three observations (listed below) is needed.

- (i) Two distinct growth kinetics: constant diffusivity regime (Regime A) where domain radii  $R \propto t^{0.5}$ , and constant contact line velocity regime (Regime B) where  $R \propto t$ .
- (ii) Transition in kinetics from Regime A to B occurs after an isolated growing domain encounters the Plateau border. A similar kinetic transition occurs when a topological instability that leads to white spot formation around the growing domain.
- (iii) The growth rates of domains in the two regimes, *i.e.* apparent diffusivities in Regime A and apparent velocities in Regime B, show different concentration dependence.

There are two models proposed in the literature to explain the domain growth kinetics in Regime A. Kralchevsky et al. [73], and later Lee et al. [80] proposed a diffusive-osmotic (DO) mechanism, theorizing that the expansion of the domain is akin to a phase transition. The thinner domain formation and growth is related to “vacancies”, which are sites with one less micelle layer than the film. The vacancies are generated from the surrounding Plateau border due to the gradient in chemical potential (or osmotic pressure) between it and the film region. Once the concentration of vacancy within the film reaches a critical level, the condensation of vacancies leads to domain nucleation. A constant flux of vacancies from the Plateau border is assumed, which results in the constant areal growth rate (see Equation (1.1)). However, the DO mechanism does not predict the scaling transition to Regime B. The dynamics of topological instability leading to white spot formation, and the effects of coalescence with the Plateau border are not captured.

Both Bergeron et al. [79] and Heinig et al. [77] argued that the outward flux of fluid from domain growth supplies an excess volume of liquid that accumulates around the domain, forming

a ridge near the contact line between thinner domain and thicker surrounding film. Drawing analogies to earlier works on hydrodynamics in spreading and dewetting by Joanny, de Gennes and coworkers [82,131,220], Heinig et al. [77] attributed the  $R \propto t^{0.5}$  scaling in Regime A to the disjoining pressure gradient across the ridge, driving the outwards expansion of the ridge. Indirectly, Langevin and coworkers [77,85] examined the domain growth rates predicted by the ridge-forming hydrodynamic model, and compared them with experimental measurements in stratifying films made of polyelectrolyte-surfactant mixtures. The authors recognized that the domain growth rates evaluated from their model do not match with the experimental values, unless the viscosity of the fluid confined in the thin film is assumed to be different from the bulk viscosity. However, the “effective viscosity” under confinement are very inconsistent, ranging from 60 time larger to 10 time smaller than the bulk values, depending on the polyelectrolyte and surfactant used. These discrepancies were attributed to the complex rheology of the solutions under thin film confinement. In the present study, we use simple surfactant micellar solutions that have Newtonian shear rheology, unlike the polyelectrolyte solutions. Furthermore, using IDIOM method, we offer the first experimental detection and characterization of the ridge (or rim) (*cf.* Figure 2.14a), thus have the capacity to closely examine the ridge model and its relation with the dynamics of domain growth. The detailed investigations are presented in Chapter 4 and 5.

For the  $R \propto t$  scaling in Regime B, two explanations were offered based on the ridge model, specifically for the case of topological instability. Beltrán and Langevin [76] argued that the ridge breaks down through the instability, and the linear time-dependence of the domain radius results from a balance between capillary driving forces and the viscous dissipation at the contact line. However, the estimated domain expansion velocities from this balance are nearly three orders of

magnitude smaller than experimental measured values, in foam films made with polyelectrolyte-surfactant mixture.

Searching for a reconciliation, Beltrán and Langevin [76] then argued that the white spots form through Rayleigh-like instability, and considered the driving force for domain growth being the gain in surface energy due to topology change from toroid-like (the ridge) to drop-like (the white spots). However, the analogy fails to explain the diversity of white spot formation and distribution, as demonstrated in Figure 3.6. Moreover, it does not explain the growth dynamics of domains in contact with the Plateau border.

In contrast to the previous studies, we postulate that the domain growth dynamics in both regimes can be described under the framework of thin film hydrodynamics and lubrication theory, where the basic equation for film thickness evolution reads:

$$\frac{\partial h}{\partial t} + \frac{1}{r} \frac{\partial}{\partial r} \left[ \frac{rh^3}{12\eta} \frac{\partial}{\partial r} (\sigma K + \Pi) \right] = 0 \quad (3.1)$$

Here the relevant pressure that drives the process is both the local Laplace pressure term (depends on surface tension,  $\sigma$ , and local curvature,  $K$ ) and the disjoining pressure contributions,  $\Pi$  [221]. The disjoining pressure in stratifying foam films displays a highly non-monotonic, oscillatory behavior, due to the supramolecular structural contribution. The balance between the thickness dependence disjoining pressure and local curvature induced Laplace pressure sculpts the shapes of domains, ridges and white spots. The manifestation of the balance of pressures and thin film hydrodynamics is presented in the following chapters, and the key ideas are summarized next.

The ridge formed in Regime A is small in thickness difference, compared to the outside film (as shown in Figure 2.14, and ridge shapes shown in the following chapters). So the surface curvature is small, and the Laplace pressure is dominated by disjoining pressure in part of the ridge. The thickness evolution equation then resembles a diffusion equation:

$$\frac{\partial h}{\partial t} = -D_{eff} \nabla^2 h, \text{ where } D_{eff} = -\frac{h_{\infty}^3}{12\eta} \frac{\partial \Pi}{\partial h} \Big|_{h=h_{\infty}} \quad (3.2)$$

Where  $h_{\infty}$  is the outside film thickness. The disjoining pressure gradient,  $\partial \Pi / \partial h$ , can be assumed constant since the thickness deviation from  $h_{\infty}$  is small. This diffusion-like fluid transport results in the Regime A kinetics, and the growth of ridge size and thickness.

Due to the non-monotonic nature of  $\Pi(h)$ , the ridge thickness could reach a critical value, where  $\partial \Pi / \partial h$  changes sign (*cf.* Figure 2.8). The thickness beyond this critical one is unstable, leading to topological instability. The thicker white spots or mesas have large volumes and lower disjoining pressures. The fluid flowed out from the thinner domain is collected in these white spots, instead of accumulating axisymmetrically in the ridge. The diffusive-like dynamics of ridge expansion then no longer controls the expansion of the thinner domain, and the transition to the constant velocity regime takes place. Alternatively, before critical ridge thickness is reached, the domain can impinge onto the film Plateau border, which acts as reservoirs for the drained fluid. In either case, flows are developed within the ridge area towards the reservoir (white spots or the Plateau border), as evidenced by the observations of rapid movements of small, newly-developed white spots towards bigger ones or towards the Plateau border.



The concentration dependence of the apparent diffusivity observed in Regime A (Figure 3.9a) can be attributed to the concentration dependence of the disjoining pressure gradient, which in general increases with increasing surfactant (more precisely, micelle) concentration. Similarly, it increases as number of micelle layers in the film decreases, which is consistent with the trend of the diffusivity. In Regime B, however, the concentration dependence becomes more complex since much more factors may need to be considered in determining the apparent velocity. Development of instability, size, thickness and mobility of the white spots, strength of the flows within the ridge, and also the magnitude of driving forces of Laplace and disjoining pressure, all could contribute to the observed contact line velocity. In addition, Marangoni effects, thin film domain line tension, and possible breakdown of the small-slope lubrication approximation when the white spots become much thicker than the rest of the film, are all possibly involved, and are still all poorly understood. Their roles in the dynamics of domain growth remain elusive, and needs more experimental and theoretical efforts to unravel.

### 3.5 Conclusions

In this chapter, the dynamics of the growth of a single, thinner domain during the process of thin film stratification is examined experimentally. IDIOM method is used to visualize and characterize the evolution the stratifying micellar film, while specially designed tracking scheme is used to track the movement and growth of a thinner domain.

The radius of an isolated domain grows as  $R \propto t^{0.5}$  (Regime A), displaying a constant apparent diffusivity, in agreement with published studies. After the growing domain comes in contact with the Plateau border, the domain radii grows as  $R \propto t$  (Regime B), indicating the

contact line between domain and the thicker film moves at a constant velocity. This scaling transition is being reported for the first time. For isolated domain, a similar transition could occur with a topological instability at the contact line which leads to formation of white spots around the growing domain. When varying the surfactant concentration, the variation of the apparent diffusivity,  $D$ , in Regime A and the apparent contact line velocity,  $V$ , in Regime B are very different. While  $D$  increases monotonically with increasing SDS micelle concentration, the concentration dependence of  $V$  is non-monotonic.

We show that a lubrication-based thin film hydrodynamics model, accounting for the effect of supramolecular structural oscillatory disjoining pressure, is promising in explaining the two distinct kinetic regimes of domain growth, the regime transition through topological instability or contact with Plateau border, and the concentration dependence of the apparent growth rates in both regimes. It shows that the formation, evolution and stability of the ridge formed around the growing domain is of critical importance. Ridge formation and stability, and hydrodynamics of domain growth in stratification of foam films will be the focus of the following chapters.

## **CHAPTER 4.**

### **FORMATION AND EVOLUTION OF A RIDGE DURING DOMAIN GROWTH IN STRATIFYING FOAM FILMS**

#### **4.1 Introduction**

The dynamics and stability of stratifying foam film is closely linked to the formation and growth dynamics of thinner, darker domains within the thicker film, as demonstrated in the previous chapter. Upon examining the growth of a single domain, we concluded that the formation, evolution and stability/instability of a ridge adjacent to the thinner growing domain is directly involved in determining the growth kinetics and growth rate. Several authors [77,79] have postulated that the liquid drained out from the expanding domain accumulates and forms a ridge surrounding the circular contact line between thinner domain and thick film. However, the experimental evidence of ridge formation remains indirect. Other authors [73,80] therefore argued that the domain expansion is more akin to a thermodynamic phase transition (condensation of “vacancies”), without considering the hydrodynamics of ridge formation. We intend to demonstrate the importance of the ridge formation, by experimentally detect and characterize the ridge, and model its shape and time evolution.

More generally, in free surface flows, fluid often accumulates near the moving contact line, deforms the surface and forms a ridge or rim. Ridges are formed during growth of a dry patch when liquid dewets from a solid [200] or a liquid [222] substrate, or during growth of a hole in rupturing free standing liquid film [223]. The similarities in dynamics between liquid dewetting from a substrate and stratifying free-standing film were first recognized by de Gennes [82] and further mentioned by Brochard and Redon [178]. In the last thirty years, dewetting of supported

films with one solid-liquid interface has been a focus of extensive studies [167]. Experimental and theoretical studies on ridge formation and evolution during dewetting are found to be valuable for understanding pattern formation [189], contact line motion [224], intermolecular and surface forces [192], and rheological effects [225] in the flow in supported films. In contrast, little progress has been made in free-standing films. The characterization of ridge formation in free-standing stratifying film is proven rather challenging: due to lack of a solid substrate and shorter time scale (on the order of seconds) of the dynamics, some of the widely used techniques in polymer dewetting studies (e.g. AFM) are therefore not suitable. The newly-developed IDIOM protocol (presented in Chapter 2) has been shown to offer the required spatial and temporal resolution, in order to detect the nanoscopic ridge structures that spontaneously appear in stratifying micellar foam films (as shown in Figure 2.14a).

In this chapter, we provide the first detailed experimental visualization and characterization of a ridge formed during domain expansion in free standing stratifying foam films made of surfactant micelle solution. Features of the nanoscale ridge shape, and dynamics of its development and instability are explicitly determined and examined. We develop a thin film hydrodynamic model based on lubrication approximation, incorporating the influence of supramolecular structural forces.

We also investigate for the first time the onset and growth of topological instability within the ridge that leads to white spot formation. We experimentally resolve the thickness evolution and symmetry breaking of the ridge that occurs when the instability sets in. The instability leads to formation of white spots in the ridge that continue to grow over time, while other portions of the ridge is not perturbed by the instability. Thickness variations of both the white spots formed and the remaining ridge are analyzed. The oscillatory nature of the supramolecular structural

disjoining pressure is found to have significantly role in the dynamics of the instability, and the evolution of the thinner domain, the ridge and the white spots.

## 4.2 Methods

The stratifying foam films are made with SDS micellar solutions in the thin film apparatus, and their thicknesses during stratification are profiled with the IDIOM protocols, as described in detail in Section 2.2. The porous plate film holding cell is preferentially used to conduct experiments on ridge detection and characterization, as it allows better control over the applied driving pressure. Additionally the porous plate thin film balance setup (shown in Figure 2.3) is used for measuring the equilibrium disjoining pressure using a pressure transducer.

The direct disjoining pressure measurement mostly follows the procedure described by Dimitrova et al. [105], and is summarized here briefly. The pressure transducer (Omega, PX409-001G5V) is directly connected to the liquid within the porous plate cell and monitors the pressure difference between the liquid thin film and the atmospheric pressure. Special care is taken to ensure no air bubble is entrapped in the connection to avoid error in pressure determination. After the foam film is formed by withdrawing liquid from the presoaked porous plate, the withdrawal is stopped to allow the film to evolve under fixed pressure, until a metastable film thickness is reached. The disjoining pressure at this equilibrium state can then be inferred from the measured pressure by:

$$\Pi = P_c = P_{trans} + \rho g \Delta H \quad (4.1)$$

where  $P_{trans}$  is the pressure measured by the pressure transducer, and  $\Delta H$  is the liquid height difference between the transducer and the thin film. Careful measurement of  $\Delta H$  is carried out before each experiment to accurately account for the hydrostatic pressure difference.

The measurement of disjoining pressure is accompanied by the simultaneous measurement of the metastable film thickness by the IDIOM protocol. By varying the volume of liquid within the porous plate cell (and therefore the size of the thin film) using the syringe pump, the applied pressure is varied. The procedure allows us to map out the stable branches of the disjoining pressure isotherm  $\Pi(h)$ . Due to the relatively small porosity of the plate (10-15  $\mu\text{m}$ ), the fluid flows inside are associated with considerable viscous drag during pressure change. The measurement is therefore only taken after the measured pressure is allowed to relax to a constant value. Typically a five minute waiting time after each pressure change is sufficient to ensure equilibrium.

A slightly modified procedure is used for the characterization of ridge formation during domain growth. After a metastable film thickness is reached, instead of incremental changes in pressure, a continuous pressure ramp is applied until the thickness stepping takes place via domain nucleation and expansion. The ramp rate is kept low, by withdrawing liquid from the film cell with very small flow rate (on the order of  $\mu\text{L}/\text{min}$ ). This procedure ensures that the thin film is kept near equilibrium until the onset of domain nucleation, and it improves the consistency of experimental results upon repetition.

### 4.3 Axisymmetric ridge shape and its evolution

#### 4.3.1 Equilibrium disjoining pressure measurement

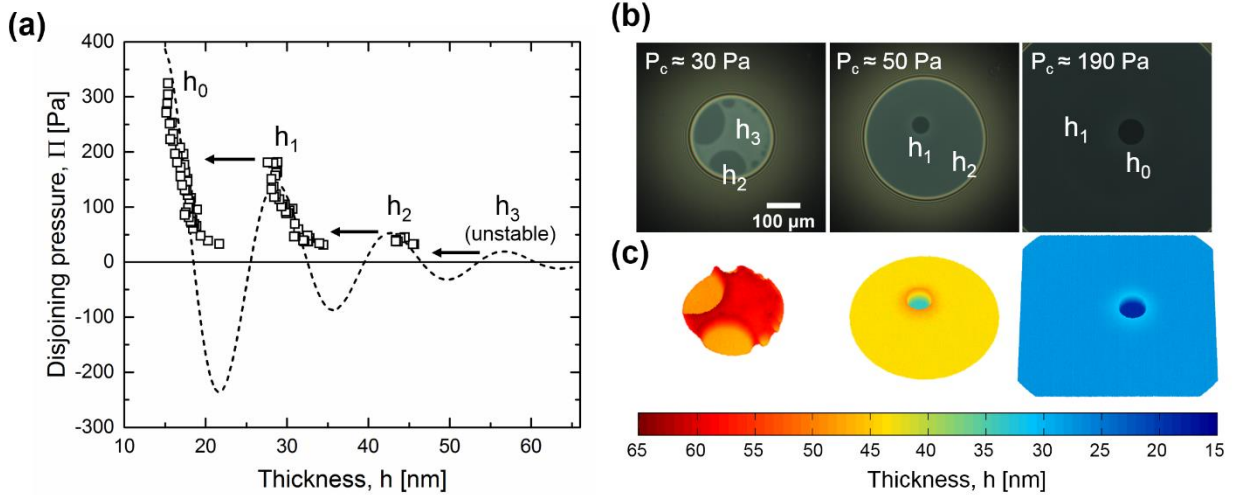


**Figure 4.1** Equilibrium disjoining pressure measurement in stratifying foam film. (a) Oscillatory disjoining pressure isotherm,  $\Pi$  vs.  $h$ , in 50 mM SDS solution. Experimental measurements are feasible only at discrete metastable thickness branches ( $h_0$ ,  $h_1$ ,  $h_2$ ), shown in hollow squares. The arrows show the pressures at which transitions from thicker to thinner branches take place. (b) Snapshots during the transitions between thickness branches. (c) Color coded thickness map of micrographs in (b), constructed using the IDIOM method.

The disjoining pressure isotherm measured for a stratifying foam film made with 50 mM ( $\sim 6 \times \text{CMC}$ ) SDS solution is shown in Figure 4.1a. The contribution of oscillatory structural forces is evident after the film thickness  $h$  reaches under about 60 nm. Four thickness steps are observed during the course of film stratification, and three stable branches of disjoining pressure are measured, when the driving force of drainage  $P_c$  is counter balanced by the disjoining pressure  $\Pi$ . Experimentally, the disjoining pressure can only be accessed only when  $\partial\Pi/\partial h < 0$  and

$\Pi(h) = P_c \geq 35 \text{ Pa}$  (minimum of  $P_c$  is set by the geometry of the porous plate cell) [123].

However the oscillatory nature of the supramolecular structural disjoining pressure can still be inferred by fitting the experimental data from the stable portions, as shown by the dash line. The damping oscillation period is found to be  $\Delta h = 13.0 \text{ nm}$ , close to the stratification step size,  $\Delta h = 13.5 \text{ nm}$ , presented in Figure 2.7.

At the pressure maxima of each stable branch, the film becomes unstable to thickness or pressure perturbations, and transition to the next stable branch occurs via nucleation and growth of a thinner, circular domain. The micrographs and corresponding IDIOM thickness maps are presented in Figure 4.1b&c. The applied pressure and film thickness at which the nucleation and growth of thinner domain occurs shows good repeatability, due to the well-controlled pressure ramp protocol.

### 4.3.2 Ridge shape and evolution

The growth of an isolated thinner domain during film stratification from thickness branch  $h_2$  to  $h_1$  is shown in Figure 4.2. With contrast enhancement to the micrographs, a “halo” is visible around the growing domain in Figure 4.2a. This indicates the formation of a ridge with slightly higher thickness outside the domain. The IDIOM method is used to resolve the film thickness with high spatial (measurement at every pixel with  $\sim 0.5 \mu\text{m}/\text{pixel}$ , and thickness resolution of  $\sim 1 \text{ nm}$ ) and temporal (500 frames per second) resolution. A ridge is detected to form around the flat thinner domain. The thickness of the ridge exceeds the thickness of the surrounding film only by a few nanometers as shown in the color-coded thickness map in Figure 4.2b. This is the first piece of experimental evidence that quantitatively characterizes the ridge formation and growth



accompanying domain growth during foam film stratification. The ridge grows in both height and width over time, concomitantly with the expansion of thinner domain. At a later stage (shown in Figure 4.2b at  $t = 2.5$  s), topological instabilities develop within the ridge region, leading to the formation of thicker white spots, or nanoscopic mesas (*cf.* Figure 2.14b).

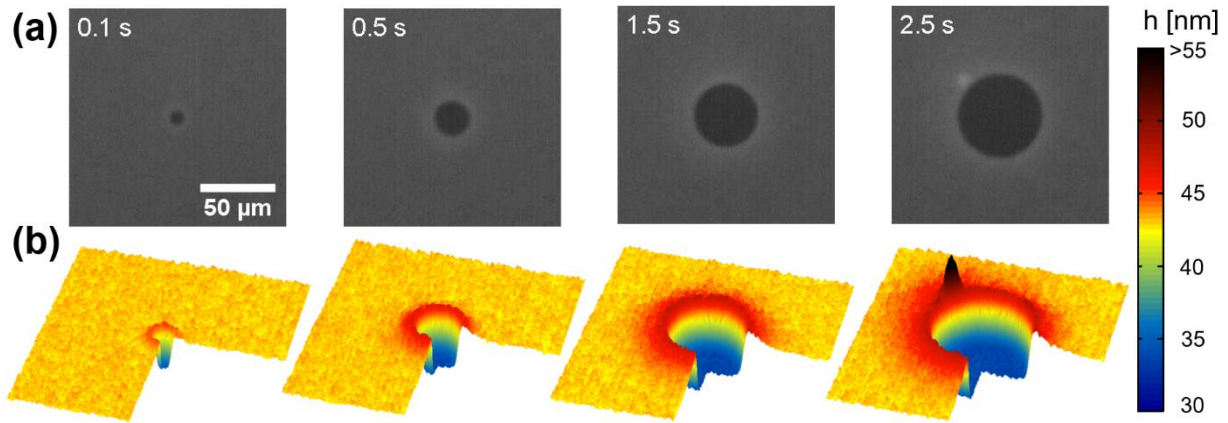


**Figure 4.2** Domain growth and ridge formation during stratification. (a) Experimental montage of a growing domain during thickness transition from  $h_2$  to  $h_1$  under  $P_c \approx 50$  Pa. Time labeled indicates the time after the thinner domain emerges. (b) Thickness maps from using IDIOM method. The maps are cut open to show the cross-sections and the thinner domains inside.

The detailed shape of the ridge and its evolution over time is shown in Figure 4.3. Here we first discuss only the shape and its evolution of the axisymmetric ridge before the topological instabilities. The film thicknesses are averaged circumferentially to obtain the ridge profile as thickness,  $h$  vs. the distance to the center of the growing thinner domain,  $r$ .

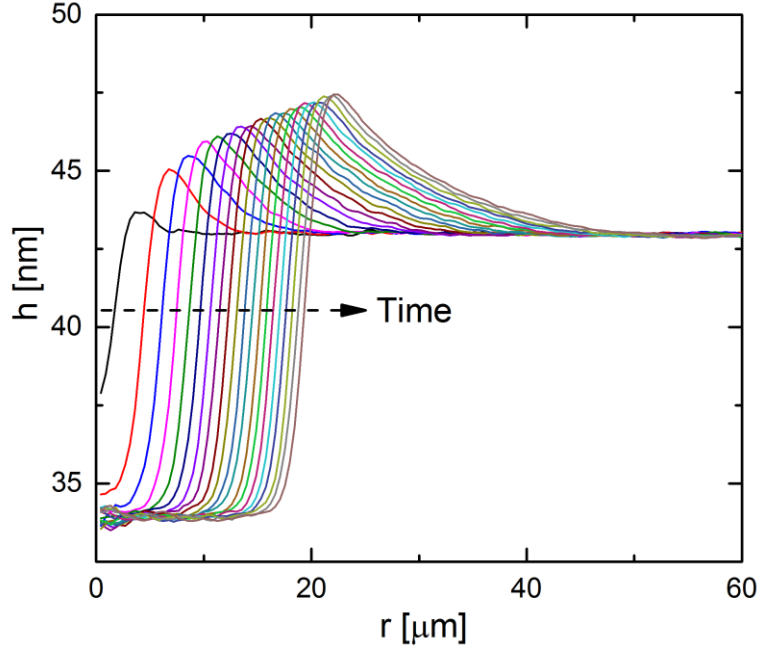


**Figure 4.3** Time evolution of the axisymmetric ridge thickness profile, plotted as thickness vs. distance to the domain center. The time interval of successive profiles is 0.1 s.

The thickness profiles,  $h$  vs.  $r$ , show that the thinner domain reaches a constant thickness quickly after initial nucleation, consistent with the observations from the micrographs and IDIOM thickness maps (Figure 4.2). The ridge forms and grows in size over the whole period of time as the nearly flat thinner domain expands out. The shape of the ridge remains relatively unchanged, showing significant asymmetry: the transition from the thinner domain thickness,  $h_d$ , to the maximum ridge thickness,  $h_{\max}$ , is much steeper than the transition from the ridge peak to the outside film thickness,  $h_{\infty}$ . A monotonic decay of thickness into  $h_{\infty}$  is observed. In contrast, the ridges formed during dewetting of supported films are often reported (*e.g.* by Seemann et al. [200]) to have thickness undershoots before merging into the outside unperturbed film.

It is worth emphasizing that the real foam films have two gas-liquid interfaces, and both deform during the domain growth process, as sketched in Figure 4.4a. Care is therefore needed when analyzing the thickness profiles measured in Figure 4.3, as the slopes and curvatures in the shown profiles originate from both interfaces. Also illustrated in Figure 4.4a, the ridge and domain geometry is in fact very “flat”: its lateral span is nearly three orders of magnitude larger than the vertical coordinate. The schematic of ridge profiles is drawn far off-scale.

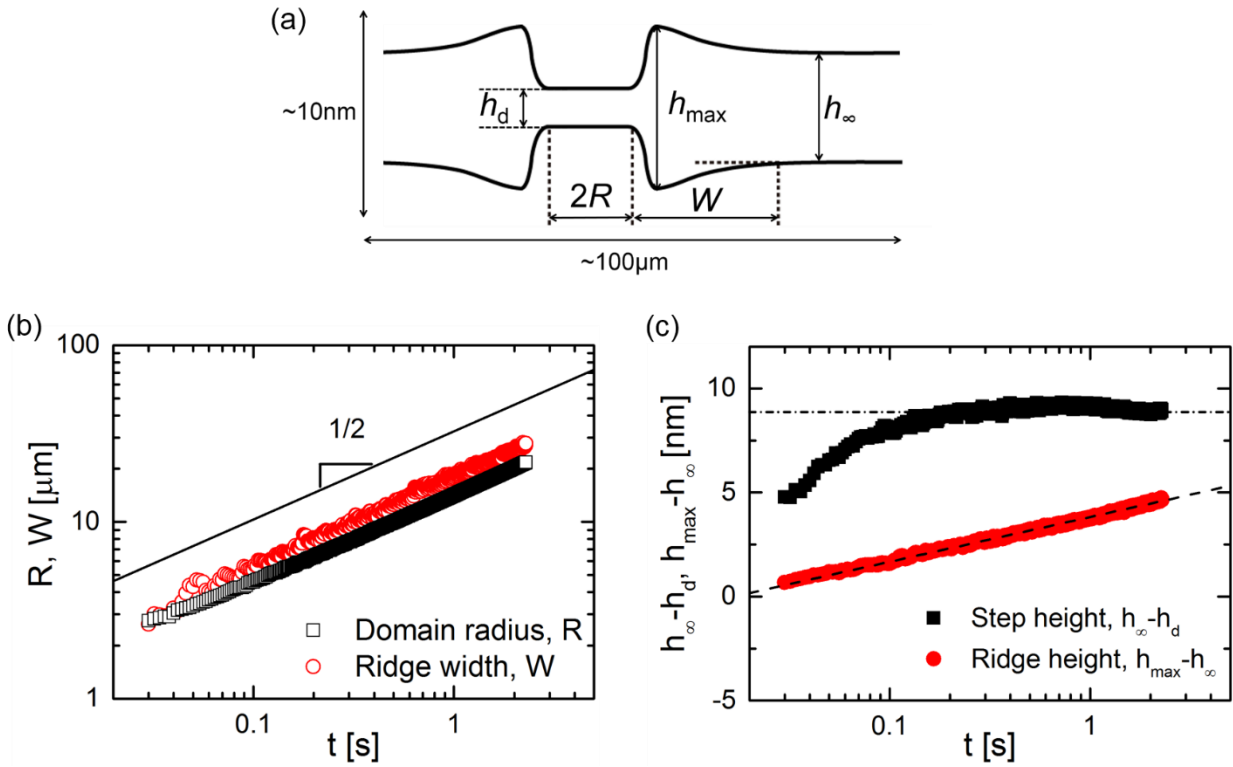


**Figure 4.4** The shape and its evolution of the ridge formed around a growing domain. (a) A schematic representation of the ridge. (b) Time dependence of domain radius  $R$  and ridge width  $W$ , plotted in logarithmic scale. the solid line shows is slope of  $t^{0.5}$  scaling. (c) Time dependence of the thickness difference between outside film and thinner domain,  $h_{\infty} - h_d$ , and the maximum thickness of the ridge,  $h_{\max} - h_{\infty}$ , plotted on a semi-logarithmic scale.

The dynamics of the ridge formation and evolution is characterized by following the thickness profile of the ridge frame by frame. Figure 4.4b shows the time dependence of lateral sizes of the domain and the ridge. The radius of the thinner domain,  $R$ , is found to be proportional to  $t^{0.5}$ , in agreement with results in Chapter 3 (for Regime A) and previous reports [73,78]. The width of the ridge,  $W$ , is found to exhibit the same scaling exponent, *i.e.*  $W \propto t^{0.5}$ . The width of the ridges formed during dewetting of polymeric films has been extensively characterized, and it determines the viscous dissipation, and the slippage length [173]. For free-standing stratifying foam films, the scaling for growth of the ridge width is determined here for the first time.

The time-dependent thicknesses of the domain and the ridge is plotted in Figure 4.4c. The thickness of the thinner domain over time is reported with regard to the outside film thickness, as  $h_{\infty} - h_d$  vs.  $t$ . The thinner domain is established relatively fast, within about 0.1 s after domain nucleation. After that the thickness of the thinner domain remains constant for the rest of the process. On the other hand, the maximum thickness of the ridge,  $h_{\max} - h_{\infty}$ , increases throughout the process, until topological instability takes place in the ridge. The ridge height growth deaccelerates over time, resulting in an apparent logarithmic time dependence, *i.e.*  $h_{\max} - h_{\infty} \propto \log t$ . The maximum relative thickness remains small ( $h_{\max} - h_{\infty} < 5$  nm) compare to the total thickness of the film (~50 nm). In contrast, much larger ridges (same order of magnitude as the film thickness) were observed in the context of dewetting [189,195,197,200]. The small ridges in stratifying foam film can be attributed to the disjoining pressure gradient inside the ridge, which reduces the fluid accumulation at the ridge apex and sculpts the much flatter, wider and asymmetric ridge.

The thickness profiles of the ridge shape can be integrated to obtain the volume of liquid. The following equations are used to track the volume drained from the thinner domain and the volume accumulated in the ridge:

$$\Delta V_{ridge} = 2\pi \int_{R(t)}^{\infty} r(h - h_{\infty}) dr \quad (4.2)$$

$$\Delta V_{domain} = 2\pi \int_0^{R(t)} r(h - h_{\infty}) dr \quad (4.3)$$

The volumes are set to be relative to the initial flat film with thickness  $h_{\infty}$ . Figure 4.5a illustrates the regions in the thickness profile to which the two integrations are applied. The time evolutions of both volumes and their sum are shown in Figure 4.5b. The volume within the area of growing domain,  $\Delta V_{domain}$ , decreases linearly with time, which is expected for a domain with uniform thickness expanding with  $R \propto t^{0.5}$  (or area  $A \propto t$ ). More importantly, the volume inside the ridge,  $\Delta V_{ridge}$ , increases at approximately the same rate, and the total volume of the system is conserved during the domain expansion process. This result suggests that the expansion of the domain is indeed a local phenomenon, with outwards flux diminishing far away from the ridge. In explaining domain growth kinetic with the diffusive osmotic (DO) mechanism (discussed more in Section 1.2.3 and 3.4), Kralchevsky et al. [73] argued for a non-local process that the domain grows due to a constant flux of “vacancy” from the outside Plateau border. This mechanism seems to be in contradiction with our experimentally observed local dynamics.

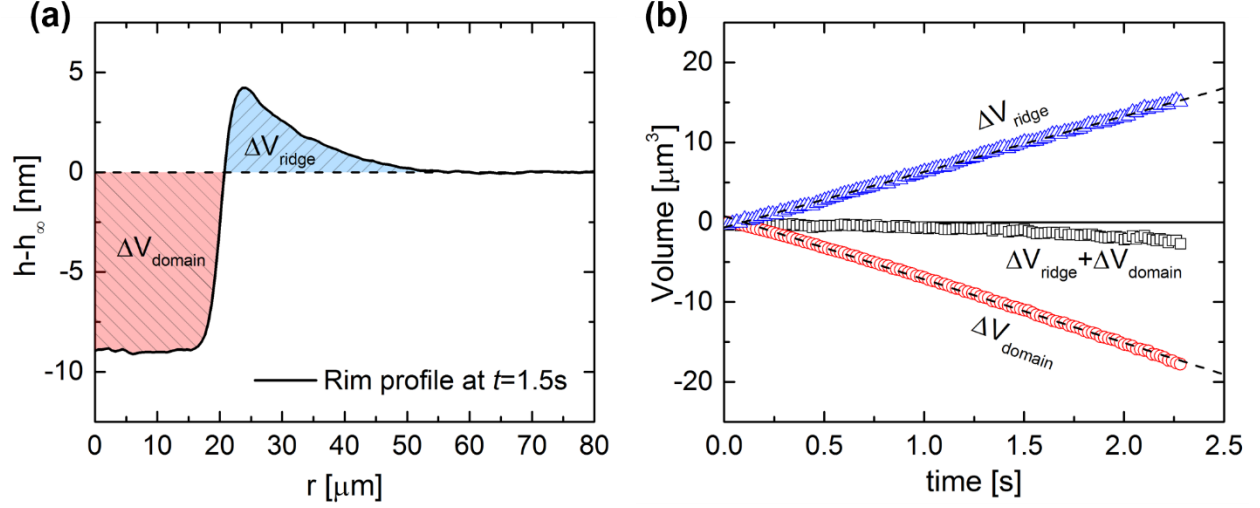


**Figure 4.5** Volume conservation during domain expansion. (a) The rim profile obtained experimentally at  $t = 1.5$  s. The color marked regions are integrated separately to obtain the fluid volume drained from the domain,  $\Delta V_{\text{domain}}$ , and the volume accumulated in the rim,  $\Delta V_{\text{ridge}}$ . (b) The time dependence of  $\Delta V_{\text{domain}}$ ,  $\Delta V_{\text{ridge}}$  and their sum.

### 4.3.3 Thin film equation and scaling analysis of the ridge formation

The ridge formed during domain expansion has an asymmetric, noncircular cross section. Such profiles imply that the Laplace pressure, which is proportional to the local curvature of the gas-liquid interface, is not uniform within the ridge. In fact, the shape asymmetry of ridge cross-sectional profile is a manifestation of the balance between the thickness-dependent, long-range, oscillatory disjoining pressure and the curvature-dependent local Laplace pressure.

To better understand the shape and evolution of the ridge, we develop a lubrication-based thin film hydrodynamics model for the formation of the ridge. In a free standing thin film with no-slip boundary condition on both surfaces, the following equation describes the spatial and temporal change of the film thickness:

$$\frac{\partial h}{\partial t} + \frac{1}{r} \frac{\partial}{\partial r} \left[ \frac{rh^3}{12\eta} \frac{\partial}{\partial r} (\sigma K + \Pi) \right] = 0 \quad (4.4)$$

The equation is also presented in Section 3.4 as Equation (3.1). The two terms in the parenthesis of Equation (4.4) are the contributions from the Laplace pressure arises from the local surface curvature, and the disjoining pressure arises from the structural surface forces, respectively. Here  $\eta \approx 1 \text{ mPa}\cdot\text{s}$  is the fluid viscosity (assuming water viscosity),  $\sigma \approx 35 \text{ mN/m}$  is the surface tension determined by pendant drop tensiometry, and the curvature of the film surface  $K$  is given by

$$K = \frac{0.5h_{rr}}{\left[1 + (0.5h_r)^2\right]^{3/2}} \approx \frac{h_{rr}}{2} \quad (4.5)$$

Where  $h_r = \frac{\partial h}{\partial r}$ ,  $h_{rr} = \frac{1}{r} \frac{\partial}{\partial r} \left( r \frac{\partial h}{\partial r} \right)$  denote differentiation. The factor 0.5 comes from the two air-liquid interfaces in the system (as showing in Figure 4.4a). The approximation is applied due to the small slopes in the thin film, i.e.  $h_r \rightarrow 0$ .

The following dimensionless quantities are introduced to Equation (4.4) for scaling analysis:

$$\bar{h} = \frac{h}{\Delta h}, \bar{r} = \frac{r}{L}, \bar{t} = \frac{t}{\tau}, \bar{\Pi} = \frac{\Pi}{\Pi_\infty} \quad (4.6)$$

Here we choose the period of oscillatory disjoining pressure  $\Delta h$  to scale the thickness of the film, and a characteristic length scale  $L$  in the  $r$ -direction, whose magnitude will be discussed in the following section. The time is scaled by a stretched visco-capillary time scale,  $\tau = 24\eta L / \sigma \varepsilon^3$ , in which the small parameter,  $\varepsilon = \Delta h / L$ , is the geometrical aspect ratio. This time scale is often used

in capillary-dominated thin film flows [145]. The disjoining pressure,  $\Pi(h)$ , is scaled by the disjoining pressure of the unperturbed surrounding film,  $\Pi_\infty = \Pi(h_\infty)$ . Since the outside film remains at an equilibrium thickness during the domain expansion and ridge formation, the disjoining pressure there remains balanced by the applied capillary pressure,  $P_c$ . Therefore experimentally  $\Pi_\infty$  can be estimated by the measurable applied pressure, *i.e.*  $\Pi_\infty \cong P_c$ . Combining Equation (4.4), 4.5 and (4.6), the non-dimensionalized form of thin film equation is:

$$\frac{\partial \bar{h}}{\partial \bar{t}} + \frac{1}{\bar{r}} \frac{\partial}{\partial \bar{r}} \left( \bar{r} \bar{h}^3 \frac{\partial \bar{h}_{rr}}{\partial \bar{r}} \right) + \Theta \frac{1}{\bar{r}} \frac{\partial}{\partial \bar{r}} \left( \bar{r} \bar{h}^3 \frac{\partial \bar{\Pi}}{\partial \bar{r}} \right) = 0 \quad (4.7)$$

Where the dimensionless number  $\Theta = \frac{2L^2 \Pi_\infty}{\sigma \Delta h}$  compares the disjoining pressure ( $\sim \Pi_\infty$ ) with the Laplace pressure contribution ( $\sim \sigma \Delta h / 2L^2$ ).  $\Theta$  has some similarities to a Schedluko's number [226],  $S = \frac{A_H}{6\pi L^2}$ , which is equivalent to  $\Theta$  when the disjoining pressure is dominated by van der Waals interaction (with  $A_H$  being the Hamaker constant). In such case, the disjoining pressure scales as  $\Pi_\infty \sim \Pi_{vdw} = A_H / 6\pi h^3$ , which leads to  $\Theta = A_H L^2 / 3\pi \sigma h^4 = \frac{\varepsilon^4}{2} S$ . In the present study however, the supramolecular structural oscillatory forces make dominant contribution to the disjoining pressure.

$\Theta$  can also be viewed as the comparison between the experimental length scale and a critical length:  $\Theta = (L/L_c)^2$ , where critical crossover length scale is given by



$$L_c = \sqrt{\frac{\sigma}{2\Pi_\infty/\Delta h}} \quad (4.8)$$

which is resulted from the balance of Laplace and disjoining pressure. For small ridge features where  $L \ll L_c$ , we have  $\Theta \ll 1$ , and the shapes are controlled by Laplace pressure. Larger features ( $L \gg L_c$ ) are instead controlled by disjoining pressure. In the present study, using value  $\Delta h \approx 13$  nm,  $\Pi_\infty \approx P_c \approx 50$  Pa, and  $\sigma \approx 35$  mN/m, the critical length scale is found by Equation (4.8) to be  $L_c \approx 2$   $\mu\text{m}$ .

An alternative way for nondimensionlization is to use a disjoining pressure scaled characteristic time,  $\tau_\Pi = 12\eta/\Pi_\infty\epsilon^2$ . The two choices of time scale is related by the dimensionless number  $\Theta$ , *i.e.*  $\tau/\tau_\Pi = \Theta = (L/L_c)^2$ . The thin film equation non-dimensionalized with  $\tau_\Pi$  then becomes:

$$\frac{\partial \bar{h}}{\partial \bar{t}} + \frac{1}{\Theta} \frac{1}{\bar{r}} \frac{\partial}{\partial \bar{r}} \left( \bar{r} \bar{h}^3 \frac{\partial \bar{h}_{rr}}{\partial \bar{r}} \right) + \frac{1}{\bar{r}} \frac{\partial}{\partial \bar{r}} \left( \bar{r} \bar{h}^3 \frac{\partial \bar{\Pi}}{\partial \bar{r}} \right) = 0 \quad (4.9)$$

Equation (4.9) is equivalent to Equation (4.7), with the dimensionless parameter  $1/\Theta$  in front of the Laplace pressure term. The choice of characteristic time scale does not affect the results of further scaling analysis.

#### 4.3.4 Asymptotic solutions of the ridge

Due to the extremely asymmetric ridge cross-sectional shape, as shown in Figure 4.3, the choice of  $r$ -direction length scale  $L$  vary for the build-up part of the ridge from the thinner domain

to the peak of the ridge, and for the leeward part of the ridge from the ridge peak to the outside unperturbed film. The ramification of this length scale separation is rather remarkable: comparing to the critical length scale  $L_c \approx 2 \mu\text{m}$ , in the build-up part the ridge the characteristic length scale is close to  $L \approx 1 \mu\text{m} \approx L_c$ . In the leeward part of the ridge, the length scale is much larger,  $L \approx 10 \mu\text{m} \gg L_c$ . In addition, the characteristic time scale  $\tau$  also vary significantly with  $L$ , from  $\tau = \frac{24\eta L}{\sigma \varepsilon^3} \approx 0.25 \text{ s}$  in the build-up part, to  $\tau \approx 2.5 \times 10^3 \text{ s}$  in the leeward part. These differences in length and time scales suggest two asymptotic cases of the ridge profile, which lead to differences in ridge shape and its evolution. Indeed, we find that the experimentally resolved ridge thickness profiles have different time-dependent properties on either side.

**The build-up part.** In this part of the ridge,  $L \approx L_c$  and  $\Theta \approx 0.22 \sim 1$ , indicating that both Laplace pressure and disjoining pressure are involved in the dynamics. The characteristic time scale  $\tau \approx 0.25 \text{ s}$  is smaller than the experimental observed time scale of domain expansion (on the order of seconds). This implies the shape of the ridge in the build-up part should approach a long-time quasi-steady state solution, where the time dependent  $\partial h / \partial t$  term from Equation (4.4) can be neglected. After integrating twice with a flat thinner domain boundary conditions  $h(r=0) = h_0$ ,  $h_r(r=0) = 0$ , Equation (4.4) becomes:

$$\sigma K + \Pi = \Pi_d \quad (4.10)$$

where  $\Pi_d = \Pi(h_d)$  is the disjoining pressure in the flat thinner domain. Equation (4.10) resembles the augmented Young-Laplace equation, which is used to study equilibrium shape

profiles of deformable bubbles, drops, thin films, and three phase contact lines on a wetted solid surface [151,221].

In Figure 4.6, the thickness profiles in the build-up part of the ridge fall onto a single line when shifted to  $h-h_\infty$  vs.  $r-R$ . The experimental results show that though the maximum height of the ridge increases over time, a constant contact angle between the thinner domain and the ridge is maintained during the domain expansion. The angle is measured to be  $2\phi = 0.2 \pm 0.1^\circ$ , where the factor 2 is introduced to account for the two gas-liquid interfaces. This contact angle can be derived from the solutions of Equation (4.10) [221,227], as well as from thermodynamics using the Gibbs–Duhem equation [120,228], and it is closely related to the thickness-dependent surface energy of the thin film.

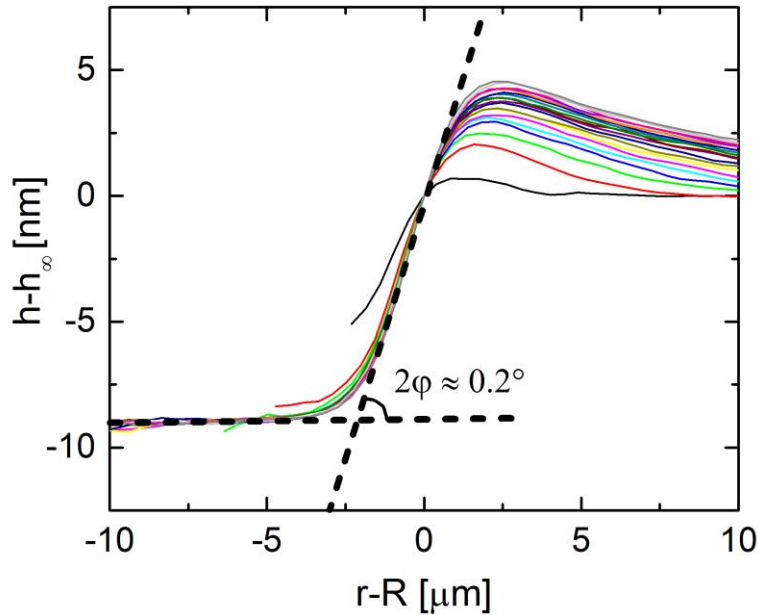


**Figure 4.6** The build-up part of the ridge profiles plotted as  $h-h_\infty$  vs.  $r-R$ . By the lateral shift the profiles, it shows that the build-up part of the ridge shape remain unchanged during domain growth.

The measurement of the contact angle between stratification layers is sparse and often indirect in the literature [73,76], due to its small value and dynamic nature. Our results agrees these indirect measurements, but come from a more direct approach of measuring spatial variations of film thickness. A more quantitative comparison between experimental measurements and solution of Equation (4.10) is presented in the next chapter.

**The leeward part.** For this side of the ridge, where the thickness decays slowly to the outside unperturbed film thickness, we have  $L \gg L_c$  and  $\Theta \approx 22 \gg 1$ . The characteristic time scale is  $\tau \approx 3 \times 10^3$  s, much larger than the experimental time scale. These estimations indicate that the leeward part of the ridge shape is time dependent, and the flow is mainly driven by the disjoining pressure, while the contribution from Laplace pressure (the second term in Equation (4.7)) can be neglected. The Equation (4.4) then becomes:

$$\frac{\partial h}{\partial t} + \frac{1}{12\eta r} \frac{\partial}{\partial r} \left( rh^3 \frac{d\Pi}{dh} \frac{\partial h}{\partial r} \right) = 0 \quad (4.11)$$

Upon inspecting Equation (4.11), we can treat it as a diffusion equation in cylindrical coordinates, with an effective diffusivity that depends on the film thickness and disjoining pressure isotherm:

$$D_{eff} = D_{eff}(h, \Pi) = -\frac{h^3}{12\eta} \frac{d\Pi}{dh} \quad (4.12)$$

The effective diffusion equation with the diffusivity in a power-law form of  $D_{eff} = D_{eff}(h^m)$  has been widely discussed, in the context of thin film hydrodynamics (mainly spreading or dewetting) [83]. The integer power  $m$  varies for specific problems, *e.g.*  $m = 2$  for

Navier-slippage-dominated thin film flows. The particular example of free standing films involving supramolecular structural disjoining pressure received little or no attention. Here we show that Equation (4.11), with appropriate boundary conditions for the presented domain expansion process, leads to a self-similar thickness profile in the leeward part of the ridge. With zeroth-order approximation to the effective diffusivity, the equation can be also solved analytically to give an asymptotic solution.

The diffusion problem involves a moving boundary around the growing thinner domain. This boundary condition is similar to that found in heat transfer problems involving phase transition, specifically at the phase changing front. In this problem, we have shown in Figure 4.5 that the fluid volume inside the ridge increases at the expense of the liquid volume removed from the growing thinner domain, *i.e.*

$$\Delta V_{ridge} = -\Delta V_{domain} \quad (4.13)$$

The two volumes are obtained using Equation (4.2) and (4.3). The integration in Equation (4.3) can be simplified by assuming the growing thinner domain has a constant uniform thickness  $h_d$ . Experimental observations indicate that this assumption is valid except during the very early stage of domain growth ( $t < 0.1$  s, see Figure 4.4c). The volume change within the thinner flat domain then becomes:

$$\Delta V_{domain} \approx \pi R(t)^2 (h_d - h_\infty) \quad (4.14)$$

Recalling that the radius of the thinner domain follow  $R \propto t^{0.5}$  in this regime (see Figure 4.4b), the integral boundary condition Equation (4.13) can then be rewritten as:

$$\int_{\sqrt{Dt}}^{\infty} r(h(r,t) - h_{\infty}) dr = C_1 t \quad (4.15)$$

Where  $C_1 = -(h_d - h_{\infty})D/2$  is a constant, and  $D = dR^2/dt$  is the growth rate of the thinner domain. The linear time dependence of volume within the ridge is in agreement with experimental results in Figure 4.5b.

The other boundary condition is given by flat unperturbed film far away from the ridge, *i.e.*  $h(r \rightarrow \infty) = h_{\infty}$ . And the initial condition is  $h(t=0) = h_{\infty}$ .

We now assume a similarity solution to Equation (4.11) in the form of

$$h(r,t) - h_{\infty} = t^{\alpha} f(\xi), \text{ where } \xi \equiv r/t^{\beta} \quad (4.16)$$

Here  $\xi$  is the similarity variable. Combining Equation (4.15) and (4.16) results in:

$$t^{\alpha+2\beta-1} \int_{\xi_0}^{\infty} \xi f(\xi) d\xi = C_1 = \text{Const.} \quad (4.17)$$

Where the lower integration limit is  $\xi_0 = D^{\frac{1}{2}} t^{\left(\frac{1}{2}-\beta\right)}$ . To keep Equation (4.17) time independent requires  $1/2 - \beta = 0$  and  $\alpha + 2\beta - 1 = 0$ , thus  $\beta = 1/2$  and  $\alpha = 0$ . The similarity variable then becomes:

$$\xi \equiv r/t^{1/2} \quad (4.18)$$

By substituting in Equation (4.18) to Equation (4.11), we obtain:

$$\frac{\xi}{2} \frac{dh}{d\xi} + \frac{1}{\xi} \frac{d}{d\xi} \left( D_{\text{eff}} \xi \frac{dh}{d\xi} \right) = 0 \quad (4.19)$$

Equation (4.19) is indeed independent on  $r$  and  $t$ . The solution to the diffusion equation is therefore self-similar in the form of  $h(r, t) - h_\infty = f(r/t^{1/2})$ , regardless of the form  $D_{eff}$  takes,

Equation (4.19) can be solved analytically if a zeroth order approximation is made for the diffusivity, assuming the diffusivity is a constant within the, *i.e.*  $D_{eff} \approx D_{eff}(h_\infty) = -\frac{h_\infty^3}{12\eta} \frac{d\Pi}{dh} \Big|_{h=h_\infty}$ .

This approximation is justified since the thickness in the ridge does not significantly deviate from the outside film thickness  $h_\infty$ . The solution then reads: [229]

$$h - h_\infty = -\frac{h_\infty - h_d}{Ei(-c) + e^{-c}/c} Ei\left(-c \frac{r^2}{Dt}\right) \quad (4.20)$$

where function  $Ei(x) = -\int_{-x}^{\infty} \frac{e^{-u}}{u} du$  is the exponential integral function, and  $c$  is a dimensionless

parameter  $c = \frac{D}{4D_{eff}} = -\frac{dR^2}{dt} \Big/ \frac{h_\infty^3}{3\eta} \frac{d\Pi}{dh} \Big|_{h=h_\infty}$ .

The same approximated solution to the ridge shape is also obtained by Heinig et al. [77] in studying the domain growth dynamics during stratification with polyelectrolyte-surfactant mixture. However, Heinig et al. [77] provided the approximated solution without experimental ridge characterization and scaling analysis for the full thin film hydrodynamic Equation (4.4). They assumed the local curvature induced Laplace pressure to be negligible. As a result, the shape and evolution of the build-up part the ridge is not discussed, and the transition from thinner domain to the ridge peak is approximated by an instantaneous thickness jump from  $h_d$  to  $h_{\max}$  at  $r = R$  (as sketched in Figure 2 in ref [77]). The value of  $h_{\max}$  from their solution is then time-independent, inconsistent with our experimental observed logarithmic ridge growth (shown in Figure 4.4c). In

addition, they prescribed the self-similarity of ridge shape without proper justification, while we here provide the derivation in Equation (4.16)-(4.19).

The self-similarity of the ridge profiles is confirmed with experimental results by plotting  $h-h_\infty$  vs.  $r/(Dt)^{1/2}$ , as shown in Figure 4.7. The leeward part of the thickness profiles from all time collapse into a single line. Deviation is found in the very early stage ( $t < 0.1$ s), perhaps due to the fact that the thinner domain has not been fully established, which is consistent with the thickness evolution shown in Figure 4.4c.

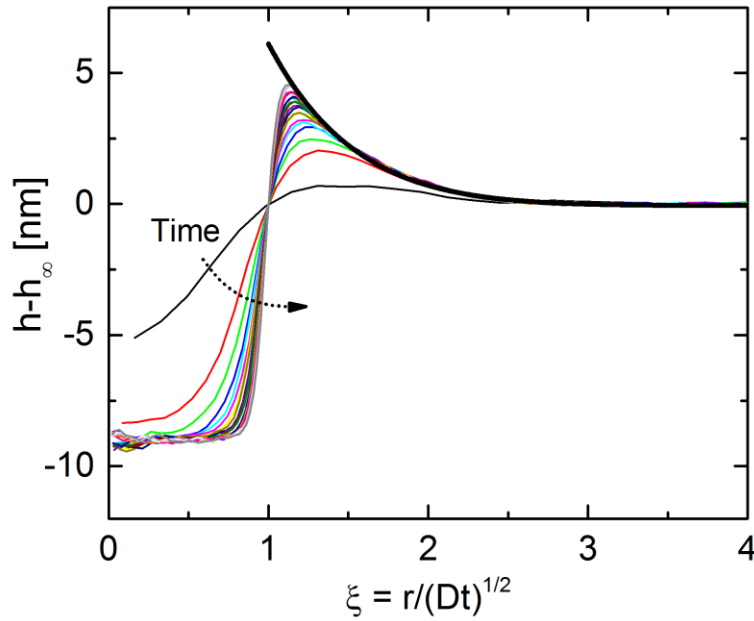


**Figure 4.7** Rescaled ridge thickness profiles plotted as  $h-h_\infty$  vs.  $r/(Dt)^{1/2}$ . Solid black line shows the fit from Equation (4.20) to the leeward part of the rescaled profiles.



In order to compare the analytical solution given by Equation (4.20) with the experimentally resolved ridge profiles, we obtain values  $h_\infty - h_d = 9.0$  nm and  $D = 206$   $\mu\text{m}^2/\text{s}$  directly from the experiments (see Figure 4.4b&c), and set  $c$  as the sole fitting parameter to fit the leeward part of the rescaled ridge profiles to Equation (4.20). In Figure 4.7, the solid black line shows a very good fit to the leeward part of all ridge profiles, with fitting parameter  $c = 0.35$ . The value of  $c$  can also be estimated through its definition  $c = -D \left/ \frac{h_\infty^3}{3\eta} \frac{d\Pi}{dh} \right|_{h=h_\infty}$ . Here the outside film

thickness  $h_\infty \approx 43$  nm, and the first order derivative of disjoining pressure can be estimated as

$$\left. \frac{d\Pi}{dh} \right|_{h=h_\infty} \approx \frac{P_c}{0.25\Delta h} \approx 15 \text{ Pa/nm}. \quad c \text{ then turns out to be } \sim 0.52, \text{ larger than the fitted value of } 0.35.$$

This slight discrepancy can be attributed to the high order terms of  $D_{\text{eff}}$ , inaccuracy in estimating

$$\left. \frac{d\Pi}{dh} \right|_{h=h_\infty}, \text{ or possible small contribution from the neglected Laplace pressure.}$$

### 4.3.5 Discussion

We have shown experimentally for the first time, that an axisymmetric ridge, with small thickness (several nanometers), large width (tens of micrometers) and asymmetrical cross section, is formed around the growing thinner domain, during the process of domain expansion in stratifying foam films. The liquid that drains out of the thinner domain accumulates in the ridge. The width of the ridge exhibits time dependence same as the domain radius, *i.e.*  $R, W \propto t^{0.5}$ . In the build-up part of the ridge, *i.e.* the side facing the flat thinner domain, a constant contact angle is established and maintained at  $\sim 0.2^\circ$  throughout domain expansion. In the leeward part, where

the ridge thickness decays to the outside film thickness  $h_\infty$ , the ridge profiles are found to be self-similar ( $h - h_\infty = f(r/t^{1/2})$ ). The shape and dynamics of the ridge is modeled using lubrication-based thin film equation (Equation (4.4)), which considers both Laplace and supramolecular structural disjoining pressure driving the flow. Through dimensional analysis, the experimentally observed ridge shape and evolution is captured by the asymptotic solutions. The leeward part of ridge is well fitted by an analytical solution of the model obtained with zeroth order approximation. Our results strongly supports the theory that the domain growth dynamics in stratifying foam films are modulated by the formation and evolution of the ridge, while the diffusive osmotic mechanism [73] fails in accounting for the existence of such ridge.

We now compare the experimental findings with the existing models that predict ridge (rim) formation in stratifying foam films. Bergeron et al. [79] proposed the “hole sheeting” hydrodynamic model and numerically solved it to obtain the evolution of thinner domain and the ridge. Bergeron et al. [79] predicted that a second maxima manifests itself in the ridge profile at late stage of domain expansion (see Figure 1.6), and leads to instability of ridge and formation of white spots. However, a thickness profile with a clear second maxima is not observed in our experimental results, even right before the white spots emerge. The disjoining pressure isotherm used in their hole sheeting model included van der Waals, electrostatic and structural oscillatory contributions, but the parameters for calculation are chosen rather arbitrarily, therefore might not reflect the real disjoining pressure. Their model also included a drainage flux from the film to the surrounding Plateau border, *i.e.* the surrounding film outside the growing domain is not assumed at equilibrium, and having constant thickness  $h_\infty$ , but rather evolving over time.

The other “rim formation” model of is proposed by Heinig et al. [77], in order to explain the domain growth dynamics in stratification in films made with surfactant-polyelectrolyte mixture. The governing equation of this model neglects any Laplace pressure contribution to the dynamics, hence is identical to Equation (4.11). As a result, they reached the same approximated analytical solution as Equation (4.20). However the shape and dynamics of the build-up part of the ridge, where the surface curvature induced Laplace pressure is non-negligible, are not captured. An instant thickness jump from thinner domain thickness  $h_d$  to the maximum ridge thickness  $h_{\max}$  is assumed at  $r = R$ , instead of a small apparent contact angle ( $\sim 0.2^\circ$ ) observed experimentally.

The ridge shape resolved here in stratifying foam film is also compared to the ridge (liquid front, rim) formed in liquid dewetting from a solid substrate. Though similarities in the thin film geometry and underlying physics are recognized (see review in Section 1.5), many unique features are observed in ridges in stratifying foam films: (i) it is small in thickness (several nanometers) and relative to that, large lateral width (several tens of micrometers); (ii) the shape of the ridge is asymmetric with non-circular cross section, and the thickness decay into the outside film thickness is monotonic; (iii) the radius of the domain and the width of the ridge grows as  $R, W \propto t^{0.5}$ . In comparison, the ridge in the dewetting case often has larger thickness (more than 100 nm), and has circular cross section. When the Laplace pressure is dominating the dynamics, Seemann et al. [200] shows that the ridge shape follows a “travelling wave” solution, and the ridge merges into the outside film with an undershoot trough. During dewetting, the radius of dry patch (analogous to the thinner domain grows linearly with time [178,230].

Asymmetric ridge shape can arise during dewetting of polymeric films, but they are typically results of slippage [173], non-linear friction between film and substrate [231], rheological

effect of the dewetting fluid [195], or presence of residual stresses in polymer film [197]. In the stratifying foam film, the film is free of a solid substrate, and is made from Newtonian solution. Therefore none of the slippage or rheological effects are responsible to the observed asymmetrical ridge shape, as well as the unique square root time dependence of domain radius and ridge width. The supramolecular structural oscillatory disjoining pressure plays a crucial role in shaping the ridge and determining its growth dynamics. While models for thin film dewetting are developed to include effects of several types of surface forces (mainly van der Waals and/or electrostatic repulsion interactions) [146,190,192], the oscillatory structural component is absent in these studies. Given the rich and diverse pattern formation resulted in the surface forces [188,191], it is not surprising that the presence of structural oscillatory forces greatly alters the shape and evolution of the ridge in the present study.

One of the challenges in modeling liquid spreading/dewetting dynamics is the stress singularity at the moving contact line [165,166], which has to be alleviated through “precursor film” that pre-wets the solid substrate, or local surface slippage at the contact line region [144]. In the case of stratifying foam films, this singularity is absent since there is no well-defined solid-liquid-gas three phase contact line. The contact line present is between different thicknesses of the same liquid (thinner domain and the ridge). In fact, the thinner domain can be viewed as equivalent to a precursor film whose thickness is determined by the oscillatory disjoining pressure. The well-defined, measurable thickness of the thinner domain makes stratifying foam film a potentially useful model system for studying precursor film-based hydrodynamic models.

Overall, the dynamics of formation and growth of the axisymmetric ridge during domain expansion in stratifying foam films are valuable not only in the context of foam stability and lifetime, but also helpful in better understanding of thin film hydrodynamics, contact line motion

and the underlying surface forces. Our experimental characterization of the ridge provides unprecedented details of its shape and evolution, which are not available to the existing models [77,79]. A more detailed and careful analysis, based on Equation (4.4) and explicitly includes the effects of supramolecular structural oscillatory disjoining pressure, is needed for fully understand the dynamics. Efforts and progress made in this direction is presented in the next chapter.

## 4.4 The ridge after topological instability

### 4.4.1 Formation of white spots within the ridge

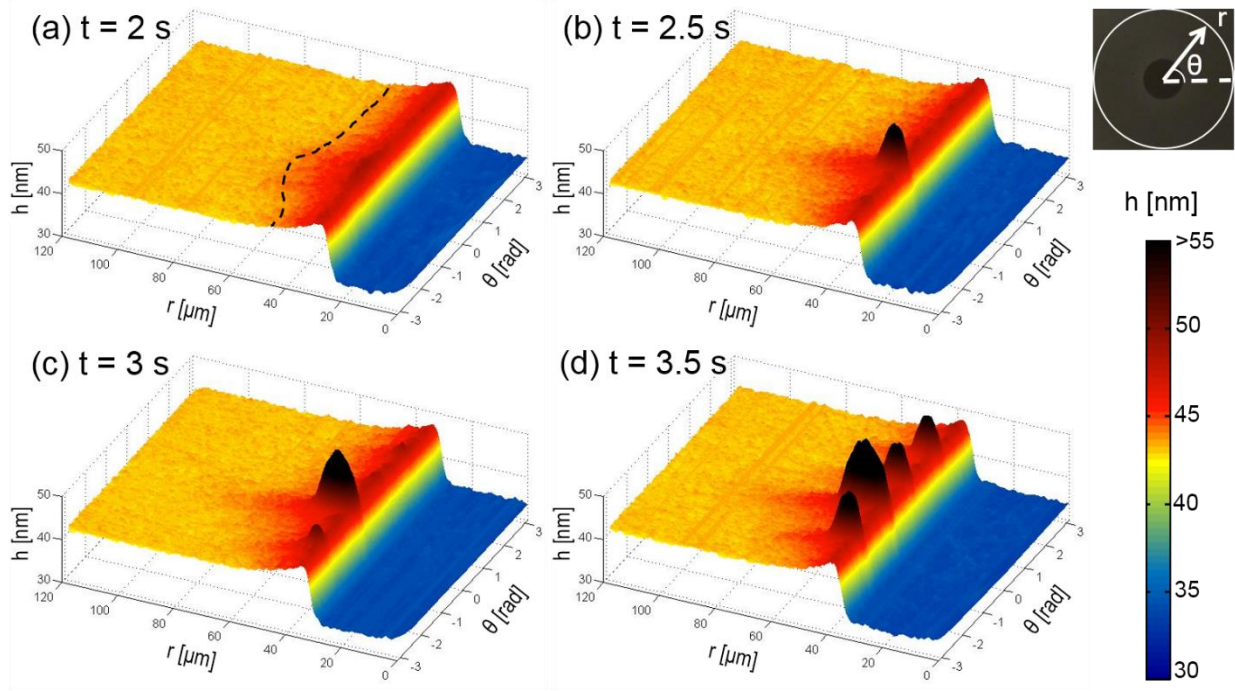


**Figure 4.8** Formation of white spots. The thickness  $h$  is plotted against distance to the domain center,  $r$ , and the rotation angle,  $\theta$ . The process starts with ridge protruding into the outside film, before thicker circular region develops adjacent to the domain contact line.

As the ridge grows in width and thickness over time, topological instability can develop within the ridge and eventually form much thicker white spots (mesas). In Figure 4.8, the growth of white spots is demonstrated by plotting the spatial distribution of thickness  $h(r, \theta)$  obtained by IDIOM protocol against the polar coordinates  $r$  and  $\theta$ . Several intriguing features are observed, and reported in the context of the topological instability for the first time:

- (i) During the formation and growth of white spot, the contact line between the thinner domain and the ridge are intact and remain circular (appear straight in the  $r\theta$ -coordinates). This is in contrast with typical ridge (rim) instabilities observed in spreading/dewetting liquids [178,225,232], where the contact line is significantly deformed and the thicker spots (drops) eventually detach from the contact line and get left behind in the thinner(dry) patch.
- (ii) Before white spots become visible in the micrographs (at  $t \approx 2.5$  s), the ridge is already deformed. In particular, as shown by the dash line in Figure 4.8a, the ridge starts to deform by protruding into the seemingly flat surrounding film. No periodic undulation is observed, the deformation is concentrated at the site where the first white spot forms later.
- (iii) The white spots (the thicker circular regions) are formed without spatial periodicity or temporal simultaneity.
- (iv) The ridge does not break down when white spots are formed, it gets deformed only at locations occupied by a white spot.

Indeed observations (iii) and (iv) show that the white spot formation cannot be attributed to the breakdown of the ridge through Rayleigh-type instability [76,79].

The detailed time evolution of the thickness within the ridge is illustrated in Figure 4.9, by plotting the maximum thickness in the ridge (and white spots),  $h_{\max}$ , as a function of  $\theta$  and  $t$ . The “fingers” in Figure 4.9 show the formation of white spots, how they grow in lateral size and thickness over time, as well as their movement along the domain-ridge contact line and eventual coalescence. It’s also worth noting that the unperturbed region in the ridge, *i.e.* locations where no

white spot is developed (marked in the white rectangle in Figure 4.9), the ridge shape is preserved throughout the domain expansion process. This region can therefore be used in characterizing dynamics of the remaining ridge after topological instability, the results of which are shown in the next section.

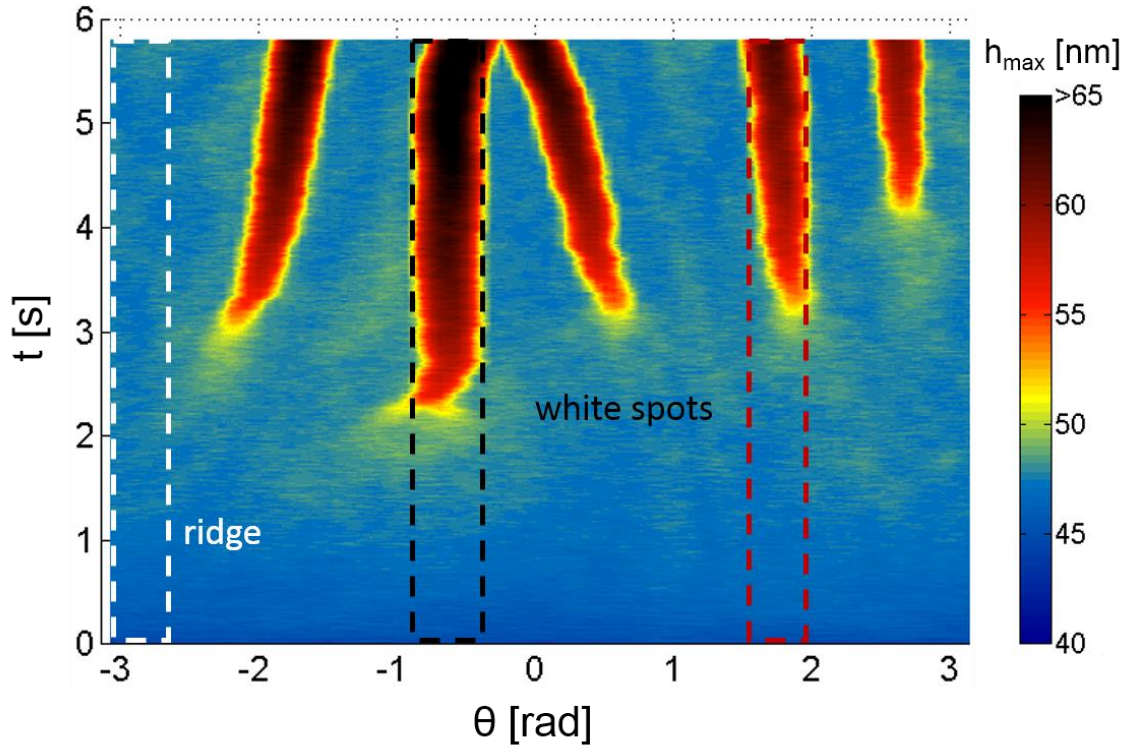


**Figure 4.9** Time and spatial evolution of maximum thickness  $h_{\max}$  within the ridge region.  $h_{\max}$  is shown by the color coding and plotted against time  $t$  and rotation angle  $\theta$ . The formation of much thicker white spots over time appears as fingers in the plot. The thickness evolution of two white spots and one unperturbed ridge region, within the dash rectangles, are followed in Figure 4.10&11.

We first focus on the growth of white spots. The maximum thickness within the white spots is tracked for two different white spots, marked in black and red dash line in Figure 4.9. The time



dependences of maximum thicknesses within in the marked regions are plotted in Figure 4.10. Both regions showed three growth regimes, and remarkably, the transitions between the three regimes correspond very well with the stable/unstable transition of the oscillatory disjoining pressure isotherm  $\Pi(h)$ . The isotherm is obtained through equilibrium pressure measurement and is fitted with a damped oscillation function is Figure 4.1a. The fitting result is replotted in Figure 4.10 as  $h$  vs.  $\Pi$  for better comparison with the thickness of growing white spots. During the ridge and white spots formation, initially the axisymmetric ridge is developed, and  $h_\infty$  slowly increases as the ridge grows.  $h_\infty$  in this regime stays in the stable branch of disjoining pressure isotherm, where  $\partial\Pi/\partial h < 0$ . Once the critical thickness is reached,  $h_\infty$  enters the unstable ( $\partial\Pi/\partial h > 0$ ) portion of the isotherm. Instability is developed in the ridge, and  $h_\infty$  rapidly increases, forming the thicker white spots. The rise in  $h_\infty$  slows down significantly, after it again enters the stable branch of disjoining pressure. The white spots continue to grow, since the magnitude of disjoining pressure becomes much smaller after one complete oscillation, and other driving forces (*e.g.* Laplace pressure) may become more significant.

The quantitative characterizations of the white spots formation and their evolutions, strongly point towards a mechanism in which disjoining pressure variation within the ridge is the dominating cause of topological instability and white spot growth. The inclusion of oscillatory disjoining pressure is essential for better understanding the dynamics within the ridge before or after the topological instability.

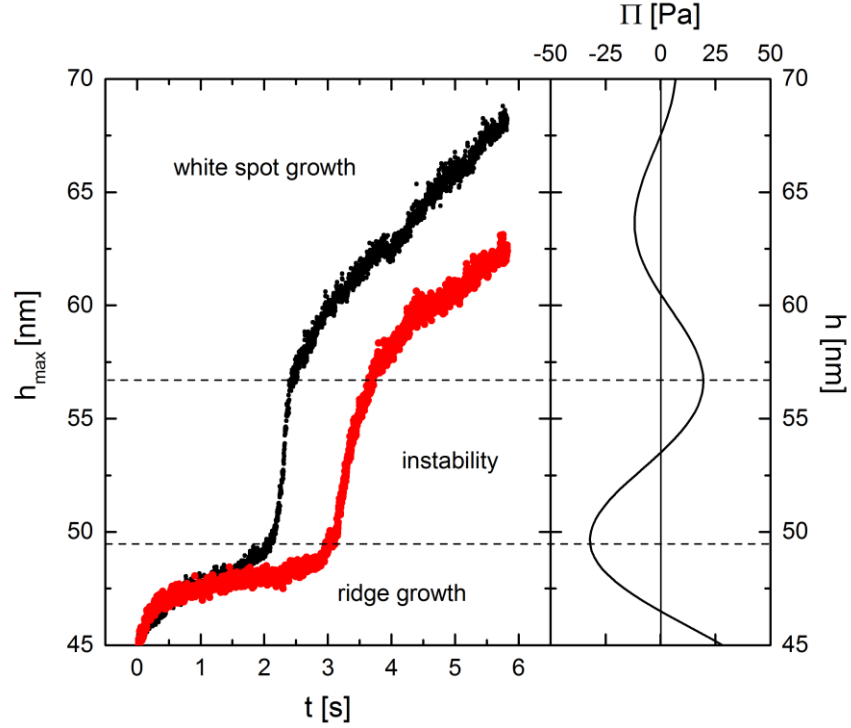


**Figure 4.10** Time dependence of maximum thickness in two white spots,  $h_{\max}$ . The evolution is corresponded to the disjoining pressure isotherm obtained by fitting equilibrium measurement (Figure 4.1(a)). The initial ridge goes through instability (indicated by rapid thickness increase) when its thickness enters the unstable region of the disjoining pressure isotherm.

#### 4.4.2 Evolution of the remaining ridge after instability

Both Figure 4.8 and Figure 4.9 illustrated that the ridge surrounding the expanding domain does not break down completely after topological instability has taken place. We here characterize the changes in shape and evolution of the remaining ridge, with the presence of much thicker white spots.

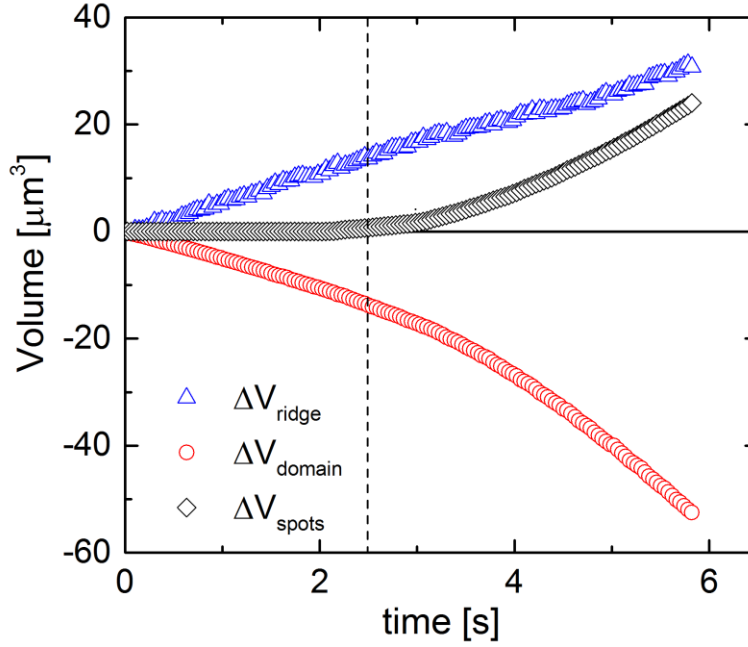


**Figure 4.11** Distribution of change in liquid volume in different part of the domain growth geometry. The dash line shows the time of topological instability and white spot formation.

Extending the integral approach discussed in 4.3.2 in context of axisymmetric ridge (shown in Figure 4.5), the distribution of liquid volume drained from the growing thinner domain is tracked by directly integrate the IDIOM thickness maps. Since the pixel resolution of the micrographs from our image system is  $0.5 \mu\text{m}/\text{pixel}$ , the liquid volume in one pixel area is given by  $0.25 \mu\text{m}^2 \times h$ . The pixel volumes then get summed up for different regions distinguished through thickness thresholding and image edge detection. The time dependence of liquid volume in each part is shown in Figure 4.11. Before the onset of visible topological instability (marked with the vertical dash line at  $t \approx 2.5 \text{ s}$ ), the plot is similar to Figure 4.5b, and the liquid drained out from an expanding domain all accumulates in the axisymmetric ridge. The white spots are absent and occupy zero volume. After the topological instability, the growth of the thinner domain (hence the volume drained from it) accelerates, and the volume in the white spots grows rapidly. However, the drained

liquid does not completely flow into the white spots: the volume of the ridge still increases. However the increase in volume is not due to the cross-sectional growth of the ridge, rather the expansion of the thinner domain ( $R \propto t$ ) increases the radius the ridge. In fact, the cross-sectional shape of ridge stops changing after the topological instability.

The ridge shape evolution before and after the topological instability is summarized in Figure 4.12, by characterizing the ridge region of  $-\pi < \theta < -2.8$  (marked in white dash line in Figure 4.9), which remains unperturbed by the formation of white spots. The growth kinetics of the thinner domain switches from  $R \propto t^{0.5}$  to  $R \propto t$  scaling (Figure 4.12a) with the topological instability, consistent with results in Section 3.3.3. After the instability, the ridge stops growing and its shape becomes unchanged over time, as show in Figure 4.12b by plotting the thickness profiles as  $h - h_\infty$  vs.  $r - R$ . Both the width (Figure 4.12c) and the maximum thickness (Figure 4.12d) of the ridge change their growth kinetics (*i.e.*  $W \propto t^{0.5}$ ,  $h_{\max} - h_\infty \propto \log t$ ) at the onset of the topological instability, and become constants afterwards. The experimental results in Figure 4.12c&d appear to fluctuate more than the results from the axisymmetric ridge (*e.g.* Figure 4.4), due to that only the small region ( $\sim 0.3$  rad) of thickness data is taken into analysis.

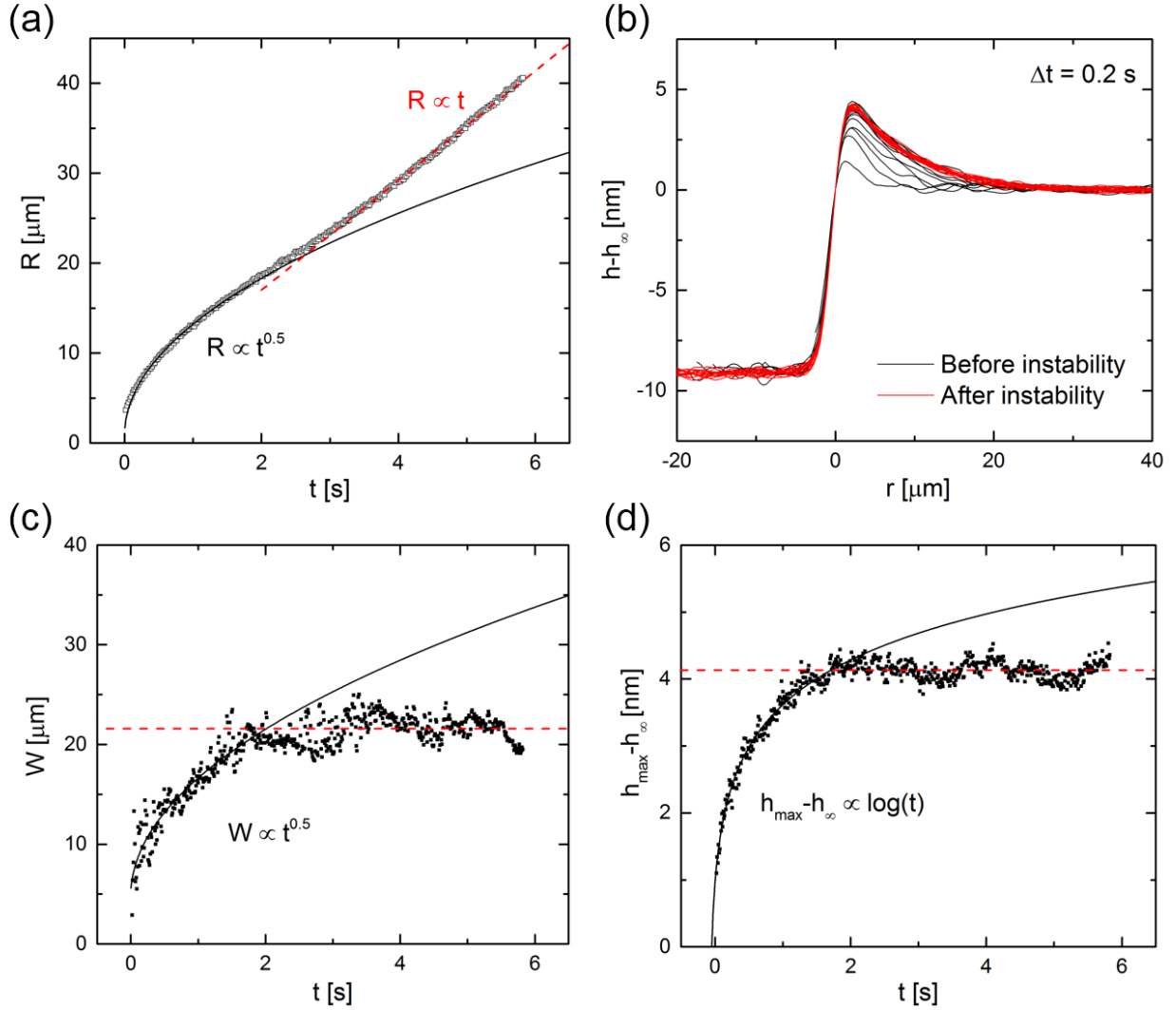


**Figure 4.12** Evolution of the remaining ridge after topological instability (Marked in white rectangle in Figure 4.9). (a) Domain radius *vs.* time, the scaling changes from  $R \propto t^{0.5}$  to  $R \propto t$  onset of instability. (b) the shifted thickness profiles of the ridge,  $h - h_{\infty}$  *vs.*  $r - R$ . The ridge shape stops growing after the instability. (c) Ridge width *vs.* time. It stops growing after instability. (d) Maximum thickness of the ridge *vs.* time. It also stops increasing after instability.

The Regime A domain growth kinetics ( $R \propto t^{0.5}$  for domain radius) is a result of the diffusion-like growth and expansion of the axisymmetric ridge, and when the kinetics transition to Regime B ( $R \propto t$  for domain radius), the ridge shape stops further growing and no longer controls

the dynamics of domain growth. These experimental observations are consistent with the discussion on domain growth kinetics in Section 3.4. Indeed, the majority of the drained liquid from the expanding thinner domain flows into the white spots, and their growth is influenced by oscillatory disjoining pressure isotherm. The ridge does not disappear after topological instability, nor does the thickness and width of the ridge show any detectable spatial or temporal undulation. These observations show that the white spot formation is not resulted from breakdown of the ridge through Rayleigh-type instability.

## 4.5 Conclusions

In this chapter, we experimentally visualize and characterize the ridge formed around a growing thinner domain during stratification of micellar foam film, using the IDIOM protocol. The nanometer sized ridge is detected and analyzed in detail for the first time, thanks to the high spatial and temporal resolution achieved through the imaging system and IDIOM protocol.

An axisymmetric ridge is formed during the domain growth initially. The cross-sectional shape of the ridge is found to be highly asymmetrical, with a sharp build-up from the thinner domain thickness to the maximum ridge thickness, and a slow decay from the maximum to the outside unperturbed film thickness. The width of the ridge has the same time dependence as the radius of the thinner domain, *i.e.*  $R, W \propto t^{0.5}$ , while the maximum thickness shows an apparent logarithmic growth. Through scaling analysis to lubrication-based thin film equation, two types of asymptotic behavior are recognized for different parts of the ridge profile. The build-up part of the ridge shape is time independent, with a constant contact angle between thinner domain and the

ridge directly measured to be  $\sim 0.2^\circ$ . The leeward part of the ridge shows self-similarity, and can be fitted by an approximated analytical asymptotic solution.

After the topological instability, white spots (much thicker circular regions) develop within the ridge area and change the domain growth kinetics to Regime B. The ridge, however, does not break down through the instability, instead its growth in width and thickness cease after instability. On the other hand, the formation of white spots is found unlikely to be through Rayleigh-type instability of the ridge, but rather driven by the non-monotonic shape of the supramolecular structural disjoining pressure. The oscillatory nature of the disjoining pressure leads to rapid thickness jump during white spot growth, the range of which correspond to the unstable region of the disjoining pressure isotherm.

The characterization of ridge formation and growth in foam film stratification, yields critical insights into the dynamics and stability of foam films, and the effect of supramolecular structural forces. Hydrodynamically, analogies are drawn to the ridge (rim) observed at liquid front of thin film dewetting from a solid substrate. However owing to the unique geometry and surface forces involved in stratifying foam films, it also provides new perspective to hydrodynamics of free surface flows, in particular, the contact line motion, the precursor film model, and the instabilities not only induced by capillarity, but also involves the surface forces or disjoining pressure.

## CHAPTER 5.

# MODELING OF THE RIDGE FORMATION AND GROWTH DURING DOMAIN GROWTH IN STRATIFYING FOAM FILMS

### 5.1 Introduction

Stratification of micellar foam films involves nucleation of thinner domains that grow at the expense of thicker surrounding film. The formation and growth of the ridge around the expanding thinner domain is characterized experimentally for the first time in this study, as described in the previous chapter. The ridge growth displays two regimes: formation and growth of axisymmetric ridge in Regime A, and topological instabilities and white spot (mesa) formation in Regime B. Before the topological instability sets in, the axisymmetric ridge displays the following features captured for the first time using IDIOM measurements: a highly asymmetric cross-sectional profile, small thickness ( $< 5$  nm maximum thickness difference from the unperturbed film), and time dependence of  $R, W \propto t^{0.5}$ ,  $h_{\max} - h_{\infty} \propto \log t$ . All of these features are distinct from the ridge shapes typically observed in thin films dewetting from solid substrates. Moreover, the ridge evolution can be described by a quasi-steady-state evolution in the build-up part, and a self-similar profile in the leeward part. The shape and dynamics of the ridge are modulated by the oscillatory nature of the underlying supramolecular structural disjoining pressure. In Section 4.3.3, we described a lubrication-based thin film hydrodynamics model, and shown that the asymptotic behavior of the ridge profile can be predicted by scaling analysis. In this chapter we carry out a detailed investigation of the thin film equation, including the influence of oscillatory supramolecular structural disjoining pressure, and numerically solve the equation for the domain growth process in and the associated axisymmetric ridge formation.



The driving pressure of the film thickness evolution is the combination of disjoining pressure and Laplace pressure induced by local curvature of the gas-liquid interfaces. While extensive research has been carried out on the role of disjoining pressure originated from van der Waals and electrostatic interactions in thin film flow and instabilities, the effect of structural oscillatory disjoining pressure on the hydrodynamics of stratifying foam films remains elusive, particularly for charged supramolecular structures (*e.g.* ionic micelles). In this chapter, we describe a comprehensive model for estimating the oscillatory disjoining pressure isotherm in thin films containing ionic micelles. This semi-empirical model provides an explicit formula for  $\Pi(h)$ , which is then included in the thin film hydrodynamic model.

The hydrodynamics of thin films depends greatly on the boundary conditions used for the two interfaces [84] (see Section 1.5.2). In the case of stratifying micellar foam films, the conventional wisdom has been to apply no-slip boundary condition on the gas-liquid interfaces, given that high surfactant population on the interfaces immobilizes them significantly [79,95,104]. No-slip condition is also used in deriving thin film hydrodynamic equations presented in the previous chapters, *e.g.* Equation (3.1) and Equation (4.4). In this chapter, we examine the proper boundary condition for the gas-liquid interfaces in stratifying foam films in detail. We compare the ridge shape formed during domain growth, with three different interface condition: no slip, no stress [130] and surfactant-laden [179]. We find the no-slip boundary condition to predict the identical ridge shape as the surfactant-laden model, demonstrating the validity the no-slip condition.

By combining the thin film hydrodynamic model and the disjoining pressure isotherm, we numerically resolve the dynamics of domain growth and ridge shape formed during film

stratification, and perform extensive comparisons between the numerical solution and experimental observations. We also validate the asymptotic solutions obtained by scaling analysis presented in Section 4.3.3 and 4.3.4, and discuss the concentration and thickness dependence of the ridge shape and the domain expansion. The model for axisymmetric ridge is also extended to study the topological instability and the formation of 1D “white spots” numerically. The experimentally observed the growth dynamics after instability of the ridge, white spots, and the domain, are captured by the 1D hydrodynamic model. We anticipate that the comprehensive theoretical framework that combines the thin film thermodynamics and the hydrodynamics will lead to deeper understanding of the rich and complex dynamics in stratifying foam films, and in thin film flows in general.

## 5.2 Model and numerical methods

### 5.2.1 Thin film equation

The thin film hydrodynamics equation is derived from Navier Stokes equation and continuity equation, using lubrication approximation. A detailed derivation is given in Section 1.5. In the case of the stratifying foam film, the thickness profile  $h(r, t)$  near an axisymmetric growing domain is given by:

$$\frac{\partial h}{\partial t} + \frac{1}{r} \frac{\partial}{\partial r} \left( r M(h) \frac{\partial P}{\partial r} \right) = 0 \quad (5.1)$$

This equation is a more general form of the thin film equation presented in Section 4.3.3 as Equation (4.4). Here  $M(h)$  is the mobility function that is related to the boundary conditions on the two gas-liquid interfaces. Various possible boundary conditions for the free surface and their

ramifications are reviewed in detail in Section 1.5.2. In the present case of thin ( $h < 100$  nm) foam films made with concentrated surfactant solution ( $> 5 \times \text{CMC}$ ), we mainly consider the assumption that the interfaces are immobile and apply no-slip boundary conditions, which leads to:

$$M(h) = \frac{h^3}{12\eta} \quad (5.2)$$

The immobile interface is a reasonable assumption for micellar solutions, given that the air-liquid interfaces are densely populated by surfactant monomers. Experimental and theoretical efforts were made to more accurately account for the stresses on the interfaces, by including surfactant adsorption/desorption and surface diffusion [148,179], surface viscoelasticity [180,233], and ion transfer in charged surfactant system [184,187]. The immobile surface assumption, however, has been widely accepted in modeling the foam films made with solution over CMC that exhibit stratification [77,79,104], and the assumption has shown reasonable agreement with drainage experimental results [186]. We here use the no-slip condition as the starting point, while for the sake of completeness, the effect of varying boundary conditions are discussed on the resulting model predictions of domain growth and ridge formation.

The driving force of the domain growth is the gradient of pressure  $\partial P / \partial r$ , which includes two contributions: the Laplace pressure varying with the local interface curvature, and disjoining pressure varying with local film thickness:

$$P = \sigma K + \Pi(h) \quad (5.3)$$

Where the curvature,  $K$ , is calculated with Equation 4.5. And the disjoining pressure isotherm is assumed to take a damped oscillation form:

$$\Pi(h) = \Pi_{os}(h) = A \exp \left[ d_0 - \frac{(h - h_0)}{\lambda} \right] \cos \left[ \frac{2\pi(h - h_0)}{\Delta h} \right] \quad (5.4)$$

The disjoining pressure in micellar foam films originates from contributions by various intermolecular and surface forces, including van der Waals attraction, electrostatic repulsion, supramolecular structural forces, steric repulsion, etc. [18,125]. Here in the model for stratifying foam films, the van der Waals attraction, electrostatic repulsion and steric repulsion between the two surfactant populated air-liquid interfaces are neglected, since these interactions are relatively short-ranged ( $< 20$  nm,  $< 10$  nm for steric). When one or more micelle layers are present in the foam film, the film thickness is usually larger, and the longer-ranged supramolecular structural force provide the dominant contribution to the disjoining pressure. Therefore in the following sections, the disjoining pressure only includes the supramolecular structural oscillatory disjoining pressure in the stratifying foam film. Experimentally, the domain growth process recorded and characterized are in thin films with at least two layers of micelle (so that  $h_\infty > 30$  nm), in order to make meaningful comparison with the model predictions.

The parameters in Equation (5.4) include the oscillation amplitude  $A$ , a pre-factor  $d_0$ , the exponential decay length  $\lambda$ , the final film thickness  $h_0$ , and oscillation period  $\Delta h$ . The estimation of these parameters and their dependence on surfactant concentration will be discussed in the next section.

The following dimensionless quantities are introduced to non-dimensionalize Equation (5.1):

$$\bar{h} = \frac{h - h_\infty}{\Delta h}, \quad \bar{r} = \frac{r}{L}, \quad \bar{t} = \frac{\sigma \varepsilon^3}{24\eta L} t, \quad \bar{\Pi} = \frac{\Pi}{\Pi_\infty} \quad (5.5)$$

Where the geometric aspect ratio here is given by  $\varepsilon = \Delta h/L$ . The dimensionless thickness is shifted so that the dimensionless unperturbed thickness becomes  $\bar{h}_\infty = 0$ . In Section 4.3.3, a slightly different non-dimensionlization scheme is used  $\bar{h} = h/\Delta h$  in Equation (4.6). This difference does not alter the dynamics but makes comparison among thicknesses and concentrations more convenient. In Section 4.3.3, the values for characteristic length scale in radial direction,  $L$ , were chosen differently for build-up and leeward part of the asymmetric cross-section of the ridge, in order to demonstrate the different asymptotic behavior. Here a single value of  $L$  ( $L = 1 \mu\text{m}$ ) is used to present the results of numerical solution.

Combining Equation (5.1) - (5.3) and (5.5) leads to the following dimensionless thin film hydrodynamic equation:

$$\frac{\partial \bar{h}}{\partial \bar{t}} + \frac{1}{\bar{r}} \frac{\partial}{\partial \bar{r}} \left[ \bar{M} \bar{r} \frac{\partial}{\partial \bar{r}} \left( \frac{1}{\bar{r}} \frac{\partial}{\partial \bar{r}} \left( \bar{r} \frac{\partial \bar{h}}{\partial \bar{r}} \right) \right) \right] + \Theta \left[ \frac{1}{\bar{r}} \frac{\partial}{\partial \bar{r}} \left( \bar{M} \bar{r} \frac{\partial \bar{\Pi}}{\partial \bar{r}} \right) \right] = 0 \quad (5.6)$$

where dimensionless mobility function  $\bar{M} = \left( \bar{h} + \frac{h_\infty}{\Delta h} \right)^3$  and dimensionless group  $\Theta = \frac{2L^2 \Pi_\infty}{\sigma \Delta h}$ .

### 5.2.2 Disjoining pressure isotherm

In the last few decades, many investigations have discovered oscillatory structural forces in various systems under confinement, including simple solvent, micelles, nanoparticles and polyelectrolytes [125]. The explicit  $\Pi_{os}(h)$  in micellar solutions of non-ionic surfactant,

developed based on hard sphere models [135,136], is successfully applied to experimental results in foam films [97] and in colloidal force measurement [139]. For electrically charged particles (e.g. SDS micelles), due to the inter- and intra-micellar electrostatic interactions, the oscillatory disjoining pressure isotherm  $\Pi_{os}(h)$  and its concentration dependence is only modeled via density functional theory calculations or Monte Carlo simulations [137,140]. An explicit theoretical expression of  $\Pi_{os}(h)$  in the form of Equation (5.4) is still not available in charged systems [142]. As a zeroth-order approximation, Nikolov et al. [56] proposed charged SDS micelles can be treated as hard spheres with an effective diameter:

$$d_{eff} = 2(r_c + \kappa^{-1}) \quad (5.7)$$

Where  $r_c$  is the core radius of the micelle, and  $\kappa^{-1}$  is the Debye length, which characterizes the size of the counter-ion atmosphere around the micelle. In the case of no additional electrolyte in the surfactant solution,  $\kappa$  can be calculated by:

$$\kappa^2 = 8\pi L_B \left[ CMC + \frac{\alpha}{2}(c_s - CMC) \right] \quad (5.8)$$

where  $c_s$  is the surfactant concentration,  $CMC$  is the critical micelle concentration,  $\alpha$  is the degree of micelle ionization, and  $L_B$  is the Bjerrum length and equals to 0.72 nm for water at the room temperature of 298 K.

The effective size of micelles,  $d_{eff}$ , are then used to compute the effective volume fraction of the micellar solution with:

$$\varphi_{eff} = \frac{\pi d_{eff}^3 (c_s - CMC) N_A}{6 N_{agg}} \quad (5.9)$$

where  $N_A$  is Avogadro constant, and the  $N_{agg}$  is the aggregation number of the surfactant micelles. For SDS micelles,  $N_{agg}$  is well-known to increase with increasing surfactant concentration, mainly due to the change in solution ionic strength. Quina et al. [234] found an empirical power law relation between  $N_{agg}$  and the total counterion concentration given by:

$$N_{agg} = 164 \left[ \alpha c_s + (1 - \alpha) CMC \right]^{\frac{1}{4}} \quad (5.10)$$

This prediction showed good agreement with experimental measurements using a variety of techniques over a wide range of concentration [234]. It is used here to estimate aggregation number based on surfactant concentration.

By treating SDS micelles as hard spheres with effective diameter  $d_{eff}$  and volume fraction  $\varphi_{eff}$ , we attempt to use the semi-empirical model developed by Kralchevsky et al. [135] to compute to required parameters in Equation (5.4):

$$\frac{\Delta h}{d_{eff}} = \sqrt{\frac{2}{3}} + 0.237 \Delta \varphi_{eff} + 0.633 (\Delta \varphi_{eff})^2 \quad (5.11)$$

$$\frac{\lambda}{d_{eff}} = \frac{0.487}{\Delta \varphi_{eff}} - 0.420 \quad (5.12)$$

$$d_0 = \frac{d_{eff}^3}{\Delta h^2 \lambda} \quad (5.13)$$

$$A = \Pi_{osmotic} = \rho kT \frac{1 + \varphi_{eff} + \varphi_{eff}^2 - \varphi_{eff}^3}{(1 - \varphi_{eff})^3} \quad (5.14)$$

Where  $\Delta\varphi_{eff} = 0.741 - \varphi_{eff}$  and  $\rho = \frac{(c_s - CMC)N_A}{N_{agg}}$  is the number density of micelles. The dimensionless decay length,  $\bar{\lambda} = \lambda/\Delta h$ , is therefore obtained by taking ratio of Equation (5.12) and (5.11):

$$\bar{\lambda} = \frac{\lambda}{\Delta h} = \frac{0.487/\Delta\varphi_{eff} - 0.420}{\sqrt{2/3} + 0.237\Delta\varphi_{eff} + 0.633(\Delta\varphi_{eff})^2} \quad (5.15)$$

It is well-documented, however, that Equation (5.11) significantly under-predicts the oscillation period  $\Delta h$  measured experimentally. Instead,  $\Delta h$  is found to be very close to the mean distance between the micelles in the bulk solution [99,128]:

$$\Delta h \approx \left( \frac{c_s - CMC}{N_{agg}} \right)^{-1/3} \quad (5.16)$$

In Figure 5.1, the prediction from Equation (5.16) (black solid line) are shown to agree, better than that from Equation (5.11) (blue dash line), with the measured  $\Delta h$  from foam film stratification experiments using IDIOM protocols. We therefore modify the Kralchevsky et al. [135] model by replacing Equation (5.11) with Equation (5.16).



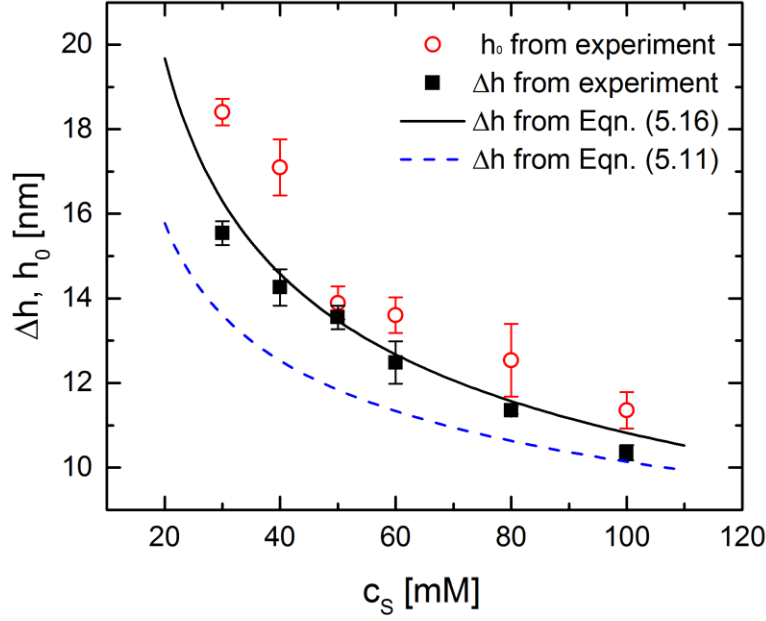


**Figure 5.1** Comparison between IDIOM measured  $\Delta h$  and  $h_0$  with predictions from Equation (5.11) and Equation (5.16), as a function of surfactant concentration. The values of  $\Delta h$  and  $h_0$  are similar and agree more with Equation (5.16).

The final film thickness  $h_0$  denotes the thickness at which micelles are depleted from the thin film, and the structural disjoining pressure equals the osmotic pressure of the micelles, *i.e.*  $\Pi_{os}(h_0) = \Pi_{osmotic} = A \cdot h_0$  in a real foam film is controlled by the DLVO interactions between the two surfactant monolayers on the gas-liquid interfaces. In the presented model, we assume that

$$h_0 \approx \Delta h \quad (5.17)$$

As shown in Figure 5.1, the simple estimation in Equation (5.17) is supported by the experimental measurements by IDIOM, which generally show values  $h_0 \approx \Delta h \pm 3 \text{ nm}$ . More detailed, DLVO theory based models (*e.g.* ref [128]) are developed to predict the value of  $h_0$ , however more assumptions and parameters are needed to account for effects of charge distribution, surface

potential, thickness dependent Hamakar constant, etc. Our further examination shows that the numerically solved dynamics of domain growth and ridge formation are not greatly affected by changing the exact value of  $h_0$  by a few nanometers, therefore Equation (5.17) is considered a sufficient estimation.

The set of nine equations presented above (Equation (5.7)-(5.10) & (5.13)-(5.17)) provides an estimation of all the parameters in the oscillatory disjoining pressure isotherm (Equation (5.4)), with only one input variable being the concentration of surfactant solution.

### 5.2.3 Model setup for domain growth dynamics

We apply the disjoining pressure isotherm  $\Pi(h)$  estimated above to the thin film hydrodynamic equation (Equation (5.6)) for studying domain growth dynamics and ridge formation during thin film stratification. We numerically solve the equation for a single thinner domain growing on the thicker film with thickness:

$$h_{\infty} = h_0 + n\Delta h = (n+1)\Delta h \quad (5.18)$$

Where  $n$  denotes the number of micelle layers contained in the unperturbed thicker film. Domain nucleation and growth is considered to take place when the thickness of the film is at a local maxima of the disjoining pressure isotherm. Further thinning of the film results in unstable thickness where  $d\Pi/dh > 0$ , and a thickness jump through domain formation and growth is induced (as shown in previously in Figure 2.8 and here in Figure 5.2).

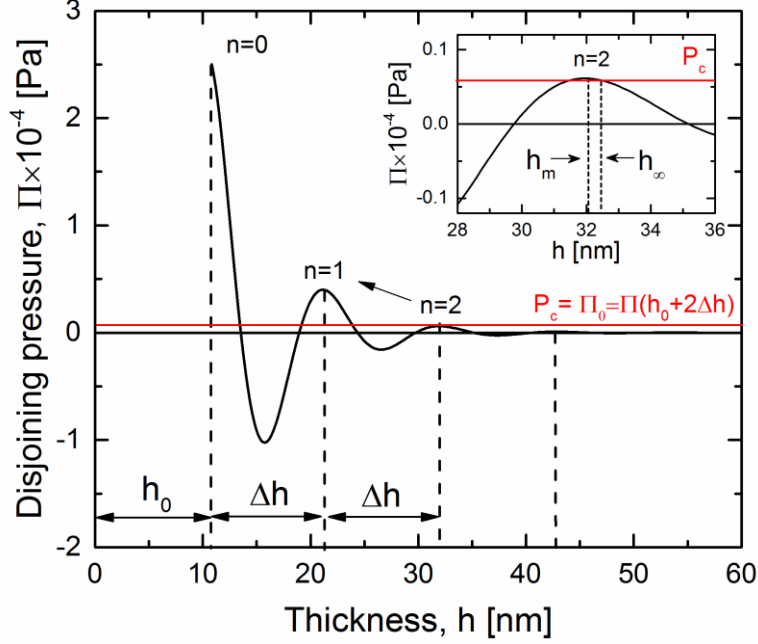


**Figure 5.2** Illustration of the starting film thickness for domain growth study. The thickness transition from  $n = 2$  to  $n = 1$  is induced with the starting film thickness of  $h_\infty = h_0 + 2\Delta h$ , where is the disjoining pressure  $\Pi_\infty$  is balanced by applied pressure  $P_c$ . The inset shows the region around  $h = h_\infty$ . The local disjoining pressure maxima is reached at  $h_m$ , however the difference between  $h_\infty$  and  $h_m$  is negligible.

Strictly speaking, the local maxima in oscillatory disjoining pressure is not yet reached at thickness  $h_\infty$  calculated by Equation (5.18). The thickness  $h_m$ , for which the disjoining pressure maxima is reached can be calculated analytically by

$$h_m = (n+1)\Delta h - \frac{\Delta h}{\pi} \tan^{-1} \left( \frac{\sqrt{4\pi^2\lambda^2 + \Delta h^2} - 2\pi\lambda}{\Delta h} \right) \quad (5.19)$$

In the range of parameters relevant to the domain expansion dynamics (*i.e.*  $\Delta h \sim O(\lambda)$ ), the difference between  $h_\infty$  and  $h_m$  is usually small  $h_\infty - h_m < 0.05\Delta h$ , as shown in the inset of

Figure 5.2. Experimentally, it is found that domain growth could indeed occur before  $h_m$  is reached, due to inevitable thickness and pressure perturbations from the environment (air flow, vibrations or fluid evaporation). Therefore the use of the significantly simplified Equation (5.18) appears reasonable to calculate the starting film thickness for domain nucleation and growth.

By applying Equation (5.18), we obtain the explicit expressions for the dimensionless disjoining pressure for using in Equation (5.6) :

$$\bar{\Pi}(\bar{h}) = \exp\left(-\frac{\bar{h}}{\lambda}\right) \cos(2\pi\bar{h}) \quad (5.20)$$

Also in Equation (5.6), the dimensionless group  $\Theta$  is given by:

$$\Theta = \frac{2L^2\Pi_\infty}{\sigma\Delta h} = \frac{2L^2A}{\sigma\Delta h} \exp\left(d_0 - \frac{n}{\lambda}\right) \quad (5.21)$$

And the expression of dimensionless mobility function with no-slip boundary condition:

$$\bar{M}(\bar{h}) = (\bar{h} + n + 1)^3 \quad (5.22)$$

Equation (5.6) can now be solved for the thickness profile during domain formation and expansion,  $\bar{h}(\bar{r}, \bar{t})$ , with only two input variables: concentration of the surfactant solution  $c_s$ , and the number of micelle layers in the starting film,  $n$ . All the other constant parameters used in both the hydrodynamic model and the disjoining pressure isotherm estimation are listed in Table VI.

**Table VI** Parameters used in the hydrodynamic equation and disjoining pressure estimation

Parameter	Value	Source
Viscosity, $\eta$	1 mP·s	Assumed water viscosity
Surface tension, $\sigma$	35 mN/m	Measured by pedant drop tensiometry
r-direction length scale, $L$	1 $\mu\text{m}$	Appropriate length scale obtained from experimentally resolved ridge profile
Critical micelle concentration, $CMC$	8.5 mM	Measured by pedant drop tensiometry
Degree of SDS micelle ionization, $\alpha$	0.27	Ref [235,236]
Micelle radius, $r_c$	2.1 nm	Ref [237–239]

#### 5.2.4 Numerical solving scheme

The dimensionless thin film hydrodynamic equation (Equation (5.6)) is numerically solved for a single domain nucleating at  $r = 0$  and growing unboundedly. The boundary conditions include symmetry at the film center,  $d\bar{h}/d\bar{r} = 0$  at  $\bar{r} = 0$ , and a flat unperturbed film far away from the domain,  $\bar{h} = d\bar{h}/d\bar{r} = d^2\bar{h}/d\bar{r}^2 = 0$  at  $\bar{r} \rightarrow \infty$ . The initial condition is a sinusoidal disturbance applied from  $\bar{r} = 0$  to a maximum of  $\bar{r} = 5$  with a small amplitude less than 0.15. Different initial conditions are examined to show little effect on the ridge once the flat growing domain is established. Here we focus primarily on the formation and evolution of the ridge surrounding an established thinner domain, as it appears to control the domain expansion dynamics as well as the overall stratification dynamics.

The dimensionless thin film hydrodynamics equation (Equation (5.6)), with the appropriate dimensionless disjoining pressure isotherm given by Equation (5.20), is solved using a central finite difference scheme for spatial discretization, and Crank-Nicholson for time stepping. The resulting sets of non-linear equations are solved with Newton's method in MATLAB R2014a by utilizing the *fsolve* solver. The Jacobian sparsity pattern is defined explicitly for faster convergence. The spatial grid is continuously added at large  $\bar{r}$  to maintain the flat unperturbed film boundary condition far away from the rim. Since the ridge shape is found to be significantly asymmetrical, the spatial grid density is adjusted according to the slope of the thickness profile,  $d\bar{h}/d\bar{r}$ . This scheme generates finer grid at the sharp, steep build-up part of the ridge, while coarser grid is adequate for the slower decay of the leeward part of the ridge. Some numerical results are reproduced with uniform grid with the highest density,  $\Delta\bar{r}=0.05$ , to ensure the adjustment scheme does not alter the solutions. Since the expansion of the thinner domain slows down over time ( $R \propto t^{1/2}$  in Regime A), the time step  $\Delta\bar{t}$  is also adjusted in the solving scheme, by thresholding an estimated maximum error of the thickness [240]:

$$E^k = \max \left( \frac{2\Delta\bar{t}_k}{\Delta\bar{t}_{k-1}} \frac{\Delta\bar{t}_{k-1}\bar{h}_{k+1} + \Delta\bar{t}_k\bar{h}_{k-1} - (\Delta\bar{t}_{k-1} + \Delta\bar{t}_k)\bar{h}_k}{(\Delta\bar{t}_{k-1} + \Delta\bar{t}_k)\bar{h}_k} \right) \quad (5.23)$$

$E$  is given a tolerance range ( $10^{-3}$  to  $10^{-4}$ ). If  $E$  is found less than the lower bound, the time step  $\Delta\bar{t}$  is doubled; conversely if  $E$  is larger than the upper bound,  $\Delta\bar{t}$  is halved. In a typical run, the initial time step is chosen to be extremely small at  $\Delta\bar{t}=10^{-9}$  (dimensionally corresponds to several nanosecond), and it quickly raises to  $\Delta\bar{t} \sim 10^{-2}$  after the initial domain nucleation.

## 5.3 Results and discussion

### 5.3.1 Ridge shape and evolution compared with experimental results

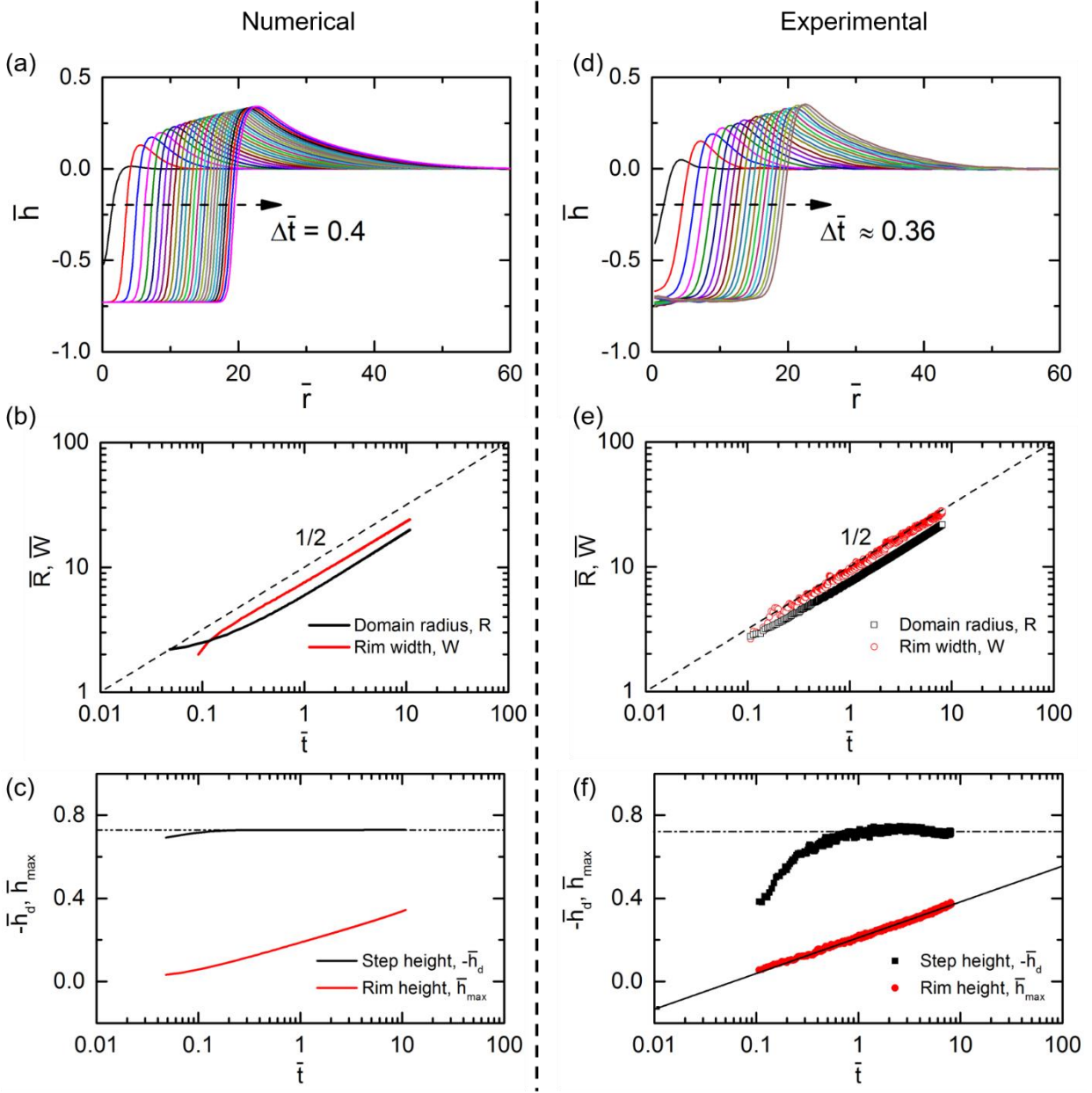


**Figure 5.3** Comparison between experimental and numerical ridge profiles and evolution. (a)-(c) Numerically resolved ridge shape and evolution, with  $c_s = 50$  mM,  $n = 2$ , (b)-(f) Experimentally resolved ridge shape and evolution, obtained by non-dimensionalization of results presented in Figure 4.3 and Figure 4.4.

Figure 5.3 shows the domain and ridge formation obtained experimentally and numerically for  $c_s = 50 \text{ mM}$  and  $n = 2$ . The numerically resolved film thickness evolution (Figure 5.3a) shows that, after the initial perturbation, the thickness quickly decreases until a stable flat thinner domain is formed. Adjacent to the growing domain, a ridge is formed and it grows both in height and width over time. The numerical resolved ridges are consistent with the experimental ridge profiles (shown in Figure 5.3d), non-dimensionalized from results presented in Section 4.3.2.

The dimensionless radius of thinner domain,  $\bar{R} = R/L$ , and the width of the ridge,  $\bar{W} = W/L$ , are found to both grow over time with scaling  $\bar{R}, \bar{W} \propto \bar{t}^{0.5}$  at approximately  $\bar{t} > 0.1$ , which agree very well with the experimental results (Figure 5.3b&e). The early time deviations from the  $1/2$  scaling is attributed to the time taken to establish the flat thinner domain and the ridge from the initial perturbation. The dimensionless thinner domain thickness,  $-\bar{h}_d = (h_\infty - h_d)/\Delta h$ , and the maximum ridge thickness,  $\bar{h}_{\max} = (h_{\max} - h_\infty)/\Delta h$ , are plotted against dimensionless time,  $\bar{t}$ , in Figure 5.3c&f. The numerical result (Figure 5.3c) shows that the flat domain with constant thickness is established after  $\bar{t} \sim 0.1$ . The early time deviation corresponds well with that found in Figure 5.3b. On the other hand, Figure 5.3f shows that it takes longer for  $-\bar{h}_d$  to reach a constant value in the experiment, which is likely due to the fact that the IDIOM thickness mapping of a small domain ( $\sim 10$  pixels in the micrograph) at small time scale ( $t < 0.01 \text{ s}$ ) is less accurate. The maximum thickness of the ridge  $\bar{h}_{\max}$  are better resolved, and both experimental and numerical results show an apparent logarithmic time dependence, *i.e.*  $\bar{h}_{\max} \propto \log \bar{t}$ .

The comparison between experimental and model results is presented in Figure 5.4, for the detailed thickness profiles of the ridge at the same thinner domain radius of  $\bar{R} = 20$ . The profiles



match very well, especially for the leeward part of the ridge (after  $\bar{r} - \bar{R} > 10$ ). The slight deviation in the build-up part of the ridge is probably due to experimental resolution limits, given that the thickness varies rapidly (more than 15 nm over  $\sim 10$  pixel length) from the thinner domain to the apex of ridge in this region. The overall quantitative agreement of the model thickness profiles with experiments shows the applicability of the thin film hydrodynamic model and the validity of the approximate form of the disjoining pressure.

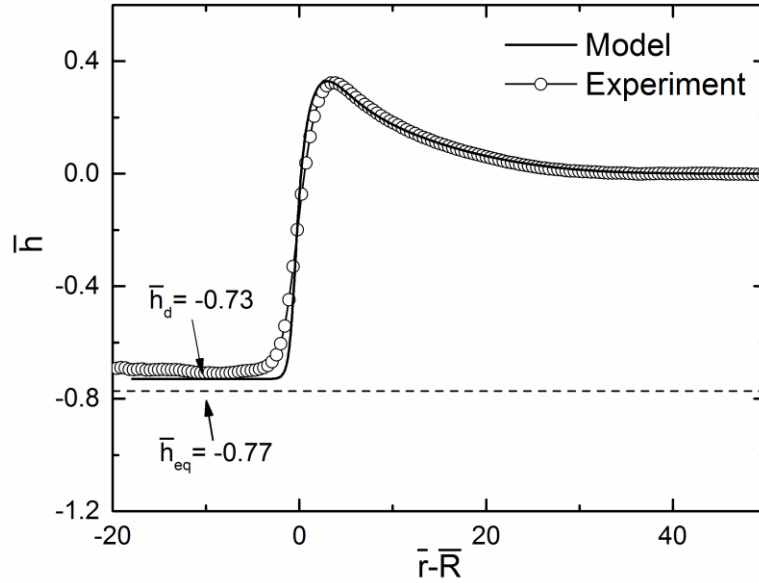


**Figure 5.4** Comparison of ridge shape (at  $\bar{R} = 20$ ) obtained from experiment and numerical solution. The dash line shows the thickness of the thinner domain that would be in mechanical equilibrium with the applied capillary pressure.

It is worth noting that both the model and the experiment show that thickness of the established flat thinner domain is  $\bar{h}_d \approx -0.73$ . This thickness is larger than the equilibrium film thickness  $\bar{h}_{eq} \approx -0.77$  (shown as dash line in Figure 5.4), which satisfies  $\bar{\Pi}(\bar{h}_{eq}) = \bar{\Pi}(0)$ . In

dimensional terms,  $h_{eq}$  satisfies  $\Pi(h_{eq}) = \Pi(h_{\infty}) = P_c$ , so that the applied capillary pressure  $P_c$  is balanced by the disjoining pressure at this thickness. In a growing domain, however, the domain thickness,  $\bar{h}_d$ , despite being constant throughout the domain expansion, is not at equilibrium ( $\Pi(h_d) < \Pi(h_{\infty})$ ). This pressure difference between inside domain and outside thicker film is necessary to drive the outward flow that leads to domain expansion and ridge formation. In reality, the domain does not keep growing unboundedly. Once the whole film area is occupied by the thinner film, its thickness then further decreases to equilibrate with the outside capillary pressure. These findings suggest that caution should be taken, when using the step size between two consecutive layers  $h_{\infty} - h_d$  to estimate the period of oscillatory disjoining pressure,  $\Delta h$ . This method is a common practice seen in the literature [55,69,81,128], but it has to be ensured that, not only  $P_c$  used is sufficiently small compare to the local disjoining pressure maxima, so that  $h_{\infty} - h_{eq} \approx \Delta h$ , but also sufficient time is given to ensure equilibrium ( $h = h_{eq}$ ) is truly reached before the thickness measurement. The  $\Delta h$  determination reported in our studies followed such protocol [31,81].

### 5.3.2 Discussion on boundary conditions

The thickness profiles shown in Figure 5.4a is obtained by solving Equation (5.6) with the no-slip boundary conditions in the two gas-liquid interfaces, which results in the mobility function given in Equation (5.2), the dimensionless version of which being:

$$\bar{M} = \frac{12\eta M}{\Delta h} = \left( \bar{h} + \frac{h_{\infty}}{\Delta h} \right)^3 \cong \left( \bar{h} + n + 1 \right)^3 \quad (5.24)$$

As reviewed in Section 1.5.2, the no-slip condition is appropriate for in high concentration and/or large molecule surfactant solution, as the gas-liquid interfaces are significantly immobilized by adsorbed surfactants [95]. However it is possible to construct models in which surface mobility is introduced by considering the surfactant adsorption and diffusion dynamics, as well as surface rheology. Many thin film drainage models have been developed to account for the slippage or mobility of the interfaces, as summarized in Table II. Here we consider two representative models to study the effect of interfacial mobility on domain growth and ridge formation.

The first model is the model by Radoëv, Dimitrov and Ivanov [179] (refer to as RDI model thereafter) for drainage of thin film made from surfactant solution. The drainage flows in the thin film lead to spatial variation in surfactant concentration on the interfaces, therefore induce Marangoni stresses. The stresses are considered to be modulated by diffusion-limited surfactant transportation between the bulk and the interfaces, and the 2D diffusion of surfactant within the interfaces. By coupling the thin film equation with mass balances of the surfactant, a mobility factor is obtained, comparing drainage velocity result from RDI model with the no-slip Reynolds' velocity. To the zeroth order approximation, this mobility factor is applicable to our study of thickness profile during domain expansion, by modifying the mobility function in Equation (5.2) to:

$$M(h)_{RDI} = f \frac{h^3}{12\eta} = \left( 1 + \frac{3\eta D}{E_0 \alpha_0} + \frac{6\eta D_s}{h E_0} \right) \frac{h^3}{12\eta} \quad (5.25)$$

where  $D$  and  $D_s$  are the bulk and surface diffusivity of the surfactant, respectively,  $\alpha_0 = (\partial\Gamma/\partial c)_0$  is the adsorption length,  $E_0 = -(\partial\sigma/\partial \ln \Gamma)_0$  is the Gibbs elasticity. The dimensionless mobility function is therefore:

$$\overline{M}(\bar{h})_{RDI} = (1 + N_D)(\bar{h} + n + 1)^3 + N_{DS}(\bar{h} + n + 1)^2 \quad (5.26)$$

where  $N_D = 3\eta D / E_0 \alpha_0$  accounts for the surfactant adsorption from the bulk, and  $N_{DS} = 6\eta D_s / \Delta h E_0$  accounts for the surface diffusion. The values of the parameters used for calculating the dimensionless numbers are difficult to obtain through experimental measurements (*e.g.* tensiometry, interfacial rheometry, etc.), especially for surfactant solutions with high concentrations over CMC. Here we use values reported by Karakashev et al. [184] for SDS solutions below CMC, as order of magnitude estimations. The values are:  $D = 6 \times 10^{-10} \text{ m}^2/\text{s}$ ,  $D_s = 9 \times 10^{-10} \text{ m}^2/\text{s}$ ,  $\alpha_0 = 2 \times 10^{-7} \text{ m}$  and  $E_0 = 3 \text{ mN/m}$ . The resulting estimation for the two dimensionless number are  $N_D = 3 \times 10^{-3} \ll 1$  and  $N_{DS} = 0.1$ , so the contribution from surfactant adsorption is negligible.

As briefly illustrated in Section 1.5.2, when only the surface diffusion term is retained, the RDI model becomes equivalent to a Navier slippage model, with the slip length  $\Delta h N_{DS} \approx 1 \text{ nm}$ . Compared to the film thickness of  $h \sim 10 \text{ nm}$ , the slip length is very small. It therefore confirms that the no-slip boundary condition is a valid approximation.

While the RDI model results in a small deviation from the completely immobile surfaces, we choose the second model to demonstrate the changes in domain expansion and ridge shape at the opposite extreme, *i.e.* with completely mobile surfaces. The model is developed by Erneux and Davis [130] (referred to as the ED model thereafter), and as discussed in Section 1.5.2, consists two coupled equations, Equation (1.18) and Equation (1.19). The model is adapted to include the oscillatory disjoining pressure present in the stratifying foam film. The dimensionless form of the equations in polar coordinates is obtained with dimensionless quantities defined in Equation (5.5):

$$\frac{\partial \bar{h}}{\partial \bar{t}} = -\frac{1}{\bar{r}} \frac{\partial}{\partial \bar{r}} \left[ \bar{r} (\bar{h} + n + 1) \bar{U}_s \right]$$

$$\frac{2}{Oh_\varepsilon^2} \left( \frac{\partial \bar{U}_s}{\partial \bar{t}} + \bar{U}_s \frac{\partial \bar{U}_s}{\partial \bar{r}} \right) = \frac{\varepsilon^2}{3} \left\{ \frac{1}{\bar{r} (\bar{h} + n + 1)} \frac{\partial}{\partial \bar{r}} \left[ \bar{r} (\bar{h} + n + 1) \left( \frac{\partial \bar{U}_s}{\partial \bar{r}} + \frac{\bar{U}_s}{2\bar{r}} \right) \right] \right\} + \Theta \frac{\partial \bar{\Pi}}{\partial \bar{r}} + \frac{\partial}{\partial \bar{r}} \left[ \frac{1}{\bar{r}} \frac{\partial}{\partial \bar{r}} \left( \bar{r} \frac{\partial \bar{h}}{\partial \bar{r}} \right) \right] \quad (5.27)$$

where the dimensionless surface velocity is defined as  $\bar{U}_s = \frac{U_s \tau}{L} = \frac{24\eta}{\sigma \varepsilon^3} U_s$ , where  $\tau$  is the

previously defined time scale.  $Oh_\varepsilon = \frac{24}{\varepsilon^2} \frac{\eta}{\sqrt{\rho \sigma \Delta h}}$  is the scaled Ohnesorge number,  $\varepsilon = \Delta h / L$  and

$\Theta = \frac{2L^2 \Pi_\infty}{\sigma \Delta h}$  are the same as before. Equation (5.27) is solved for both  $\bar{h}(\bar{r}, \bar{t})$  and  $\bar{U}_s(\bar{r}, \bar{t})$

simultaneously, using the same disjoining pressure isotherm and similar numerical solving scheme.

Figure 5.5 shows the comparison of the ridge shapes obtained from both RDI and ED models, as well as the results shown in Figure 5.4 from no-slip model and experiments. The ridge shapes plotted are from the same thinner domain radius of  $\bar{R} = 20$ . As expected, the predicted shape from RDI model is much closer to the no-slip model than that from the completely mobile surface (ED) model. In fact, given the small values of  $N_D$  and  $N_{DS}$ , the resulting ridge shape is indistinguishable from the no-slip model result. On opposite extreme, the ED model predicts a ridge with much smaller thickness and larger width, drastically different from the experimentally resolved ridge shape.

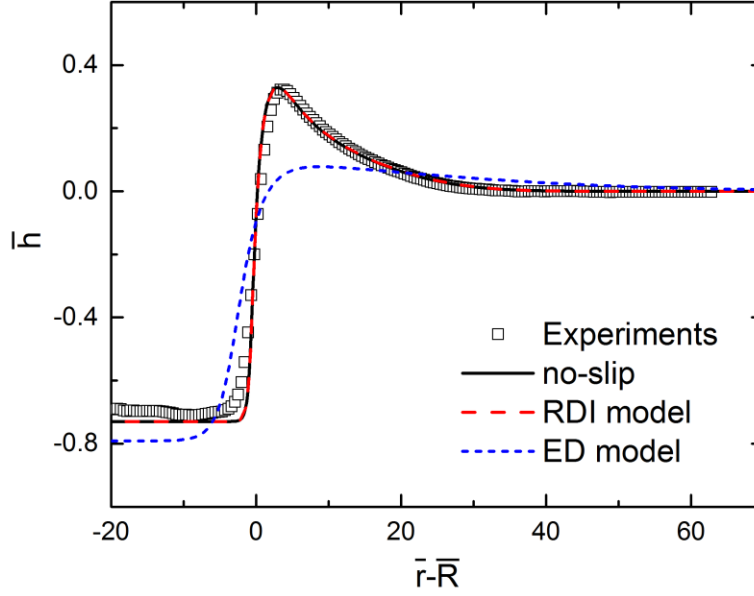


**Figure 5.5** Comparison of ridge shapes solved from different models for boundary condition on gas-liquid interfaces. Both no-slip and surfactant adsorption included RDI model (Equation (5.26)) agree with experimental results and are identical with each other, while the completely mobile surface ED model (Equation (5.27)) shows significant deviation.

Figure 5.5 indicates that the gas-liquid interfaces of the micellar stratifying foam films are at least closer to being completely immobile than being mobile. Detailed models accounting for the surface mobility can be applied, but their effects on the ridge shape are not significant. The simple no-slip boundary condition is found to be sufficient to predict the experimental resolved ridge shapes, therefore it is used throughout our further exploration of dynamics of domain expansion and ridge evolution.

### 5.3.3 Force contributions and validation of asymptotic solutions

The asymmetrical nature of the ridge cross-sectional profile, as discussed in Section 4.3.4, led us to choose two different characteristic length scale,  $L$ , in  $r$ -direction for different parts of the

ridge. Apart from the separation of length scales, the build-up and leeward part of the ridge show different shape evolutions which are captured by distinct asymptotic behaviors. In the build-up part of the ridge, the shape is at quasi-steady state, resulting from the balance of gradient of the local Laplace pressure and the thickness dependence disjoining pressure. In the leeward part of the ridge, the Laplace pressure contribution is negligible compared to the disjoining pressure contribution. The ridge shape is self-similar and follows  $h(r,t) = f(r/t^{1/2})$  in this part. These predictions are consistent with experimental observed ridge profiles (see Figure 4.6 and Figure 4.7).

In the framework of Equation (5.6), we define that the time dependent term as Term I, the Laplace pressure term as Term II, and the disjoining pressure term as Term III. The magnitude of each of the three terms is determined as a function of  $\bar{r}$  and  $\bar{t}$ , during the numerical time stepping. Therefore the results from dimensional analysis can be validated by directly comparing the contributions of the three terms. In Figure 5.6, the absolute values of the three terms are plotted with the corresponding ridge thickness profile at  $\bar{R} = 20$ . In good agreement with the dimension analysis predictions, two asymptotic regions are identified (marked in different colors). In the build-up part of the ridge, Term I remains about two orders of magnitude smaller than Term II and III, while after the maximum thickness of the ridge is reached, Term II quickly drops off and Term I and III are almost identical in magnitude in the leeward part of the ridge. The numerical calculations of the three terms therefore explicitly verify the predictions from scaling analysis.

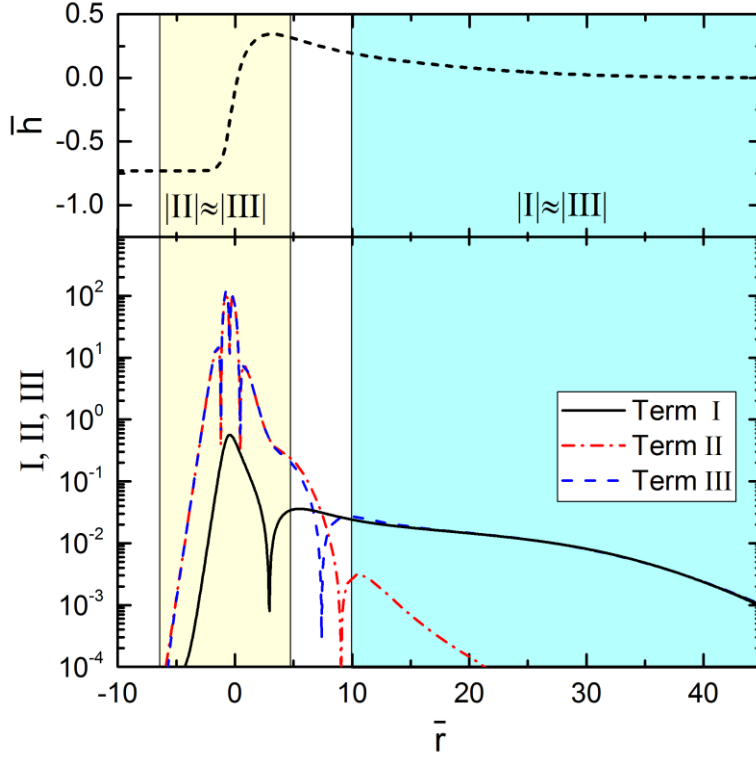


**Figure 5.6** Comparison of the magnitude of three terms in Equation (5.6). The thickness profile (top) and the corresponding absolute value of the three terms (bottom) are obtained with  $c_s = 50 \text{ mM}$ ,  $n = 2$ , at the time point when  $\bar{R} = 20$ . The two regions of asymptotes are marked in different colors.

The asymptotic solutions of the thickness profiles in the two regimes are extracted from the corresponding balances. In the build-up part of the ridge, neglecting Term I and integrating the remaining twice with the flat thinner domain boundary condition, *i.e.*  $\bar{h}' = \bar{h}'' = 0$  at  $\bar{h} = \bar{h}_d = -0.73$ , leads to:

$$\frac{\partial^2 \bar{h}}{\partial x^2} = \Theta(\bar{\Pi}_d - \bar{\Pi}(\bar{h})) \quad (5.28)$$



Where  $\bar{\Pi}_d = \bar{\Pi}(\bar{h} = \bar{h}_d)$ . Here we linearized the local curvature and substituted  $\bar{r}$  with  $\bar{x}$ , given

that  $\frac{\partial^2 \bar{h}}{\partial \bar{r}^2} \gg \frac{1}{\bar{r}} \frac{\partial \bar{h}}{\partial \bar{r}}$ . Equation (5.28) is a dimensionless version of Equation (4.10), and it is similar

to a dimensionless augmented Young-Laplace equation, with small slope approximation. In presence of a non-monotonic disjoining pressure isotherm, thin film with non-uniform thickness could satisfy Equation (5.28). The possibilities of non-flat, yet at equilibrium thin films have been explored theoretically [145,221], particularly for films supported by solid substrate. However, experimental evidence is still lacking for formation of non-flat structures with such film [221]. The ridge shape in free-standing stratifying films modulated by oscillatory disjoining pressure, in particular the time-independent shape in the build-up part, can provide valuable insights to the augmented Young-Laplace equation.

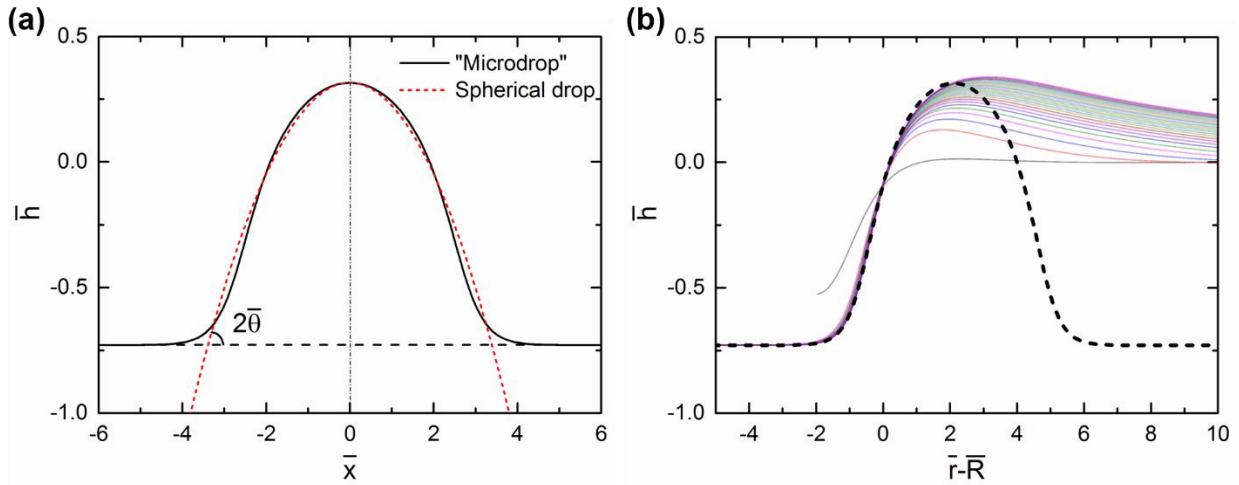


**Figure 5.7** Asymptotic solution of the shape of the build-up part of the ridge. (a) The “microdrop” geometry obtained by solving the augmented Young-Laplace equation (Equation (5.28))

One of the possible solution of the thickness profile is a “microdrop” (Figure 5.7a) geometry [221], obtained by numerically solving Equation (5.28) with the boundary conditions  $\bar{h}(x \rightarrow \pm\infty) = \bar{h}_d$  and  $\bar{h}(x=0) = \bar{h}_{apex}$ , where  $\bar{h}_{apex}$  is the apex thickness of the drop and given by:

$$\bar{\Pi}_d (\bar{h}_{apex} - \bar{h}_d) - \int_{\bar{h}_d}^{\bar{h}_{apex}} \bar{\Pi} dh' = 0 \quad (5.29)$$

Figure 5.7b shows the comparison between the laterally-shifted ridge profiles from numerical solution for  $c_s = 50$  mM and  $n = 2$ . The build-up part of the ridge shape is time-independent, consistent with the experimental observation (Figure 4.6) and the prediction from scaling analysis. It also matches with the equilibrium shape of the “microdrop” very well, showing the validity of the asymptotic solution given by Equation (5.28).

Although the “true contact angle” between the “microdrop” (or equivalently, the build-up part of the ridge) and the flat thin film (or the thinner domain) should be zero, since  $\partial\bar{h}/\partial x = 0$  at  $\bar{h} = \bar{h}_d$ , a “macroscopic contact angle”,  $\bar{\theta}$ , can still be defined by following the definition of the contact angle of macroscopic liquid drops on the solid surface: excluding disjoining pressure effect and assuming a spherical drop shape. This “spherical drop” thickness profile is then solved by setting  $\bar{\Pi}(h) = 0$  in Equation (5.28), as shown in red dash line in Figure 5.7a. The contact angle is marked at  $\bar{h} = \bar{h}_d$  and calculated by:

$$2 \tan \bar{\theta} = \sqrt{-2\Theta \bar{\Pi}_d (\bar{h}_{max} - \bar{h}_d)} = \sqrt{-2\Theta \int_{\bar{h}_d}^{\bar{h}_{apex}} \bar{\Pi} dh'} \quad (5.30)$$

It is noted that the thickness profile in Figure 5.7 is the combined thickness variation from two gas-liquid interfaces. In contrast, contact angles are commonly defined on one interface, hence

the factor 2 on the left hand side of Equation (5.30). In dimensional terms, the contact angle is very small,  $2\theta \approx 2 \tan \theta \sim O(\varepsilon)$ . Thus Equation (5.30) leads to:

$$\cos \theta \approx 1 - \frac{\theta^2}{2} \approx 1 + \frac{1}{2\sigma} \int_{h_d}^{h_{apex}} \Pi dh' \quad (5.31)$$

This contact angle is consistent with the contact angle derived from a thermodynamic perspective. From the Gibbs–Duhem equation [120,228], the effect of disjoining pressure manifests as a thickness dependent surface energy  $\sigma_f$ :

$$2\sigma_f(h) = 2\sigma + \int_h^\infty \Pi(h') dh' \quad (5.32)$$

Where the bulk surface energy (surface tension)  $\sigma = \sigma_f(h \rightarrow \infty)$  is modified by the integral disjoining pressure. Combining Equation (5.32) with the force balance at contact line between the “microdrop” and the thinner flat film, *i.e.*  $2\sigma_f(h = h_{apex}) \cos \theta = 2\sigma_f(h = h_d)$ , the contact angle  $\cos \theta$  can be then solved to obtain the same expression as Equation (5.31).

The contact angle shown in Figure 5.7 is calculated to be  $\theta = 0.22^\circ$ . The experimental estimation of the same condition ( $c_s = 50$  mM and  $n = 2$ , shown in Figure 4.6) is about  $0.1^\circ$ , close to the numerical calculation. The deviation could be a result of experimental limitations in determining the exact thickness profile in the build-up part of the ridge, since this region is small, only  $\sim 5 \mu\text{m}$  ( $\sim 10$  pixels) wide, yet the thickness variation is large ( $\sim 15$  nm). As a comparison, the leeward part of the ridge is much wider ( $\sim 20 \mu\text{m}$ ) and has much less thickness variation ( $\sim 5$  nm). Overall, the thin film model results are in agreement with the experimentally observed time-independent ridge formation and evolution, both with scaling analysis, and with numerical solution.

Excellent quantitative agreement is also found between the asymptotic and the full numerical solution, as shown in Figure 5.7b.

In the leeward part of the ridge, we neglect term II in Equation (5.6) and, similar to the analysis done in Section 4.3.4, introduce the dimensionless similarity variable

$\bar{\xi} = \bar{r}/\bar{R} = \bar{r}/(\bar{D}t)^{1/2}$ , where  $\bar{D} = \frac{\partial \bar{R}^2}{\partial t}$  is the dimensionless growth rate of thinner domain. This

leads to:

$$\frac{\partial \bar{h}}{\partial \bar{\xi}} + \frac{2}{\bar{\xi}^2} \frac{\partial}{\partial \bar{\xi}} \left( \bar{D}_{eff} \bar{\xi} \frac{\partial \bar{h}}{\partial \bar{\xi}} \right) = 0 \quad (5.33)$$

Where  $\bar{D}_{eff}(\bar{h}) = -\Theta M(\bar{h}) \frac{\partial \bar{\Pi}(\bar{h})}{\partial \bar{h}}$  is the dimensionless effective diffusivity. Figure 5.8 shows the

rescaled ridge profiles from the full numerical solution. The leeward part of ridge approaches the self-similar asymptote after the initial stage of domain nucleation, same as observed in the

experiment (Figure 4.7). Specifically, the film thickness at  $\bar{\xi} = 1.5$  is followed over time (Figure 5.8 inset) to show that the thickness in the leeward part of the ridge reaches constant after  $\bar{t} \approx 3$ .

Since, as shown in Figure 5.6,  $\bar{\xi} = 1.5$  is approximately where the self-similar region starts (where Term II in Equation (5.6) becomes negligible), we use the plateau thickness there, *i.e.*

$\bar{h}(\bar{\xi} = 1.5) = 0.19$ , as one of boundary conditions for solving the asymptotic Equation (5.33)

numerically. The other boundary condition is from the undisturbed film far away from the ridge,

*i.e.*  $\bar{h}(\bar{\xi} \rightarrow \infty) = 0$ . The resulting asymptotic thickness profile (dash line in Figure 5.8) agrees very

well with the rescaled ridge profiles obtained from the full numerical solution, demonstrating the validity of the dimensional analysis and the asymptotic equation.

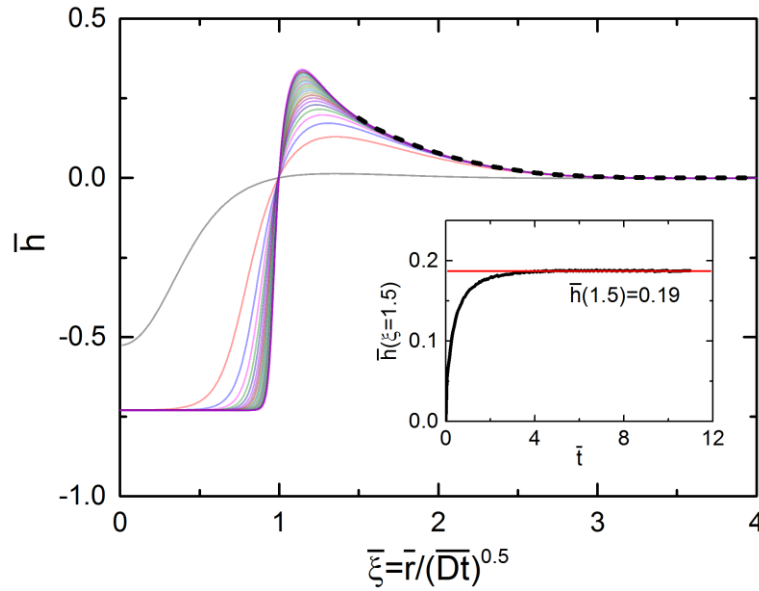


**Figure 5.8** Numerical resolved ridge thickness profiles plotted as  $\bar{h}$  vs.  $\bar{r}/(\bar{D}\bar{t})^{1/2}$ . Black dash line shows solution from Equation (5.33) that coincide the leeward part of the rescaled profiles. Inset: the thickness at  $\bar{\xi} = 1.5$  plotted against time. It quickly plateaus to  $\bar{h}(\bar{\xi} = 1.5, \bar{t} > 3) = 0.19$  after the initial domain formation period.

### 5.3.4 Thickness and concentration dependence of the ridge shape

The formation of thinner domains in stratifying foam films is a result of interplay of thin film hydrodynamics and thermodynamics. The thickness and concentration dependences of the film free energy, and consequently the disjoining pressure, as well as the hydrodynamic mobility, is reflected in the thickness profiles of the ridge formed during domain expansion.

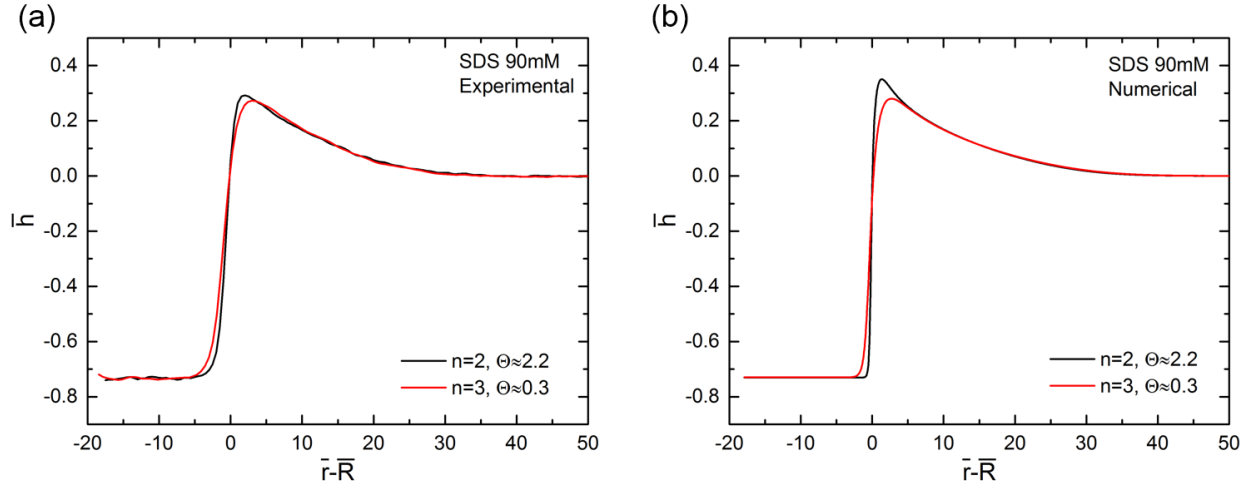


**Figure 5.9** Effect of the number of micelle layer contained in the thin film,  $n$ , on the ridge shape. (a) Experimental and (b) numerical results from  $c_s = 90$  mM and  $\bar{R} = 20$  are qualitatively in agreement. Varying  $n$  does not change the ridge shape in the leeward part. The slope of thickness is increased in the build-up part of the ridge, when  $n$  is reduced.

The effects of the film thickness on the shape of the ridge formed are multi-fold. We focus the discussion here on the effects of thickness by varying  $n$  on the resulting ridge shape, since the outside film thickness during domain expansion follows  $h_\infty = h_0 + n\Delta h$  (Equation (5.18)), and for a specific surfactant concentration, both  $h_0$  and  $\Delta h$  are predetermined leaving  $n$  the only variable. In the framework of Equation (5.6),  $n$  is involved in determining both the relative magnitude of disjoining pressure,  $\Theta$ , and the mobility of the foam film,  $\bar{M}$ , as shown by Equation (5.21) and Equation (5.22). In Figure 5.9, the  $n$  dependence of the ridge shape is presented for foam film with SDS 90 mM, from both experimental and numerical results. All ridge shapes are obtained at the same domain size  $\bar{R} = 20$  for comparison. From both experiments and numerical solution, it is clear that changing  $n$  from 2 to 3 does not alter the ridge shape in the leeward part. In the build-up part of the ridge, a smaller  $n$  (therefore, a larger  $\Theta$ ) leads to a larger slope in thickness profile and

a larger maximum thickness. The “macroscopic contact angle” increases with decreasing  $n$  (increasing  $\Theta$ ), which is consistent with Equation (5.30). Qualitative agreement between the experimental results and the numerical predictions is reached, and the observed trend is repeatable in the experiments. Quantitative differences between the results are mostly at the region of ridge apex, where inaccuracies in experimental thickness determination may be more pronounced.

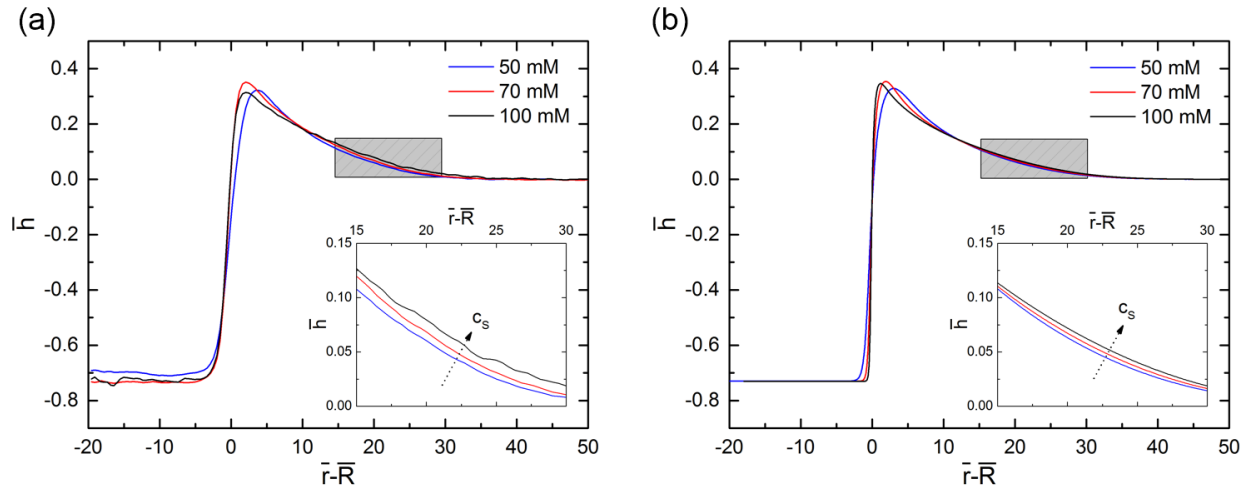


**Figure 5.10** Effect of surfactant concentration on the ridge shape. (a) Experimental and (b) numerical results from three SDS concentration,  $n = 2$ , and  $\bar{R} = 20$  are qualitatively in agreement. The insets magnify the thickness profile within the regions marked in gray to show the small differences in ridge shape in the leeward part.

The oscillatory disjoining pressure isotherm is largely dictated by the concentration of the surfactant solution, as illustrated in Section 5.2.2. Variations in the concentration  $c_s$  would lead to change in every parameter for estimating the disjoining pressure isotherm (Equation (5.4)). As a result, the concentration dependence of the ridge shape is not straightforward. In Figure 5.10, the ridge shapes from three different surfactant concentrations are compared. In the build-up part of

the ridge, the “macroscopic contact angle” generally increases with increasing concentration, while the maximum ridge thickness does not show a clear, monotonic trend. For the leeward part of the ridge, the shape of the ridge does not vary significantly over the range of concentration studied, but a clear trend of thickness increase upon increasing concentration is still observed, in both experimental and numerical results (Figure 5.10 insets).

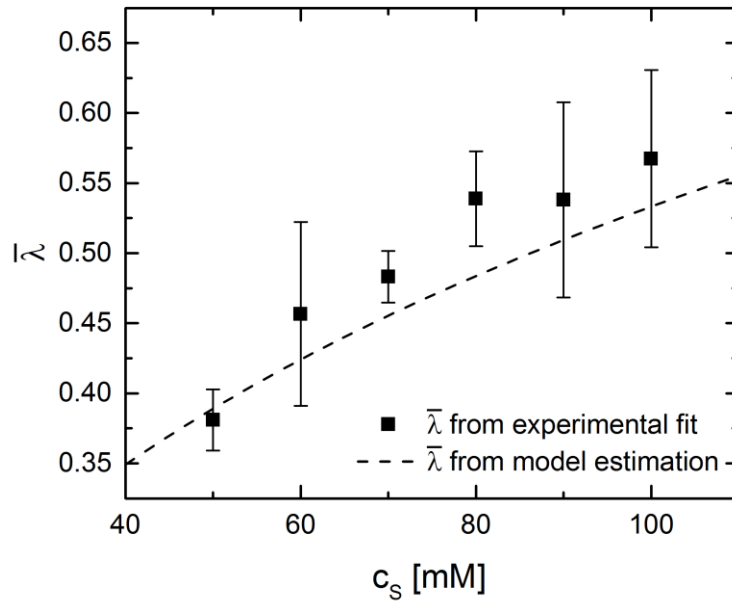


**Figure 5.11** Dimensionless decay length,  $\bar{\lambda}$ , obtained through numerically fitting the thickness profile of the leeward part of experimentally resolved ridge shape, and through model estimation from Equation (5.15). The error bars show standard deviations of the data from at least three replications.

With further numerical investigation, we concluded that the key parameter that leads to the small thickness differences in the leeward part of ridge is the decay length,  $\lambda$ , in the disjoining pressure isotherm. In contrast to the extensive studies in the literature [56,97,99,128,139,241] on



the oscillation period of the disjoining pressure isotherm,  $\Delta h$ , and its concentration dependence, the decay length and its concentration dependence is much less discussed and remains largely uncharacterized. The effect of decay length on the ridge profile provides us a new indirect approach to experimentally infer the magnitude and variation of the decay length. By numerically fitting the IDIOM resolved thickness profile of the leeward part of the ridge, we are able to extract the dimensionless decay length,  $\bar{\lambda} = \lambda/\Delta h$ , for multiple surfactant concentration. Despite of the small differences between thickness profiles from different concentration (the differences are clear only after magnification in Figure 5.10), the obtained values of  $\bar{\lambda}$  are comparable to the model estimations given by Equation (5.15), as shown in Figure 5.11. In the concentration range studied, unlike  $\Delta h$  and  $h_0$  which show monotonic decrease with increasing concentration (Figure 5.1), the dimensionless decay length  $\bar{\lambda}$  shows a monotonic increase when the surfactant concentration is increased, in both experiments and model estimates. To the best of our knowledge, this is the first report of the concentration dependence of the oscillation decay length of disjoining pressure in stratifying foam films.

The thickness and concentration dependences of the thinner domain expansion are also probed. The ridge resolved from the 1D thin film model Equation (5.6) corresponds to the domain expansion Regime A, in which the domain and the ridge shape remains axisymmetric. The diffusive expansion rates of the domain,  $D$ , are extracted from numerically resolved thickness profiles over time, and compared with experimental measured growth rates in Regime A (reported in Figure 3.9a). Figure 5.12 shows good quantitative agreements of concentration dependences of  $D$ , for both  $n = 2$  and 3. The experimental results for  $n = 1$  are excluded for comparison, since at

this small thickness range, forces other than supramolecular structural force (DLVO forces in particular) become too significant to be neglected in disjoining pressure calculation.

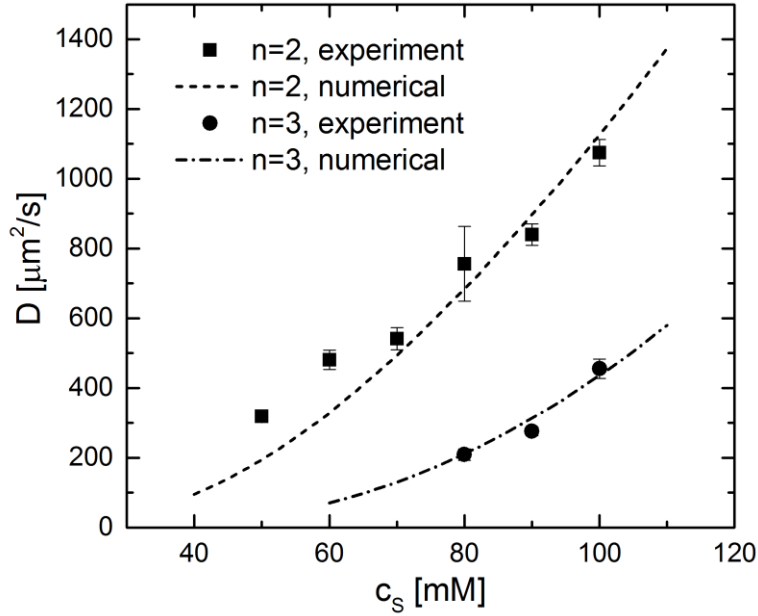


**Figure 5.12** The diffusive growth rate of domain expansion,  $D = dR^2/dt$ , versus surfactant concentration,  $c_s$ , from both experimental and numerical measurements.

### 5.3.5 Ridge shape at later time

In this study, the thin film model presented is solved in one spatial dimension,  $r$ , (Equation (5.6)). Therefore the angular dependence of ridge shape is intrinsically not captured by this model. This is particularly important when the domain expansion enters the Regime B, with topological instability occurring and white spots formed around the contact line (experimentally discussed in Section 4.4). Despite that the detailed angular variations in ridge thickness and the white spot

forming instability is absent, the numerical resolved 1D ridge at later time still show many features reminiscent to the topological instability and white spot formation.

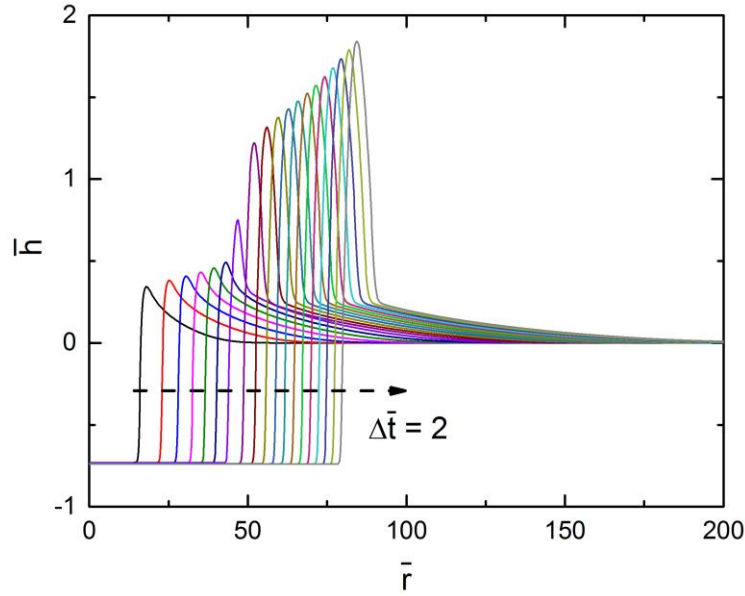


**Figure 5.13** Numerical ridge shape and evolution with  $c_s = 70 \text{ mM}$ ,  $n = 2$ . After  $\bar{t} \approx 12$ , the maximum ridge thickness increase rapidly.

In Figure 5.13, the ridge shapes are numerically computed for  $c_s = 70 \text{ mM}$  and  $n = 2$  for a long time period (until  $\bar{t} = 40$ ). A clear transition takes place after  $\bar{t} \approx 12$ , where the maximum thickness of the ridge sharply increases to  $\bar{h}_{\max} > 1$ . The peak thickness then sharply drops down to the typical ridge thickness range, before the slow decay into the outside film thickness  $\bar{h}_{\infty} = 0$ . The shape change of the thickness profile after  $\bar{t} \approx 12$  is akin to the topological instability observed experimentally, and the sharp thickness peak can be treated as a 1D “white spot” formed between the thinner domain and the slow decaying ridge. Indeed, when the maximum ridge thickness is

followed over time, the resulting Figure 5.14 is very similar to the experimental results for maximum thickness of white spots (Figure 4.10). The 1D “topological instability” also starts when the ridge thickness enters the unstable region where  $d\bar{\Pi}/d\bar{h} > 0$ . The thickness then quickly raises to form the 1D “white spot”, until stable disjoining pressure is reached again in next oscillation. The growth of the 1D “white spot” then slows down and controlled more by the Laplace pressure since the magnitude of disjoining pressure becomes small.

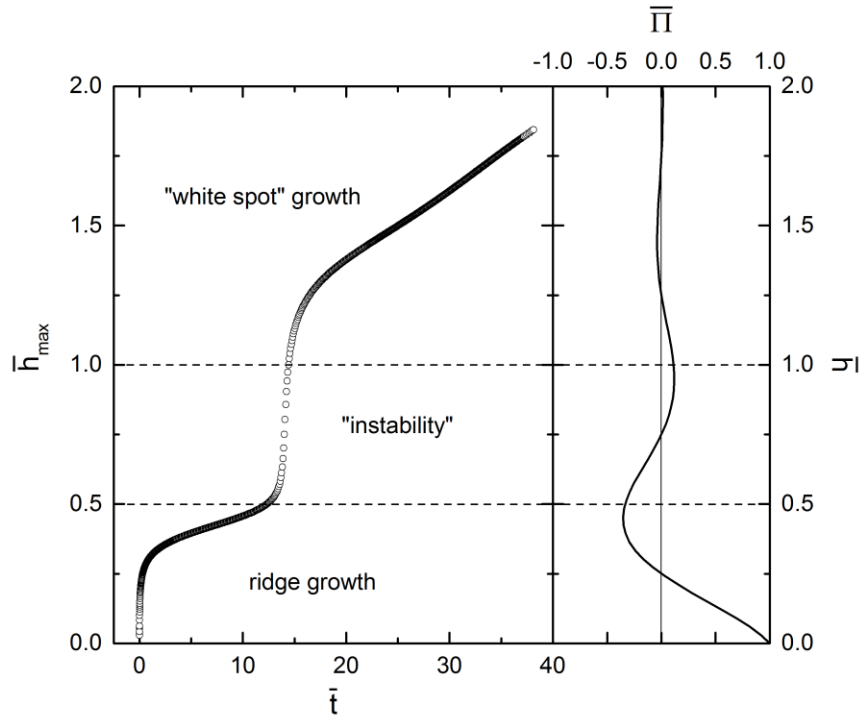


**Figure 5.14** Time dependence of maximum thickness  $\bar{h}_{\max}$ . The evolution is corresponded to the disjoining pressure isotherm (plotted as  $\bar{h}$  vs.  $\bar{\Pi}$ ).

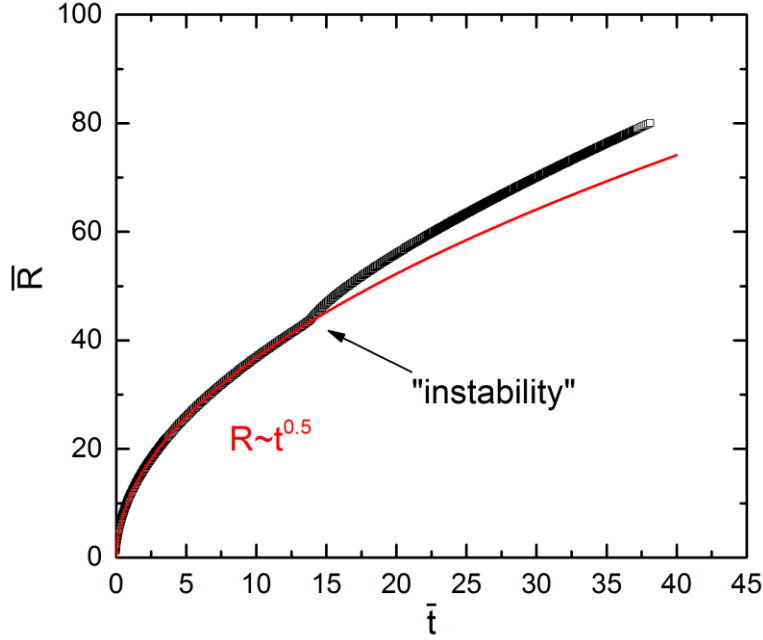


**Figure 5.15** Time dependence of thinner domain radius. After the onset of 1D “instability” the domain expansion deviates from the  $R \propto t^{1/2}$  scaling, but the experimental linear scaling is not exactly recovered.

One of the significant manifestation of the topological instability in experiments is that it changes the domain expansion kinetics from Regime A ( $R \propto t^{1/2}$ ) to Regime B ( $R \propto t$ ), as extensively discussed in Section 3.3.3 (*cf.* Figure 3.5). The 1D “instability” obtained from numerical solution also affects the expansion kinetics of the thinner domain. As shown in Figure 5.15, the radius of the domain clearly deviates from the  $R \propto t^{1/2}$  after the onset of 1D “instability” ( $\bar{t} \approx 12$ ). However, the linear relationship expected for Regime B is not recovered, possibly due to the significantly different ridge geometries after instability. After all, the intrinsically axisymmetric 1D “white spot” is expected to have a different impact on the domain expansion kinetics, from the individual circular white spots observed experimentally. Further analysis shows an approximate  $R \propto t^{0.55}$  dependence to hold when the 1D “white spot” is fully established ( $\bar{t} > 15$ )

after the initial “instability” region (*cf.* Figure 5.14). This scaling seems to be shared in trials with different concentration and thickness, after “white spot” formation.

Overall, despite of the limitations of the 1D thin film model, it demonstrates that the instability is induced by the oscillatory nature of the disjoining pressure, and it significantly alters the domain expansion and ridge growth dynamics. Consistent with the experimental observations in Section 4.4, the “instability” and the associated changes in dynamics are not analogous to Rayleigh-type instability. The ridge does not break down during the instability, rather the 1D “white spot” co-exists with the remaining of the ridge outside, and its thickness variation is closely related to the stability of the disjoining pressure isotherm.

### **5.3.6 Limitations of 1D thin film model**

The 1D thin film model of Equation (5.6) has been demonstrated to quantitatively predict the dynamics of domain expansion, shape of axisymmetric ridge formed and its evolution. However, the topological instability and the formation and growth of white spots are associated with symmetry breaking of the ridge. The experimental observations in Figure 3.6 show the lack of symmetry and periodicity of distribution of white spots, which cannot be captured by the 1D thin film model. Moreover, the 1D model cannot be applied for studying non-axisymmetric domain growth dynamics, *e.g.* when the domain is in contact with the Plateau border, or when multiple domains grow, interact and coalesce.

In order to further replicate the experimental observations in white spot formation and distribution, effect of the Plateau boarder, and also possible interactions between multiple growing domains or white spots, a detailed 2D thin film model is needed to resolve the thickness profile in

two spatial dimensions,  $h(x, y, t)$ . Analogous to Equation (5.6), the 2D lubrication based thin film equation reads:

$$\frac{\partial \bar{h}}{\partial \bar{t}} + \frac{\partial}{\partial \bar{x}} \left[ \bar{M} \frac{\partial}{\partial \bar{x}} \left( \frac{\partial^2 \bar{h}}{\partial \bar{x}^2} + \frac{\partial^2 \bar{h}}{\partial \bar{y}^2} \right) \right] + \frac{\partial}{\partial \bar{y}} \left[ \bar{M} \frac{\partial}{\partial \bar{y}} \left( \frac{\partial^2 \bar{h}}{\partial \bar{x}^2} + \frac{\partial^2 \bar{h}}{\partial \bar{y}^2} \right) \right] + \Theta \left[ \frac{\partial}{\partial \bar{x}} \left( \bar{M} \frac{\partial \bar{\Pi}}{\partial \bar{x}} \right) + \frac{\partial}{\partial \bar{y}} \left( \bar{M} \frac{\partial \bar{\Pi}}{\partial \bar{y}} \right) \right] = 0 \quad (5.34)$$

Models like Equation (5.34) has been shown in the dewetting literature to excel in predicting contact line instability and pattern formation in thin films [84,188,189,191]. Significantly more computing time is needed to perform the 2D numerical solving procedure, which limits the size of the domain under investigation. As shown in Figure 5.16, solution of Equation (5.34) successfully reproduces the axisymmetric ridge and domain. The shape and evolution are found identical compared to the corresponding solution from 1D model, as expected.

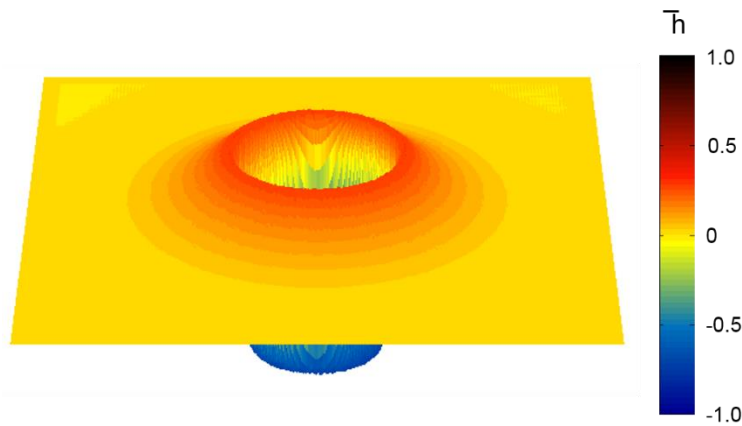


**Figure 5.16** Example of axisymmetric ridge shape captured by 2D thin film model

However, the ridge after “instability” does not show the topological changes observed in experiments. Instead, the ridge continues to grow axisymmetrically, with the maximum ridge thickness reaching (and passing over) the unstable disjoining pressure region. No circular, thicker spot is formed in the thick ridge, even after applying small amplitude perturbation to the ridge. With large thickness perturbation (on the order of the  $h_{\max} - h_{\infty}$ ), which is absent experimentally, thick spots do form around the contact line. However, similar to those observed in dewetting films (*cf.* Figure 1.15b), the thicker spots then disrupt and undulate the circular contact line of the thinner domain, move much slower than the expanding contact line and eventually get left behind in the thinner domain. This is in sharp contrast to the experimental observations that contact line remains circular and the white spots move along the contact line as it expands.

Moreover, the thinner domain developed with the 2D model is lack of the apparent line tension shown in experiments. The experimental domain contact line keeps its circularity throughout the expansion process, regardless of the surrounding white spots or other domains, and the domain quickly (in  $< 1$  s time) regains the circular shape after coalescence of two or more domains. Heinig and Langevin [86] therefore prescribed a phenomenological line tension to the domain contact line when they studied the relaxation after domain coalescence, drawing analogy to that between domains of different phases in lipid monolayer [242]. In contrast, when two domains are set up to expand side by side in the 2D numerical model, they grow into contact and merge without shape relaxation. The merged, peanut shaped domain continues to expand, without the tendency to retain circular shape. We suspect that the line tension of the thinner domain is a fundamental thermodynamic property of the domain contact line that has not been included in the existing thin film hydrodynamic model.



The lack of apparent line tension, together with possible Marangoni effects and higher order contributions to the disjoining pressure, *i.e.*  $\Pi(h, dh/dx, \dots)$  [243], could all contribute to the discrepancies in the experimental and model results after topological instability. The nature of these effects are relatively poorly understood, and their manifestations in thin film hydrodynamics are mostly unexplored (except for Marangoni effects). Further theoretical understanding in these aspect are essential to full decipher the rich and complex dynamics exhibited during stratification of micellar thin films.

## 5.4 Conclusions

In this chapter, the lubrication-based thin film model is solved numerically to model the domain expansion and ridge formation dynamics during foam film stratification. The supramolecular structural oscillatory disjoining pressure isotherms are estimated for the charged SDS micellar solutions. The explicit damped oscillation function is obtained with parameter values in the literature and surfactant concentration being the only input variable. The thin film hydrodynamic model is then solved with specifically written solving scheme for optimized efficiency and accuracy.

The numerically resolved shapes of expanding domain and growing ridge surrounding it are quantitatively in agreement with the experimental results obtained by IDIOM. The asymmetrical ridge shape, time dependence of domain radius, ridge width and maximum thickness, are all reproduced by the numerical solution. Moreover, the asymptotic behavior of the ridge shape evolution, predicted by scaling analysis, is confirmed through explicit calculations of relative magnitude of different terms in the governing equation (Equation (5.6)). The asymptotic time-

independent shape in the build-up part of the ridge show resemblances to the non-flat equilibrium thin film predicted in the literature, while the self-similar shape in the leeward part of the ridge is consistent with experimental observations.

When the surfactant concentration and number of micelle layers in the film are varied, the model solution successfully predicts the changes in ridge shape. Indirectly, part of the experimentally resolved ridge shape can be fitted to the numerical thickness profiles to obtain values of decay length in the oscillatory disjoining pressure function, which cannot be determined accurately through direct equilibrium disjoining pressure measurement. The experimentally measured diffusive growth rates of the thinner domain are also recovered by the numerical solution, further confirming the hydrodynamic nature of the domain expansion dynamics.

Despite of the absence of angular dependence of the thickness profile in the 1D thin film model, it is still capable to illustrate the nature of the white spot forming topological instability observed experimentally in the later stage of domain expansion. The instability is driven by the oscillatory disjoining pressure, when the thickness of the ridge accesses the unstable branch of disjoining pressure isotherm. Though the some of the features of this instability is captured in the axisymmetric model, further numerical calculations with the 2D model suggest that the presented lubrication based thin film model is not sufficient to fully describe the formation, growth and interactions of the white spots, as well as multiple thinner domains.

Overall, it is demonstrated that the hydrodynamic model is a powerful tool to predict and understand the dynamics of foam film stratification. The numerical results match the IDIOM measurement quantitatively, further confirming the validity of the novel experimental protocol, and the resulting first-time characterization of ridge shape and evolution during domain expansion.

The use of the model and the numerical scheme can potentially be extended to the entire film thinning process, in order to gain more insight in the stability and lifetime of stratifying or non-stratifying foam films. On the other hand, the discrepancies from experimental observations after the topological instability can potentially lead to better understanding of the thermodynamic properties of the stratifying foam films, such as surface energy, disjoining pressure, and line tension, particularly at the non-flat transition region between different thicknesses.

## **CHAPTER 6.**

### **CONCLUSIONS**

The stability and lifetime of colloidal system like foams, emulsions and colloidal sols are important for many industrial applications and our daily life. The hydrodynamics and thermodynamics of thin liquid films that separate bubbles, drops or particles are essential to the overall stability of the colloidal systems. Free-standing foam films containing micelles (as well as nanoparticles, polyelectrolyte-surfactant mixtures or smectic liquid crystals) thins in a step-wise fashion termed stratification, when the film thickness reaches below  $\sim 100$  nm. The stratification occurs via layer-by-layer removal of the micelles, and gives rise to rich patterns and dynamics, involving the coexistence and evolution of domains and nanostructures of discretely different thickness. While the previous investigations of the stratification phenomenon mostly focused on the equilibrium states, and the nature and strength of the non-DLVO, supramolecular structural oscillatory disjoining pressure responsible for stratification, the rich and complex dynamics exhibited throughout the step-by-step transition of thickness is relatively unexplored and poorly understood. In this study, we probe the dynamics of thickness transition during stratification of micellar foam films, through both experimental characterization of the stratifying foam films, and theoretical modelling efforts to understand the underlying physics.

We developed a novel Interferometry Digital Imaging Optical Microscopy (IDIOM) protocol, in order to characterize the landscape of stratifying free-standing thin films. The IDIOM protocol combines the principles of interferometry, optical microscopy and digital image analysis, and allows us to profile the thickness of free-standing foam film with high spatial ( $< 1$  nm in thickness,  $< 1$   $\mu\text{m}$  in lateral position) and temporal ( $< 1$  ms) resolution. Unlike the conventional

interferometry application to thin film studies, which obtain an average thickness from a 1-100  $\mu\text{m}$  sampling region, the IDIOM protocol measures spatial variation of film thickness over an extended area, and captures the formation and evolution of nanoscopic structures and patterns during film drainage and evolution. Using the IDIOM protocol, exquisite thickness maps were constructed for stratifying films made from sodium dodecyl sulfate (SDS) micellar solutions. The complex dynamics during the step-wise thinning, which might have been overlooked using conventional interferometry, were captured completely by the IDIOM. Emergence and growth of nanoscopic ridges, mesas and craters during the stratification process were recognized experimentally for the first time. In particular, the formations and evolutions of craters (thinner domains) and ridges were analyzed and discussed in detail.

Two distinct regimes in the expansion dynamics of a single thinner domain were recognized through image analysis. The initial isolated domain growth with its radius proportional to square root of time,  $R \propto t^{1/2}$ , with a constant apparent growth diffusivity (Regime A), after domain coalescence with the Plateau border surrounding the foam film, the circular domain was deformed, and the boundary between the thinner domain and the rest of the film expands linearly over time, *i.e.*  $R \propto t$ , with a constant apparent contact line velocity (Regime B). For isolated domain, a similar transition could occur when a topological instability sets in at the domain boundary, which also leads to formation of white spots around the growing domain. Though a few studies [73,77,79] have examined the expansion of isolated domains, and showed the diffusion-like domain growth in Regime A, the regime transition occurred when domain coalesces with the Plateau border was reported here for the first time. The similarities between the two types of scaling transition were recognized and discussed. One of the claims of the existing thin film hydrodynamic models is that the domain expansion dynamics and the scaling transitions is linked

to the existence of a ridge formed around the growing domain. Yet experimental evidence of ridge formation was lacking in the literature.

By utilizing IDIOM protocol, we visualized and characterized, for the first time, of the nanoscale ridge formed around the expanding thinner domain during film stratification. The axisymmetric ridge profiles were constructed, and its shape and evolution were analyzed in detail. The ridge in stratifying free-standing films was postulated in the literature [76,82,178] to be analogous to ridges formed during liquid dewetting from a solid substrate. However, we find that the ridge shows distinctive features in both its shape and evolution dynamics, due to presence of the distinctive non-DLVO, supramolecular oscillatory surface forces. A model based on lubrication approximation to the thin film hydrodynamics, including the effect of supramolecular structural oscillatory disjoining pressure, was then developed and asymptotic solutions were found through dimensional analysis. The solution showed two different asymptotic scaling arise during ridge evolution, in agreement with the experimental observations. By numerically solving the thin film hydrodynamic equation, the model predicted ridge shape, evolution dynamics, and concentration/thickness dependences, are all in quantitative agreement with the experimental results.

At later stage of the expansion of an isolated domain, white spots can be formed around within the ridge and change the domain growth kinetics to Regime B. Previous studies [76,79] suggested the instability leading to white spot formation is akin to a Rayleigh-type instability of the toroidal shaped ridge. Our experimental characterization of this topological instability, and model calculation disagree with such claim. We showed that the axisymmetric ridge does not break down through periodic undulation and becomes the much thicker white spots, instead the white spots develop within the ridge region and co-exist with the remaining ridge after the instability.

The presented experimental and theoretical results suggested that the instability is induced by the unstable branches of the oscillatory disjoining pressure isotherm, rather than by capillarity as in the case of Rayleigh instability. After the instability, the liquid drained from the expanding thinner domain accumulates in the white spots, while the regions in the ridge unperturbed by the topological instability cease further growth. The non-axisymmetric formation and distribution of white spots observed in the experiments requires a full two-dimensional hydrodynamic model to describe, but many features of the disjoining pressure induced instability were captured by the simple one dimensional model.

The thin film hydrodynamic model can be further refined by including other properties of the stratifying foam films (e.g. line tension of the domain), which will require further insights in the thermodynamics or hydrodynamics of the system. Overall, the application of IDIOM protocols, the characterization and modeling of dynamics of domain expansion, ridge formation, evolution and instability, have led to better understand the stratification phenomenon, the hydrodynamics of free-standing foam films, and the nature and influence of the underlying non-DLVO structural forces.

## REFERENCES

- [1] Magrabi SA, Dlugogorski BZ, Jameson GJ. A comparative study of drainage characteristics in AFFF and FFFP compressed-air fire-fighting foams. *Fire Saf J* 2002;37:21–52.
- [2] Farrokhpay S. The significance of froth stability in mineral flotation - A review. *Adv Colloid Interface Sci* 2011;166:1–7.
- [3] Pugh RJ. Foaming, foam films, antifoaming and defoaming. *Adv Colloid Interface Sci* 1996;64:67–142.
- [4] Laba D. Rheological properties of cosmetics and toiletries. New York: Marcel Dekker, Inc.; 1993.
- [5] Bureiko A, Trybala A, Kovalchuk N, Starov V. Current applications of foams formed from mixed surfactant-polymer solutions. *Adv Colloid Interface Sci* 2014;222:670–7.
- [6] Liger-Belair G, Polidori G, Jeandet P. Recent advances in the science of champagne bubbles. *Chem Soc Rev* 2008;37:2490.
- [7] Bridie AL, Wanders TH, Zegveld W, van der Heijde HB. Formation, prevention and breaking of sea water in crude oil emulsions “chocolate mousses.” *Mar Pollut Bull* 1980;11:343–8.
- [8] Schilling K, Zessner M. Foam in the aquatic environment. *Water Res* 2011;45:4355–66.
- [9] Evans DF, Wennerstrom H. Colloidal domain: where physics, chemistry, biology, and technology meet. 2nd ed. Wiley-VCH; 1999.
- [10] Cantat I, Cohen-Addad S, Elias F, Graner F, Höhler R, Pitois O, et al. Foams: structure and dynamics. Oxford: Oxford University Press; 2013.
- [11] Kraynik AM. Foam flows. *Annu Rev Fluid Mech* 1988;20:325–57.
- [12] Prud’homme RK, Khan SA. Experimental results on foam rheology. vol. 234. New York: Marcel Dekker, Inc.; 1996.
- [13] Höhler R, Cohen-Addad S. Rheology of liquid foam. *J Phys Condens Matter* 2005;17:R1041–69.
- [14] Stone HA, Koehler SA, Hilgenfeldt S, Durand M. Perspectives on foam drainage and the influence of interfacial rheology. *J Phys Condens Matter* 2002;15:S283–90.
- [15] Evans ME, Kraynik AM, Reinelt DA, Mecke K, Schröder-Turk GE. Networklike propagation of cell-level stress in sheared random foams. *Phys Rev Lett* 2013;111:138301.
- [16] Ivanov IB. Thin liquid films. New York: Marcel Dekker, Inc.; 1988.
- [17] Weaire D, Hutzler S. The physics of foams. Oxford: Oxford University Press; 1999.
- [18] Bergeron V. Forces and structure in thin liquid soap films. *J Phys Condens Matter* 1999;11:R215–38.
- [19] de Gennes P-G, Brochard-Wyart F, Quere D. Capillarity and wetting phenomena: Drops, Bubbles, Pearls, Waves. New York: Springer; 2004.



- [20] Ruckenstein E, Jain RK. Spontaneous rupture of thin liquid films. *J Chem Soc* 1974;70:132–47.
- [21] Venerus DC, Simavilla DN. Tears of wine : new insights on an old phenomenon. *Sci Rep* 2015;5:16162.
- [22] Quéré D. Fluid coating on a fiber. *Annu Rev Fluid Mech* 1999;31:347–84.
- [23] Deegan RD, Bakajin O, Dupont TF, Huber G, Nagel SR, Witten TA. Capillary flow as the cause of ring stains from dried liquid drops. *Nature* 1997;389:827–9.
- [24] Hermans E, Saad Bhamla M, Kao P, Fuller GG, Vermant J. Lung surfactants and different contributions to thin film stability. *Soft Matter* 2015;11:8048–57.
- [25] Wong H, Fatt I, Radke C. Deposition and thinning of the human tear film. *J Colloid Interface Sci* 1996;184:44–51.
- [26] Braun RJ. Dynamics of the tear film. *Annu Rev Fluid Mech* 2012;44:267–97.
- [27] Bhamla MS, Giacomini CE, Balemans C, Fuller GG. Influence of interfacial rheology on drainage from curved surfaces. *Soft Matter* 2014;10:6917–25.
- [28] Rosen MJ. Surfactants and interfacial phenomena. Hoboken: John Wiley & Sons; 2004.
- [29] Denkov ND, Tcholakova S, Golemanov K, Ananthpadmanabhan KP, Lips A. The role of surfactant type and bubble surface mobility in foam rheology. *Soft Matter* 2009;5:3389.
- [30] Safouane M, Saint-Jalmes A, Bergeron V, Langevin D. Viscosity effects in foam drainage: Newtonian and non-newtonian foaming fluids. *Eur Phys J E* 2006;19:195–202.
- [31] Zhang Y, Yilixiati S, Pearsall C, Sharma V. Nanoscopic terraces, mesas, and ridges in freely standing thin films sculpted by supramolecular oscillatory surface forces. *ACS Nano* 2016;10:4678–83.
- [32] Wasan DT, Nikolov AD, Kralchevsky PA, Ivanov IB. Universality in film stratification due to colloid crystal formation. *Colloids and Surfaces* 1992;67:139–45.
- [33] Hooke R. Micrographia: or some physiological descriptions of minute bodies made by magnifying glasses, with observations and inquiries thereupon. London: The Royal Society; 1665.
- [34] Newton I. Opticks: Or, a treatise of the reflections, refractions, inflexions and colours of light. vol. 1. London: William Innys; 1704.
- [35] Plateau J. Experimental and theoretical statics of liquids subject to molecular forces only. vol. 1. Paris: Gauthier-Villars; 1873.
- [36] Reinold AW, Rucker AW. On the thickness of soap films. *Proc R Soc London* 1877;26:334–45.
- [37] Reinold AW, Rucker AW. On the thickness and electrical resistance of thin liquid films. *Proc R Soc London* 1893;53:394–8.
- [38] Johonnott ES. XLVIII. Thickness of the black spot in liquid films. *Philos Mag Ser 5* 1899;47:501–22.
- [39] Johonnott ES. LXVIII. The black spot in thin liquid films. *Philos Mag Ser 6* 1906;11:746–

53.

- [40] Stansfield H. Observations and photographs of black and grey soap films. *Proc R Soc London A Math Phys Eng Sci* 1906;77:314–23.
- [41] Lawrence ASC. Soap films: a study of molecular individuality. London: G. Bell and Sons; 1929.
- [42] Perrin J. La stratification des lames liquides. *Ann Phys-Paris* 1918;10:160–84.
- [43] Wells P V. Thickness of stratified films. *Ann Phys* 1921;16:69–110.
- [44] Dewar J. Studies on liquid films. *J Franklin Inst* 1922;193:145–88.
- [45] Devaux H. Dünne Lamellen und ihre physikalischen Eigenschaften. *Kolloid-Zeitschrift* 1932;58:260–76.
- [46] Perrin J. Jean Baptiste Perrin - Nobel lecture: discontinuous structure of matter 1926.
- [47] Friedel G. The mesomorphic states of matter. *Annales de Physique*, 1922, p. 273–474.
- [48] Friberg S, Linden SE, Saito H. Thin films from liquid crystals. *Nature* 1974;251:494–5.
- [49] Manev E, Proust JE, Ter-Minassian-Saraga L. Structural disjoining pressure in thin films of liquid crystals - II.: Study of symmetrical and asymmetrical equilibrium films. *Colloid Polym Sci* 1977;255:1133–5.
- [50] Oswald P, Pieranski P. Nematic and cholesteric liquid crystals: concepts and physical properties illustrated by experiments. CRC Press; 2005.
- [51] Lyklema J, H. B. Stratification in free liquid films. *Nature* 1971;233:19.
- [52] Manev ED, Sazdanova SV, Rao AA, Wasan DT. Foam Stability - He Effect Op a Liquid Crystalline Phase on the Drainage and Transition Behavior of Foam Films. *J Dispers Sci Technol* 1982;3:435–63.
- [53] Manev ED, Sazdanova S V., Wasan DT. Stratification in Emulsion Films. *J Dispers Sci Technol* 1984;5:111–7.
- [54] Nikolov AD, Wasan DT, Kralchevsky PA, Ivanov IB. Ordered structures in thinning micellar foam and latex films. In: Sogami NI and I, editor. Ordering and organisation in ionic solutions, Kyoto, Japan: World Scientific, Singapore; 1988, p. 302–414.
- [55] Nikolov AD, Wasan DT. Ordered micelle structuring in thin films formed from anionic surfactant solutions. I. Experimental. *J Colloid Interface Sci* 1989;133:1–12.
- [56] Nikolov AD, Kralchevsky PA, Ivanov IB, Wasan DT. Ordered micelle structuring in thin films formed from anionic surfactant solutions. II. Model development. *J Colloid Interface Sci* 1989;133:13–22.
- [57] Nikolov AD, Wasan DT. Dispersion stability due to structural contributions to the particle interaction as probed by thin liquid film dynamics. *Langmuir* 1992;8:2985–94.
- [58] Krichevsky O, Stavans J. Micellar stratification in soap films: A light scattering study. *Phys Rev Lett* 1995;74:2752–5.
- [59] Denkov N, Yoshimura H, Nagayama K, Kouyama T. Nanoparticle arrays in freely suspended vitrified films. *Phys Rev Lett* 1996;76:2354–7.

- [60] Basheva E, Danov K, Kralchevsky P. Experimental study of particle structuring in vertical stratifying films from latex suspensions. *Langmuir* 1997;7463:4342–8.
- [61] Marinova KG, Gurkov TD, Dimitrova TD, Alargova RG, Smith D. Role of oscillatory structural forces for interactions in thin emulsion films containing micelles. *Society* 2011;7463:2011–9.
- [62] Bergeron V, Radke CJ. Disjoining pressure and stratification in asymmetric thin-liquid films. *Colloid Polym Sci* 1995;273:165–74.
- [63] Wasan DT, Nikolov AD. Spreading of nanofluids on solids. *Nature* 2003;423:156–9.
- [64] Koczko K, Nikolov AD, Wasan DT, Borwankar RP, Gonsalves A. Layering of sodium caseinate submicelles in thin liquid films— a new stability mechanism for food dispersions. *J Colloid Interface Sci* 1996;178:694–702.
- [65] Kolarić B, Förster S, von Klitzing R. Interactions between polyelectrolyte brushes in free-standing liquid films: influence of ionic strength. *Adsorption and Nanostructure*, Berlin, Heidelberg: Springer Berlin Heidelberg; 2001, p. 195–9.
- [66] Espert A, von Klitzing R, Poulin P, Colin A, Zana R, Langevin D. Behavior of soap films stabilized by a cationic dimeric surfactant. *Langmuir* 1998;14:4251–60.
- [67] Bergeron V, Langevin D, Asnacios A. Thin-Film forces in foam films containing anionic polyelectrolyte and charged surfactants. *Langmuir* 1996;12:1550–6.
- [68] Asnacios A, Espert A, Colin A, Langevin D. Structural forces in thin films made from polyelectrolyte solutions. *Phys Rev Lett* 1997;78:4974–7.
- [69] Beltrán CM, Guillot S, Langevin D. Stratification phenomena in thin liquid films containing polyelectrolytes and stabilized by ionic surfactants. *Macromolecules* 2003;36:8506–12.
- [70] Kleinschmidt F, Stubenrauch C, Delacotte J, von Klitzing R, Langevin D. Stratification of foam films containing polyelectrolytes. Influence of the polymer backbone's rigidity. *J Phys Chem B* 2009;113:3972–80.
- [71] Kristen N, von Klitzing R. Effect of polyelectrolyte/surfactant combinations on the stability of foam films. *Soft Matter* 2010;6:849.
- [72] von Klitzing R, Kolarić B, Jaeger W, Brandt A. Structuring of poly(DADMAC) chains in aqueous media: a comparison between bulk and free-standing film measurements. *Phys Chem Chem Phys* 2002;4:1907–14.
- [73] Kralchevsky PA, Nikolov AD, Wasan DT, Ivanov IB. Formation and expansion of dark spots in stratifying foam films. *Langmuir* 1990;6:1180–9.
- [74] Sethumadhavan GN, Nikolov AD, Wasan DT. Stability of liquid films containing monodisperse colloidal particles. *J Colloid Interface Sci* 2001;240:105–12.
- [75] Sethumadhavan GN, Nikolov A, Wasan D. Film stratification in the presence of colloidal particles. *Langmuir* 2001;17:2059–62.
- [76] Beltrán CM, Langevin D. Stratification kinetics of polyelectrolyte solutions confined in thin films. *Phys Rev Lett* 2005;94:217803.
- [77] Heinig P, Beltrán CM, Langevin D. Domain growth dynamics and local viscosity in

- stratifying foam films. *Phys Rev E - Stat Nonlinear, Soft Matter Phys* 2006;73:51607.
- [78] Sonin AA, Langevin D. Stratification dynamics of thin films made from aqueous micellar solutions. *Europhys Lett* 1993;22:271–7.
  - [79] Bergeron V, Radke C. Hole formation and sheeting in the drainage of thin liquid films. *Langmuir* 1992;8:3027–32.
  - [80] Lee J, Nikolov A, Wasan D. Stratification of a foam film formed from a nonionic micellar solution: experiments and modeling. *Langmuir* 2016;32:4837–47.
  - [81] Zhang Y, Sharma V. Domain expansion dynamics in stratifying foam films: experiments. *Soft Matter* 2015;11:4408–17.
  - [82] de Gennes P-G. Dynamics of drying and film-thinning. In: Meunier J, Langevin D, Boccaro N, editors. *Physics of Amphiphilic Layers*, vol. 21, Springer Berlin Heidelberg; 1987, p. 64–71.
  - [83] Leal LG. *Advanced transport phenomena (fluid mechanics and convective transport processes)*. Cambridge: Cambridge University Press; 2007.
  - [84] Oron A, Davis SH, Bankoff SG. Long-scale evolution of thin liquid films. *Rev Mod Phys* 1997;69:931–80.
  - [85] Delacotte J, Rio E, Restagno F, Uzüm C, von Klitzing R, Langevin D. Viscosity of polyelectrolytes solutions in nanofilms. *Langmuir* 2010;26:7819–23.
  - [86] Heinig P, Langevin D. Domain shape relaxation and local viscosity in stratifying foam films. *Eur Phys J E* 2005;18:483–8.
  - [87] Rayleigh L. On the instability of jets. *Proc London Math Soc* 1878;10:4–13.
  - [88] Páram E, Fernández-Nieves A. Generation and stability of toroidal droplets in a viscous liquid. *Phys Rev Lett* 2009;102:234501.
  - [89] Zhang Z, Hilton GC, Yang R, Ding Y. Capillary rupture of suspended polymer concentric rings. *Soft Matter* 2015;11:7264–9.
  - [90] Mysels KJ. *Soap films: studies of their thinning and a bibliography*. Pergamon Press; 1959.
  - [91] Tabor RF, Grieser F, Dagastine RR, Chan DYCC. Measurement and analysis of forces in bubble and droplet systems using AFM. *J Colloid Interface Sci* 2012;371:1–14.
  - [92] Vakarelski IU, Manica R, Tang X, O'Shea SJ, Stevens GW, Grieser F, et al. Dynamic interactions between microbubbles in water. *Proc Natl Acad Sci* 2010;107:11177–82.
  - [93] Derjaguin BV, Titijevskaya AS. Static and kinetic stability of free films and froths. *Prog Surf Sci* 1993;43:74–82.
  - [94] Nikolov AD, Wasan DT. A novel method for studying the dynamic behavior of both plane-parallel and curved thin liquid films. *Colloids Surfaces A Physicochem Eng Asp* 1997;123–124:375–81.
  - [95] Sheludko A. Thin liquid films. *Adv Colloid Interface Sci* 1967;450:391–464.
  - [96] Scheludko A, Exerowa D. Instrument for interferometric measurements of the thickness of microscopic foam films. *CR Acad Bulg Sci* 1959;7:123–32.

- [97] Basheva ES, Kralchevsky PA, Danov KD, Ananthapadmanabhan KP, Lips A. The colloid structural forces as a tool for particle characterization and control of dispersion stability. *Phys Chem Chem Phys* 2007;9:5183–98.
- [98] Karakashev SI, Ivanova DS, Angarska ZK, Manev ED, Tsekov R, Radoev B, et al. Comparative validation of the analytical models for the Marangoni effect on foam film drainage. *Colloids Surfaces A Physicochem Eng Asp* 2010;365:122–36.
- [99] Anachkov SE, Danov KD, Basheva ES, Kralchevsky PA, Ananthapadmanabhan KP. Determination of the aggregation number and charge of ionic surfactant micelles from the stepwise thinning of foam films. *Adv Colloid Interface Sci* 2012;183–184:55–67.
- [100] Taylor SD, Czarnecki J, Masliyah J. Aqueous foam films stabilized by sodium naphthenates. *J Colloid Interface Sci* 2006;299:283–90.
- [101] Velez OD, Constantinides GN, Avraam DG, Payatakes AC, Borwankar RP. Investigation of thin liquid films of small diameters and high capillary pressures by a miniaturized cell. *J Colloid Interface Sci* 1995;175:68–76.
- [102] Mysels KJ, Jones MN. Direct measurement of the variation of double-layer repulsion with distance. *Discuss Faraday Soc* 1966;42:42.
- [103] Exerowa D, Scheludko A. Porous plate method for studying microscopic foam and emulsion films. *CR Acad Bulg Sci* 1971;24:47–50.
- [104] Bergeron V, Radke C. Equilibrium measurements of oscillatory disjoining pressures in aqueous foam films. *Langmuir* 1992;1:3020–6.
- [105] Dimitrova TD, Leal-Calderon F, Gurkov TD, Campbell B. Disjoining pressure vs thickness isotherms of thin emulsion films stabilized by proteins. *Langmuir* 2001;17:8069–77.
- [106] Cascão Pereira LG, Johansson C, Blanch HW, Radke CJ. A bike-wheel microcell for measurement of thin-film forces. *Colloids Surfaces A Physicochem Eng Asp* 2001;186:103–11.
- [107] Pereira LGC, Johansson C, Radke CJ, Blanch HW. Surface forces and drainage kinetics of protein-stabilized aqueous films. *Langmuir* 2003;19:7503–13.
- [108] Beltramo PJ, Hooghten R Van, Vermant J. Millimeter-area, free standing, phospholipid bilayers. *Soft Matter* 2016;12:4324–31.
- [109] Barigou M, Davidson JF. Soap film drainage: theory of experiment. *Chem Eng Sci* 1994;49:1807–19.
- [110] Huibers PDT, Shah DO. Multispectral determination of soap film thickness. *Langmuir* 1997;13:5995–8.
- [111] Sarma TK, Chattopadhyaya A. Simultaneous measurement of flowing fluid layer and film thickness of a soap bubble using a UV-visible spectrophotometer. *Langmuir* 2001;17:6399–403.
- [112] Boys C V. Soap bubbles, Their colors and the forces which mold them. London: Society for Promoting Christian Knowledge; 1912.
- [113] Manev E, Tsekov R, Radoev B. Effect of thickness non-homogeneity on the kinetic behaviour of microscopic foam film. *J Dispers Sci Technol* 1997;18:6–7.

- [114] Karakashev SI, Nguyen A V., Manev ED, Phan CM. Surface foam film waves studied with high-speed linescan camera. *Colloids Surfaces A Physicochem Eng Asp* 2005;262:23–32.
- [115] Karakashev SI, Nguyen A V., Manev ED. A novel technique for improving interferometric determination of emulsion film thickness by digital filtration. *J Colloid Interface Sci* 2007;306:449–53.
- [116] Kitagawa K. Thin-film thickness profile measurement by three-wavelength interference color analysis. *Appl Opt* 2013;52:1998–2007.
- [117] Sett S, Sinha-Ray S, Yarin AL. Gravitational drainage of foam films. *Langmuir* 2013;29:4934–47.
- [118] Gerasimova ATT, Angarska JKK, Tachev KDD, Yampolskaya GPP. Drainage and critical thickness of foam films from mixed solutions of bovine serum albumin and n-dodecyl-B- $\beta$ -maltoside. *Colloids Surfaces A Physicochem Eng Asp* 2013;438:4–12.
- [119] Gibbs JW. The scientific papers of J. Willard Gibbs. vol. 1. Longmans, Green and Company; 1906.
- [120] De Feijter J., Rijnbout J., Vrij A. Contact angles in thin liquid films. I. Thermodynamic description. *J Colloid Interface Sci* 1978;64:258–68.
- [121] Eriksson JC, Toshev BV. Disjoining pressure in soap film thermodynamics. *Colloids and Surfaces* 1982;5:241–64.
- [122] Derjaguin BV, Churaev NV. On the question of determining the concept of disjoining pressure and its role in the equilibrium and flow of thin films. *J Colloid Interface Sci* 1978;66:389–98.
- [123] de Vries AJ. Foam stability: Part V. Mechanism of film rupture. *Recl Des Trav Chim Des Pays-Bas* 1958;77:441–61.
- [124] Vrij A. Possible mechanism for the spontaneous rupture of thin, free liquid films. *Discuss Faraday Soc* 1966;42:23.
- [125] Israelachvili JN. Intermolecular and surface forces: second edition. London: Academic press; 1991.
- [126] Derjaguin BV, Landau LD. The theory of stability of highly charged lyophobic sols and coalescence of highly charged particles in electrolyte solutions. *Acta Physicochim URSS* 1941;14:633.
- [127] Verwey EJW, Overbeek JTG. Theory of the stability of lyophobic colloids. New York: Elsevier; 1948.
- [128] Danov KD, Basheva ES, Kralchevsky PA, Ananthapadmanabhan KP, Lips A. The metastable states of foam films containing electrically charged micelles or particles: Experiment and quantitative interpretation. *Adv Colloid Interface Sci* 2011;168:50–70.
- [129] Zhang WW, Lister JR. Similarity solutions for van der Waals rupture of a thin film on a solid substrate. *Phys Fluids* 1999;11:2454–62.
- [130] Erneux T, Davis SH. Nonlinear rupture of free films. *Phys Fluids A* 1993;5:1117–22.
- [131] Joanny JF, de Gennes P-G. Upward creep of a wetting fluid : a scaling analysis. *J Phys*

- 1986;47:121–7.
- [132] Vaynblat D, Lister JR, Witelski TP. Rupture of thin films by van der Waals forces: Evolution and self-similarity. *Phys Fluids* 2001;13:1130.
  - [133] Richetti P, Kékicheff P. Direct measurement of depletion and structural forces in a micellar system. *Phys Rev Lett* 1992;68:1951–4.
  - [134] Israelachvili JN, Adams GE. Measurement of forces between two mica surfaces in aqueous electrolyte solutions in the range 0–100 nm. *J Chem Soc Faraday Trans 1 Phys Chem Condens Phases* 1978;74:975.
  - [135] Kralchevsky PA, Denkov ND. Analytical expression for the oscillatory structural surface force. *Chem Phys Lett* 1995;240:385–92.
  - [136] Trokhymchuk A, Henderson D, Nikolov A, Wasan DT. A simple calculation of structural and depletion forces for fluids/suspensions confined in a film. *Langmuir* 2001;17:4940–7.
  - [137] Chu XL, Nikolov AD, Wasan DT. Monte Carlo simulation of inlayer structure formation in thin liquid films. *Langmuir* 1994;10:4403–8.
  - [138] Blawdziewicz J, Wajnryb E. Phase equilibria in stratified thin liquid films stabilized by colloidal particles. *Europhys Lett* 2005;71:7.
  - [139] Christov NC, Danov KD, Zeng Y, Kralchevsky PA, von Klitzing R. Oscillatory structural forces due to nonionic surfactant micelles: Data by colloidal-probe AFM vs theory. *Langmuir* 2010;26:915–23.
  - [140] Pollard ML, Radke CJ. Density-functional liquid films modeling of structure and forces in thin micellar. *J Chem Phys* 1994;101:6979–91.
  - [141] Trokhymchuk A, Henderson D, Nikolov A, Wasan DT. Computer modeling of ionic micelle structuring in thin films. *J Phys Chem B* 2003;107:3927–37.
  - [142] Kralchevsky PA, Danov KD, Anachkov SE. Depletion forces in thin liquid films due to nonionic and ionic surfactant micelles. *Curr Opin Colloid Interface Sci* 2015;20:11–8.
  - [143] de Gennes P-G. Wetting: Statics and dynamics. *Rev Mod Phys* 1985;57:827–63.
  - [144] Bonn D, Eggers J, Indekeu J, Meunier J. Wetting and spreading. *Rev Mod Phys* 2009;81:739–805.
  - [145] Kalliadasis S, Thiele U. Thin films of soft matter. New York: Springer; 2007.
  - [146] Mukherjee R, Sharma A. Instability, self-organization and pattern formation in thin soft films. *Soft Matter* 2015;11:8717–40.
  - [147] Karakashev SI, Manev ED. Hydrodynamics of thin liquid films: Retrospective and perspectives. *Adv Colloid Interface Sci* 2015;222:398–412.
  - [148] Danov K, Valkovska D, Ivanov I. Effect of surfactants on the film drainage. *J Colloid Interface Sci* 1999;211:291–303.
  - [149] Saint-Jalmes A. Physical chemistry in foam drainage and coarsening. *Soft Matter* 2006;2:836.
  - [150] Tsekov R, Ruckenstein E. Dimple formation and its effect on the rate of drainage in thin

- liquid films. *Colloids Surfaces A Physicochem Eng Asp* 1994;82:255–61.
- [151] Chan DYC, Klaseboer E, Manica R. Film drainage and coalescence between deformable drops and bubbles. *Soft Matter* 2011;7:2235.
  - [152] Joye J-L, Hirasak GJ, Miller CA. Asymmetric drainage in foam films. *Langmuir* 1994;3174–9.
  - [153] Reynolds O. On the theory of lubrication and its application to Mr. Beauchamp Tower's experiments, including an experimental determination of the viscosity of olive oil. *Philos Trans R Soc London* 1886;177:157–234.
  - [154] Middleman S. Modeling axisymmetric flows: dynamics of films, jets and drops. San Diego: Academic Press; 1995.
  - [155] Bouchama F, di Meglio J-M. Rheological studies of freely suspended soap films. *Colloid Polym Sci* 2000;278:195–201.
  - [156] Stevenson P. Remarks on the shear viscosity of surfaces stabilised with soluble surfactants. *J Colloid Interface Sci* 2005;290:603–6.
  - [157] Zell ZA, Nowbahar A, Mansard V, Leal LG, Deshmukh SS, Mecca JM, et al. Surface shear inviscidity of soluble surfactants. *Proc Natl Acad Sci U S A* 2014;111:3677–82.
  - [158] Németh Z, Sedev R, Ivanova R, Kolarov T, Exerowa D. Thinning of microscopic foam films formed from a mixture of bovine serum albumin and Pluronic L62. *Colloids Surfaces A Physicochem Eng Asp* 1999;149:179–84.
  - [159] Sedev R, Exerowa D. DLVO and non-DLVO surface forces in foam films from amphiphilic block copolymers. *Adv Colloid Interface Sci* 1999;83:111–36.
  - [160] Sharma V, Jaishankar A, Wang Y, Mckinley GH. Rheology of globular proteins: apparent yield stress, high shear rate viscosity and interfacial viscoelasticity of bovine serum albumin solutions. *Soft Matter* 2011;7:5150–60.
  - [161] Monteux C, Fuller GG, Bergeron V. Shear and dilational surface rheology of oppositely charged polyelectrolyte/surfactant microgels adsorbed at the air-water interface. influence on foam stability. *J Phys Chem B* 2004;108:16473–82.
  - [162] Saint-Jalmes A, Peugeot ML, Ferraz H, Langevin D. Differences between protein and surfactant foams: Microscopic properties, stability and coarsening. *Colloids Surfaces A Physicochem Eng Asp* 2005;263:219–25.
  - [163] Thete SS, Anthony C, Basaran OA, Doshi P. Self-similar rupture of thin free films of power-law fluids. *Phys Rev E* 2015;92:23014.
  - [164] Ilton M, Couchman MMP, Salez T, Fowler PD, Rapha E, Dalnoki-veress K. Capillary levelling of free-standing liquid nanofilms 2016;arXiv:1602.05538v1.
  - [165] Huh C, Scriven LE. Hydrodynamic model of steady movement of a solid/liquid/fluid contact line. *J Colloid Interface Sci* 1971;35:85–101.
  - [166] Elizabeth B. Dussan V. SHD. On the motion of a fluid-fluid interface. *J Fluid Mech* 1974;65:71.
  - [167] Blossey R. Thin liquid films: Dewetting and polymer flow (theoretical and mathematical



- physics). Dordrecht: Springer; 2012.
- [168] Baumchen O, Jacobs K. Slip effects in polymer thin films. *J Phys Condens Matter* 2010;22:33102.
  - [169] de Gennes P-G. Viscometric flows of tangled polymers. *Proc Acad Sci Ser B* 1979;288:219–20.
  - [170] Brochard-Wyart F, Gay C, de Gennes P-G. Slippage of polymer melts on grafted surfaces. *Macromolecules* 1996;29:377–82.
  - [171] Redon C, Brochard-Wyart F, Rondelez F. Dynamics of dewetting. *Phys Rev Lett* 1991;66:715–8.
  - [172] Redon C, Brzoska JB, Brochard-Wyart F. Dewetting and slippage of microscopic polymer films. *Macromolecules* 1994;27:468–71.
  - [173] Reiter G, Khanna R. Real-time determination of the slippage length in autophobic polymer dewetting. *Phys Rev Lett* 2000;85:2753–6.
  - [174] Damman P, Baudelet N, Reiter G. Dewetting near the glass transition: transition from a capillary force dominated to a dissipation dominated regime. *Phys Rev Lett* 2003;91:216101.
  - [175] Brochard-Wyart F, de Gennes P-G, Hervet H, Redon C. Wetting and slippage of polymer melts on semi-ideal surfaces. *Langmuir* 1994;10:1566–72.
  - [176] Reiter G, Sharma A. Auto-optimization of dewetting rates by rim instabilities in slipping polymer films. *Phys Rev Lett* 2001;87:166103.
  - [177] Bäümchen O, Marquant L, Blossey R, Münch A, Wagner B, Jacobs K. Influence of slip on the Rayleigh-Plateau rim instability in dewetting viscous films. *Phys Rev Lett* 2014;113:14501.
  - [178] Brochard-Wyart F, Redon C. Dynamics of liquid rim instabilities. *Langmuir* 1992;8:2324–9.
  - [179] Radoëv BP, Dimitrov DS, Ivanov IB. Hydrodynamics of thin liquid films effect of the surfactant on the rate of thinning. *Colloid Polym Sci* 1974;252:50–5.
  - [180] Ivanov IB, Dimitrov DS. Hydrodynamics of thin liquid films. *Colloid Polym Sci* 1974;252:982–90.
  - [181] Barber AD, Hartland S. Effects of surface viscosity on the axisymmetric drainage of planar liquid films. *Can J Chem Eng* 1976;54:279–84.
  - [182] Singh G, Hirasaki G, Miller C. Effect of material properties on the drainage of symmetric, plane parallel, mobile foam films. *J Colloid Interface Sci* 1996;184:92–105.
  - [183] Karakashev SI, Nguyen AV. Effect of sodium dodecyl sulphate and dodecanol mixtures on foam film drainage: Examining influence of surface rheology and intermolecular forces. *Colloids Surfaces A Physicochem Eng Asp* 2007;293:229–40.
  - [184] Karakashev SI, Ivanova DS. Thin liquid film drainage: Ionic vs. non-ionic surfactants. *J Colloid Interface Sci* 2010;343:584–93.
  - [185] Karakashev SI, Tsekov R. Electro-marangoni effect in thin liquid films. *Langmuir*

- 2011;27:2265–70.
- [186] Karakashev SI, Tsekov R, Ivanova DS. Dynamic effects in thin liquid films containing ionic surfactants. *Colloids Surfaces A Physicochem Eng Asp* 2010;356:40–5.
  - [187] Tsekov R, Ivanova DS, Slavchov R, Radoev B, Manev ED, Nguyen A V., et al. Streaming potential effect on the drainage of thin liquid films stabilized by ionic surfactants. *Langmuir* 2010;26:4703–8.
  - [188] Sharma A, Khanna R. Pattern formation in unstable thin liquid films under the influence of antagonistic short- and long-range forces. *J Chem Phys* 1999;110:4929–36.
  - [189] Becker J, Grün G, Seemann R, Mantz H, Jacobs K, Mecke KR, et al. Complex dewetting scenarios captured by thin-film models. *Nat Mater* 2003;2:59–63.
  - [190] Ghatak A, Khanna R, Sharma A. Dynamics and morphology of holes in dewetting of thin films. *J Colloid Interf Sci* 1999;212:483–94.
  - [191] Sharma A, Verma R. Pattern formation and dewetting in thin films of liquids showing complete macroscale wetting: from “pancakes” to “swiss cheese.” *Langmuir* 2004;20:10337–45.
  - [192] Seemann R, Herminghaus S, Jacobs K. Dewetting patterns and molecular forces: A reconciliation. *Phys Rev Lett* 2001;86:5534–7.
  - [193] Sharma A. Equilibrium contact angles and film thicknesses in the apolar and polar systems: role of intermolecular interactions in coexistence of drops with thin films. *Langmuir* 1993;9:3580–6.
  - [194] Sharma A, Khanna R. Pattern formation in unstable thin liquid films. *Phys Rev Lett* 1998;81:3463–6.
  - [195] Reiter G. Dewetting of highly elastic thin polymer films. *Phys Rev Lett* 2001;87:18–21.
  - [196] Brochard-Wyart F, Debregeas G, Fondecave R, Martin P. Dewetting of supported viscoelastic polymer films: birth of rims. *Macromolecules* 1997;30:1211–3.
  - [197] Reiter G, Hamieh M, Damman P, Sclavons S, Gabriele S, Vilmin T, et al. Residual stresses in thin polymer films cause rupture and dominate early stages of dewetting. *Nat Mater* 2005;4:754–8.
  - [198] Reiter G. Probing properties of polymers in thin films via dewetting. In: Kanaya T, editor. *Glass Transition, Dynamics and Heterogeneity of Polymer Thin Films*, Berlin, Heidelberg: Springer Berlin Heidelberg; 2012, p. 29–63.
  - [199] Snoeijer JH, Eggers J. Asymptotics of the dewetting rim. *Phys Rev E* 2010;82:56314.
  - [200] Seemann R, Herminghaus S, Jacobs K. Shape of a liquid front upon dewetting. *Phys Rev Lett* 2001;87:196101.
  - [201] Bäumchen O, Fetzer R, Klos M, Lessel M, Marquant L, Hähl H, et al. Slippage and nanorheology of thin liquid polymer films. *J Phys Condens Matter* 2012;24:325102.
  - [202] Duyvis EM. The equilibrium thickness of free liquid films. BOOK. Drukkerij Pasmans, 1962.
  - [203] Adelizzi EA, Troian SM. Interfacial slip in entrained soap films containing associating

- hydrosoluble polymer. *Langmuir* 2004;20:7482–92.
- [204] Berg S, Adelizzi EA, Troian SM. Experimental study of entrainment and drainage flows in microscale soap films. *Langmuir* 2005;21:3867–76.
  - [205] Exerowa D, Kruglyakov PM. Foam and foam films: theory, experiment, application. Amsterdam: Elsevier; 1998.
  - [206] Wasan DT, Nikolov AD. Thin liquid films containing micelles or nanoparticles. *Curr Opin Colloid Interface Sci* 2008;13:128–33.
  - [207] Patist A, Kanicky JR, Shukla PK, Shah DO. Importance of micellar kinetics in relation to technological processes. *J Colloid Interface Sci* 2002;245:1–15.
  - [208] Tulpar A, Van Tassel PR, Walz JY. Structuring of macroions confined between like-charged surfaces. *Langmuir* 2006;22:2876–83.
  - [209] Pollard ML, Radke CJ. Effective viscosities in thin ionic micellar liquid films. *AIChE J* 1996;42:2005–13.
  - [210] Hoot JE. Photometry with DSLR cameras. The Society for Astronomical Sciences 26th Annual Symposium on Telescope Science, 2007, p. 67–72.
  - [211] Jensen TJ. Budget astrophotography: Imaging with your DSLR or webcam. Springer; 2015.
  - [212] Kloppenborg BBK, Pieri R, Eggenstein H-BB, Maravellias G, Pearson T, Maravelias G. A demonstration of accurate wide-field V-band photometry using a consumer-grade DSLR camera. *J Am Assoc Var Star Obs* 2012;40:815–33.
  - [213] Sharma V, Park K, Srinivasarao M. Colloidal dispersion of gold nanorods: Historical background, optical properties, seed-mediated synthesis, shape separation and self-assembly. *Mater Sci Eng R Reports* 2009;65:1–38.
  - [214] Schwaebel T, Menning S, Bunz UHF. Photoscopy: spectroscopic information from camera snapshots? *Chem Sci* 2014;5:1422.
  - [215] Garcia JE, Wilksch PA, Spring G, Philp P, Dyer A. Characterization of digital cameras for reflected ultraviolet photography; Implications for qualitative and quantitative image analysis during forensic examination. *J Forensic Sci* 2014;59:117–22.
  - [216] Sharma V, Crne M, Park JO, Srinivasarao M, Ghiradella H, Srinivasarao M, et al. Structural origin of circularly polarized iridescence in jeweled beetles. *Science* 2009;325:449–51.
  - [217] Sharma V, Crne M, Park JO, Srinivasarao M. Bouligand structures underlie circularly polarized iridescence of scarab beetles: a closer view. *Mater Today Proc* 2014;1:161–71.
  - [218] Pike TW. Using digital cameras to investigate animal colouration: Estimating sensor sensitivity functions. *Behav Ecol Sociobiol* 2011;65:849–58.
  - [219] Garcia JE, Rohr D, Dyer AG, Anderson M, Andersson S, Örnberg J, et al. Trade-off between camouflage and sexual dimorphism revealed by UV digital imaging: the case of Australian Mallee dragons (*Ctenophorus fordii*). *J Exp Biol* 2013;216:4290–8.
  - [220] Hervet H, de Gennes P-G. The dynamics of wetting: Precursor films in the wetting of “dry” solids. *C R Acad Sci* 1984;299 II:499–503.
  - [221] Starov VM, Velarde MG, Radke CJ. Wetting and spreading dynamics. CRC press; 2007.

- [222] Brochard-Wyart F, Martin P, Redon C. Liquid/liquid dewetting. *Langmuir* 1993;9:3682–90.
- [223] Brenner MP, Gueyffier D. On the bursting of viscous films. *Phys Fluids* 1999;11:737–9.
- [224] Fetzer R, Jacobs K, Münch A, Wagner B, Witelski TP. New slip regimes and the shape of dewetting thin liquid films. *Phys Rev Lett* 2005;95:127801.
- [225] Gabriele S, Coppée S, Reiter G, Damman P. On the mechanics of rim instabilities in viscoelastic polymer thin films. *Eur Phys J Spec Top* 2009;166:55–61.
- [226] Malhotra AK, Wasan DT. Stability of foam and emulsion films: effects of the drainage and film size on critical thickness of rupture. *Chem Eng Commun* 1986;48:35–56.
- [227] Kuchin IV, Matar OK, Craster RV, Starov VM. Influence of the disjoining pressure on the equilibrium interfacial profile in transition zone between a thin film and a capillary meniscus. *Colloids Interface Sci Commun* 2014;1:18–22.
- [228] Ivanov IB, Toshev BV. Thermodynamics of thin liquid films - II. Film thickness and its relation to the surface tension and the contact angle. *Colloid Polym Sci* 1975;253:593–9.
- [229] Carslaw HS, Jaeger JC. *Conduction of heat in solids*. 2nd ed. Oxford: Oxford University Press; 1959.
- [230] Brochard-Wyart F, Daillant J. Drying of solids wetted by thin liquid films. *Can J Phys* 1990;68:1084–8.
- [231] Vilmin T, Raphaël E, Damman P, Sclavons S, Gabriele S, Hamieh M, et al. The role of nonlinear friction in the dewetting of thin polymer films. *Europhys Lett* 2006;73:906–12.
- [232] Edmonstone BD, Craster R V., Matar OK. Surfactant-induced fingering phenomena beyond the critical micelle concentration. *J Fluid Mech* 2006;564:105.
- [233] Sonin A., Bonfillon A, Langevin D. Thinning of soap films: The role of surface viscoelasticity. *J Colloid Interface Sci* 1994;162:323–30.
- [234] Quina FH, Nassar PM, Bonilha JBS, Bales BL. Growth of sodium dodecyl sulfate micelles with detergent concentration. *J Phys Chem* 1995;99:17028–31.
- [235] Sasaki T, Hattori M, Sasaki J, Nukina K. Studies of aqueous sodium dodecyl sulfate solutions by activity measurements. *Bull Chem Soc Jpn* 1975;48:1397–403.
- [236] Bales BL, Almgren M. Fluorescence quenching of pyrene by copper(II) in sodium dodecyl sulfate micelles. Effect of micelle size as controlled by surfactant concentration. *J Phys Chem* 1995;99:15153–62.
- [237] Jalili S, Akhavan M. A coarse-grained molecular dynamics simulation of a sodium dodecyl sulfate micelle in aqueous solution. *Colloids Surfaces A Physicochem Eng Asp* 2009;352:99–102.
- [238] Bruce CD, Berkowitz ML, Perera L, Forbes MDE. Molecular dynamics simulation of sodium dodecyl sulfate micelle in water: Micellar structural characteristics and counterion distribution. *J Phys Chem B* 2002;106:3788–93.
- [239] Itri, R.; Amaral LQ. Distance distribution function of sodium dodecyl sulfate micelles by x-ray scattering. *J Phys Chem* 1991;95:423–7.

- [240] Diez JA, Kondic L. Computing three-dimensional thin film flows including contact lines. *J Comput Phys* 2002;183:274–306.
- [241] Klapp SHL, Grandner S, Zeng Y, von Klitzing R. Charged silica suspensions as model materials for liquids in confined geometries. *Soft Matter* 2010;6:2330.
- [242] Stone HA, McConnell HM. Hydrodynamics of quantized shape transitions of lipid domains. *Proc R Soc A Math Phys Eng Sci* 1995;448:97–111.
- [243] Dai B, Leal LG, Redondo A. Disjoining pressure for nonuniform thin films. *Phys Rev E - Stat Nonlinear, Soft Matter Phys* 2008;78:1–9.

## APPENDIX

This appendix includes permissions or licenses obtained for reprinted figures and tables from the holders of copyright. The reprinted figures & tables in this study and their sources:

### Figure 1.5

[73] Kralchevsky P, Nikolov A, Wasan D, Ivanov I. Formation and expansion of dark spots in stratifying foam films. *Langmuir* 1990;6:1180–9.

### Figure 1.6

[79] Bergeron V, Radke C. Hole formation and sheeting in the drainage of thin liquid films. *Langmuir* 1992;8:3027–32.

### Figure 1.10

[104] Bergeron V, Radke C. Equilibrium measurements of oscillatory disjoining pressures in aqueous foam films. *Langmuir* 1992;1:3020–6.

### Figure 1.15

[176] Reiter G, Sharma A. Auto-optimization of dewetting rates by rim instabilities in slipping polymer films. *Phys Rev Lett* 2001;87:166103.

[198] Reiter G. Probing properties of polymers in thin Films via dewetting. In: Kanaya T, editor. *Glas. Transition, Dyn. Heterog. Polym. Thin Film.*, Berlin, Heidelberg: Springer Berlin Heidelberg; 2012, p. 29–63.

### Figure 2.3, 2.6, 2.7, 2.8, 2.9, 2.14 (Published as the first author)

[31] Zhang Y, Yilixiati S, Pearsall C, Sharma V. Nanoscopic terraces, mesas, and ridges in freely standing thin films sculpted by supramolecular oscillatory surface forces. *ACS Nano* 2016;10:4678–83.

### Figure 2.2, 3.2, 3.3, 3.4, 3.5, 3.8, Table V (Published as the first author)

[81] Zhang Y, Sharma V. Domain expansion dynamics in stratifying foam films: experiments. *Soft Matter* 2015;11:4408–17.

The permissions or licenses are listed in the order above.



# RightsLink®

[Home](#)
[Create Account](#)
[Help](#)


**Title:** Formation and expansion of dark spots in stratifying foam films

**Author:** P. Kralchevski, A. Nikolov, D. T. Wasan, et al

**Publication:** Langmuir

**Publisher:** American Chemical Society

**Date:** Jun 1, 1990

Copyright © 1990, American Chemical Society

**LOGIN**

If you're a **copyright.com** user, you can login to RightsLink using your copyright.com credentials. Already a **RightsLink** user or want to [learn more?](#)

## PERMISSION/LICENSE IS GRANTED FOR YOUR ORDER AT NO CHARGE

This type of permission/license, instead of the standard Terms & Conditions, is sent to you because no fee is being charged for your order. Please note the following:

- Permission is granted for your request in both print and electronic formats, and translations.
- If figures and/or tables were requested, they may be adapted or used in part.
- Please print this page for your records and send a copy of it to your publisher/graduate school.
- Appropriate credit for the requested material should be given as follows: "Reprinted (adapted) with permission from (COMPLETE REFERENCE CITATION). Copyright (YEAR) American Chemical Society." Insert appropriate information in place of the capitalized words.
- One-time permission is granted only for the use specified in your request. No additional uses are granted (such as derivative works or other editions). For any other uses, please submit a new request.

If credit is given to another source for the material you requested, permission must be obtained from that source.

[BACK](#)
[CLOSE WINDOW](#)

Copyright © 2016 [Copyright Clearance Center, Inc.](#) All Rights Reserved. [Privacy statement](#). [Terms and Conditions](#). Comments? We would like to hear from you. E-mail us at [customercare@copyright.com](mailto:customercare@copyright.com)

**RightsLink®**[Home](#)[Create Account](#)[Help](#)

**Title:** Hole formation and sheeting in the drainage of thin liquid films  
**Author:** V. Bergeron, A. I. Jimenez-Laguna, C. J. Radke  
**Publication:** Langmuir  
**Publisher:** American Chemical Society  
**Date:** Dec 1, 1992

Copyright © 1992, American Chemical Society

[LOGIN](#)

If you're a **copyright.com** user, you can login to RightsLink using your copyright.com credentials. Already a **RightsLink** user or want to [learn more?](#)

**PERMISSION/LICENSE IS GRANTED FOR YOUR ORDER AT NO CHARGE**

This type of permission/license, instead of the standard Terms & Conditions, is sent to you because no fee is being charged for your order. Please note the following:

- Permission is granted for your request in both print and electronic formats, and translations.
- If figures and/or tables were requested, they may be adapted or used in part.
- Please print this page for your records and send a copy of it to your publisher/graduate school.
- Appropriate credit for the requested material should be given as follows: "Reprinted (adapted) with permission from (COMPLETE REFERENCE CITATION). Copyright (YEAR) American Chemical Society." Insert appropriate information in place of the capitalized words.
- One-time permission is granted only for the use specified in your request. No additional uses are granted (such as derivative works or other editions). For any other uses, please submit a new request.

If credit is given to another source for the material you requested, permission must be obtained from that source.

[BACK](#)[CLOSE WINDOW](#)

Copyright © 2016 [Copyright Clearance Center, Inc.](#) All Rights Reserved. [Privacy statement.](#) [Terms and Conditions.](#)  
Comments? We would like to hear from you. E-mail us at [customer care@copyright.com](mailto:customer care@copyright.com)





# RightsLink®

[Home](#)
[Create Account](#)
[Help](#)


**ACS Publications**  
Most Trusted. Most Cited. Most Read.

**Title:** Equilibrium measurements of oscillatory disjoining pressures in aqueous foam films

**Author:** V. Bergeron, C. J. Radke

**Publication:** Langmuir

**Publisher:** American Chemical Society

**Date:** Dec 1, 1992

Copyright © 1992, American Chemical Society

[LOGIN](#)

If you're a **copyright.com** user, you can login to RightsLink using your copyright.com credentials. Already a **RightsLink** user or want to [learn more?](#)

## PERMISSION/LICENSE IS GRANTED FOR YOUR ORDER AT NO CHARGE

This type of permission/license, instead of the standard Terms & Conditions, is sent to you because no fee is being charged for your order. Please note the following:

- Permission is granted for your request in both print and electronic formats, and translations.
- If figures and/or tables were requested, they may be adapted or used in part.
- Please print this page for your records and send a copy of it to your publisher/graduate school.
- Appropriate credit for the requested material should be given as follows: "Reprinted (adapted) with permission from (COMPLETE REFERENCE CITATION). Copyright (YEAR) American Chemical Society." Insert appropriate information in place of the capitalized words.
- One-time permission is granted only for the use specified in your request. No additional uses are granted (such as derivative works or other editions). For any other uses, please submit a new request.

If credit is given to another source for the material you requested, permission must be obtained from that source.

[BACK](#)
[CLOSE WINDOW](#)

Copyright © 2016 [Copyright Clearance Center, Inc.](#) All Rights Reserved. [Privacy statement](#). [Terms and Conditions](#).  
Comments? We would like to hear from you. E-mail us at [customercare@copyright.com](mailto:customercare@copyright.com)

# AMERICAN PHYSICAL SOCIETY LICENSE TERMS AND CONDITIONS

Aug 26, 2016

This Agreement between Yiran Zhang ("You") and American Physical Society ("American Physical Society") consists of your license details and the terms and conditions provided by American Physical Society and Copyright Clearance Center.

License Number	3936351433450
License date	Aug 26, 2016
Licensed Content Publisher	American Physical Society
Licensed Content Publication	Physical Review Letters
Licensed Content Title	Auto-Optimization of Dewetting Rates by Rim Instabilities in Slipping Polymer Films
Licensed Content Author	Günter Reiter and Ashutosh Sharma
Licensed Content Date	Oct 1, 2001
Licensed Content Volume Number	87
Type of Use	Thesis/Dissertation
Requestor type	Student
Format	Electronic
Portion	image/photo
Number of images/photos requested	1
Portion description	Figure 1
Rights for	Main product
Duration of use	Life of Current Edition
Creation of copies for the disabled	no
With minor editing privileges	no
For distribution to	United States
In the following language(s)	Original language of publication
With incidental promotional use	no
The lifetime unit quantity of new product	0 to 499
The requesting person/organization is:	Yiran Zhang
Order reference number	
Title of your thesis / dissertation	Dynamics of Stratifying Foam Films
Expected completion date	Sep 2016
Expected size (number of pages)	200

Requestor Location	Yiran Zhang 810 S Cliton St.  CHICAGO, IL 60607 United States Attn: Yiran Zhang
Billing Type	Invoice
Billing Address	Yiran Zhang 810 S Cliton St.  CHICAGO, IL 60607 United States Attn: Yiran Zhang
Total	0.00 USD
Terms and Conditions	

### Terms and Conditions

The American Physical Society (APS) is pleased to grant the Requestor of this license a non-exclusive, non-transferable permission, limited to **[print and/or electronic]** format, depending on what they chose, provided all criteria outlined below are followed.

1. You must also obtain permission from at least one of the lead authors for each separate work, if you haven't done so already. The author's name and affiliation can be found on the first page of the published Article.
2. For electronic format permissions, Requestor agrees to provide a hyperlink from the reprinted APS material using the source material's DOI on the web page where the work appears. The hyperlink should use the standard DOI resolution URL, <http://dx.doi.org/{DOI}>. The hyperlink may be embedded in the copyright credit line.
3. For print format permissions, Requestor agrees to print the required copyright credit line on the first page where the material appears: "Reprinted (abstract/excerpt/figure) with permission from [(FULL REFERENCE CITATION) as follows: Author's Names, APS Journal Title, Volume Number, Page Number and Year of Publication.] Copyright (YEAR) by the American Physical Society."
4. Permission granted in this license is for a one-time use and does not include permission for any future editions, updates, databases, formats or other matters. Permission must be sought for any additional use.
5. Use of the material does not and must not imply any endorsement by APS.
6. Under no circumstance does APS purport or intend to grant permission to reuse materials to which it does not hold copyright. It is the requestors sole responsibility to ensure the licensed material is original to APS and does not contain the copyright of another entity, and that the copyright notice of the figure, photograph, cover or table does not indicate that it was reprinted by APS, with permission from another source.
7. The permission granted herein is personal to the Requestor for the use specified and is not transferable or assignable without express written permission of APS. This license may not be amended except in writing by APS.
8. You may not alter, edit or modify the material in any manner.
9. You may translate the materials only when translation rights have been granted.
10. You may not use the material for promotional, sales, advertising or marketing purposes.
11. The foregoing license shall not take effect unless and until APS or its agent, Copyright Clearance Center (CCC), receives payment in full in accordance with CCC Billing and Payment Terms and Conditions, which are incorporated herein by reference.
12. Should the terms of this license be violated at any time, APS or CCC may revoke the license with no refund to you and seek relief to the fullest extent of the laws of the USA.

Official written notice will be made using the contact information provided with the permission request. Failure to receive such notice will not nullify revocation of the permission.

13. APS reserves all rights not specifically granted herein.

14. This document, including the CCC Billing and Payment Terms and Conditions, shall be the entire agreement between the parties relating to the subject matter hereof.

**Other Terms and Conditions**

Version 1.1

**Questions? [customercare@copyright.com](mailto:customercare@copyright.com) or +1-855-239-3415 (toll free in the US) or +1-978-646-2777.**

---

**SPRINGER LICENSE  
TERMS AND CONDITIONS**

Aug 26, 2016

This Agreement between Yiran Zhang ("You") and Springer ("Springer") consists of your license details and the terms and conditions provided by Springer and Copyright Clearance Center.

License Number	3936321227817
License date	Aug 26, 2016
Licensed Content Publisher	Springer
Licensed Content Publication	Springer eBook
Licensed Content Title	Probing Properties of Polymers in Thin Films Via Dewetting
Licensed Content Author	Günter Reiter
Licensed Content Date	Jan 1, 2012
Type of Use	Thesis/Dissertation
Portion	Figures/tables/illustrations
Number of figures/tables/illustrations	1
Author of this Springer article	No
Order reference number	
Original figure numbers	figure 4
Title of your thesis / dissertation	Dynamics of Stratifying Foam Films
Expected completion date	Sep 2016
Estimated size(pages)	200
Requestor Location	Yiran Zhang 810 S Cliton St.  CHICAGO, IL 60607 United States Attn: Yiran Zhang
Billing Type	Invoice
Billing Address	Yiran Zhang 810 S Cliton St.  CHICAGO, IL 60607 United States Attn: Yiran Zhang
Total	0.00 USD
Terms and Conditions	

**Introduction**

The publisher for this copyrighted material is Springer. By clicking "accept" in connection with completing this licensing transaction, you agree that the following terms and conditions



apply to this transaction (along with the Billing and Payment terms and conditions established by Copyright Clearance Center, Inc. ("CCC"), at the time that you opened your Rightslink account and that are available at any time at <http://myaccount.copyright.com>).

#### Limited License

With reference to your request to reuse material on which Springer controls the copyright, permission is granted for the use indicated in your enquiry under the following conditions:

- Licenses are for one-time use only with a maximum distribution equal to the number stated in your request.

- Springer material represents original material which does not carry references to other sources. If the material in question appears with a credit to another source, this permission is not valid and authorization has to be obtained from the original copyright holder.

- This permission

- is non-exclusive
- is only valid if no personal rights, trademarks, or competitive products are infringed.
- explicitly excludes the right for derivatives.

- Springer does not supply original artwork or content.

- According to the format which you have selected, the following conditions apply accordingly:

• **Print and Electronic:** This License include use in electronic form provided it is password protected, on intranet, or CD-Rom/DVD or E-book/E-journal. It may not be republished in electronic open access.

• **Print:** This License excludes use in electronic form.

• **Electronic:** This License only pertains to use in electronic form provided it is password protected, on intranet, or CD-Rom/DVD or E-book/E-journal. It may not be republished in electronic open access.

For any electronic use not mentioned, please contact Springer at [permissions.springer@spi-global.com](mailto:permissions.springer@spi-global.com).

- Although Springer controls the copyright to the material and is entitled to negotiate on rights, this license is only valid subject to courtesy information to the author (address is given in the article/chapter).

- If you are an STM Signatory or your work will be published by an STM Signatory and you are requesting to reuse figures/tables/illustrations or single text extracts, permission is granted according to STM Permissions Guidelines: <http://www.stm-assoc.org/permissions-guidelines/>

For any electronic use not mentioned in the Guidelines, please contact Springer at [permissions.springer@spi-global.com](mailto:permissions.springer@spi-global.com). If you request to reuse more content than stipulated in the STM Permissions Guidelines, you will be charged a permission fee for the excess content.

Permission is valid upon payment of the fee as indicated in the licensing process. If permission is granted free of charge on this occasion, that does not prejudice any rights we might have to charge for reproduction of our copyrighted material in the future.

-If your request is for reuse in a Thesis, permission is granted free of charge under the following conditions:

This license is valid for one-time use only for the purpose of defending your thesis and with a maximum of 100 extra copies in paper. If the thesis is going to be published, permission needs to be reobtained.

- includes use in an electronic form, provided it is an author-created version of the thesis on his/her own website and his/her university's repository, including UMI (according to the definition on the Sherpa website: <http://www.sherpa.ac.uk/romeo/>);

- is subject to courtesy information to the co-author or corresponding author.

#### Geographic Rights: Scope

Licenses may be exercised anywhere in the world.

Altering/Modifying Material: Not Permitted

Figures, tables, and illustrations may be altered minimally to serve your work. You may not

alter or modify text in any manner. Abbreviations, additions, deletions and/or any other alterations shall be made only with prior written authorization of the author(s).

#### Reservation of Rights

Springer reserves all rights not specifically granted in the combination of (i) the license details provided by you and accepted in the course of this licensing transaction and (ii) these terms and conditions and (iii) CCC's Billing and Payment terms and conditions.

#### License Contingent on Payment

While you may exercise the rights licensed immediately upon issuance of the license at the end of the licensing process for the transaction, provided that you have disclosed complete and accurate details of your proposed use, no license is finally effective unless and until full payment is received from you (either by Springer or by CCC) as provided in CCC's Billing and Payment terms and conditions. If full payment is not received by the date due, then any license preliminarily granted shall be deemed automatically revoked and shall be void as if never granted. Further, in the event that you breach any of these terms and conditions or any of CCC's Billing and Payment terms and conditions, the license is automatically revoked and shall be void as if never granted. Use of materials as described in a revoked license, as well as any use of the materials beyond the scope of an unrevoked license, may constitute copyright infringement and Springer reserves the right to take any and all action to protect its copyright in the materials.

#### Copyright Notice: Disclaimer

You must include the following copyright and permission notice in connection with any reproduction of the licensed material:

"Springer book/journal title, chapter/article title, volume, year of publication, page, name(s) of author(s), (original copyright notice as given in the publication in which the material was originally published) "With permission of Springer"

In case of use of a graph or illustration, the caption of the graph or illustration must be included, as it is indicated in the original publication.

#### Warranties: None

Springer makes no representations or warranties with respect to the licensed material and adopts on its own behalf the limitations and disclaimers established by CCC on its behalf in its Billing and Payment terms and conditions for this licensing transaction.

#### Indemnity

You hereby indemnify and agree to hold harmless Springer and CCC, and their respective officers, directors, employees and agents, from and against any and all claims arising out of your use of the licensed material other than as specifically authorized pursuant to this license.

#### No Transfer of License

This license is personal to you and may not be sublicensed, assigned, or transferred by you without Springer's written permission.

#### No Amendment Except in Writing

This license may not be amended except in a writing signed by both parties (or, in the case of Springer, by CCC on Springer's behalf).

#### Objection to Contrary Terms

Springer hereby objects to any terms contained in any purchase order, acknowledgment, check endorsement or other writing prepared by you, which terms are inconsistent with these terms and conditions or CCC's Billing and Payment terms and conditions. These terms and conditions, together with CCC's Billing and Payment terms and conditions (which are incorporated herein), comprise the entire agreement between you and Springer (and CCC) concerning this licensing transaction. In the event of any conflict between your obligations established by these terms and conditions and those established by CCC's Billing and Payment terms and conditions, these terms and conditions shall control.

#### Jurisdiction

All disputes that may arise in connection with this present License, or the breach thereof,

8/26/2016

RightsLink Printable License

shall be settled exclusively by arbitration, to be held in the Federal Republic of Germany, in accordance with German law.

**Other conditions:**

V 12AUG2015

Questions? [customercare@copyright.com](mailto:customercare@copyright.com) or +1-855-239-3415 (toll free in the US) or +1-978-646-2777.

---





# RightsLink®

[Home](#)
[Create Account](#)
[Help](#)


**ACS Publications**  
Most Trusted. Most Cited. Most Read.

**Title:** Nanoscopic Terraces, Mesas, and Ridges in Freely Standing Thin Films Sculpted by Supramolecular Oscillatory Surface Forces

**Author:** Yiran Zhang, Subinuer Yilixiati, Collin Pearsall, et al

**Publication:** ACS Nano

**Publisher:** American Chemical Society

**Date:** Apr 1, 2016

Copyright © 2016, American Chemical Society

[LOGIN](#)

**If you're a copyright.com user,** you can login to RightsLink using your copyright.com credentials. Already **a RightsLink user** or want to [learn more?](#)

## Quick Price Estimate

**Permission for this particular request is granted for print and electronic formats, and translations, at no charge. Figures and tables may be modified. Appropriate credit should be given. Please print this page for your records and provide a copy to your publisher. Requests for up to 4 figures require only this record. Five or more figures will generate a printout of additional terms and conditions. Appropriate credit should read: "Reprinted with permission from {COMPLETE REFERENCE CITATION}. Copyright {YEAR} American Chemical Society." Insert appropriate information in place of the capitalized words.**

**I would like to...** ?

reuse in a Thesis/Dissertation ▼

**Requestor Type** ?

Author (original work) ▼

**Portion** ?

50% or more of original article ▼

**Format** ?

Print and Electronic ▼

**Select your currency**

USD - \$ ▼

**Quick Price**

Click Quick Price

This service provides permission for reuse only. If you do not have a copy of the article you are using, you may copy and paste the content and reuse according to the terms of your agreement. Please be advised that obtaining the content you license is a separate transaction not involving Rightslink.

[QUICK PRICE](#)
[CONTINUE](#)

To request permission for a type of use not listed, please contact [the publisher](#) directly.

Copyright © 2016 [Copyright Clearance Center, Inc.](#) All Rights Reserved. [Privacy statement.](#) [Terms and Conditions.](#) Comments? We would like to hear from you. E-mail us at [customercare@copyright.com](mailto:customercare@copyright.com)

# Domain expansion dynamics in stratifying foam films: experiments

Y. Zhang and V. Sharma, *Soft Matter*, 2015, **11**, 4408

DOI: 10.1039/C5SM00066A

If you are not the author of this article and you wish to reproduce material from it in a third party non-RSC publication you must [formally request permission](#) using RightsLink. Go to our [Instructions for using RightsLink page](#) for details.

Authors contributing to RSC publications (journal articles, books or book chapters) do not need to formally request permission to reproduce material contained in this article provided that the correct acknowledgement is given with the reproduced material.

Reproduced material should be attributed as follows:

- For reproduction of material from NJC:  
Reproduced from Ref. XX with permission from the Centre National de la Recherche Scientifique (CNRS) and The Royal Society of Chemistry.
- For reproduction of material from PCCP:  
Reproduced from Ref. XX with permission from the PCCP Owner Societies.
- For reproduction of material from PPS:  
Reproduced from Ref. XX with permission from the European Society for Photobiology, the European Photochemistry Association, and The Royal Society of Chemistry.
- For reproduction of material from all other RSC journals and books:  
Reproduced from Ref. XX with permission from The Royal Society of Chemistry.

If the material has been adapted instead of reproduced from the original RSC publication "Reproduced from" can be substituted with "Adapted from".

In all cases the Ref. XX is the XXth reference in the list of references.

If you are the author of this article you do not need to formally request permission to reproduce figures, diagrams etc. contained in this article in third party publications or in a thesis or dissertation provided that the correct acknowledgement is given with the reproduced material.

Reproduced material should be attributed as follows:

- For reproduction of material from NJC:  
[Original citation] - Reproduced by permission of The Royal Society of Chemistry (RSC) on behalf of the Centre National de la Recherche Scientifique (CNRS) and the RSC
- For reproduction of material from PCCP:  
[Original citation] - Reproduced by permission of the PCCP Owner Societies
- For reproduction of material from PPS:  
[Original citation] - Reproduced by permission of The Royal Society of Chemistry (RSC) on behalf of the European Society for Photobiology, the European Photochemistry Association, and RSC
- For reproduction of material from all other RSC journals:  
[Original citation] - Reproduced by permission of The Royal Society of Chemistry

If you are the author of this article you still need to obtain permission to reproduce the whole article in a third

## VITA

NAME: Yiran Zhang

EDUCATION: B. Eng. Southeast University, Nanjing, China, 2010  
M.S. New Jersey Institute of Technology, Newark, NJ, 2012  
Ph.D. University of Illinois at Chicago, Chicago, IL, 2016

HONORS: University Fellowship, University of Illinois at Chicago, Chicago, IL, 2016  
Student Travel Awards, Society of Rheology, 2015  
Graduate Student Council Travel Awards, UIC, 2014, 2015

PROFESSIONAL MEMBERSHIP: American Physics Society  
American Chemistry Society  
Society of Rheology

PUBLICATION: Zhang Y, Yilixiati S, Pearsall C, Sharma V. Nanoscopic Terraces, Mesas, and Ridges in Freely Standing Thin Films Sculpted by Supramolecular Oscillatory Surface Forces. *ACS Nano* 2016;10:4678–83.  
Zhang Y, Sharma V. Domain expansion dynamics in stratifying foam films: experiments. *Soft Matter* 2015;11:4408–17.  
Dinic J, Zhang Y, Jimenez LN, Sharma V. Extensional Relaxation Times of Dilute, Aqueous Polymer Solutions. *ACS Macro Lett* 2015;4:804–8.  
Zhang Y, Bredael G, Armenante PM. Dissolution of prednisone tablets in the presence of an arch-shaped fiber optic probe in a USP dissolution testing apparatus 2. *J Pharm Sci* 2013;102:2718–29.